Single Droplet Drying at High Temperatures

Wael Ahmed Mohammed Ebrahim

Submitted in accordance with the requirements for the degree of
Doctor of Philosophy

The University of Leeds
School of Chemical and Process Engineering

August 2019

The candidate confirms that the work submitted is his/her own and that appropriate credit has been given where reference has been made to the work of others.

This copy has been supplied on the understanding that it is copyright material and that no quotation from the thesis may be published without proper acknowledgement.

Acknowledgements

I would like to acknowledge my supervisor Professor Andrew Bayly for his supervision during my PhD studies. I am also very grateful for his feedback during the write-up of this thesis. I would also like to thank my co-supervisor Professor Philip Threlfall-Holmes, for fruitful meetings and his help in the re-modification of the single droplet drying rig.

I would also like to express my thanks to Leeds University technicians namely, Mr Gurdev Singh Bhogal, Mr Kevin Dyer and Mr Robert Harris for their help in the set-up of the single droplet drying rig.

I would also like to acknowledge Mr Karrar Al-Dirawi for his help with the use of the high-speed camera to capture single droplet experiments. I am also grateful to Mr Ahmed Othman and Mr Tien Nguyen for proofreading parts of this thesis.

Last but not least, I would like to express an immense amount of gratitude for my parents for their unconditional support, love and encouragement.

Abstract

Particle formation in spray drying is a complex phenomenon; understanding and predicting the particle structures formed requires a deep understanding of the link between drying kinetics, morphology evolution and key material properties. This is further complicated when drying at high temperatures above the boiling point of the droplet due to boiling driven effects, including internal bubble expansion which can influence morphology evolution and thus results in diverse morphologies. This work investigates the effect of boiling on the drying rate, morphology evolution and the structure of final dried particles. The novelty in the methodology of this work involved the development a single droplet drying apparatus where the mass can be measured directly using a microbalance with a high resolution (six digits to a gram) combined with measurements of the droplet size and temperature. The single droplet drying apparatus was validated by drying pure water droplets. This apparatus is then utilised to measure drying kinetics and monitor the morphology evolution of droplets of aqueous solutions of sucrose, sodium silicate and hydroxypropyl methylcellulose (HPMC), as well as HPMC-acetone-water solutions. To study the effect of boiling on the morphology evolution, drying kinetics and final structures, single droplet drying experiments are conducted at air temperatures in the range of 60-180 ˚C and across a range of initial solute concentrations.

The systematic study on the three different systems (sucrose, silicate and HPMC) enhanced the scope of the work in this thesis and allowed for a comprehensive investigation of drying above the boiling point. The novel elements of this work include the consideration of a film-forming material, HPMC, which interestingly upon drying results in the formation of a skin layer and a phase change which dominate the drying behaviour and suppress the effects of boiling and bubble nucleation. The properties of the skin formed are altered when drying a HPMC-acetone-water system. The use of water/organic solvent mixture to manipulate the skin of the particle and the final morphology at a high temperature range is studied in this work for the first time to the best of our knowledge.

The effect of boiling on the morphology evolution and drying rate are also reported and related to the evolution of rheological and mechanical properties. Drying of sucrose solution droplets results in inflation/deflation cycles, which enhance the evaporation rate. Sucrose droplets exhibit liquid-like behaviour during boiling and thus the droplets collapse at the end of the inflation/deflation cycles. On the other hand, the drying of aqueous solutions of sodium silicate results in inflation and less degree of collapse. As a result, "puffed" dried particles are produced. The differences in behaviours above boiling are further investigated by analysis of drying kinetics such as droplet diameter, droplet temperature and evaporation rate. The structures obtained from the single droplet drying experiments are also compared with laboratory spray drying in the case of drying of aqueous solutions of HPMC or silicate.

Table of Contents

List of Figures

List of Tables

Nomenclature

A	area	mm^2
$C_{p,a}$	heat capacity of air	J/kg.K
$C_{p,w}$	heat capacity of water	J/kg.K
$C_{p,s}$	heat capacity of solid	J/kg.K
d	diameter	mm
d_d	diameter of the droplet	m^2/s
$d_{d,0}$	initial diameter of the droplet	mm
d_l	diameter of the droplet at locking	mm
d_f	final diameter	mm
D	diffusion coefficient of solute	m^2/s
D_v	diffusivity of water vapour in air	m^2/s
h_a	heat transfer coefficient	W/m^2.K
k	evaporation rate	m^2/s
k_a	thermal conductivity of air	W/mol.K
k_B	Boltzmann's constant	
k_m	mass transfer coefficient	m/s
M_w	molecular weight of water	kg/mol
m	mass	kg
m_d	mass of the droplet	kg
m_w	mass of water	kg
m_s	mass of solid	kg
p	pressure	Pascal
P_T	total pressure	Pascal
p_{sat}	saturated vapour pressure	Pascal
R	universal gas constant	J/K.mol
r	radius	mm
r_d	radius of the droplet	mm
r_H	hydrodynamic radius of a molecule	mm
t	time	s
T_d	temperature of the droplet	K
T_{air}	temperature of the air	K
T_{avg}	film temperature	K
v	velocity	m/s
v_{air}	velocity of the air	m/s
x	weight fraction	
x_w	weight fraction of water	
x_s	weight fraction of solids	
$y_{v,s}$	water vapour mole fraction at the droplet surface	
$y_{v,a}$	water vapour mole fraction in air	

Dimensionless numbers

Nu Nusselt number
Pe Péclet number
Pr Prandtl number
Re Reynolds number
Sh Sherwood number
Sc Schmidt number

Greek letters

μ viscosity   kg/m.s
λ Latent heat of vaporisation   J/kg
ρ density   kg/m^3

Subscripts, superscripts

0   Initial
a   air
avg   average
d   droplet
f   final
l   locking
T   total
v   Of vapour
w   Of water

Abbreviation

CDC   Characteristic drying curve
ECD   Electron capture detector
HPMC   Hydroxypropyl methylcellulose
IR   Infrared
PEEK   Polyether ether ketone
PEO   Poly(ethylene oxide)
REA   Reaction engineering approach
SDD   Single droplet drying
SEM   Scanning Electron Microscopy
SF6   Sulphur hexafluoride
TCD   Thermal conductivity detector
VI   Virtual instrument

Chapter 1 Introduction

1.1 Background and motivation

Spray drying is the most common method of producing dried particles in industry. It is used across a wide range of industries to produce dry solids in powder, granulate or agglomerate form. In spray drying, a feed of liquid containing dissolved and/or suspended solids is atomised into droplets and then contacted with hot air. The moisture in the droplets undergoes evaporation under controlled temperature and airflow conditions to produce dry powder, which is discharged from the base of the tower. Spray drying is not just a process for removing water; it is a particle formation process, the product of which will have certain property and performance requirements. Depending on the process conditions and the bulk physicochemical properties, spray drying generates a wide range of particle structures such as solid, puffed, buckled or hollow particles (Walton and Mumford, 1999a; Vehring, 2008). Such structures and morphologies strongly depend on various factors including the external drying history of the droplet; the internal resistance to water diffusion which depends on the nature of structure formed during drying and the mechanical properties of the material being dried. The final morphology of the dried particles influences various aspects of particle quality such as its density, flowability, size, dispersibility and brittleness (Walton and Mumford, 1999a; Vehring et al., 2007). Therefore, understanding the particle formation from the initial droplets and the key factors that control the final particle features are vital for achieving optimum powder properties.

It is challenging to undertake particle formation studies in the spray dryer due to the variability between individual particles arising from the complexity of the process, and the large number of droplets being atomised and dried simultaneously. Many alternative approaches have been devised for drying a single droplet under a controlled environment: filament suspension, levitation (typically acoustic or less commonly aerodynamic), sessile drying and free-falling studies. Single droplet approaches offer an easier approach to visualise and record the drying of a droplet that cannot be easily accessed on an industrial scale. Single droplet drying studies have been used to establish four drying stages: constant drying stage, falling rate stage, a boiling stage and a final heating stage. Spray-dried materials have been

categorised into crystalline materials, skin forming materials and suspensions or colloids (Walton and Mumford, 1999a). Skin forming materials are materials that form particles with a skin-like polymeric appearance and are composed of a continuous non-liquid phase.

The estimation of final size and structure of particles is more challenging when drying at high temperatures. Industrial applications of spray drying involve drying at high temperatures as it increases the output of the spray dryer. However, at such high temperature, the droplet temperature reaches boiling as results of restriction of mass transfer. During boiling, vapour pressure causes bubble expansion inside the droplet and results in an increase in the internal pressure of the droplet, which strongly influences the final structure and the drying rates of the droplets. The boiling driven effects on morphology evolution and the response of the crust/skin covering the droplet to the pressure build-up is dependent on the rheo-mechanical properties of the skin/shell on the droplet surface. Different drying routes can occur during boiling, depending on the rheo-mechanical properties of the crust formed during drying (Charlesworth and Marshall Jr, 1960). There can be inflation and rupture; inflation/deflation cycles (Hecht et al., 2000) or cracking behaviour (Walton and Mumford, 1999a). These subsequent drying behaviours and final dried-particle morphology depend on the properties of the shell or film regions. Skin-forming materials show inflation/deflation cycles, e.g. skim milk (Walton and Mumford, 1999a) and coffee extract (Charlesworth and Marshall Jr, 1960; Hecht et al., 2000) while less pliable crystalline materials undergo partial inflation or form hollow or semi-hollow dried-particles. Polymers, particulates, inorganics, emulsions will show different behaviours when dried at high temperatures. Final particle properties and drying rates are influenced by the initial moisture content, pre-boiling drying history and post boiling history. This thesis focuses on the effects driven by boiling and look to address key limitations in current understanding.

1.2 Aims and objectives

This work seeks to understand the effects driven by boiling on the dried particle structure, properties and drying rate. It also seeks to compare the structures and sizes of the dried particles obtained from drying below and above boiling for different compositions. The main objectives of this thesis are summarised as follows:

- Design, commissioning and validation of a single droplet drying apparatus that has the capability to operate at a wide range of drying conditions. A particular emphasis is on the incorporation of an accurate mass loss measurement method that can be used to obtain the drying rates at the boiling stage.

- Explore the link between material properties and drying behaviour as well as morphology evolution above the boiling point by consideration of different compositions exhibiting different material properties evolution during drying. Materials of considerable industrial interest, namely sucrose, hydroxypropyl methylcellulose (HPMC) and sodium silicate have been selected. These materials were selected as they provide a range of material properties. For example, sucrose is a low viscosity material, whilst HPMC is a material with film-forming properties and high viscosity.

- Investigate the mechanisms occurring during boiling, which result in differences in the morphology evolution and the structure of the final dried particles.

- Investigate the link between the morphological developments and the drying rate, particularly during boiling for different compositions at different air temperatures and initial solute concentrations.

- Mapping of key particle and drying metrics such as final size and porosity, locking parameters, boiling onset parameters as a function of air temperature, composition and initial solute concentration.

- Comparison of structures from laboratory spray drying and single droplet drying.

1.3 Thesis structure

The thesis outline is given as follows:

Chapter 2 covers the relevant state of the art for the work carried on this thesis. First, it gives an overview of the experimental techniques used to the study drying behaviour and morphology evolution. Chapter 2 then reviews in detail all the work conducted on drying at high temperatures above the droplet boiling point, highlighting current gaps in the literature. Studies on particle formation and morphology development are also covered with a focus on the role of mechanical and rheological properties. Chapter 2 concludes by reviewing all the studies on the systems selected for this work, namely sucrose, HPMC and sodium silicate.

Chapter 3 describes the development of the experimental methods used in this study. The first part of this chapter covers the development, design and commissioning of the single droplet drying apparatus. The validation of the single droplet drying apparatus is done by comparison of measurements of single droplet drying experiments of pure distilled water with a model based on Ranz-Marshall correlations. The second part of Chapter 3 describes the lab-scale spray dryer, which is used for comparison of final dried structures to the single droplet drying experiments.

Chapter 4 covers a systematic study on the drying of aqueous solutions of sucrose with a focus on the boiling driven effects on the morphology evolution and drying rate. It presents measurements of the drying kinetics and morphology evolution of sucrose droplets at a range of drying conditions. A significant part of the work is focused on the conditions at the onset of boiling (moisture content and size) and the influence of these conditions on the morphology evolution and drying rate. A comparison of the measured drying kinetics against theoretical expectations is also carried out.

Chapter 5 focuses on the mechanisms of drying below and above boiling of aqueous solutions of sodium silicate with emphasis on the effect of boiling on the final morphology and final particle size. The link between the material properties and

morphology development is also explored by using rheological properties of sodium silicate obtained from the literature.

Chapter 6 covers a study on the drying of aqueous solutions of HPMC. HPMC is a material of considerable industrial interest and a system that exhibits strong skin forming properties. A thorough investigation of morphological development below and above boiling at high and low solid content is conducted. The interplay between morphological development, such as skin formation and boiling is covered.

Chapter 7 investigates the potential of manipulating the mechanical and rheological properties of HPMC by the addition of acetone, to alter the morphology evolution during boiling and the structure of the final dried particles.

Chapter 8 presents the main conclusions from this work and outlook on future work.

Chapter 2 Literature review

2.1 Introduction

This chapter first gives an overview of the industrial use of spray drying and research efforts in the area of spray drying. It then gives an overview of the experimental techniques used to study drying behaviour and morphology evolution during droplet drying. This includes single droplet drying methods (SDD) and free-falling systems. The working principle, history, improvement, and modification, as well as advantages and drawbacks of each method, are highlighted. A particular focus is on the filament SDD as it is the method used for this work. This chapter then reviews in detail all the work conducted on drying at high temperatures above the droplet boiling point, highlighting all the current gaps in the literature. Following on that, the work on the particle formation with particular emphasis on the role of material properties is reviewed. This includes the role of the mechanical and rheological properties during drying on the particle formation and the influence on the final shape of the dried particle. This section concludes by reviewing all the studies on the system studied in this work, namely sucrose, hydroxypropyl methylcellulose (HPMC) and sodium silicate. The rationale for the selection of these materials is also highlighted.

2.2 Industrial use of spray drying

Spray drying is an industrial drying technology with a wide range of applications in various sectors including the food and pharmaceutical industries. It is one of the most commercially and economically feasible drying techniques (Chen and Mujumdar, 2009). The concept of spray drying was first patented in 1872 by Samuel Perry (Chen and Mujumdar, 2009). The introduction of spray drying for commercial purposes occurred in 1920 and established on a large-scale basis in the 1980s (Masters, 1991). The first commercial application of spray drying involved the production of milk powder, one of the most important uses of spray drying. Spray drying is used to produce large quantities of powder due to the use of large drying chambers known as drying towers. This section details the industrial use of spray drying described as follows:

2.2.1 Spray drying in the pharmaceutical industry

The application of spray drying in the pharmaceutical industry was first explored in the 1940s and applied to extracts, inorganic medicinal salts, adrenaline and vitamin (Masters, 1991). Following this, spray drying has been used for further pharmaceutical applications for the manufacture of pharmaceutical excipients and the isolation of active ingredients that were either thermal-sensitive or difficult to crystallise. The use of spray drying in the pharmaceutical industry has increased due to the need to produce oral drugs in an amorphous state due to its contribution to enhance the bioavailability of many modern drugs (Walters et al., 2014). Spray drying is a rapid evaporation process and hence it is ideal to precipitate drugs from solutions in an amorphous state. Other factors for the use of spray drying in the pharmaceutical industry include the production of inhalable drugs such as Pfizer's Exubera, microcapsules for controlled-release formulations or taste masking and advanced powder forms such as direct compressible and readily wet-able powders (Walters et al., 2014).

2.2.2 Spray drying in the food industry

In the food industry, spray drying is used to produce a range of ingredients such as milk powder, whey/casein powder, cheese powder, instant coffee/tea powder, juice powder, cereal powder and dried infant foods (Selvamuthukumaran, 2019). The advantages of using spray drying in the food industry include the ability to control the characteristics of the product and enhance the overall performance. For example, the end products have low moisture content and high bulk density which enhance the product shelf life and contributes to the reduction of packaging and storage costs (Selvamuthukumaran, 2019). The high quality and functionality of spray-dried products are due to the short drying time combined with the evaporative cooling period which protects the suspended particles from overheating. These vital characteristics protect heat sensitive food constituents such as nutrients which lead to high retention of the bioactivity of the spray-dried product (Selvamuthukumaran, 2019).

2.2.3 Spray drying in the detergent industry and other industries

The commercial use of spray drying in the detergent industry started in the 1930s to produce detergent powders, which have dominated the laundry market since its launch. This is because spray-dried detergent powders offer a huge advantage over other forms of detergents such as liquid detergents (Masters, 1991). For example, detergent powders have low moisture content and thus it is easier to maintain the stability of complex materials such as enzymes and bleach for a long period of time. Detergent powders also contain higher percentages of inorganic materials used as water hardness removers, which tend to be cheaper. The manufacturing of detergent powders is done using counter-current spray dryers as they offer the advantage of having higher thermal efficiency over co-current spray dryers (Masters, 1991). Spray drying is also used in other industries including cosmetics, fine chemicals, pigments and agrochemicals (Chen and Mujumdar, 2009).

2.3 Research in the area of spray drying

The main research effort in the area of spray drying focuses on understanding flow patterns and particle trajectories in spray drying towers to optimise spray-dried powder characteristics and trouble shoot any operational or product quality issues. The study of flow patterns inside drying towers is key to understanding various issues within spray drying including agglomeration, wall deposition, aroma loss and thermal degradation as well as other possible reactions including crystallization (Langrish, 2007). Considerable effort is dedicated to understanding flow patterns to reduce wall deposition and thermal degradation of particles by altering flow patterns in the drying chambers (Langrish, 2007). Understanding flow patterns in spray drying include a combination of modelling efforts (using CFD, Computational fluid dynamics) and pilot scale testing. The challenge faced in understanding flow patterns is the need to have a full understanding of particle drying kinetics and particles agglomeration. This includes the evolution of particle properties during drying. Therefore, considerable research efforts have focused on particle formation which combines with studies on spray drying towers to predict spray-dried powder characteristics. Most particle formation studies have been conducted using single

droplet drying approaches as they offer an alternative easier approach where the evolution of particle formation can be monitored closely. The combination of particle formation studies and studies on spray drying towers can facilitate the manipulation of spray dryers design and conditions to generate complex powders that meet powder properties demands including particle size and shape, bulk density and flow properties.

2.4 A review of single droplet drying techniques

2.4.1 Introduction

In the spray drying process, billions of droplets of different sizes are produced by the atomiser and subsequently sprayed into the drying tower. These droplets follow different trajectories within the dryer, where the surrounding conditions change continuously and thus, droplet temperature and moisture content exhibit varied changing histories (Masters, 1991). Such changes occurring in each droplet are hard to monitor accurately during the intermediate stage of drying due to the fact that a large number of droplets is dried simultaneously in a huge tower. Because of the difficulty in droplet sampling, a traditional spray lacks the capability to evaluate the correlation of these functionalities to the changes in droplet temperature and moisture content. To overcome these challenges, single droplet drying (SDD) techniques were developed. SDD is a recognised technique used to monitor drying kinetics and morphological development for an isolated droplet subjected to controlled drying conditions. This technique "mimics" the droplet convective drying process encountered in spray drying. The SDD technique was initially developed to measure the drying kinetics of single droplets. It was extended to monitor the morphological changes of a single droplet during the transition of the droplet to a particle. Fu et al. (2012a) demonstrated that a single droplet drying device should satisfy three criteria to generate accurate measurements; these include:

- The size of the single droplet used as a model droplet can be controlled and reproduced.
- The temperature, velocity, humidity of the air stream used for drying the air droplet can be varied and controlled to facilitate the understanding of the

heat and mass transfer phenomena occurring during the drying process of a single droplet.

- The monitoring techniques of the variation in the droplet kinetics variables such as mass, temperature, and diameter are accurate and robust in producing quantitative data.

Single droplet drying techniques have undergone a lot of changes and modifications to meet these three criteria. SDD systems can be classified into four groups based on the approach used to suspend the single droplet during drying. Illustrations of these four categories are provided in Figure 2.1. These techniques involve the use of imaging to track the morphological changes and the drying behaviour of the droplet. This information facilitates the understanding of the process and consequently allows for modelling the drying behaviour of an industrial spray dryer.
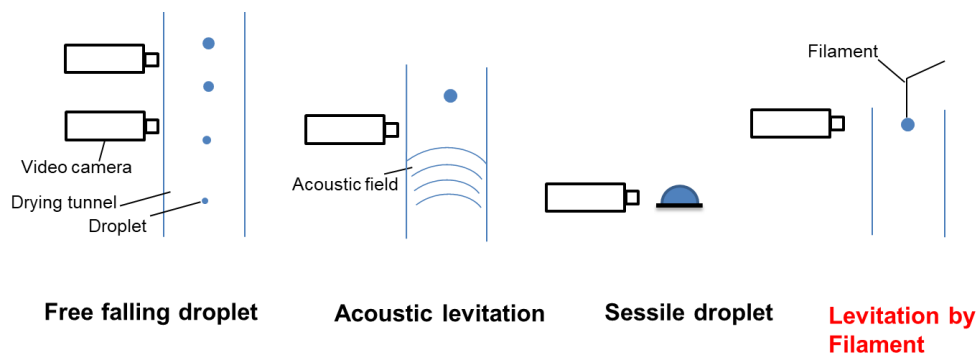
Figure 2.1 The four types of single droplet drying systems (adapted from Fu et al. (2012a))

2.4.2 Sessile droplet

This technique involves depositing a droplet on a hydrophobic substrate placed in a chamber where drying conditions can be controlled. It involves the use of a dispenser to make droplets and optical instruments to closely monitor the evolution of the droplet morphology (Perdana et al., 2011). Sessile technique has been used to study morphology development and particle formation during drying of food products such as whey and casein protein in various studies (Both et al., 2018a; Both et al., 2018b; Both et al., 2019; Sadek et al., 2013; Sadek et al., 2016). It has also been used to study skin formation and mechanical instabilities during drying of polymer droplets (Pauchard and Allain, 2003b; Pauchard and Allain, 2003c; Pauchard and Allain, 2003a; Pauchard and Couder, 2004a; Pauchard and Couder, 2004b). A good review of the technique has been given in Schutyser et al. (2012). A more in-depth

description of relevant studies that focused on the studies of particle formation is given in Sections 2.7.1 & 2.7.2. Sessile droplet set-up can also be used to study the evolution of components inside the droplet using high sensitivity digital camera (Marín et al., 2011) or small-angle x-ray scattering (Chen et al., 2012). Although sessile droplet is useful to monitor particle formation, most of these studies were conducted at low air temperature. It is expected that at high air temperatures, which is the main focus of this work, sessile droplet set-up would be unsuitable due to the significant effect of heat conduction from the substrate. The surface of the substrate is also expected to influence the mechanism of bubble nucleation during the boiling stage.

2.4.3 Free-falling single droplet drying systems

The free-falling system does not involve any support for the generated single droplet. A droplet or stream of mono-dispersed droplets of identical properties are allowed to free-fall through the tower, and therefore free-falling system provides the closest representation of the drying conditions inside a traditional spray dryer. In the free-falling system, the feed solution is pressurised through a capillary glass tube surrounded by zirconate /lead titanate ceramic (Wu et al., 2007). The feed solution passing through the tube is subjected to a pulse of a sinusoidal electrical signal generated by a pulse controller connected to the piezoelectric ceramic component. The frequency of the electrical signal can be altered to allow for a continuous generation of monodisperse droplets. This system can also incorporate glass capillary tubes of different orifice sizes, allowing the system to generate monodisperse particles with varied sizes.

The main disadvantage of the free-falling system is the challenges faced in monitoring the drying kinetics of the free-falling droplets. In most cases, indirect measurements are used to determine the evaporation rate of the droplets; for example, by determining the droplet terminal velocity (Kinzer and Gunn, 1951) or the changes in droplet diameter at different distances from the atomising nozzle using light scattering (Vehring et al., 2007). More direct approaches to monitor the moisture content in the droplet during drying were used by Wallack et al. (1990) and El-Sayed et al. (1990) where sampling ports were installed along the drying tower

and further away from the droplet generator. These sampling ports were also used to collect particles for morphology characterization. Although this technique offers a good method to characterise the final morphology and indirectly measure the drying rate based on the diameter measurements, there is no method to measure the droplet temperature or the mass loss.

2.4.4 Acoustic levitation of single droplet

In the acoustic levitation setup, the droplet is suspended in the air by an acoustic field at a fixed position where the changes in droplet morphology and drying kinetic parameters are recorded (Davis et al., 1981). The diameter changes of a single droplet can be determined by evaluating the projected shadow captured by a camera (Kastner et al., 2001; Schiffter and Lee, 2007a; Schiffter and Lee, 2007b; Mondragon et al., 2011; Mondragon et al., 2012). The evaluation of the evaporation rate in the acoustic levitator is more complex. Kastner et al. (2001) reported two approaches to measure the drying rate in each drying stage. In the first stage, the evaporation rate was determined based on the decreased droplet volume while in the second drying stage the evaporation rate was evaluated by changes of the droplet/particle opposition in the acoustic field. Groenewold et al. (2002) added a dew point hygrometer to the system to provide a continuous on-line measurement of the droplet moisture content during drying. The measured data were used to construct droplet drying curves by determining the partial vapour pressure of the outlet air. In addition to the complexity of measuring evaporation rate, acoustic levitation system also entails the disadvantage of the effects of the ultrasonic field on the droplet drying behaviour. Groenewold et al. (2002) reported that acoustic levitation approach returns a higher drying rate and lower moisture content in comparison to those measured using a microbalance, signifying the influence of ultrasonic waves during measurement. Yarin et al. (1999) also reported that heat and mass transfer coefficient obtained from acoustic levitator are higher than those determined from free-falling droplets.

2.4.5 Filament single droplet drying

The filament SDD systems involve an intrusive method for supporting the generated droplet. The droplet is suspended at the tip of thin filament (glass, or other materials) or glass capillary tube during the entire drying process. As the droplet is stationary, filament SDD systems offer a relatively easy method for monitoring the three droplet kinetics parameters; mass, diameter, and temperature. Therefore, it has been widely used in previous studies to investigate the droplet drying kinetics. The changes in the droplet mass during drying are measured by connecting the glass filament or capillary tube to an external micro-balance, analysing the moisture content of exit air or by calibration from the filament movement.

2.4.5.1 Filament SDD system for measuring droplet kinetics

Several improvements and modification to the techniques used for measurement of drying kinetics have been made to enhance the accuracy of the measurements. This part reviews all the different setups and the pros and cons of each modification. Single droplet drying studies were initially developed to study the evaporation of pure liquid droplets (Fuchs, 1934; Frossling, 1938; Langstroth et al., 1950). These were then extended by Ranz and Marshall (1952b) and Ranz and Marshall (1952c) to study drying of droplets with dissolved solids. They utilised a glass capillary tube to produce a single droplet and also to suspend the droplet during drying. Later studies used a similar design, but the glass capillary was replaced by glass filament. The measurement of the droplet temperature was achieved by inserting a thermocouple into the drying droplet. Using the filament single droplet drying set-up, Ranz-Marshall Correlations for heat and mass transfer in a droplet were established. These are given as follows:

$$Nu = 2 + 0.60\,Re^{1/2}Pr^{1/3} \qquad (2.1)$$

$$Sh = 2 + 0.60\,Re^{1/2}Sc^{1/3} \qquad (2.2)$$

Although the setup by Ranz and Marshall (1952b) and Ranz and Marshall (1952c) had the capability to measure the temperature and diameter of the drying droplet, mass measurements were not possible. Charlesworth and Marshall Jr (1960) incorporated a method to measure the droplet mass based on the displacement of the filament with mass loss. A glass filament balance was used to evaluate the mass changes of

the droplet being dried. The glass filament consisted of a long horizontal filament with one end fixed to a scale and the other connected to a shorter finer filament at right angles, as shown in Figure 2.2. The free end of the glass filament was used to suspend the droplet. After the droplet was suspended, the glass filament deflected based on the mass of the droplet. The fixed end was adjustable to allow the free end to relocate to its original position. The droplet mass was correlated to the distance of fixed end displacement. As drying progressed, the glass filament balance was used to measure the actual droplet mass at different time intervals.
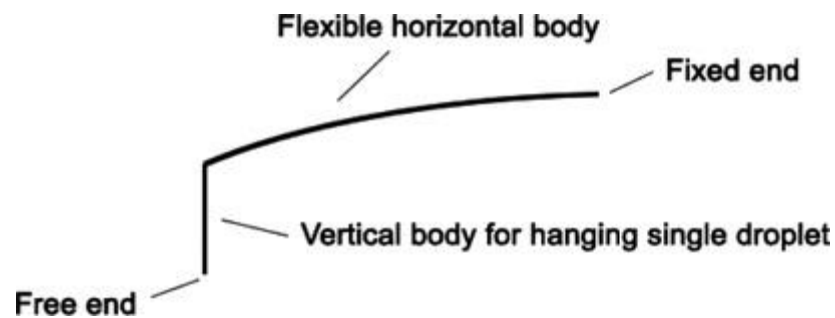
Figure 2.2 A systematic illustration of the glass filament used by Charlesworth and Marshall Jr (1960) to measure the cha**nges of the droplet mass during air drying (Fu et al., 2012a).**

Sano and Keey (1982) employed a similar design concept to that of Charlesworth and Marshall Jr (1960) to measure the changes in droplet mass during the drying process. The measurements were conducted by interrupting the drying at frequent time intervals. A micrometer was incorporated over which the fixed end of the glass filament moved to raise the free end to its initial position. Measured drying rate was then used to develop a mathematical model to describe the drying of droplets containing dissolved solids above boiling points where internal bubbles are formed. Cheong et al. (1986) used the same glass filament technique, but with slight modifications to account for the drag force of the upward airflow to accomplish a better accuracy of mass measurement. Unlike the studies discussed earlier, in which the droplet volume changes were estimated by analysing the projected droplet area recoded by a video camera, Kincaid and Longley (1989) determined the actual volume changes of a pure water droplet by suspending the droplet at the tip of the needle of a micro-syringe. The droplet volume at a certain drying rate was measured by drawing the droplet back to the syringe and recording the corresponding volume

changes. In all studies discussed above, drying experiments had to be stopped at given intervals to record the displacement of the glass filament and calculate the mass of the droplet/particle. In this way, the final mass loss profile is either obtained from a single drying run that has been interrupted several times or from endpoint readings of multiple drying rates. To overcome these limitations, Qi Lin and Chen (2002) used a video camera to allow for continuous monitoring of the displacement of the glass filament during drying whilst still following the same glass filament concept shown in Figure 2.2. Droplet mass was calculated by converting the position of the droplet/particle showing on the screen to a calibrated standard curve. Although this approached enhanced the accuracy of the glass filament SDD experiments in comparison with previous studies, it still required a rigorous amount of calibration to obtain mass measurements.

Another method of determining the mass loss is by measurement of the humidity of the gas downstream of the droplet. Hecht et al. (2000) used flowing nitrogen as a heating medium and incorporated a thermal conductivity detector (TCD) to measure the humidity of the exit air downstream of the suspended droplet. The TCD was calibrated by drying drop of water and measuring the decrease in the drop size and then comparing it with the output from TCD. This study also utilised electron capture detector (ECD) for analysis for traces of volatile components such as sulphur hexafluoride (SF_6). A similar concept was utilised by Tran et al. (2016a) where the humidity of inlet air is measured by a dew-point whilst outlet air humidity is recorded by an infrared spectrometer. The mass loss of the droplet is determined by a moisture balance of the inlet and outlet air. The drawback of this approach includes limitations of the amount of airflow going into the humidity sensor as it requires the exit air stream to be split where only a fraction of the airflow is introduced into the sensor. Another drawback is limitations to the sensor operating temperature. These sensors have an operating limit and the air is required to be cooled down before it is introduced into the sensor.

All the studies discussed earlier used an indirect method to measure the mass of the droplet; converting the glass filament displacement into droplet mass using an established calibration curve or measurement of humidity in the exit air. Adhikari et

al. (2004) proposed a method to monitor the change in the droplet mass during air drying using a micro-balance. They modified the glass filament design development by Charlesworth and Marshall Jr (1960). The flexible horizontal part was removed, and only the vertical glass filament was kept. The whole system was connected to a micro-balance and the mass losses in the droplet, as drying progressed, were recorded through a computer. The use of a balance to measure mass loss requires a very stable airflow to minimise the influence of airflow on the mass loss measurement. This method also allowed the droplet mass and temperature to be measured in a single run by the use of a thermal camera.

All studies discussed earlier demonstrate that the glass filament SDD systems have been commonly used to determine droplet kinetics of a range of materials because of their better controllability and operability in comparison to the other types of SDD experiments. Comparisons of three types of SDD systems is provided in Table 2.1. Issues with the intrusive nature of the filament and the contribution to heat conduction can be minimised by the use of small filament and material with low heat conductivity. Three different methods of mass loss measurement have been highlighted with a description of the pros and cons of each method.

2.4.5.2 Filament SDD system for studying morphology evolution

Droplet morphological changes have been widely investigated using filament SDD experiments due to their superior controllability and the ability to dry at a wide range of conditions. Filament SDD provided insights into the impact of composition and process parameters such as air temperature, air velocity and air humidity in the formation of different morphologies. Significant examples of the use of filament SDD to study the morphology developments are given in this section.

The evolution of particle morphology during drying has been captured in a previous study by El-Sayed et al. (1990) who used filament SDD to observe the droplet to particle transition of several materials, such as skim milk, coffee extracts and sugar solutions. Filament SDD systems offer a better approach for capturing the evolution of particle structure compared to the free-falling experiments. Filament SDD systems have also been used to investigate the effect of morphological development and

drying rate on the loss of volatile components such as sulphur hexafluoride, SF6, (Verderber and Judson King, 1992; Sunkel et al., 1993). It was concluded that morphological developments such as inflation and rupture strongly influence the retention of volatile substances and subsequently needs to be accounted for when drying droplets that contain flavonoids and volatile substances. Similar work was also conducted by Hecht et al. (2000) with additional process parameters investigated, including the mass loss rate of SF6 and droplet temperature. The results demonstrated the effect of internal bubble formation on enhancing the loss rate of additives. Furthermore, condensation of water vapour inside the bubble was seen to cause deflation of the partially-dried particle. Significant work on the morphology development of a wide range of materials at different drying conditions was conducted by Walton and Mumford (1999a). In this work, the morphology developments were analysed using filament SDD systems and subsequently categorised into three groups based on the different morphologies formed: crystalline materials such sodium chloride and sodium carbonate, agglomerate materials such as silica and skin-forming materials such as skim milk and gelatine. General morphology maps of these materials were constructed and are given in Figures 2.3, 2.4& 2.5.
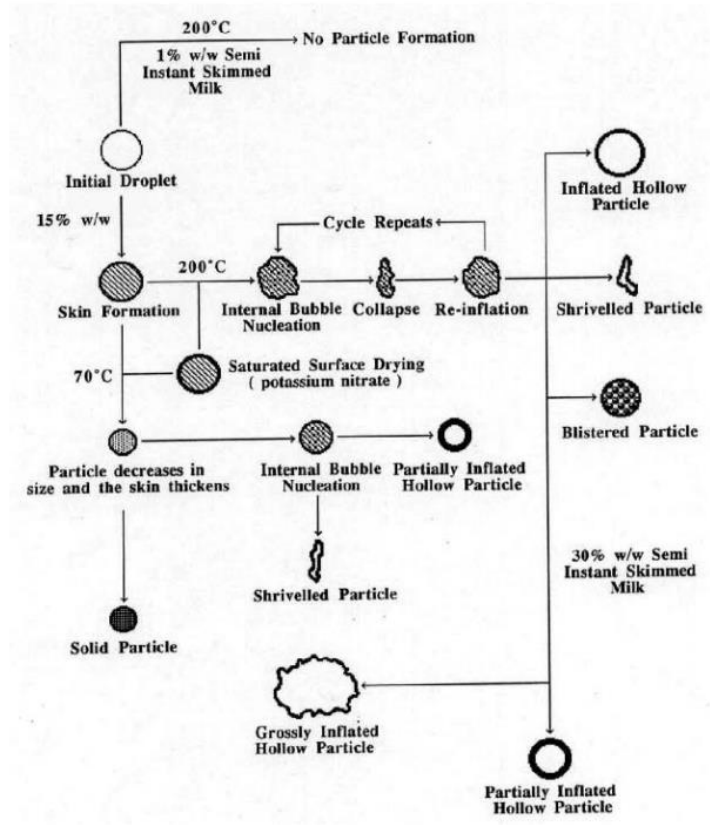
Figure 2.3 The effect of temperature and concentration on the particle morphology of skin-forming materials (Walton and Mumford, 1999a)
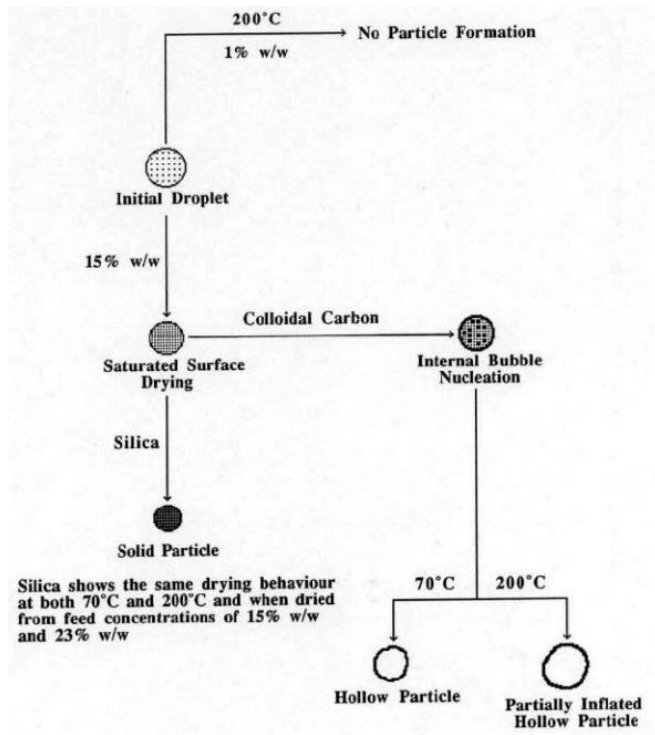
Figure 2.4 The effect of temperature and concentration on the particle morphology of agglomerate materials (Walton and Mumford, 1999a)
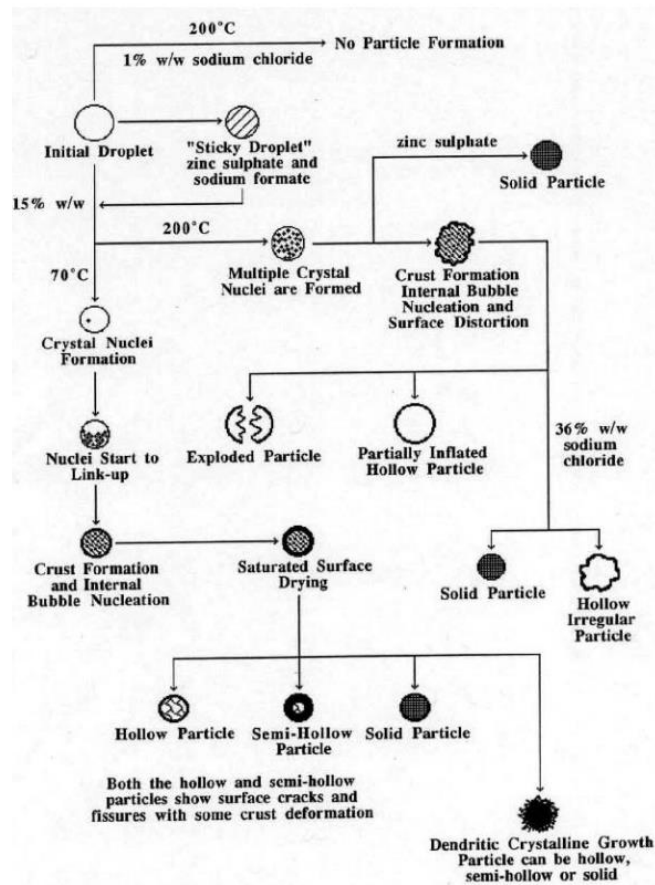
Figure 2.5 The effect of temperature and concentration on the particle morphology of crystalline materials (Walton and Mumford, 1999a)

2.4.6 Limitations of SDD methods

The advantages and disadvantages of each type of SDD system are summarised in Table 2.1. SDD approaches have several drawbacks in terms of realistic comparison to industrial spray drying. One of the major concerns is the large droplet size used in SDD, particularly the filament SDD, which is a magnitude larger than the atomised droplet in industrial spray drying. The use of the large droplet size in the SDD systems is due to the difficulty of the measurement of the kinetics of smaller droplet sizes and the associated increase of measurement error with the use of small droplet sizes. The free-fallings system is the only system where droplet size is typically similar to that produced in the spray dryer. However, the free-falling system is unsuitable for the measurement of drying kinetics such as droplet temperature and mass loss. Another drawback of the SDD techniques is the influence of the experimental set-up used for levitation (filament, ultrasonic waves) on the heat and mass transfer process. Further, in the SDD setups, the droplets are dried in stationary state

droplets, unlike spray drying where droplets are in motion. Although SDD approaches have several drawbacks, they still provide valuable insights into the drying mechanisms such as shrinkage behaviour of droplets, transport phenomena, skin formation and morphology evolution (Sadek et al., 2014; Schutyser et al., 2018).

In terms of the usefulness of SDD to predict particle morphology in a spray dryer, several studies have reported similarities between structures produced from SDD methods and spray drying. Studies by Walton and Mumford (1999a) and Walton and Mumford (1999b) shows good agreement between structures produced from spray drying and those produced from single droplet drying. El-Sayed et al. (1990) demonstrated that the morphologies obtained from the filament SDD and free-falling experiments showed similar morphologies to commercial spray-dried coffee. Furthermore, Fu et al. (2012b) reported that the shape of crystals of lactose from filament SDD was similar to those obtained from the spray dryer. Therefore, these studies suggest that the droplet size had minimal impact on the structure of the final dried particle.

Table 2.1 A summary of a comparison between the three types of single droplet drying systems (adapted from Fu et al. (2012a))

	Freefall	Glass filament	Acoustic levitated
Advantages	The changes in drying conditions closely follow that of an actual spray dryer	Less complexity in the measurement of drying kinetics and visualisation of the droplet as drying is progressed	Less complexity in the measurement of drying kinetics and visualisation of the droplet as drying is progressed
Disadvantages	complexity in the measurement of drying kinetics and visualisation of the droplet as drying is progressed	Intrusion nature of the filament into the droplet, however, it can be minimised	A possible influence of the acoustic waves on the mass transfer process
Support method	No support	Using acoustic field	By inserting the tip of fine glass filament into the droplet
Intrusive into droplet	No	No	yes
Approaches of drying rate measurement	- Direct approaches, for example, through the determination the distance the droplet travelled inside the tower or collection of droplets at different heights of the tower.	- Direct methods for example by connecting the glass filament to the microbalance - Continuous measurement during drying	- Indirect methods including transforming the droplet diameter changes or droplet position changes into mass changes
Capability to mimic actual spray drying process	Very possible; can be extended to become an enhanced spray-drying process for certain applications	Not possible; drying kinetics are influenced by intrusive glass filament	Not possible; drying kinetics are influenced by acoustic waves

2.5 Stages of particle drying

The removal of moisture from droplets in spray dryers involves heat and mass transfer and is also associated with simultaneous particle formation process. Drying rate and the structure of the final dried particle depend on the air properties such as temperature, humidity and the transport properties as well as droplet properties such as temperature, diameter and relative velocity (Handscomb et al., 2009).

A typical temperature history of a droplet with dissolved or suspended solids drying in a spray dryer is shown in Figure 2.6. As drying begins, the droplet heats up to the wet-bulb temperature and the drying rate increases (A-B), the drying rate increases

till point B where thermal equilibrium is attained between the solid and its surroundings. Thereupon, the droplet stays at the wet bulb temperature where the drying occurs at a constant rate with a moisture saturated surface. In the B-C line, the dynamic equilibrium is sustained between the energy lost by evaporating moisture and that transferred to the particle from the drying gas. This is known as the constant rate drying period where the moisture flux from the surface remains almost constant. The surface of the material being dried as well as the vapour above remains saturated with moisture during the entire constant-rate period. In addition, the solid surface remains at the wet-bulb temperature so long as convection is the only mechanism of heat transfer to the droplet.

The falling rate or second drying stage commences when the moisture can no longer be supplied to the surface of the droplet at a sufficient rate to sustain moisture saturation. Consequently, the drying rate decreases and the droplet temperature rises. The transition between the falling rate and the constant rate stages occurs at a critical moisture content and may concur with the initiation of crust formation. The critical moisture content has been shown to be a function of the drying history as well as the mass and geometry of the material being dried (Handscomb et al., 2009).
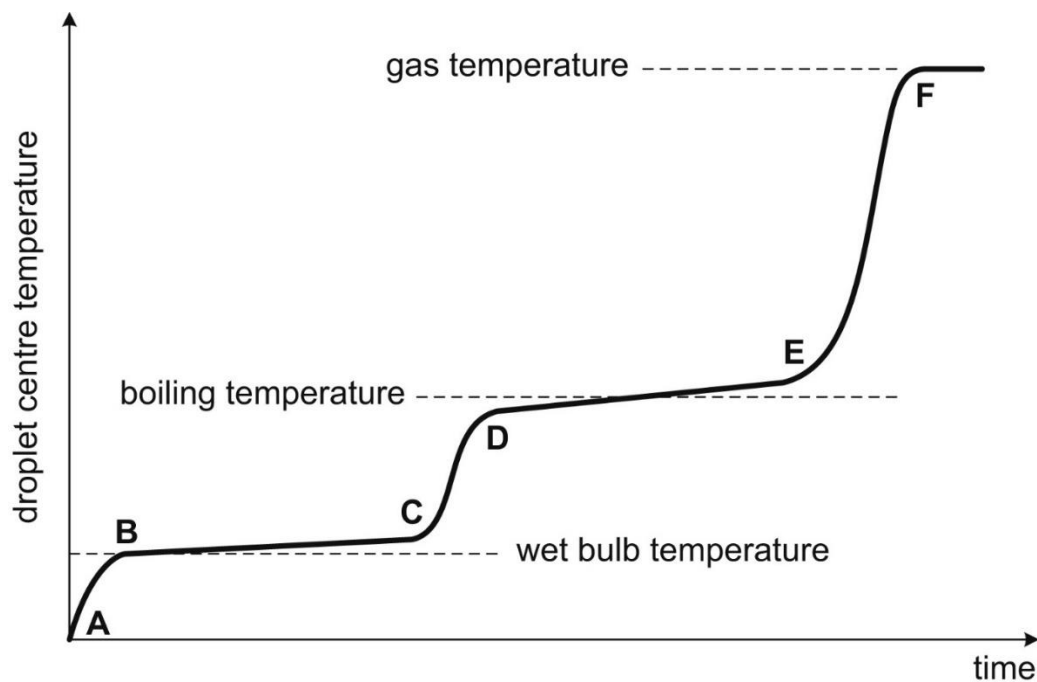
Figure 2.6 The temperature history of a liquid droplet containing dissolved solids drying in a spray dryer (Handscomb et al., 2009)

Vaporization begins if the droplet reaches the boiling temperature. Due to the considerable energy required for vaporization, sensible heating ceases. This phase is called puffing regime and drying in this phase is controlled by external heat transfer. Once free moisture in the droplet is removed, the droplet rises until it reaches the surrounding gas temperature.

2.6 Particle formation above the boiling point

This section gives a more in-depth review of the studies that have focused on the main phenomena and behaviours seen when drying at high temperatures. Boiling occurs when the droplet temperature reaches the boiling point when drying at air temperatures higher than the droplet boiling point. Vapour builds up inside the droplet resulting in an increase in the internal pressure of the particle. The behaviour following boiling strongly depends upon the permeability and mechanical characteristics of the crust/shell or skin formed on the particle surface. The particle can inflate or crack, thus allowing the vapour inside the particle to escape and alleviate the pressure difference, or it can explode and disintegrate. One of earlier studies by Charlesworth and Marshall Jr (1960) established different routes of morphology development above boiling depending on overall mechanical properties of the shell that forms on the surface of the particle during drying. These different routes are depicted in Figure 2.7. In an open porous system, the resistance to internal mass transfer remains low; consequently, the particle temperature does not reach the boiling point. A crust with less permeability results in a pressure build-up within the particle and the morphology development depends on the mechanical properties of this crust. A rigid crust results in a fractured particle from minor or major cracking. On the other hand, a plastic shell can either allow for stretching and puffing or rupture and collapse.
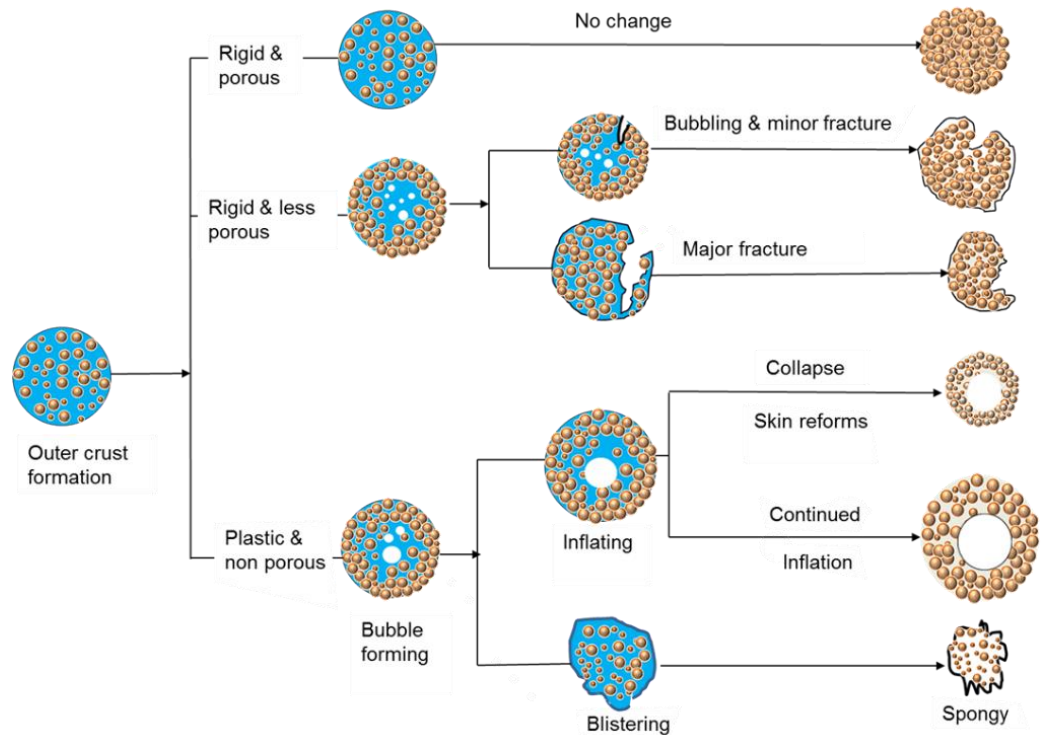
Figure 2.7 Morphology development routes when drying at temperatures above the droplet boiling temperature, depicted from (Charlesworth and Marshall Jr, 1960)

Further single droplet drying studies have highlighted the impact of boiling on morphology development. El-Sayed et al. (1990) utilised filament single droplet set-up as well as a free-falling set-up to investigate the morphology of maltodextrin, coffee, milk and sucrose at moderate and high temperatures. Different behaviours above boiling were highlighted; sucrose solution collapses after cycles of inflation/deflation to form smooth, solid particles. Maltodextrin maintained expansion at the end stage of drying which was attributed to higher viscosity than sucrose and/or lower water diffusivity. Skim milk remained unaffected during boiling without any expansion or collapse, which was attributed to the formation of a rigid surface. Effects of molecular and water diffusivity on the length of the constant rate period and size entering boiling were highlighted; for example, sucrose remains in the shrinkage period longer than maltodextrin and coffee as it has a lower molecular weight and higher diffusivity than maltodextrin and coffee extract (these enter falling rate period earlier in drying). SEM images from the free-falling set-up show a sign of expansion for maltodextrin. Similar observations were reported by Hecht et al. (2000) where they highlighted that skin forming materials possess rheological

properties that enable such droplets to undergo a series of inflation/deflation cycles. The morphology time series of coffee extract and sucrose were included. The final morphology that follows deflation and inflation cycles also were highly dependent on the material properties; final dried sucrose particles were seen to be smooth and solid, whereas coffee formed hollow particles with folds and surface irregularities.

Nešić and Vodnik (1991) conducted a single droplet drying study on colloidal silica, sodium sulphate and milk. This study highlighted that different behaviour above boiling depending on material properties, mainly focusing on the diffusivity of water through the solid shell. Colloidal silica forms very permeable and fragile crust. The diffusion coefficient of vapour through this crust was calculated as 10^{-6} m^2/s, and hence no boiling stage was reported even when drying at high temperatures. Sodium sulphate formed an impermeable and rigid crust which results in cracking and deformations above boiling. Skimmed milk formed a very permeable crust, and thus a boiling stage was not observed. This study highlighted the importance of the diffusivity of moisture through the crust on the occurrence of the boiling stage and was used to compare with a diffusion model.

A recent interesting study was conducted by Tran et al. (2016a) and focused on the evaluation of the drying kinetics of lactose/water droplets at air temperatures above and below boiling point. This study employed a filament SDD; however, an IR was incorporated to measure the humidity of the exit air and hence the mass loss from the droplet. This study evaluated the locking point below and above boiling and the occurrence of inflation/deflation cycles. Below boiling, locking was defined as the point at which the diameter becomes constant, whilst above boiling locking was determined as the minimum in diameter before the droplet enters the boiling stage. The morphology of the final particles confirmed the occurrence of puffing. This work was extended by Tran et al. (2016b) for solutions of skim milk, lactose, whey protein and lactose–whey mixtures. The experimental data collected from drying experiments, particularly conditions of skin formation, locking point and inflation/deflation parameters, were collated and implemented in an empirical sub-model to take account of the effect of the inflation/deflation cycles on the changes to particle diameter and on the drying curve.

The effects of boiling on the final size and morphology of dried particles have also been reported in a few studies. Alamilla-Beltran et al. (2005) studied the evolution of the morphology of maltodextrin in a laboratory spay dryer by collecting samples of particles at different sampling points from the atomising nozzles. The SEM images (Figure 2.8) showed puffed particles when drying at temperatures above boiling. These were evidence of the effect of boiling on the inflation of particles. In another study by Paramita et al. (2010) the effect of additives such as gelatin, decaglycerol monolaurate, or ethanol and outlet air temperature on the morphology of spray-dried gum Arabic/maltodextrin system was investigated using confocal laser scanning microscope (CLSM) and scanning electron microscopy (SEM). It was reported that spray drying at higher air temperature resulted in a higher fraction of hollow particles. Further, the additives also contributed to the increase of the fraction of hollow particles due to their role in early skin formation. Rogers et al. (2012) also investigated the effect of drying of skim milk at high air temperatures above boiling using a monodisperse spray dryer. At an inlet air temperature of 124 ˚C, no puffing was observed, and all particles obtained were buckled and contained surface folding. At higher air temperature, 181 ˚C, 50% of particles showed puffed structure with larger diameters and thin shells (Figure 2.9). The final dried particles had sizes larger than the initial droplet size.
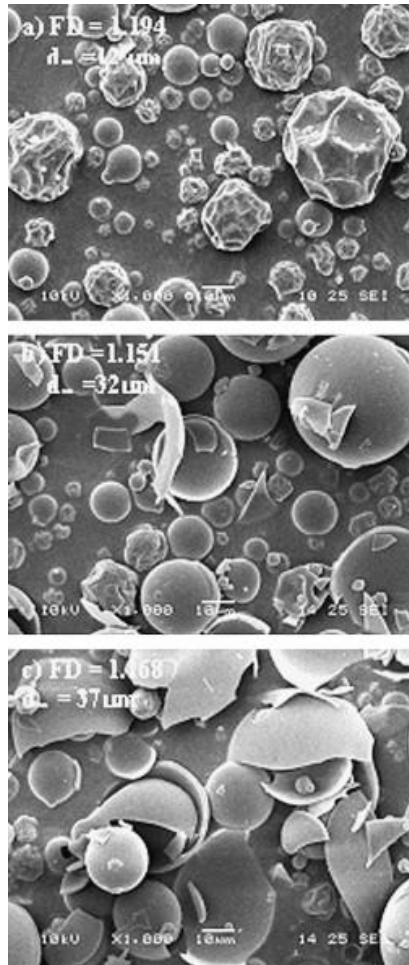
Figure 2.8 SEM images of maltodextrin-particles at several drying. SEM images in b&c showing clearly puffed broken particles due to boiling (Alamilla-Beltran et al., 2005)
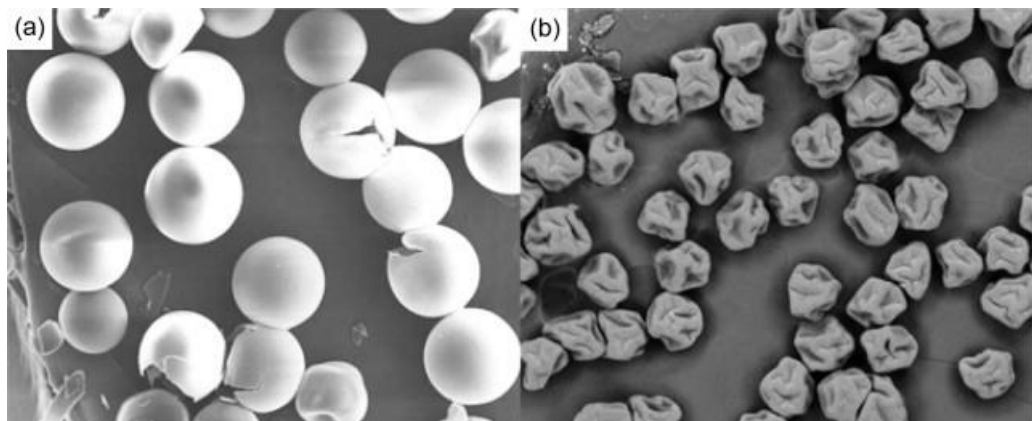
Figure 2.9 SEM Images (a) Puffed particles dried from 33 wt% fresh skim milk concentrate (180 ∘C), (b) buckled particles of 33 wt% skim milk concentrate dried at 180 ˚C (Rogers et al., 2012)

The studies discussed in this section on drying above boiling are summarised in Table 2.2.

Table 2.2: Studies on drying at temperatures above the boiling point

Author	Experimental setup	System investigated	Conclusions
Charlesworth and Marshall Jr (1960)	Filament SDD	sodium chloride sucrose coffee extract sodium sulphate ammonium nitrate	Summarised general remarks of morphologies above boiling. No detailed or systematic study of any of the systems.
Sano and Keey (1982)	Filament SDD	skim milk	Effect of inflation on the drying rate
Nešić and Vodnik (1991)	Filament SDD	Colloidal silica sodium sulphate skimmed milk	Colloidal silicate forms a permeable and fragile crust, and the boiling stage is absent. Sodium sulphate formed impermeable and rigid crust cracking and deformations above boiling. Skimmed milk very permeable crust boiling stage not observed.
Hecht et al. (2000)	Filament SDD	Coffee or sucrose solutions with a trace quantity of SF6	Sucrose drop shows inflation/deflation which collapses to form smooth solid particles. Coffee shows non-spherical bubble, final particle rough surface with a hollow inner structure.
Alamilla-Beltran et al. (2005)	Spray drying	Maltodextrin	Morphologies show puffed particles at high temperatures
Rogers et al. (2012)	Monodisperse spray drying	Commercial skim milk powder	Hollow, inflated particles were produced at higher temperatures due to boiling
Tran et al. (2016a)	Filament SDD	Lactose/water	Investigated the drying kinetics of single lactose/water at temperatures below and above the boiling point of water.

2.6.1 Summary of the state of the art of drying above boiling

The behaviours observed when drying at high temperatures strongly depend on the type of material being dried. Out of the three classes of materials (skin forming, crystallising and agglomerate), boiling would have a more significant influence on the skin forming materials due to their plastic nature. Crystallising materials are more likely to form a rigid skin due to crystallization and therefore boiling would result in cracking, the extent of which significantly depends on the size of pores within the crystallised crust. Suspensions are largely affected by the suspended particles size and the particle-particle interaction and would only lead to limited morphologies. On the other hand, skin forming materials (organic or inorganic polymers, proteins and sugars) which are widely dried in industrial applications (food and pharmaceuticals) are more likely to be affected by boiling. Skin forming materials have more complex rheological properties (including phase transitions), high molecular weight and can form skin with distinct properties. This can result in complexity in understanding the morphology development during and post boiling. A systematic study is therefore needed to understand the particle formation above boiling with a strong focus on the morphology development pre-boiling and post boiling and an understanding of the link of the morphology development to key material properties. The gaps in the literature with regards to drying above boiling are summarised in the following:

1. A detailed study on the role of boiling on the morphology development of skin forming materials. This would include a focus on the morphology development prior to boiling, during boiling and post boiling. Of particular interest is the investigation of liquid to solid transition, also known as skin formation. Furthermore, the response of this skin to boiling driven effects needs to be closely monitored. This because the properties of the skin and its response to vapour pressure have a major influence on the particle formation and final size of the particle. The characteristics of the skin are significantly influenced by the nature of the solute, the drying conditions and initial solute concentration.

2. Development of parameter maps of skin formation conditions (size and moisture content), boiling parameters (inflation/deflation parameters, moisture and size during boiling) and final dried particle metrics (porosity and size). These parameters are all solute dependent and are highly influenced by the air temperature and initial solute concentration. Therefore, a key part of this work is to analyse the influence of the material properties, drying conditions, and the structure formed during drying on these maps.

3. Comparison of single droplet drying experiments to spray drying with a particular focus on the effects of boiling. This would cover the effect of the differences in droplet size and drying time scale on the boiling stage and its subsequent influence on morphology development. The question of whether the timescale of drying in a spray dryer allows sufficient time for bubble nucleation and boiling driven effects.

In order to address the gaps highlighted above, a selection of more than one system of skin forming materials is needed. One sensible approach is the selection of material that exhibits one distinct route of drying above boiling and provide a detailed investigation of this system using single droplet drying and spray drying experimental methods. Such study utilises a combination of drying kinetics measurements, close up monitoring of morphology development and the link between these to the rheological and mechanical properties. These can be related to spray drying by characterisation of the final dried particles collected from spray drying. This study would include moving from simple systems to complex materials with high molecular weight and of complex rheological properties as phase transitions with close resemblance to systems used in industrial applications.

2.7 Influence of material properties on particle formation

This section reviews the particle formation studies that have looked at the morphology developments (such as mechanical deformations and instabilities) during droplet to particle transition and the relation of these morphology developments to key material properties such as rheological and mechanical properties. A vital part of particle formation studies is understanding the properties of skin formed during the liquid to solid transition as it plays a key role in governing the shape of the final dried particle. This involves a closer look at key properties associated with skin formation such as internal flow, sol-gel transition and evolution of rheo-mechanical properties during drying. The properties of this skin evolve during drying as a function of solute concentration and droplet temperature and further add a lot of complexity to particle formation studies.

2.7.1 Skin formation

The evaporation of water from the surface of the droplet induces a diffusional flux of the solutes towards the centre of the droplet, driven by an increase in concentration at the surface. Depending on the relation of the diffusion motion and the evaporation rate, this often leads to the formation of a skin layer. This skin layer has distinct rheological and mechanical properties, which are often not similar to bulk composition and plays a vital role in influencing the subsequent morphology development and the final shape of the dried particle. The establishment of concentration gradients was first reported by Charlesworth and Marshall Jr (1960) who demonstrated that initially, the droplet evaporates in homogenous fashion without hindrance of water transport to the surface. However, at critical solid content, water transport to the surface is hindered, and a solid phase develops at the surface of the droplet. The skin formation is due to slow diffusion of the solutes relative to the evaporation of water (Maki and Kumar, 2011). This is usually related in terms of a Péclet number which defines the extent of convection in relation to the diffusion of the solutes (Vehring et al., 2007; Manukyan et al., 2013; Baldwin et al., 2011). The convection/ advection can be represented by a characteristic velocity, u

which in the case of a drying droplet represents the velocity of the receding droplet surface, $|\frac{dr}{dt}|$. On the other hand, the diffusion can be represented by the diffusive velocity of the solute or suspended particles, D/r. Hence, the Péclet number is given as follows (Vehring et al., 2007):

$$\text{Pe} = \frac{Advective\ velocity}{Diffusive\ velocity} = \frac{u}{\frac{D}{r}} = \frac{r\,|\frac{dr}{dt}|}{D} \tag{2.3}$$

where,

D is the solute diffusion coefficient and r is the droplet radius.

Equation (2.3) can be written in terms of evaporation rate or flux, k, which can be obtained from the square law diameter, which states that the square of droplet radius evolves linearly in time (Vehring et al., 2007). The square law diameter is valid when $r\frac{dr}{dt}$ is constant and the surface area of the droplet decreases linearly as a function of drying time and is given as follows:

$$d^2(\text{t}) = d_0^2 - kt \tag{2.4}$$

Differentiating equation (2.4) to get $r\frac{dr}{dt}$ as follows:

$$\frac{d(d^2)}{dt} = -k = 8r\frac{dr}{dt} \tag{2.5}$$

Substituting $r\left|\frac{dr}{dt}\right| = \frac{k}{8}$ in to Equation (2.3) gives the following definition of Péclet number:

$$\text{Pe} = \frac{k}{8D} \tag{2.6}$$

The definition of the Péclet number given above is the most commonly used in the literature as it represents accurately the mechanisms of advection and diffusion occurring during droplet drying. This definition is stated in the study by Vehring et al. (2007) which has been cited 1202 times.

In the scenario of low Péclet number, the diffusional motion of the solutes towards the centre is more dominant than the evaporation flux of water. In this case, the

surface enrichment of solids is small, and the time required for solutes to reach saturation at the surface is close to the overall droplet drying time (Vehring et al., 2007). Therefore, there is no skin formation during drying, and solid particles are formed with a density closer to the true density of the dry components. An example of this is the drying of saccharide particles at low or moderate air temperatures (Mosén et al., 2005). The second scenario involves drying at high Péclet number where the evaporation flux of the water is more dominant than the diffusional motion of the solutes. Therefore, the radial velocity of the receding interface of the droplet catches up to the diffusional motion of the solute towards the centre and results in surface enrichment and skin formation. Typical examples of high Péclet number involve drying of proteins (Maury et al., 2005; Samborska et al., 2005; Maa et al., 1998) and polymers (Mu and Feng, 2001; Fu, 2001). These studies show wrinkled, hollow or dimpled morphologies as a result of skin formation.

A third scenario involves drying at a changing Péclet number due to changes in the evaporation rate and diffusion coefficient induced by changes in the concentration of the solutes and the droplet temperature. Typical examples of this involve phase changes such as crystallisation or phase separation such as gelation. A striking example of this is the drying of trileucine reported by Vehring et al. (2007). Initially, drying occurs at Péclet number lower than 1; however, trileucine separates into a solid phase once it reaches supersaturation. The corresponding Péclet number at this saturation is much larger than 1 as the diffusion coefficient of the separated phase becomes much lower than the dissolved molecule. This is a prime example of the role of the evolution of material properties with the drying time.

The skin formation can also be affected by other material properties such as surface activity. The role of surface activity of the composition on the skin formation and the composition of the surface layer of the final particles has been reported in previous studies. Fäldt et al. (1994) noted that the more surface-active components accumulate on the droplet surface and dominate the surface composition of the final powder. They concluded that the surface activity results in preferential accumulation of the more surface-active component on the surface resulting in the domination of protein in the composition of powder skin compared to a component that has less

surface activity such as fat or carbohydrates. These studies have used chemical analysis or electron microscopy to analyse the surface composition of the dried particle. This role of surface activity in surface enrichment has been used to modify the shape of the final particles (Kawakami et al., 2010). For example, highly surface-active solutes are more likely to induce the formation of spherical and hollow particles (Maa et al., 1997; Paramita et al., 2010).

Other properties such as solubility, molecular weight and diffusivity of the solutes can also have an influence on the mechanism of skin formation. Molecular weight can play a role in the composition of the particle surface (Kim et al., 2002; Kim et al., 2003). Solutes of high molecular weight have low diffusivity towards the centre and are more likely to accumulate at the surface of the drop resulting in earlier skin formation at the droplet surface (Fäldt and Bergenståhl, 1996; Meerdink and Vantriet, 1995). In contrast, other components such as minerals have high diffusivity and are found at the centre of the droplet (Gaiani et al., 2006). Solubility plays a role in the particle size and final structure. Lin and Gentry (2003) demonstrated that more soluble solutes result in the formation of small dense particles due to the delay in the skin formation as the saturation limit to induce solid saturation at the surface is delayed.

Although the skin formation has been reported in these studies discussed previously, the nature of this skin is still not well understood. Okuzono et al. (2006) demonstrated that the skin layer can be regarded as a region with viscoelastic behaviour, a layer of gel or glassy phase which occurs at the interface of the droplet. It should be noted that the role of the material properties on the skin formation are interdependent and are likely to be affected by the composition, initial concentration and the air temperature. Therefore, research effort is still required to answer questions such as the time of this skin formation and its thickness increase with drying time. Once the skin is formed, it can deform in various ways depending on its rheo-mechanical properties and the extent of the drying stresses. Studies that have focused on the mechanical instabilities of the skin are described in more detail in the next section.

2.7.2 Mechanical and rheological properties influence

The skin formation on the droplet surface is subjected to a considerable amount of capillary stresses due to moisture loss through the skin. This period of particle formation is vital as it determines whether the particle buckles, fractures or remains hollow. This is more complicated as once the skin forms on the surface of the droplet, the instabilities at the surface depends on the evolution of the rheological and mechanical properties of the skin. The mechanical instabilities arising after skin formation have been reported in the drying of proteins, polymers and colloidal suspensions and are reviewed in this section.

Several studies have focused on the influence of the skin formation on the final particle morphology in the studies of drying of milk. These studies have used single droplet techniques, mainly sessile setup, to focus on visually monitoring and investigating the development of particle morphology. One of the earlier studies on the morphology development on whey protein was conducted by Sadek et al. (2013) where they investigated the shape dynamics, and final structure of whey protein isolate (WPI) concentrate droplets by recording the drying behaviour on a hydrophobic substrate. After a period of water like drying, a sol-gel transition occurred at concentrations in the range of 22 and 30 wt. %. The gelation fixed the surface area while the water was still evaporating inducing buckling. Although this study reported interesting morphology developments, it was conducted in stagnant air and is, therefore, less representative of the spray drying process. Bouman et al. (2016) focused on the morphology development of whey protein in the presence of airflow, relating buckling to varying drying conditions such as temperature and initial protein concentration. This study used a sessile set-up reported in Perdana et al. (2011) where the droplet was generated using a dispenser with the ability to generate droplets down to 150 μm. They reported the formation of a hole and a vacuole which was related to skin formation at the early stage of drying. This work was extended to study the effects of the component ratio of protein (whey and casein) and carbohydrates (lactose and maltodextrin) (Both et al., 2018a; Both et al., 2018b). It was reported that the droplet composition did not impact the initial drying rate or locking point; however, it had an influence on the morphology of the final

particle. It was found that maltodextrin concentration resulted in the formation of wrinkled surface and multiple vacuoles, whilst whey protein led to smooth particles with one large vacuole. The skin formation mechanism was different; skin formation in the case of protein was induced by sol-gel transition whilst in maltodextrin systems, it was caused by the increase in viscosity which resulted in a critical skin rigidity. Both et al. (2019) sought to further understand morphology development by conducting bulk rheological properties of concentrated aqueous solutions of whey protein isolate and DE12 maltodextrin. The rheology measurements suggested jamming of the whey protein at concentrations of 50% (w/w), whereas maltodextrin remained liquid-like up to concentrations of 70% (w/w). These measurements provided an approximation of the surface concentrations required for skin formation and demonstrated that the link of particle morphology to bulk rheological properties can provide insight in morphology development (Both et al., 2019).

The studies discussed previously relied heavily on close monitoring of the droplet drying, and all demonstrated that the skin mechanical and rheological properties play a vital role in determining the subsequent morphology developments. An interesting study by Sadek et al. (2015) sought to understand the reason behind differences in the structure of final particles of whey and casein proteins; whey protein resulted in the formation of smooth spherical broken particles while casein formed twisted wrinkled particles. This was done by measurements of mechanical properties of 5 mm milk protein dried films using micro indentation. The study demonstrated the differences in morphology development can be explained by understanding the differences in mechanical characteristics between the two components. Casein reached sol-gel transition earlier which was followed by elastic and plastic regimes where the shell distorted, buckled and formed a wrinkled particle. On the other hand, whey protein became elastic at later drying time which maintained a spherical shape and then fractured later in the drying. These mechanical differences were related to the behaviour of the protein in jamming conditions, where casein micelles form soft and deformable colloids whereas whey proteins form hard spheres. Although mechanical measurements of the dried films are useful in explaining some of the differences in the mechanical properties of

different compositions, their relevance to the drying conditions of the droplet is still questionable.

Skin formation studies have also been reported to cause mechanical instabilities in the drying of polymers due to the formation of the gel/skin layer on the surface of polymer droplets during evaporation (Pauchard and Allain, 2003c; Pauchard and Allain, 2003a). This layer has distinct rheological property from the bulk solution. Many further open questions are still yet to be tackled, such as the thickness of the layer and its influence on the drying rate. Simulation efforts are conducted to answer these questions. Okuzono et al. (2006) stated a condition for the skin layer to be formed depending on the initial volume fraction of the solid components and the Péclet number. They demonstrated that when the initial volume fraction of the solids is near the volume fraction required for gel fraction and the Péclet number is high, the skin appears faster at the surface of the droplet. On the other hand, when the volume fraction is much lower than that for sol-gel transition and at low Péclet number, the skin appears later stage of drying.

The buckling phenomena after skin formation have also been described in detail for colloidal suspensions. Tsapis et al. (2005) demonstrated that the instability and buckling were due to the response of the skin to capillary forces which occurs as water evaporates through the skin, thereby the final shape of the particle is influenced by the capacity of the skin to deform. The colloidal suspensions are interesting as the particle-particle interactions within the suspension can be manipulated to change the viscoelastic properties of the skin and ultimately, the shape of the final particle. A striking example is a study conducted by Sugiyama (2006) where the viscoelastic properties of the skin were manipulated by changing the molecular weight of the dissolved poly(ethylene oxide) (PEO) in the colloidal polystyrene (PS) suspensions. It was illustrated that changing the molecular weight changes the particle-particle interaction and therefore the viscoelastic properties during drying. Droplets containing high molecular weight buckled earlier while those with low molecular weight buckled later in the drying process. Bulk rheology measurements were used to explain that high molecular weight dissolved PEO exhibited a solid-like behaviour and were, therefore, more prone to early buckling.

In contrast, low molecular weight dissolved PEO resulted in a rather liquid-like behaviour and therefore the shell had the ability to accommodate the buckling instability. As colloidal suspensions are not the main focus of this study, the reader is referred to a thorough review by Lintingre et al. (2016) on the control of particle morphology in the spray drying of colloidal suspensions.

In summary, all these studies on polymers, proteins and colloidal suspensions have demonstrated that the skin formation results in mechanical instabilities on the surface of the particle. The subsequent morphology development, the extent of instabilities and their effect on the final shape of the dried particle, depends on the viscoelastic properties of the skin. Efforts to gain information on the viscoelastic properties of the skin formed on the particle during drying have mainly included bulk rheology measurements and to a lesser extent, *ex situ* measurement of dried films. These measurements give insight into the mechanical characteristics of the skin and can be combined with morphology evolution time series from the single droplet drying experiments to further understand the mechanisms of particle formation. However, the drying history and drying conditions of the films are not analogous to those endured during droplet drying, and thereby it raises several concerns on the usefulness of these measurements and any correlations to drying conditions must be interpreted with caution. In situ measurements of the skin properties are extremely hard to achieve due to the inability of current methods to measure these properties in realistic time and size scales (Vehring, 2008). In addition, the timeline of skin formation has been determined from the morphology evolution time series as the point where shrinkage in droplet size ceases, and surface instability arises. These are dependent on the concentration profiles and the intrinsic properties of the material. The concentrations required to reach liquid to solid transitions can also be influenced by phase transitions such as gelation which can be induced by the rise of solute concentration or in some cases by temperature increase for materials that undergo heat-induced gelation. It is important to emphasise that the particle formation studies discussed above have all been conducted at temperatures below the boiling point and therefore the boiling driven effects have not been taken into account. Boiling would have a significant influence on the mechanical instabilities of

the skin as it introduces a new force acting on the skin and must be included on any drying stresses balances on the particle.

2.8 Modelling studies

The work described in this thesis is mainly based on experimental work, and therefore only a quick review of the modelling studies is given in this section which includes an introduction to the modelling approaches of single droplet drying. Single droplet drying models can be broadly divided into two categories: models based on semi-empirical approaches that uses the concept of characteristic drying curve, CDC and deterministic models which describe the droplet drying process by the use of continuity, momentum and energy equations and in some cases population balances (Mezhericher et al., 2010). Droplet-averaged models describe droplet-averaged quantities such as moisture and temperature, whereas mechanistic models give a picture of the droplet drying and thus have the capability to provide some information on the morphology such as final dried particle size and spatially resolved moisture profiles. Each category has its advantages and disadvantages as discussed below.

2.8.1 Characteristic drying curve (CDC)

The characteristic drying curve, CDC, recognises different stages of drying; constant rate period and falling rate period. It is used to model the falling period of the drying and has the advantage of requiring limited computational efforts. In this model, the drying rate is unhindered up to the critical moisture content after which the drying rate is dependent on the moisture content, according to the following equation (Keey and Suzuki, 1974):

$$N_V = \acute{N}_V \, f(\phi) \qquad\qquad (2.7)$$

where N_V is the drying rate, $\acute{N}_V$ is the rate in the first drying period (when the drying rate is limited by the rate of heat transfer to the surface) and ϕ is the characteristic moisture content calculated using:

$$\phi = \frac{\bar{X} - X_e}{X_{cr} - X_e} \qquad\qquad (2.8)$$

where $\bar{X}$ is the volume-averaged moisture content, X_{cr} is the moisture content at the critical point, and X_e is the moisture content at equilibrium.

The concept of characteristic drying curve states that for a given material, the characteristic drying curve is distinct and independent of the temperature, humidity and velocity of the gas (Keey and Suzuki, 1974). The moisture content at which the droplet enters the falling stage is determined from drying experiments and taken as constant for the material investigated. The main drawback of this approach, which disturbs the simplicity of the model, is the unsuitability of the model for drying conditions different from those used when developing the model. Fyhr and Kemp (1998) demonstrated that the critical moisture content is not material constant as it depends on the drying conditions. For example, at harsher drying conditions, the droplet enters the drying stage at higher averaged moisture content. Furthermore, the shape of the drying curve is assumed to be independent of the external conditions. However, this shape would be affected by the temperature of the particle since the temperature influences the viscosity and surface tension. This is not accounted for in the model. Despite these drawbacks, experimental data show that the CDC concept works well for small particle sizes over a moderate range of temperatures (Keey, 1992).

2.8.2 Reaction engineering approach (REA)

Chen and Xie (1997) introduced a reaction engineering approach (REA), which sustains the simplicity associated with the CDC model. The approach takes drying as being a competitive process between 'evaporation reaction' and a 'condensation reaction'. The changes in fluid flow conditions around the solid can be considered by maintaining the conventional heat and mass transfer boundary treatment. The REA approach works by utilising an empirical correlation relating partial vapour density over droplet surface to the average droplet moisture content, which needs to be determined from experiments for each material modelled at different drying moistures (Mezhericher et al., 2010). The activation energy for each given material can be obtained as a function of water content. REA was applied to several systems in many studies (Chen and Lin, 2005; Lin and Chen, 2007; Patel and Chen, 2008; Patel

et al., 2009). Novel drying models based on REA offer a good consistency with experiments, fast calculation and require fewer computer resources. However, this empirical correlation is similar to the need for a functional fitting to experimental drying curve when using a CDC approach. This restricts the application of REA for modelling droplet drying kinetics since the range of materials whose drying behaviour already studied in experiments is limited. Nonetheless, the application of the REA models together with analytical drying kinetics still have a promising potential as they offer simplicity and high accuracy at different drying conditions (Mezhericher et al., 2010).

2.8.3 Mechanistic drying models

Mechanistic drying models describe the drying process by utilising a set of heat and mass diffusion equations with initial and boundary conditions. The numerical solution of such models is rather complex and demand significant computing time and resources. This is because of the moving boundary required to account for the shrinking of the droplet diameter as a result of drying. Furthermore, these models also require knowledge of many coefficients including thermal and mass diffusivities, porosity, and critical moisture content under a range of conditions, temperatures and moisture content (Mezhericher et al., 2010). These are usually hard to obtain from literature and require experimental measurements or fitting techniques with questionable accuracy. However, the advantage of these models is that they produce good accuracy and consistency with experimental data.

2.9 Survey on the systems selected for this research work

Based on the discussion given in section 2.6, it is clear that the behaviour above boiling is largely influenced by the solute and its material properties. The main aim of the overall framework of this thesis is to understand particle formation when drying at high temperatures. This necessitates the consideration of more than one system to provide a detailed study of the behaviours observed above boiling. The systems selected also had relevance for industrial applications. This study benefited from a combination of single droplet drying approach as well as a lab-scale spray

dryer. Single droplet drying techniques allow a closer look at the particle formation and the extraction of valuable information related to locking, boiling and final size. A lab-scale spray drying was used to compare results to single droplet drying and a particular focus on the extent usefulness of single droplet drying to study drying and morphology behaviour above boiling. The comparisons are further complicated due to the variability of the structures produced from spray drying. Based on the general routes of drying given in Figure 2.7, three materials were selected, namely, sucrose, hydroxypropyl methylcellulose (HPMC) and sodium silicate. A description of each system, as well as any drying work on each system, is given below.

2.9.1 Sucrose

Sucrose is a disaccharide, a molecule composed of two monosaccharides: glucose and fructose. It was selected due to a more comprehensive characterisation of its material properties in the literature such as rheology by (Rampp et al., 2000; Telis et al., 2007; Power et al., 2013; Swindells, 1958) and diffusivity in water (Price et al., 2016; Henrion, 1964; Ekdawi-Sever et al., 2003). Drying of sucrose was conducted in previous studies. El-Sayed et al. (1990) looked at the morphology behaviour of sucrose using a filament SDD and compared structures with a free-falling system. They reported that sucrose particle collapses after inflation/deflation to form a spherical shape with very little or no voidage. The morphology evolution of sucrose has also been reported by Hecht et al. (2000), where inflation/deflation cycles were observed. However, this work was more focused on the influence of inflation/deflation cycles on the loss of volatile components rather than the effects of boiling on the morphology development and the structure of the final dried particle. A systematic study at air temperatures above and below boiling is lacking. Furthermore, the drying metrics at boiling and skin formation are also lacking for a more thorough understanding of the behaviour of drying of sucrose above boiling.

2.9.2 Hydroxypropyl methylcellulose (HPMC)

HPMC is a propylene glycol ether of methylcellulose and possesses good film-forming properties that enable protection against degradation and moisture. The unique features of HPMC such its nontoxic property, ease of handling, high

biodegradability and solubility makes it desirable for a number of applications (Sakata et al., 2006). One of the major applications of HPMC is in the pharmaceutical industry as a carrier material due to its ability to allow a slow diffusion of drugs out of the system (Siepmann and Peppas, 2001). HPMC is also used in food applications as an emulsifier, thickening and suspending agent. HPMC is modified by using different substituent which can either by CH_3, $-CH_2CH(CH_3)OH$ group, or a hydrogen atom. The methoxy ($-OCH_3$) group content, hydroxypropoxy ($-OCH_2CH(CH_3)OH$) group content and the molecular weight (Mw) have a significant influence on the physicochemical properties (Perfetti et al., 2011). The variation of contents causes changes in its properties.

Very little drying work has been done on the drying of HPMC. Wulsten et al. (2009) used single-droplet drying levitator to study the drying of itraconazole/HPMC formulations to determine the influences of the polymer on the drying rate and dried particle morphology. They reported that the presence of HPMC in the formulation led to the early surface skin formation, which strongly influenced drying rate. HPMC makes an interesting choice for this study due to its complex properties. The molecular weight and viscosity can be manipulated by a change of the substituents, and it can be supplied in different grades. Furthermore, the mechanical properties of HPMC can be manipulated by the use of organic solvents.

2.9.3 Sodium silicate

Sodium silicate is one of the most important soluble silicates and is widely known as "water glass" (Weldes et al., 1969). It is produced by the fusion of pure sand with soda ash or alkali metal sulfate and carbon in large furnaces at a temperature of 1300 ˚C. This is followed by dissolving of the glass in water before or after cooling. Sodium silicate is widely used in the detergent and cleaning compounds as active alkaline builders. It significantly enhances the effectiveness of the detergents and cleaners by maintaining high pH due to their buffering ability. Sodium silicate performs functions such as emulsification of mineral oil, saponification of animal and vegetable oils and fat (Weldes et al., 1969). Sodium silicate is produced as glasses and can have SiO_2:Na_2O molar ratio in the range of 1.6-3.9 (Iler, 1979).

In terms of drying work on sodium silicate, the only drying work reported in the literature was done by Walton and Mumford (1999a) using a single droplet drying set-up. They reported sodium silicate as materials which form particles with a skin-like structure. Drying of sodium silicate at 70 ˚C resulted in the formation of a solid particle, which retained its general spherical shape. At 200 ˚C, the evaporation of an aqueous silicate droplet caused the liquid to foam and bubble which on fully drying give a blistered appearance. Extensive analysis of the drying kinetics or final dried particle was not provided. The drying behaviour of sodium silicate is further complicated by its complex chemistry, such as polymerisation and gelation at high solid content, which often depends on the air temperature and the solute concentration.

2.10 Conclusions

This chapter provided a detailed review of the different SDD techniques. The review showed the advantages and disadvantages of the different SDD techniques and comparison of the applicability of these methods. The review has highlighted the suitability of the filament SDD for particle formation studies at high temperature as it can be used at a wide range of drying conditions, particularly air temperature. The usefulness of these SDD techniques on understanding particle formation studies has been highlighted. They provide an easier alternative to monitor particle formation during drying and has helped unravel various parts of particle formation such as morphology development, transport phenomena and measurement of drying kinetics. The main drawback of the SDD is the large size of the droplets compared to those produced on industrial spray dryer. Despite the differences in particle size, examples of similarities of structures produced from SDD and spray drying have been highlighted, which demonstrates the usefulness of SDD for particle formation studies.

The literature review has shown that although boiling has a significant influence on the subsequent morphology development, detailed studies on particle formation accounting for the effect of boiling are lacking. This is particularly evident for skin forming materials where their plastic nature and their response to boiling can result in diverse morphologies. The complexity of understanding the morphology development when drying above boiling is due to the significant influence of the surface structure formed on the particle during drying on the response to boiling driven effects. The structure formed is highly dependent on the material dried and is significantly influenced by the evolution of rheological and mechanical properties with the increase of temperature and solute concentration during drying. The relation between the morphology development and material properties is therefore vital for any progress on understanding morphology development in spray drying. This is even more challenging for systems with complex rheological and mechanical properties such as phase transitions. These are usually relevant and more common in industrial spray drying. The literature has shown the role of material properties on the morphology development has been conducted on some food formulations.

However, these studies were conducted at low air temperature below the droplet boiling point. The literature review has also highlighted the challenge of *in situ* measurements of material properties, particularly the viscoelastic properties of the skin on the particle during drying.

To tackle these gaps highlighted in the literature on understanding particle formation above boiling point, the literature review has highlighted a need for a thorough investigation of more than one system. The systems selected are of industrial relevance for the detergent, food and pharmaceutical industries. These systems have not been studied in detail, particularly with regards to the influence of boiling on the morphology evolution and the structure of the final dried particles.

Chapter 3 Apparatus development and quantification

3.1 Introduction

The development, design, commissioning and validation of the experimental equipment used in this work is described in detail in this chapter. The first part of this chapter describes in detail the design, installment and testing of the single droplet drying approach. The validation of the measurements methods is done by measurements of single droplet drying of pure distilled water, which are compared with theoretical expectations based on mass and energy balance calculations using Ranz-Marshall Correlations. The second part of this chapter describes the lab-scale spray dryer which is used for comparison of final dried structures to the single droplet drying experiments.

3.2 Single droplet drying

3.2.1 Selection of single droplet drying method

The single droplet drying approach was chosen as it allows for close monitoring of the droplet drying and measurement of drying kinetics. Consideration of the different single droplet drying techniques including sessile, acoustic and filament. The filament single droplet drying is the most practical due to the range of temperatures that can be applied. An acoustic levitator has a limitation of the operating temperature, and hence it was excluded in this work. This is due to the electronics included in the rig, which cannot withstand higher temperatures (Groenewold et al., 2002). Furthermore, the suspension criterion is also affected at high temperatures (Groenewold et al., 2002). Sessile droplet drying approach is also not ideal for drying at high temperatures as the source of error from the substrate increases substantially at high temperatures. The substrate also greatly affects the nucleation of the bubbles inside the droplet. The filament single droplet drying rig is therefore considered to be the most practical option for drying at high temperatures.

3.2.2 Filament single droplet drying

A disassembled rig (Threlfall-Holmes, 2009), missing vital parts and tools for controlling the process parameters and capturing the drying process, was used as

the basis of the single droplet drying rig design. Therefore, measurements methods had to be devised, installed and validated.

The approach adopted in this design is an apparatus that will operate over a wide range of droplet diameters and air velocity, temperature and humidity. The desired drying/evaporation conditions for this device to be operated are:

1. Air temperatures 25˚C to 350 ˚C
2. Air velocities 0 to 2 m/s
3. Droplet sizes from 1 to 3 mm.

The final process flow diagram of the single droplet drying apparatus is shown in Figure 3.1.
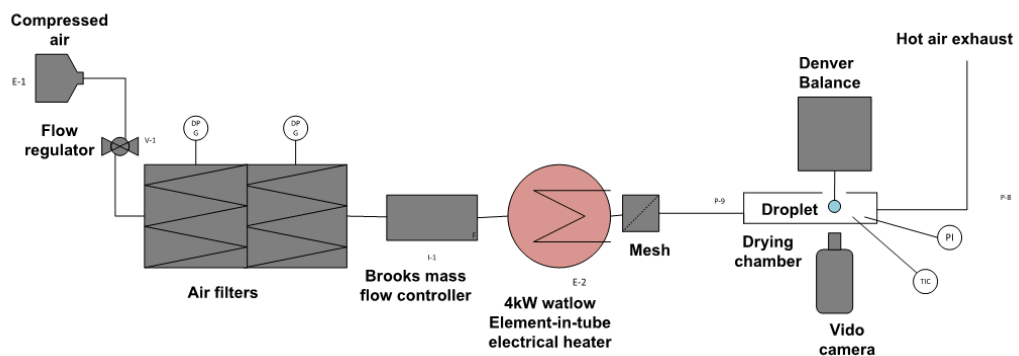
Figure 3.1 A process flow diagram of the single droplet drying rig
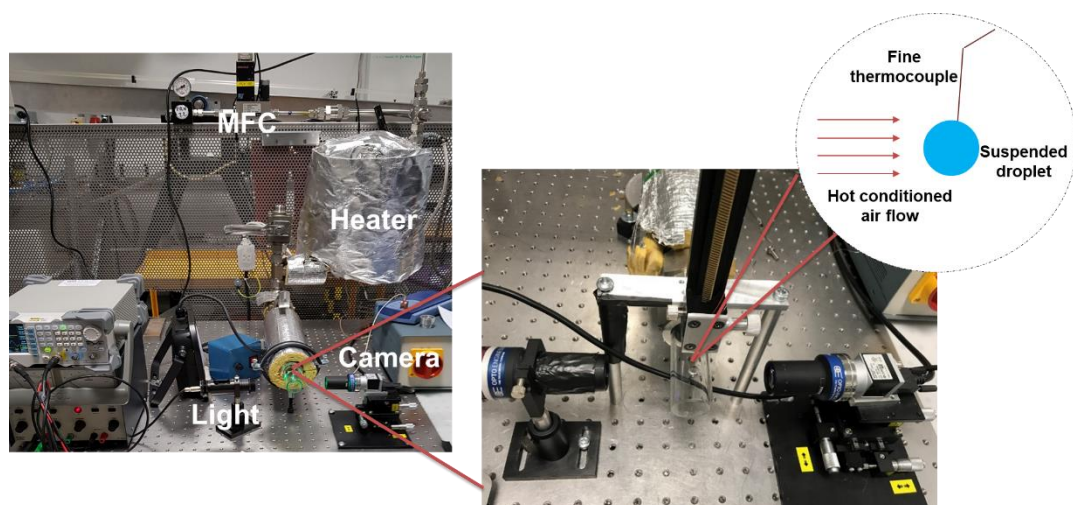
Figure 3.2 Single droplet drying rig

The rig development includes the design and control of airflow and temperature, which is vital for the success of the single droplet drying experiments. The droplet needs to be suspended in the drying chamber in uniform, pre-conditioned (temperature and humidity) airstream. The logging and synchronisation of drying kinetics including temperature, radius and mass is also an important part of the design. The design of each part of the single droplet drying apparatus is described in the following sections.

3.2.3 Control of air supply

The flow diagram, Figure 3.1, shows that the air supply includes a pressure gauge to control the pressure of the airflow. The air flowrate then passes through a thermal mass flowmeters (Brooks) with a fluid range of 0-54 litres/min. The thermal mass flowmeter is connected to USB-6211 data acquisition (DAQ) device, which is connected to a PC to control the compressed air flow rate using a LabVIEW code. A screenshot of the block diagram of this LabVIEW code is given in Appendix A, Figure A.1. The mass flow controller has been calibrated, and the calibration table is given in Table 3.1. It is of vital importance that the air passing to the drying chamber is laminar flow and steady to prevent movement of the filament. Before entering the drying chamber (where the droplet is held) the drying air is passed through 10 layers of 24-mesh screens (perpendicular to the airflow), which serves to flatten the air velocity profile.

Table 3.1 Calibration table of the mass flow controller		
Voltage (volts)	Volumetric flow rate (litres/min)	Air velocity (m/s)
0.50	6.16	0.19
1.00	12.38	0.39
1.50	18.57	0.58
2.00	24.76	0.77
2.50	30.96	0.96
3.00	37.15	1.16
3.50	43.34	1.35
4.00	49.53	1.54
4.50	55.72	1.74
5.00	61.91	1.93

3.2.4 Control of air temperature

The air is heated using a custom made 4kW helical annular electrical heater. The heater is controlled using a temperature controller which includes 2 PID LOOP. Two thermocouples are connected to the controller, one from the heater, and the other one is placed in the pipeline upstream of the bypass valves. As a safety measure, an airflow switch FST100 2R supplied from Omega was mounted in the pipeline feeding the heater and connected to the temperature controller, if the airflow passing into the heater is disconnected, the heater is switched off. The temperature controller was also configured to allow for an alarm which can be set for a maximum temperature for the heater. All pipelines in the rig were insulated with Rockwool insulation to reduce heat loss.

3.2.5 Selection and design of the drying chamber

The drying chamber is the main unit of the single droplet drying rig and the most challenging in terms of design. The key design considerations include:

1. Smooth flow: It is important that airflow over the entire length of the drying chamber is stable and has a minimum degree of turbulence to prevent distortion of the droplet and intervention with the drying process. To counter this problem, layers of mesh screens have been fitted upstream of the drying chamber. To ensure the flow maintains a flat velocity profile in the drying chamber, the distance between the mesh screens and the drying chamber must be minimum, specifically the distance to the location of droplet suspension in the drying chamber.

2. Easy access to the drying chamber: The experimental procedure of rig operation involves heating the drying chamber to the desired temperature then diverting the airflow so that the drying chamber can be opened from the air exit end and the droplet can be suspended on the hanging filament in the drying chamber. This necessitates an easy opening of the drying chamber and quick access to the location of droplet suspension.

3. The material of construction: High operating temperatures, as high as 200 °C, are used, and therefore the material must withstand such temperatures. The

material of construction must also be transparent so that it allows for visualisation of the droplet. For these reasons, borosilicate glass was selected. After carefully considering all design conditions previously discussed, a decision was made to order a customised round drying chamber, made of borosilicate glass with dimensions of (ID= 1", OD=1.25", L=1.33").

3.2.6 Data acquisition and synchronisation

3.2.6.1 Measurement of the droplet temperature

The droplet temperature is measured by suspending the droplet on the tip of a thermocouple with 200 μm diameter. The droplet temperature is logged using TC-08 Thermocouple data logger (Pico Technology). The use of IR thermal imaging camera was also explored. The setup with the thermal camera is given in Figure 3.4. An example of an image obtained from the thermal camera is shown in Figure 3.3. Preliminary tests demonstrated good agreement of temperature measurements of water droplet during drying measured by FLIR camera and a thermocouple. However, due to limitation with the availability of the FLIR camera, the droplet measurements were all conducted using a thermocouple.
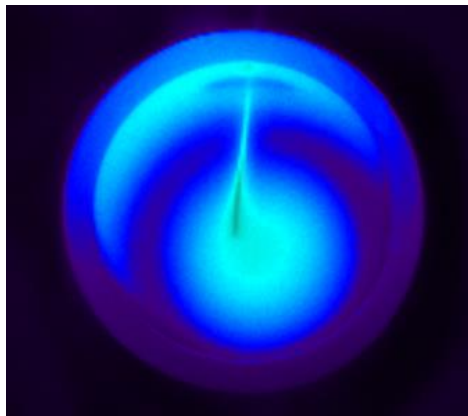
Figure 3.3 A-frame of water droplet during drying captured using a FLIR IR camera
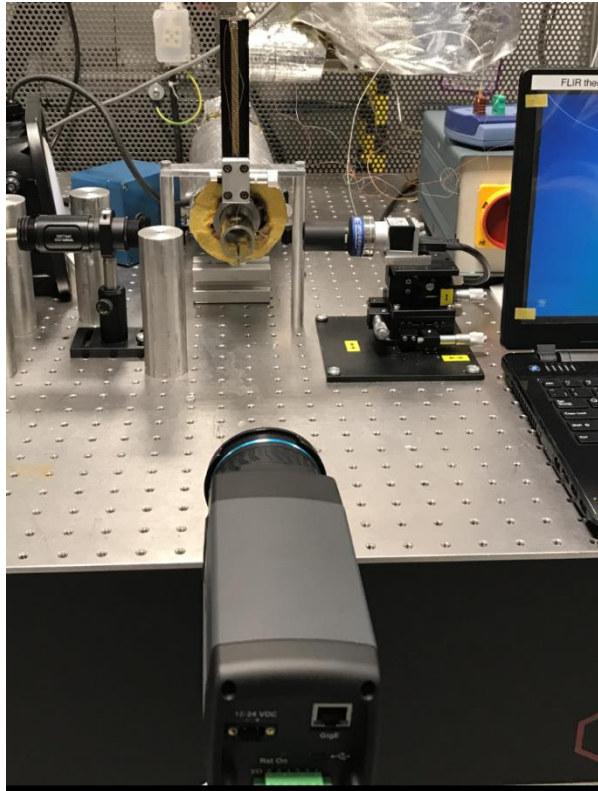
Figure 3.4 The set-up of the drying rig with a FLIR IR camera

3.2.6.2 Measurement of the droplet radius

The measurement of the droplet radius required a careful selection of lens and the camera. The requirement of the lens to be able to capture:

- The maximum size of the droplet/particle during drying
- The minimum size of the droplet/ particle during drying
- The working distance as the lens needs to be at a distance from the drying chamber to avoid the effects of hot air

The lens selection comprised a vital part of the accuracy of the acquired data from the rig as it significantly affects the diameter measurements of the droplet during drying. The ability to perform a quick high accuracy diameter measurement is therefore of vital importance. Telecentric lenses allow for a high degree of accuracy to be achieved as they demonstrate zero angular field of view, which eliminates parallax error (Edmund Optics, 2019). This is depicted in Figure 3.5.
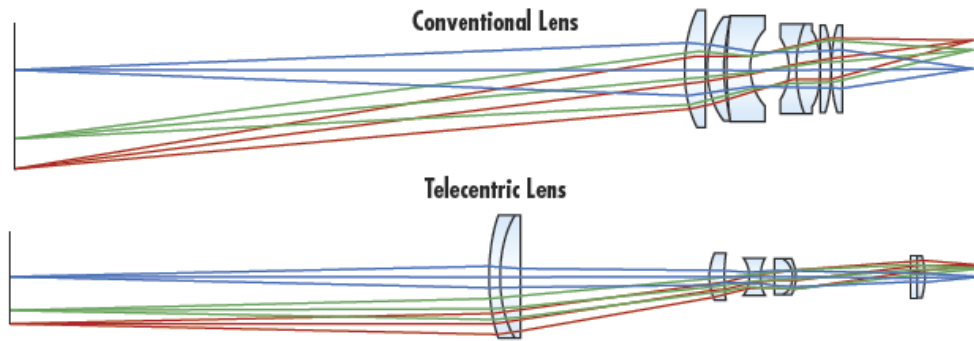
Figure 3.5 Angular field of view comparison of conventional vs telecentric lens. Telecentric lens offers zero angle field of view (Edmund Optics, 2019)

The droplet is suspended on a filament, and the drying process is recorded using a Basler Ace USB Camera (1280×1024) fitted with Matrix Detector Telecentric Lens. Matrix Detector Telecentric Lens have ½" sensor size, a working distance of 62 mm and a field of view of 6.4×4.8 mm. High Performance Telecentric Illuminators (LTC LHP) are used to provide back illumination of the droplet. These illuminators provide excellent illumination stability and precise light intensity specifically designed to give back illumination for objects imaged using a telecentric lens.

3.2.6.3 Consideration of mass measurement methods

A direct method for mass loss measurement is required, particularly in the case of drying droplets with dissolved solids as the estimation of mass loss based on diameter becomes invalid. The measurement of mass loss was the most challenging part of single droplet rig design. The initial droplet mass to be used in the droplet is in the range of 1-3.5 mg depending on the size of the droplet and the dissolved solids. The mass loss per second is expected to be in the range of 0.01-0.08 mg/s based on preliminary calculations depending on the air temperature, the material of the dissolved solids and concentration. The approaches considered for mass loss measurement include Infrared (IR) spectrometer and balances with a resolution to 6 and 7 decimal places of a gram. The comparison criteria included accuracy, resolution, response time, ease of installation, calibration requirements and compatibility with the drying procedure.

The IR has been used in a study by Tran et al. (2016a). Therefore, it was considered for this single droplet design to measure the droplet mass. The model considered

was NGA 2000 range (MLT1/2/3/4), supplied by Emerson Automation Solutions. Detail of the equipment is given in Table 3.2.

<div align="center">Table 3.2 NGA 2000 IR analyser (Emerson, 2008)</div>

Response time	4 s ≤ t90 ≤ 7 s
Permissible gas flow	0.2–1.5 l/min.
Maximum gas pressure	≤ 1500 hPa abs. (≤ 7 psig) , 1.5 bar
Sensor operating temperature	-40 to +60 °C
Lowest range	0-1000 ppm
Highest range	0-8%

The use of an infrared spectrometer for mass measurement was excluded due to several issues summarised as follows:

1- Limitation of the airflow that can be admitted into the spectrometer: the permissible gas flow through the Infrared spectrometer is in the range of 0.2-1.5 l/min which is much lower than the airflow range for this rig 0-54 l/min. This means there was a need to design a pipeline where a fraction of the airflow exiting that drying chamber can be diverted into the spectrometer to conduct the moisture analysis. This would introduce an error as the amount of air used for analysis is much lower than the overall flow rate coming out of the drying chamber.

2- The sensor operating temperature is in the range of -40 to 60˚C: The drying experiments are conducted at air temperatures in the range of 25 ˚C to 200 ˚C, much higher than the range offered by the sensor operating temperature. This means in cases where the air temperature exceeds the sensor operating temperature; the air would need to be cooled before it is fed into the spectrometer. This would be undesirable and might introduce further errors.

3- The need for repeated calibration of the device using pure water.

The seven-digit balance, XPR2U supplied from Mettler Toledo, was used to measure mass loss when drying droplets of water at ambient air temperature. Details of the balance are given in Table 3.3.

Table 3.3 Specifications - Balance XPR2U (Mettler Toledo, 2019)

Maximum Capacity	2.1 g
Readability	0.1 µg
Repeatability (typical)	0.15 µg
Minimum Weight (USP, 0.1%, typical)	0.3 mg
Guaranteed Repeatability	0.2 µg
Weighing Pan Diameter	16 mm
Material Number(s)	30279196

The trials of mass loss from water droplets during drying were unsuccessful and showed a high degree of instability of mass measurements due to the effect of airflow. Another microbalance with a resolution to 6 decimal places of a gram, MSE6.6S-000-DM Sartorius Cubis balance, was considered. Details of this balance are given in Table 3.4. The six-digit balance showed a very high potential with stable mass measurements with airflow and at high temperatures. The set-up of the microbalance in the single droplet drying apparatus is shown in Figure 3.6. Details and description of the validation of mass measurements are given 3.2.10.

Table 3.4 Specifications of the Sartorius Cubis six-digit balance (Sartorius AG, 2019)

Readability	0.001 mg
Weighing capacity	6.1 g
Levelling	Assisted
Adjustment	Internal, isoCAL
Display	Liquid-crystal display, black and white
Brand	Cubis®
Weighing pan diameter	∅ 30 mm
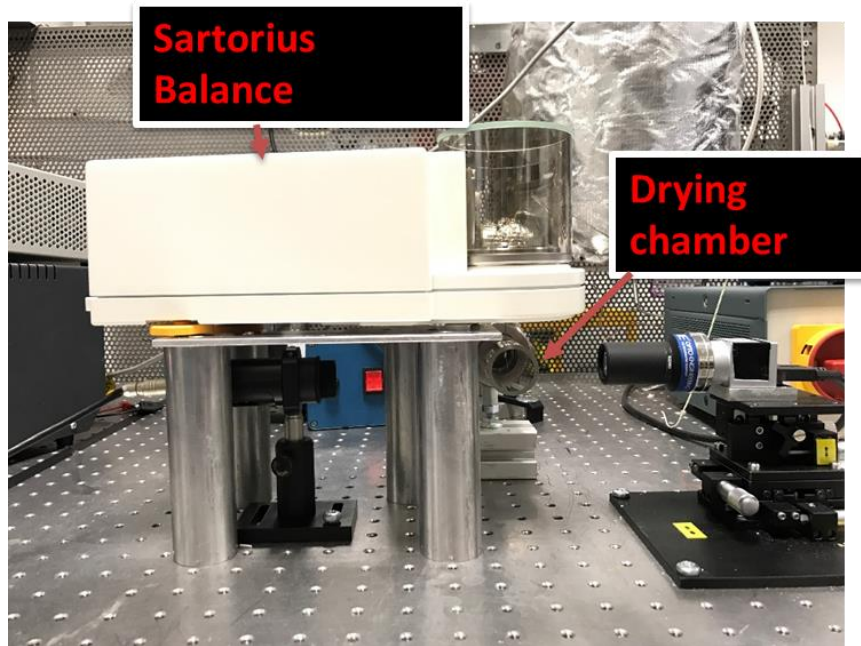
Figure 3.6 The setup of the microbalance to measure moisture loss

3.2.7 Selection of filament

The temperature measurements involved suspending the droplet on the tip of a thermocouple with 200 μm diameter. For measurement of mass, a filament made of Polyetheretherketone PEEK with a diameter of 200 μm was used for droplets suspension. This material was chosen due to its low thermal conductivity, 0.26 W/m.K (Goodfellow, 2018). The PEEK filament had a temperature limitation of 250˚C (Goodfellow, 2018). A filament with 200 μm diameter was found to be the smallest diameter at which successful suspension of droplets was achieved.

3.2.8 Experimental procedure

The experimental procedure for the single droplet drying rig are summarised as follows:

1. The compressed air is switched on and set to the desired air temperature and flow rate to achieve the target velocity and temperature in the drying chamber.

2. Once the set temperature has been reached, the air is temporarily diverted from the chamber using a bypass valve, in order to dispense the droplet in quiescent air and minimise evaporation of the droplet during the loading time.

3. The droplet is generated on a pipette tip (0.1- 2.5 µL Eppendorf Research Plus). A filament of similar size to the suspended filament is used to transfer the droplet from the tip of the Eppendorf to the tip of the suspended filament.

4. The recording of frames, droplet temperature and mass is started, and the air is diverted back to the drying chamber.

5. Once the mass loss is stable, the recording is stopped, and the air is diverted to bypass, to permit the dried particle to be removed from the filament.

3.2.9 Synchronisation and logging of data

This section describes the development of LabVIEWcodes to synchronise data logging from the following devices:

1. Basler USB3 Camera: up to 169 Frames per second

2. Pico logger temperature logger: up to 33 samples per second

3. Sartorius microbalance: up to 5 samples per second.

To achieve the synchronisation, three LabVIEW programs-subroutines, termed virtual instruments (VIs), were created to log the data from the three devices separately. Then, these three VIs codes were merged into one code where the sampling starts at time zero for all the devices. It was ensured that the synchronisation also works even when with different sampling intervals from the three devices. Images of the front panel and VI codes to log temperature, mass and camera frames are given in Appendix A.2 in Figure A.2, Figure A.3, Figure A.4 & Figure A.6, respectively.

3.2.10 Validation of experimental equipment

Validation of the measurement methods used in the single droplet drying apparatus is done by conducting experimental drying runs using pure water. The two main measurement methods are the determination of the diameter from images and the mass loss from the microbalance. Testing of the accuracy of these methods is conducted by drying runs of pure distilled water at air temperatures of 25˚C, 60 ˚C, 100 ˚C, 160 ˚C and 180 ˚C. The experimental runs are compared with the mass loss and diameter history calculated using a model based on Ranz-Marshall Correlations.

3.2.10.1 Ranz-Marshall model

The steps used in the Ranz-Marshall model are as follows:

The Nusselt number, Nu, and the Sherwood number, Sh, are determined from Ranz-Marshall Correlations given below (Ranz and Marshall, 1952a) :

$$Nu = 2 + 0.6Re^{0.5}Pr^{0.33} \tag{3.1}$$

$$Sh = 2 + 0.6Re^{0.5}Sc^{0.33} \tag{3.2}$$

Re is the Reynolds number of the droplet given by:

$$Re = \frac{v_a d_d \rho_a}{\mu_a} \tag{3.3}$$

v_a, μ_a, ρ_a are the velocity (m/s), viscosity (Pa.s) and density (kg/m³) of the air respectively. d_d is the diameter of the droplet.

Pr is the Prandtl number calculated from:

$$Pr = \frac{C_{p,a} \, \mu_a}{k_a} \tag{3.4}$$

$C_{p,a}$ is the heat capacity of air (J/kg.K), k_a is thermal conductivity of air (W/m.K)

Sc is the Schmidt number, calculated using:

$$Sc = \frac{\mu_a}{D_v \, \rho_a} \tag{3.5}$$

The heat and mass transfer coefficients, h_a and k_m respectively, are determined as follows:

$$h_a = \frac{Nu \, k_a}{d_d} \tag{3.6}$$

$$k_m = \frac{D_v \, Sh}{d_d} \tag{3.7}$$

D_v is the water vapour diffusivity in air.

The water vapour saturation pressure on the droplet surface is determined using Antoine equation:

$$log p_{sat} = A - \frac{B}{C + T_d} \tag{3.8}$$

$$y_{v,s} = \frac{p_{sat}}{p_t} \tag{3.9}$$

p_{sat} is the saturated vapour pressure at the droplet temperature, T_d. p_t is the atmospheric pressure. $y_{v,s}$ is the water vapour mole fraction at the droplet surface.

The drying rate is determined using:

$$\frac{dm_d}{dt} = -k_m \pi d_d^2 \frac{M_w}{R} \frac{P_T}{T_{avg}} (y_{v,s} - y_{v,a}) \tag{3.10}$$

m_d is the mass of the droplet. M_w is the molecular weight of water. $y_{v,s}$ is the water vapour mole fraction at the droplet surface. T_{avg} is the film temperature in Kelvin; the average of the air temperature and the droplet temperature (Adhikari et al., 2007).

The new diameter is calculated based on the drying rate as follows:

$$\frac{dm_d}{dt} = 4\pi r_d^2 \rho_d \frac{dr_d}{dt} \tag{3.11}$$

ρ_d is the density of the droplet. r_d is the droplet radius

The droplet temperature is determined based on energy balance as follows:

$$(m_d C_{p,w}) \frac{dT_d}{dt} = h_a \pi d_d^2 (T_a - T_d) + \lambda \frac{dm_d}{dt} \tag{3.12}$$

T_d and T_a are the temperatures of the droplet and air respectively. λ is the latent heat of the droplet.

The new mass of the droplet is determined using the old mass of the droplet and the drying rate:

$$m_{d,new} = m_{d,old} + \frac{dm_d}{dt} \Delta t \tag{3.13}$$

Δt is the time step

The thermophysical properties of air were determined as a function of air temperature based on equations reported by Zografos et al. (1987), summarised in Table 3.5. The computed values are summarised in Table 3.6. The water properties are determined as a function of the droplet temperature based on equations given in Table 3.7.

Table 3.5 Equations for thermophysical properties for dry air, temperature range 100 K-3000 K, atmospheric pressure (Zografos et al., 1987)

Equation	Unit
$\rho_a = 34557(T - 2.6884)^{-1}$	kg/m^3
$\mu_a = 2.5914 \times 10^{-15}T^3 - 1.4346 \times 10^{-11}T^2 + 5.0523 \times 10^{-8}T + 4.1130 \times 10^{-6}$	N.s/m^2
$C_{p,a} = (1.3864 \times 10^{-13}T^4 - 6.4747 \times 10^{-10}T^3 + 1.0234 \times 10^{-6}T^2 - 4.3282 \times 10^{-4}T + 1.0613) \times 10^3$	J/kg.K
$k_a = 1.5797 \times 10^{-17}T^5 + 0.4600 \times 10^{-14}T^4 - 2.2012 \times 10^{-10}T^3 + 2.3758 \times 10^{-7}T^2 + 17082 \times 10^{-4}T + 7.488 \times 10^{-3}$	W/m.K

Table 3.6 Dry air properties used in the Ranz-Marshall model calculation, determined using equations in Table 3.5

Property	Air temperature (˚C)					
	25	60	100	140	160	180
ρ_a (kg/m³)	1.184	1.059	0.946	0.854	0.815	0.779
$\mu_a \times 10^5$ (N.s/m²)	1.849	2.008	2.181	2.181	2.420	3.101
$C_{p,a}$ (J/kg.K)	1007	1007	1009	1013	1016	1019
k_a (W/m.K)	0.026	0.028	0.031	0.034	0.035	0.036

Table 3.7 Property equations for liquid water, temperature range 273 K-600 K, atmospheric pressure

Equation	Reference	Unit
$\rho_w = -3.0115 \times 10^{-6}T^3 + 9.6272 \times 10^{-4}T^2 - 0.11052\,T + 1022.4$	Zografos et al. (1987)	kg/m^3
$C_{p,w} = (1.7850 \times 10^{-7}T^3 - 1.9149 \times 10^{-4}T^2 - 6.7953 \times 10^{-2}T - 3.7559) \times 10^3$	Zografos et al. (1987)	J/kg.K
$\lambda = 1.91846 \times 10^6 \left(\dfrac{T}{T - 33.91}\right)^2$	Henderson-Sellers (1984)	J/kg

The diffusivity of water vapour, D_v, in air is determined using a correlation taken from Boynton and Brattain (1929), given by:

$$D_v = D_0 \left(\frac{T}{T_0}\right)^{1.75} \frac{p_0}{p} \tag{3.14}$$

where,

D_0 is the diffusivity of water vapour in air at absolute temperature (T_0) and atmospheric pressure, determined to be 0.223×10^{-5} m^2/s (Boynton and Brattain, 1929)

T is the temperature in Kelvin, in this case, it is taken as the film temperature, T_{avg}; the average of the air temperature and the droplet temperature (Adhikari et al., 2007).

3.2.10.2 Pure water drying experiments versus Ranz-Marshall model

The validation of the measurements methods incorporated in the rig design was carried out by conducting single droplet drying experiments of distilled pure water. The validations were carried out at the conditions summarised in Table 3.8. The two main methods tested include (a) the determination of the diameter measurements from the images obtained from the camera (b) the mass measurements from the Sartorius balance with a resolution to 6 decimal places of a gram described in 3.2.6.3. The PEEK filaments, described in 3.2.7, was used for droplet suspensions. Up to 5 drying runs of pure water droplets were conducted at the same condition to test the repeatability and accuracy of the data.

Table 3.8 Settings at which rig validation was conducted

Parameter	Specification
Air velocity	0.57 m/s
Droplet size	1.5-1.7 mm
Air temperature	25 ˚C, 60 ˚C, 100 ˚C, 160 ˚C and 180 ˚C
Filament	PEEK filament (200 µm diameter)
Diameter measurement method	Images converted to diameter using ImageJ
Mass measurement method	Microbalance with a resolution to 6 decimal places of a gram
Number of experimental drying repeats	5

The images of water droplet recorded during drying are processed using ImageJ2 (Schneider et al., 2012) to determine the diameter of the droplet/particle in mm units. The images are imported into ImageJ and converted into binary images with a black foreground (representing all the values that belong to the droplet as well as the visible part of the filament) and white background representing the rest. The conversion of images into binary images is based on the colour threshold between the black droplet and the white background, as shown in Figure 3.7. The visible part of the filament is cropped out using the editing tools on ImageJ. The total area of the remaining black section is determined by transforming the square pixels into calibrated square mm^2. The area of the inserted part of the filament is determined from the last image where the water has completely dried, and this area is subtracted from the total area of the droplet. The diameter of droplet/particle is the diameter of a circle with the same area as the measured projection area, and hence the diameter is calculated as follows:

$$d = \left(\frac{4 \times A}{\pi}\right)^{0.5} \tag{3.15}$$

A)   B)   C)
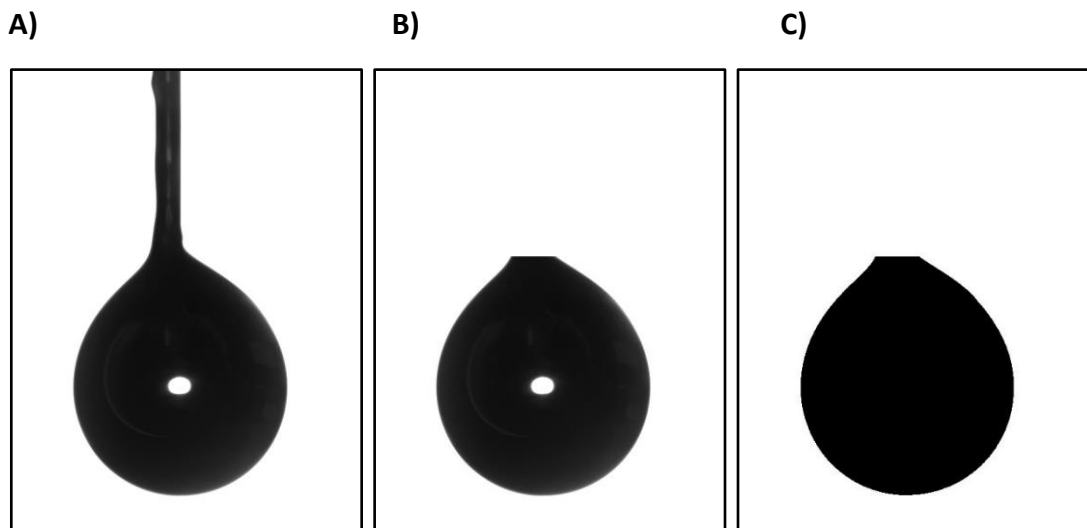
Figure 3.7 Steps of image processing using ImageJ analysis to obtain droplet diameter

Typical individual runs of the recorded mass loss and diameter versus computed model results are presented in Figure 3.8. Further single droplet drying repeats are presented in Appendix B.
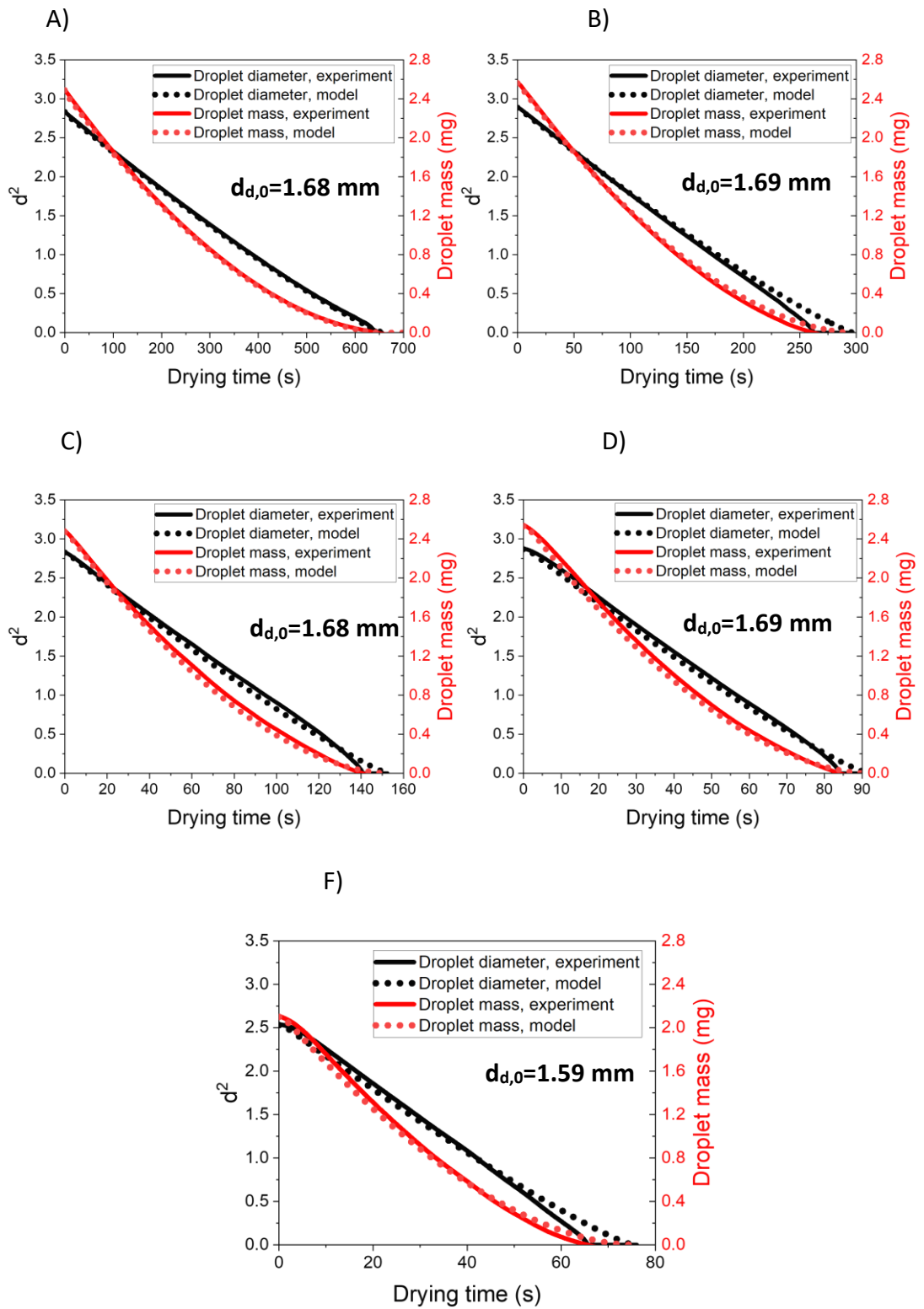
Figure 3.8 Comparison of experimental drying measurements of pure water droplets vs Ranz-Marshall model at v_{air}= 0.57 m/s and air temperatures of (A) T_{air}=25 ˚C (B) T_{air}=60˚C (C) T_{air}=100 ˚C (D) T_{air}=160 ˚C (F) T_{air}=180 ˚C

Figure 3.8 shows a strong agreement between the droplet diameter determined from experiments and that computed by Ranz-Marhsall model. The diameter measurements show deviation from the expected values towards the end of the drying. The degree of deviation towards the end of the drying increases with the increase in air temperature. The deviation towards the end of the drying is caused by the small size of the droplet, which makes the diameter measurements more challenging due to the increase of error from the filament intrusion. In addition, the increased error in diameter measurements towards the end of drying is related to the sphericity of the droplet assumed in the calculation of the diameter in Equation (3.15). The error associated with the image analysis at the end stage of drying also increases as the relative size of the filament to the droplet becomes higher. Furthermore, the error from the heat conduction also increases at the end stage of drying as the droplet size becomes smaller.

The mass measurements of the droplet during drying, shown in Figure 3.8, also show a good agreement to the mass computed from Ranz-Marshall model at all air temperatures. The agreement between experimental measurements and the model demonstrate that the effects of the filament intrusion on the drying process are negligible at the droplet size range (1.5-1.7 mm) and filament size (200 μm) used in this study. A filament with a diameter of 200 μm only makes up about 0.2% of a droplet with a volume of 2 μl. The heat conducted into the droplet along the filament remains lower than 1% of the total heat input to the droplet through convection (Charlesworth and Marshall Jr, 1960; Qi Lin and Chen, 2002). In this work, the heat conduction from the filament has further been reduced by the use of Polyetheretherketone PEEK filaments, which possess low thermal conductivity, 0.26 W/m.K (Goodfellow, 2018). The agreement between the measured and computed mass and diameter measurements proves the accuracy of the measurements methods at the range of conditions used (25-180 ˚C air temperatures, 1.4-2 mm droplet size, 0-0.57 m /s air velocity). These are the range of conditions required for the scope of this work, and therefore it can be concluded that the rig measurements have been successfully validated.

3.3 Spray drying

One of the overall objectives of this study is to compare the structures of the dried particles collected from the single droplet drying apparatus and a lab-scale spray dryer. Therefore, this part gives a brief description of the lab-scale spray dryer used in this work, depicted in Figure 3.9. This spray dryer can be operated with two or three columns. The spray dryer operating range includes 25-200 °C air temperature and air volumetric flow rate in the range of 0- 1.2 m^3/s. It can be operated with two types of nozzles; a bi-fluid nozzle and an ultrasonic nozzle. The spray dryer is equipped with a peristaltic pump to control the feed rate and a cyclone collector for obtaining the fine powder. In this study, the spray dryer has been used to dry silicate and HPMC aqueous solutions. Further details of the spray drying work of silicate and HPMC aqueous solutions are given in Chapter 5 & Chapter 6, respectively.
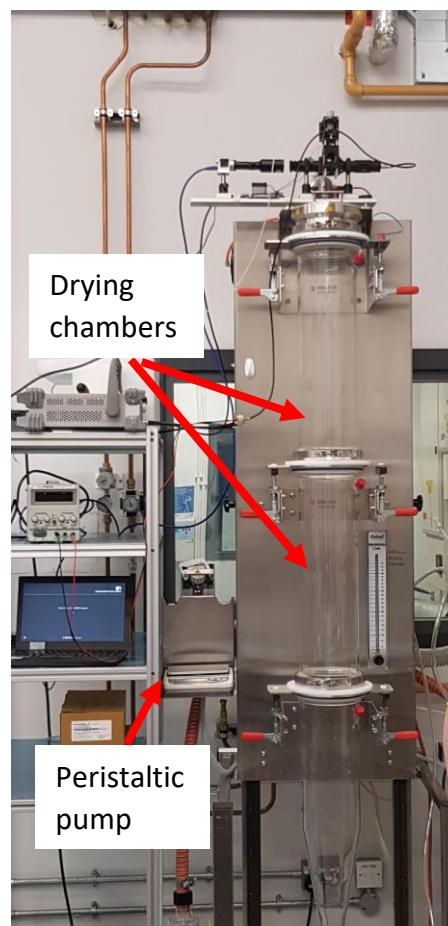
Figure 3.9 4M8-**TriX Procept Spray dryer**

3.4 Conclusion

This chapter presented the design, commissioning and validation of the single droplet apparatus. This apparatus measures the drying kinetics by a combination of optical method and a direct mass measurement method using a microbalance. By doing this, the mass loss from droplets with dissolved solids can be recorded even after the shrinkage of the particle ceases. A significant advantage of this system compared to other systems such as acoustic levitation is that high temperatures can be used, analogous to those used in spray drying. Furthermore, the use of the telecentric lens and a microbalance for mass measurements ensures that this system requires little calibration effort. In addition, the use of PEEK filaments with low heat conductivity ensures a reduced error associated with heat conduction from the filament. The validation of the measurement methods incorporated in the rig, the optical methods and the mass measurements, was conducted by drying pure water droplets and comparison of experimental measurements with a model based on Ranz-Marshall correlations. The results demonstrated a good agreement between the measured and computed mass and diameter measurements. This agreement demonstrates a good accuracy of the measurement methods at the range of conditions used; 25-180 ˚C air temperature, 1.4-2 mm droplet size and 0-0.57 m /s air velocity. These are the range of conditions required for the scope of work in this thesis, and therefore, it can be concluded that the single droplet drying apparatus has been successfully commissioned and validated.

Chapter 4 Drying of sucrose/water

4.1 Introduction

The literature review highlighted that one of the most interesting and complex outcomes of drying above the boiling temperature is inflation/deflation cycles. The inflation/deflation during boiling can result in significant changes to the surface area of the droplet/particle and evaporation rate, thereby influencing the properties of the final dried particle such as size and density. Depending on the structure of the particle formed during drying the particle can either maintain an inflated state and forms a "puffed" particle or collapse at the end of these cycles and form a solid particle. A detailed investigation of the reason behind differences in outcomes after inflation/deflation cycles is lacking. Two systems have been selected that show this contrasting behaviour after inflation/deflation cycles, silicate and sucrose. The focus of this chapter is on sucrose whilst the next chapter (Chapter 5) focuses on sodium silicate.

Drying of sucrose has been conducted in previous studies. El-Sayed et al. (1990) reported that sucrose undergoes inflation/deflation when dried above the boiling temperature. The morphology evolution of sucrose above boiling has also been reported by Hecht et al. (2000), where inflation/deflation cycles were observed. However, this work was more focused on the influence of inflation/deflation cycles on the loss of volatile components rather than the effects of boiling on the morphology development and the structure of the final dried particle. Although these studies have reported some effects of boiling on the morphology evolution, a systematic study on the drying behaviour at air temperatures above and below boiling and a range of initial solute concentrations is lacking. The complexity of understanding the morphology development during boiling is attributed to the difficulty of characterising the structure formed during drying and the dependence of this structure on the evolution of the material properties with temperature and solute concentration. The drying kinetics can give insights into the nature of the surface structure and its influence on the drying behaviour. For example, the extent of shrinkage and locking (the point where the particle shrinkage ceases) can give a measure of the rheo-mechanical nature of the surface structure formed during drying. The influence of boiling driven effects (including inflation/deflation cycles) on

the size and structure of the final particles at a different range of initial solute concentrations is yet to be investigated. Furthermore, the boiling onset parameters such as diameter and moisture content which can help understand the nature of the structure at which the particle enters the boiling stage are still undetermined. The effect of the morphology developments on the boiling rate is also not investigated in detail, particularly with consideration of the influence of air temperature and initial solute concentration. The determination of the evaporation rate prior to boiling and during boiling can give an insight into the ability of structure formed on the surface of the particle to hinder moisture transport. Furthermore, monitoring the morphology evolution such as mechanical deformations can give a qualitative measure of the rheo-mechanical properties.

To achieve these aforementioned aims, the single droplet drying apparatus was used to map the drying behaviour at a range of initial solute concentrations and air temperature below and above boiling. Single droplet drying experiments were used to closely monitor the morphology evolution and measure drying kinetics, including surface area, droplet temperature and evaporation flux at air temperatures above and below boiling. Therefore, the first part of this chapter begins by providing typical morphology evolution time series obtained from the single droplet experiments to give an insight into the overall morphology evolution at a range of drying air temperatures. The second part of this chapter presents the drying kinetics into two parts; drying kinetics below and above boiling. In both parts, the effect of the air temperature and solute concentration on the drying kinetics, including the surface area of the droplet/particle, droplet temperature and evaporation flux are closely investigated. The measured drying kinetics are also compared against a model based on Ranz-Marshall correlation to assess the effect of the developing morphology on the evaporation rate and droplet shrinkage. The drying kinetics are then used to collate parameters on the onset of boiling such as size and moisture content at different drying conditions. These parameters are used to understand the nature of the structure at which the particle enters the boiling stage and the effect of air temperature and solute concentration on the mechanisms of inflation/deflation. The interpretation of the drying kinetics results is also aided by the determination of the Péclet number.

4.2 Experimental work

Sucrose solutions were prepared by adding sucrose powder, purchased from SIGMA-ALDRICH, to distilled water. The solutions were prepared at solute concentrations of 5, 15, 30 and 45% w/w. To ensure complete dissolution of the solute in distilled water, the solutions were stirred by the use of a magnetic stirrer at 200 revolutions per minute (RPM) for 2-3 hours.

The single droplet drying apparatus, described in Chapter 3, was utilised to dry aqueous sucrose solutions at a range of conditions summarised in Table 4.1& Table 5.1. The selection of these conditions was made to map the drying behaviour at a wide range of drying conditions and offer a thorough review of sucrose drying behaviour. The procedure of single droplet drying experiments and image analysis have been described in 3.2.8 and 3.2.10.2, respectively. Laboratory spray drying of aqueous solutions of sucrose was not conducted due to the expected stickiness of sucrose on the chambers of the spray dryer.

Table 4.1 Single droplet drying conditions used to dry aqueous sucrose droplets

Parameter	Setting
Air temperatures	60 ˚C, 100 ˚C, 140 ˚C, 180 ˚C
Initial solute concentrations	5%, 15%, 30% and 45% w/w
Air velocity	0.57 m/s
Droplet size	1.4- 1.7 mm

4.3 Morphology evolution during drying

The morphology evolution of sucrose at different air temperatures is shown in Table 4.2. It can be seen that the morphology evolution can be categorised into drying below boiling and drying above boiling. Below boiling (at 60 °C and 100 °C), the droplet shrinks homogenously and maintains its spherical shape for the majority of its drying time until it stops shrinkage at a later stage of the drying time. The surface of the droplet remains smooth without any instabilities or deformations. This is an indication that the surface of the droplet remains in a liquid state for a major period of drying without the formation of an elastic structure that hinders the shrinkage of the droplet. This is further suggested by the normalised surface area profiles as a

function of drying time, which is discussed further in the drying kinetics section in 4.4.

Table 4.2: Morphology development of sucrose during single droplet drying with 15% initial solid concentration, v_{air}=0.57 m/s and different air temperatures[3]

T_{air}=60°C										1.5 mm
t(s)	0	20	40	60	80	100	120	140	180	280
T_d(°C)	17	28	29	29	30	32	35	42	54	61

T_{air}=100°C										1.5 mm
t(s)	0	15	30	45	60	75	90	105	145	175
T_d(°C)	23	39	39	40	43	55	71	83	97	99

T_{air}=140°C										1.5 mm
t(s)	0	20	40	62	72	73	83	83	94	147
T_d(°C)	28	58	70	105	112	113	127	126	133	135

T_{air}=180°C										1.5 mm
t(s)	0	10	30	31	32	35	36	37	38	77
T_d(°C)	29	84	121	120	124	137	144	150	158	177

Table 4.2 shows that above boiling (at 140 °C and 180 °C), the droplet goes through a shrinkage period followed by inflation/deflation cycles due to bubbles nucleation and vapour build-up inside the droplet. The ability of the vapour build-up to cause inflation/deflation cycles suggests that the droplet is still in a liquid state when the droplet enters the boiling stage which means there is little resistance for the inflation of the droplet. Notably, the particle collapses at the end of the inflation/deflation cycles, as is evident from the final morphology images in Table 4.2. This is due to the nature of the structure of the particle during drying which remains with little elasticity and thus incapable of maintaining an inflated state of the particle. The behaviour of inflation/deflation cycles is similar to that reported by El-Sayed et al. (1990) and Hecht et al. (2000). However, this work makes use of high-speed imaging to gain a closer look at the mechanisms occurring during the inflation/deflation cycle. The morphology time series at the moment of deflation captured by the high-speed

---

[3] A larger size replica table with better image quality is provided in Table E.3 (Appendix E)

camera is given in Figure 4.1. It can be seen that the droplet inflates in size and then the liquid outbreak occurs, leading to the droplet collapse.
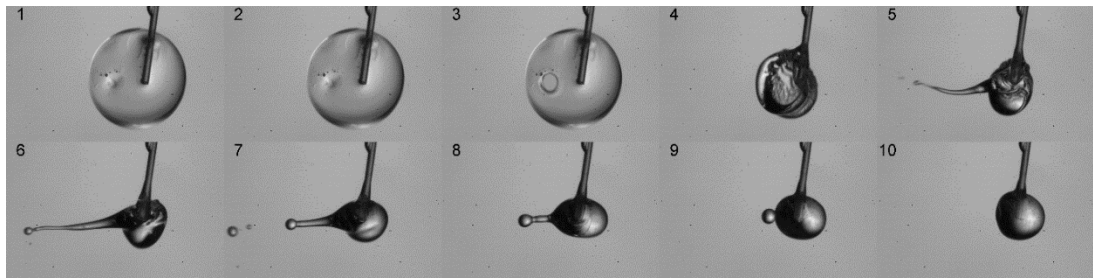
Figure 4.1 Morphology time series of the inflation/deflation cycle of 15% w/w sucrose droplet dried at 180˚C air temperature captured by a high-speed camera at 1000 frames per seconds.

The collapse at the end of the inflation/deflation cycles is in contrast with the behaviour of silicate, which is discussed in Chapter 5. The effect of the morphology developments demonstrated in this section on the drying rates is investigated by the analysis of drying kinetics, presented in the next section.

4.4 Drying kinetics

The drying kinetics are presented in terms of normalised surface area, droplet temperature and evaporation flux. The drying kinetics presented in this chapter are of typical drying runs based on 3-5 experimental single droplet drying repeats. For ease of analysis, the drying kinetics below and above boiling are presented separately. The evaporation flux is determined based on the surface area and the mass loss data, measured by the microbalance described in 3.2.6.3, using the following equation:

$$Evaporation\ flux = \frac{\frac{m_{i+1} - m_i}{t_{i+1} - t_i}}{4\pi r_{i+1}^2} \qquad (4.1)$$

Where,

r is the radius of the droplet

m is the mass of the droplet

t is the drying time

4.4.1 Drying kinetics below boiling

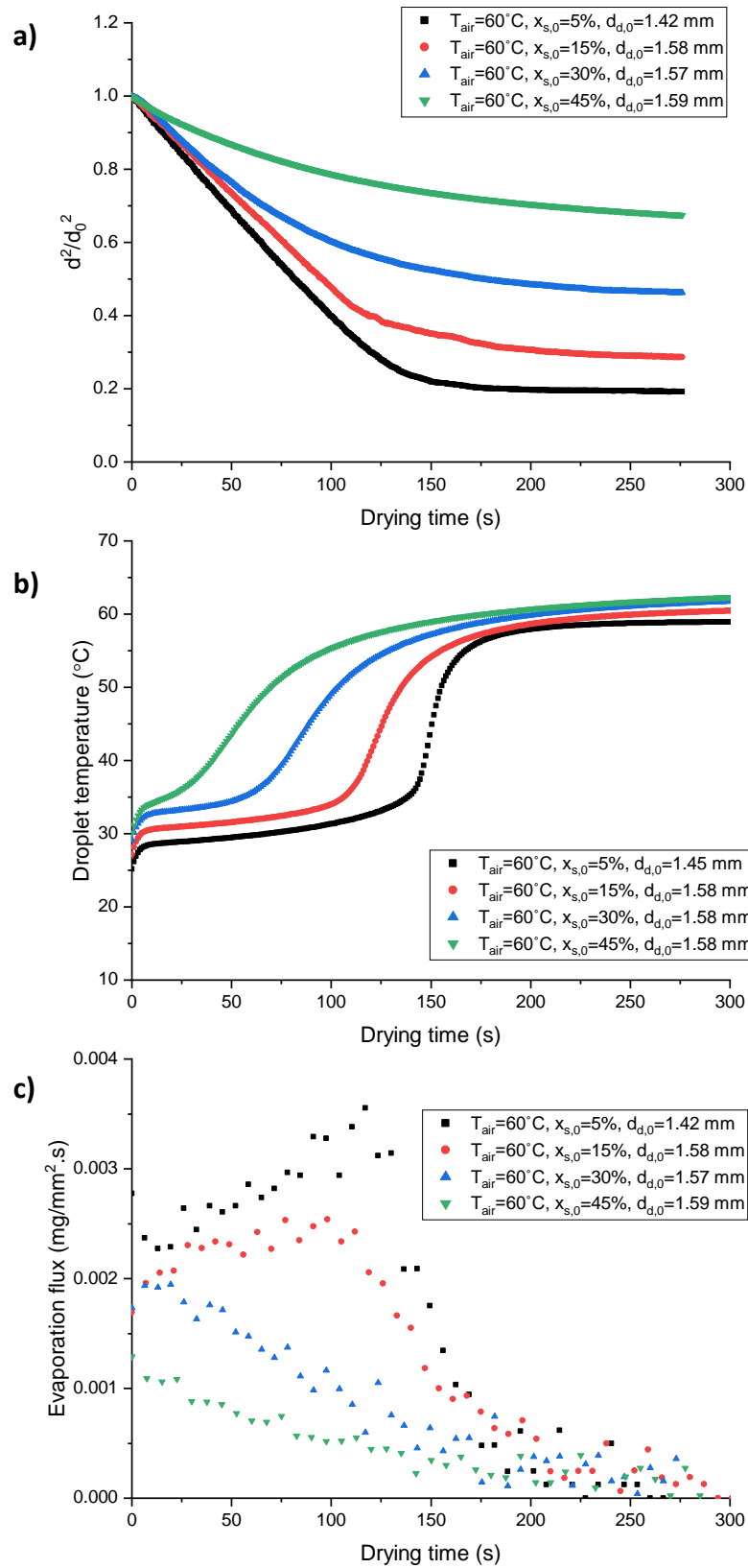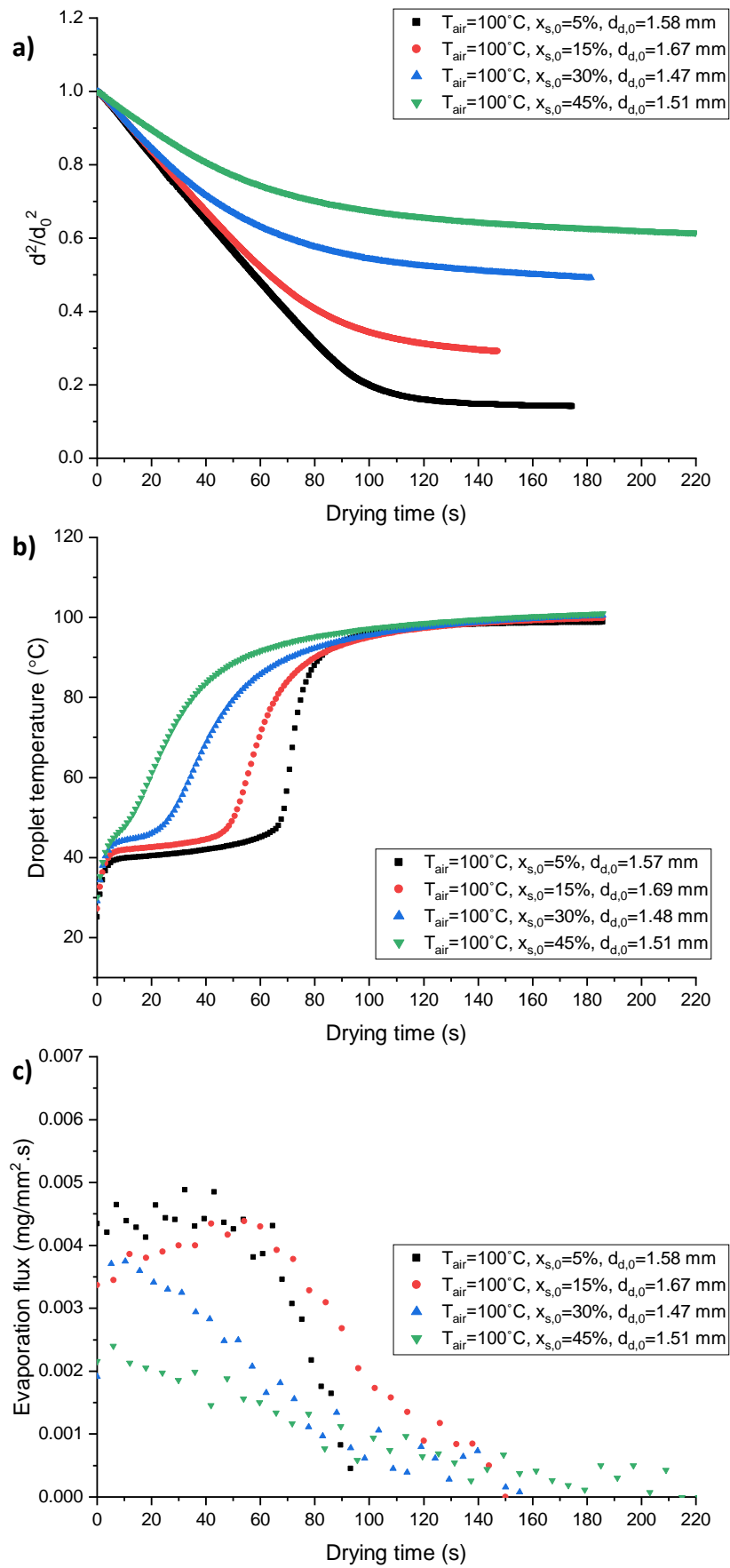

Figure 4.2 (a) Normalised surface area (b) droplet temperature (c) evaporation flux at initial solid concentrations of 5%, 15%, 30% and 45% w/w, 60°C air temperature and 0.57 m/s air velocity.

Figure 4.3 (a) Normalised surface area (b) droplet temperature (c) evaporation flux at initial solid concentrations of 5%, 15%, 30% and 45% w/w, 100˚C air temperature and 0.57 m/s air velocity.

The temperature profiles in Figure 4.2 & Figure 4.3 show that drying below the boiling temperature results in three drying stage; heating-up period, constant rate period and falling rate period. In the heating-up period, the droplet heats up to the wet-bulb temperature where the surface of the droplet remains saturated with moisture, and there is a balance between the heat added to the droplet and the heat used for moisture evaporation. The drying continues at the wet-bulb temperature until the surface of the droplet is no longer saturated with moisture and the heat added to the droplet is greater than that used for moisture evaporation. At this point, the droplet temperature exceeds the wet-bulb temperature and heats up to the air temperature. The normalised surface area plots in Figure 4.2 & Figure 4.3 show that the extent of shrinkage and the length of the constant rate period are largely dependent on the initial solute concentration. In agreement with expectation, the extent of shrinkage and the length of the constant stage period decrease with the increase in the initial solid content. The increase in the initial solid content results in a decrease in the moisture saturation at the surface at an early drying time due to the role of the high solid content in hindering the free moisture transport to the surface of the droplet. This is further supported by the calculations based on Ranz-Marshall model presented in 4.4.1.1

The evaporation flux, given in Figure 4.2 & Figure 4.3, shows an increase with the drying until it reaches a maximum and then begins decreasing. This increase in the evaporation flux to the maximum is a direct effect of the decrease in the droplet diameter, which results in an increase in the heat and mass transfer coefficients. As expected, the decrease in the evaporation flux coincides with the increase in the droplet temperature beyond the wet-bulb temperature, indicating a decrease in the moisture transport to the surface due to the increase of the solid fraction. The evaporation flux plots in Figure 4.2 & Figure 4.3 are also plotted against the moisture fraction and are presented in Figure 4.4. It can be seen that for initial mass solid content of 5%, 15% and 30%, the decrease in the evaporation flux occurs at similar moisture content.
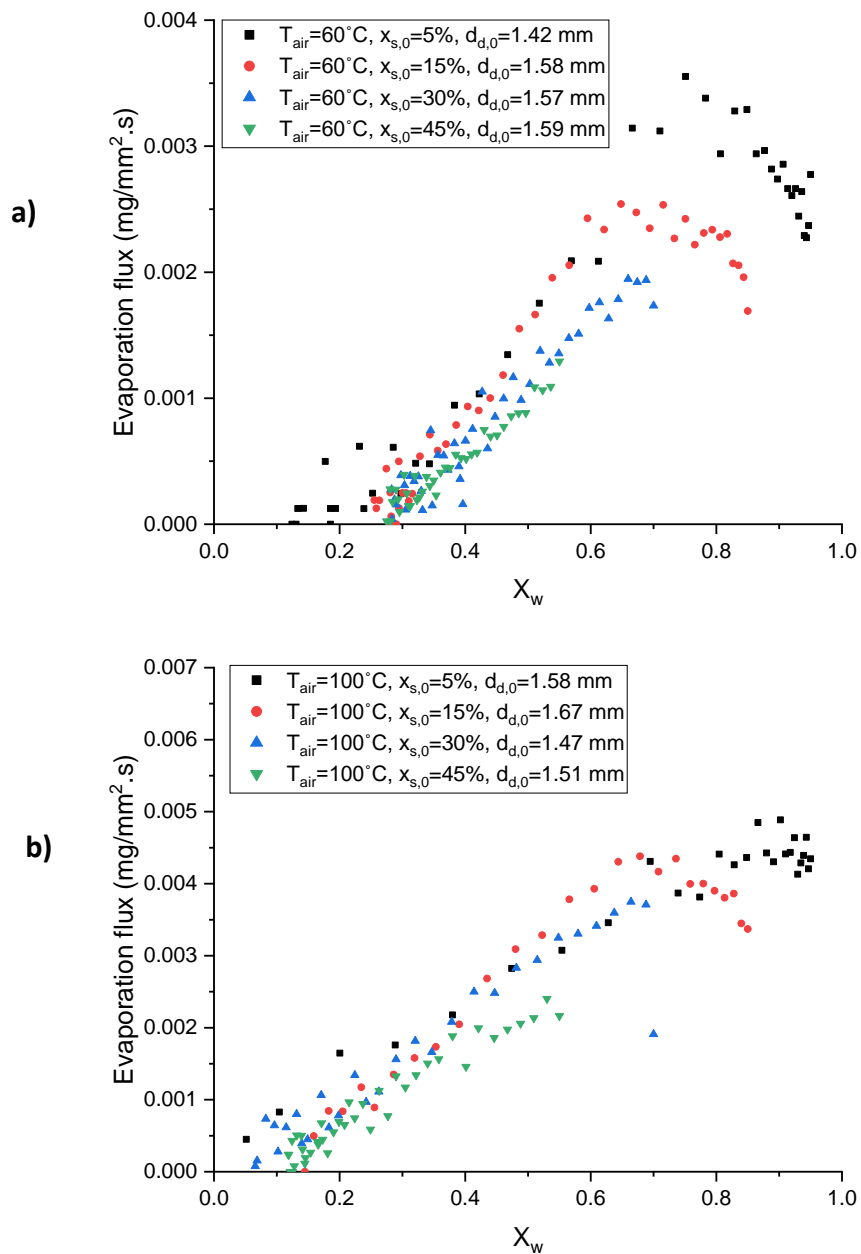
Figure 4.4 Evaporation flux versus water moisture fraction at air temperatures **of (a) 60 ˚C and (b) 100 ˚C**

4.4.1.1 Comparison versus Ranz-Marshall model

The mass and diameter measurements obtained from the rig and used to obtain the plots presented in Figure 4.2 & Figure 4.3 are compared against prediction calculated using the Ranz-Marshall model to assess the effect of the developing morphology on the drying kinetics. This is done to investigate any effects of the developing surface structure on the evaporation rate and the shrinkage of the droplet. The Ranz-Marshall model is used to describe the drying in the constant drying stage where moisture transport is unhindered by the developing surface structure. This model is

unable to account of the effect of solid on the diffusivity of moisture or the effect of the structure formed on the droplet shrinkage. The method of the Ranz-Marshall calculation has been described in section 3.2.10.1.

The comparisons of the mass and diameter measurements from the single droplet drying experiments and from the application of the Ranz-Marshall model at air temperatures of 60 ˚C and 100 ˚C are given in Figure 4.5 & Figure 4.6 respectively. At low solid content (5% and 15% w/w), the diameter and mass measurements closely follow those determined from Ranz-Marshall model, particularly in the constant rate period. At higher solid concentrations, the Ranz-Marshall deviates from the measurement particularly from the end of the short constant drying stage. This is because the moisture transport to the surface is hindered by the presence of the solute which disturbs the surface moisture saturation and thus the Ranz-Marshall model becomes inapplicable.

The comparison with Ranz-Marshall model shows that at low solid content, the final diameter of the dried particle from the model and the measurements are similar, which suggest that there is no locking of the particle. At air temperature of 60 ˚C and high solid concentrations, the final mass and diameter of the particle obtained from experiments are higher than those from Ranz-Marshall. This is because, at such low air temperatures, the droplets are not fully dried even when left in air for a long time. At 100 ˚C air temperature, the final mass and diameter of the dried particle from experiments and Ranz-Marshall Model are in agreement even at high concentration. The agreement in diameter measurements from the Ranz-Marshall model and experiment suggest that at low solid content the droplet dries without the formation of a viscoelastic layer that has the ability to restrict or hinder the shrinkage of the droplet and the droplet shrinks until it reaches its expected diameter corresponding to the solid mass. This is in agreement with the morphology evolution pictures, presented in Table 4.2, where surface structure remained smooth without any deformations which suggest no elastic nature of the surface. This can be explained by the low viscosity of sucrose even at a high concentration as shown by the viscosity measurements obtained from Telis et al. (2007) and given in Table C.2 in Appendix C.
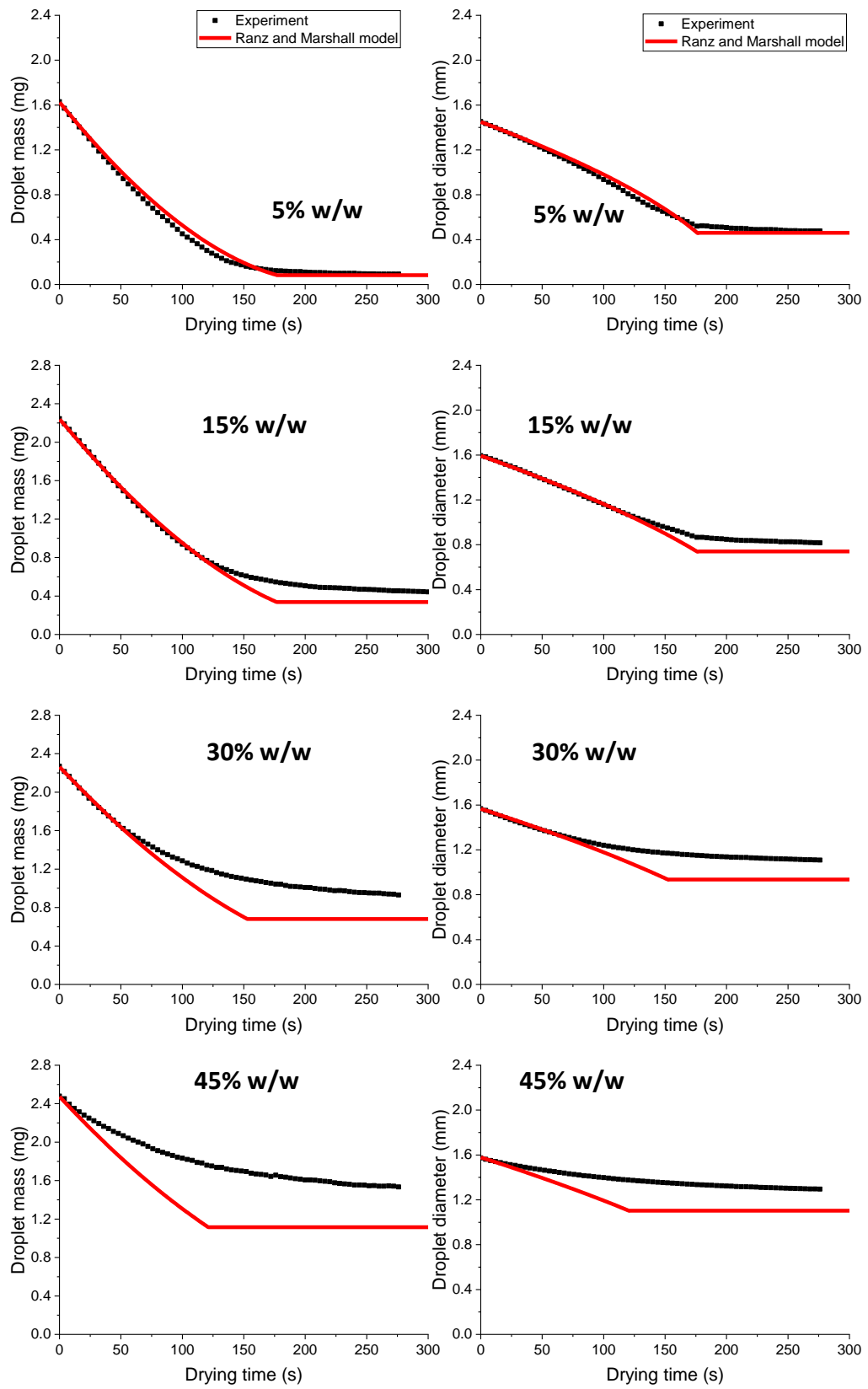
Figure 4.5 Comparison of mass and diameter experimental measurements vs Ranz-Marshall Model at air temperature of 60 ˚C and v_{air}=0.57 m/s.
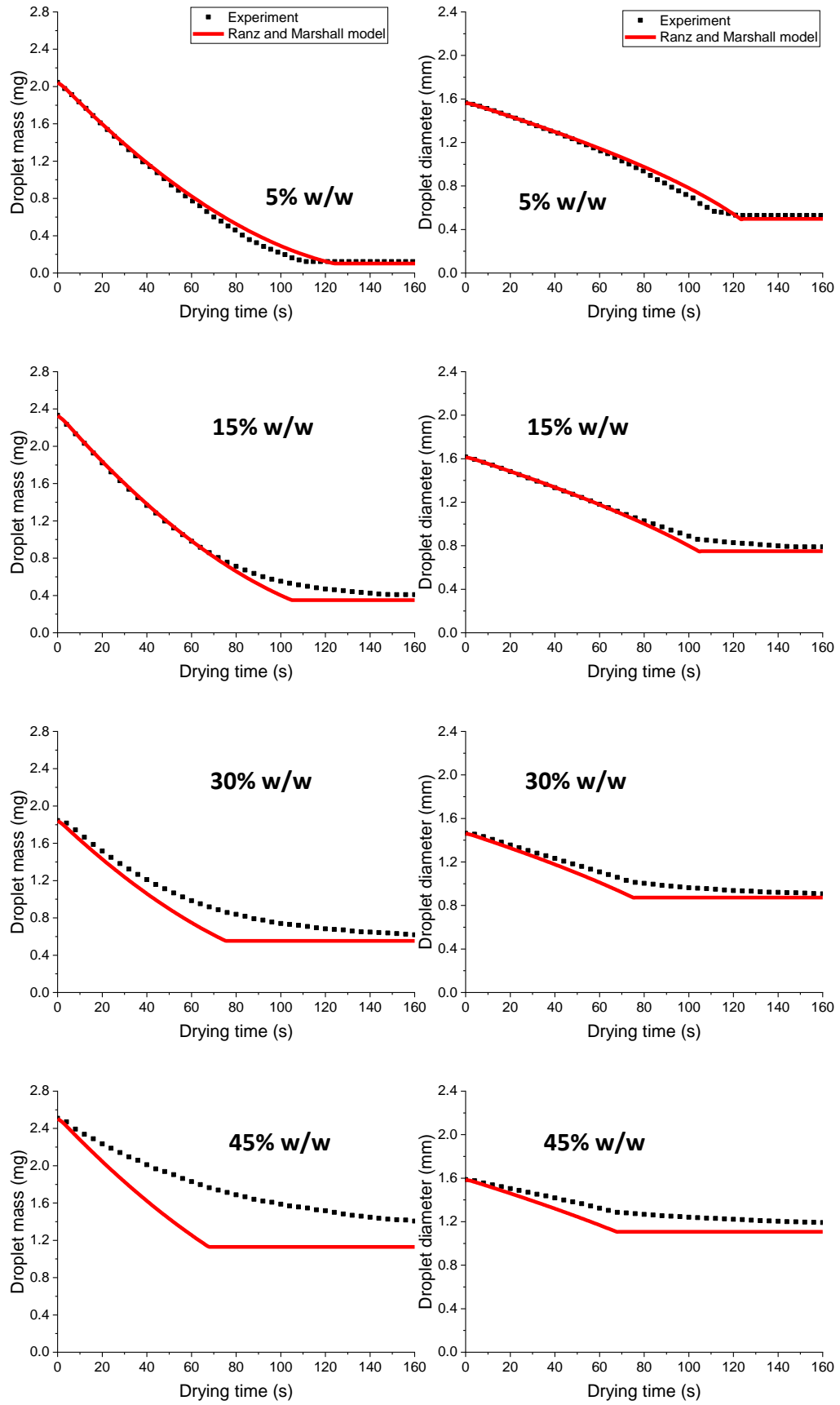
Figure 4.6 Comparison of mass and diameter experimental measurements vs Ranz-Marshall Model at air temperature of 100˚C and v_{air}=0.57 m/s

4.4.1.2 Péclet number determination

The deviation from Ranz-Marshall model, particularly at high concentration, suggests a moisture gradient within the droplet and some solute surface enrichment. This is investigated by the determination of the Péclet number. The Péclet number gives the ratio of the evaporation flux to the diffusion flux of the solute. It is given by the following equation Vehring et al. (2007) :

$$\text{Pe} = \frac{k}{8D} \tag{4.2}$$

where D is the diffusion coefficient of the solute.

k is the evaporation rate (mm^2/s) determined from the diameter measurements as a function of time as follows:

$$k = \frac{d_{i+1}^2 - d_i^2}{t_{i+1} - t_i} \tag{4.3}$$

where,

d is the droplet diameter

t is the drying time

The Péclet number is calculated using the evaporation rate determined using equation (4.3), in the constant drying period where the experimental diameter measurements and the Ranz-Marshall are in agreement based on the results presented in the previous section (4.4.1.1). The diffusion coefficient of sucrose is taken at the wet-bulb temperature, approximately 30˚C, and the initial solute concentration in the droplet. Sucrose diffusion coefficients are obtained from Ekdawi-Sever et al. (2003) based on nuclear magnetic resonance (NMR) measurements. The diffusion coefficients are 1.82×10^{-10} m^2/s, 1.62×10^{-10} m^2/s and 1.02×10^{-10} m^2/s at solute concentrations of 16%, 32% and 43% respectively (See Table C.1, Appendix C).

Figure 4.7 shows that that the Péclet number is higher than 1 at all solute concentrations and air temperatures of 60 and 100 ˚C. This suggests that there is a moisture gradient within the droplet and a degree of solute surface enrichment. It can also be seen that the Péclet number increases with the increase in initial solute

concentration due to the decrease in solute diffusion coefficient and also increases with air temperature due to the increase in the evaporation rate. It is likely that the establishment of the moisture gradient results in a lower moisture fraction at the surface and decrease in the evaporation rate at an early drying time. This is also in agreement with the diameter measurements where the final diameter is slightly higher than the expected diameter from the Ranz-Marshall model.
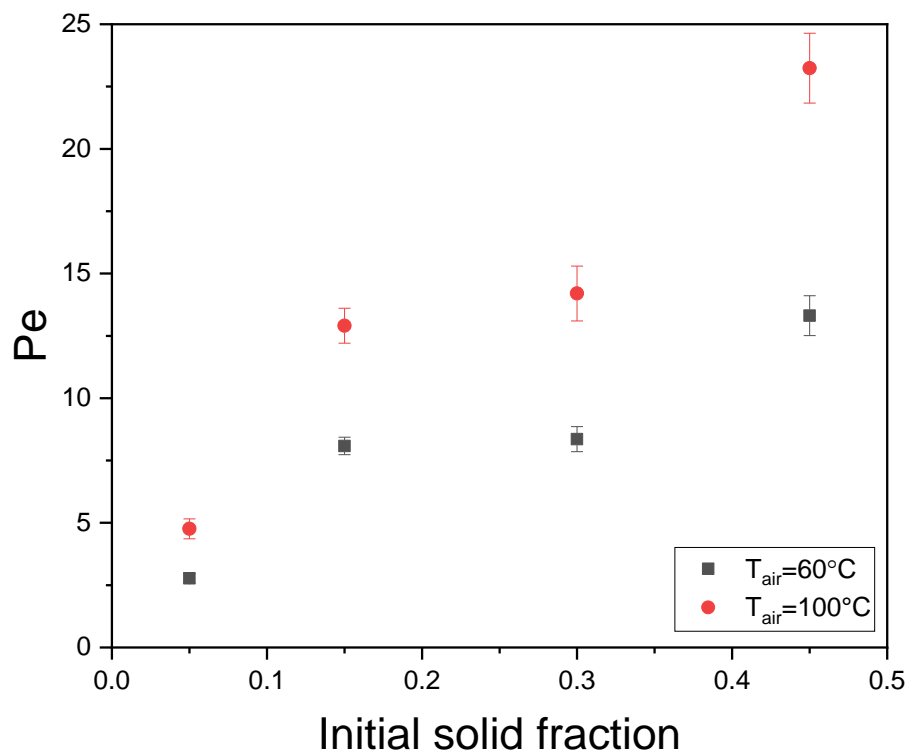
Figure 4.7 The initial Péclet number at different initial solid content and air temperatures of 60 ˚C and 100˚C. Error bars were calculated based on 5 replicates at each condition. Error bars are based on the standard deviation of the mean and represent ± 1 standard deviation.

4.4.2 Drying kinetics above boiling

Figure 4.8 (a) Normalised surface area (b) droplet temperature (c) evaporation flux at initial solid concentrations of 5%, 15%, 30% and 45% w/w, 140 ˚C air temperature and 0.57 m/s air velocity.

Figure 4.9 (a) Normalised surface area (b) droplet temperature (c) evaporation flux at initial solid concentrations of 5%, 15%, 30% and 45% w/w, 180 ˚C air temperature and 0.57 m/s air velocity.
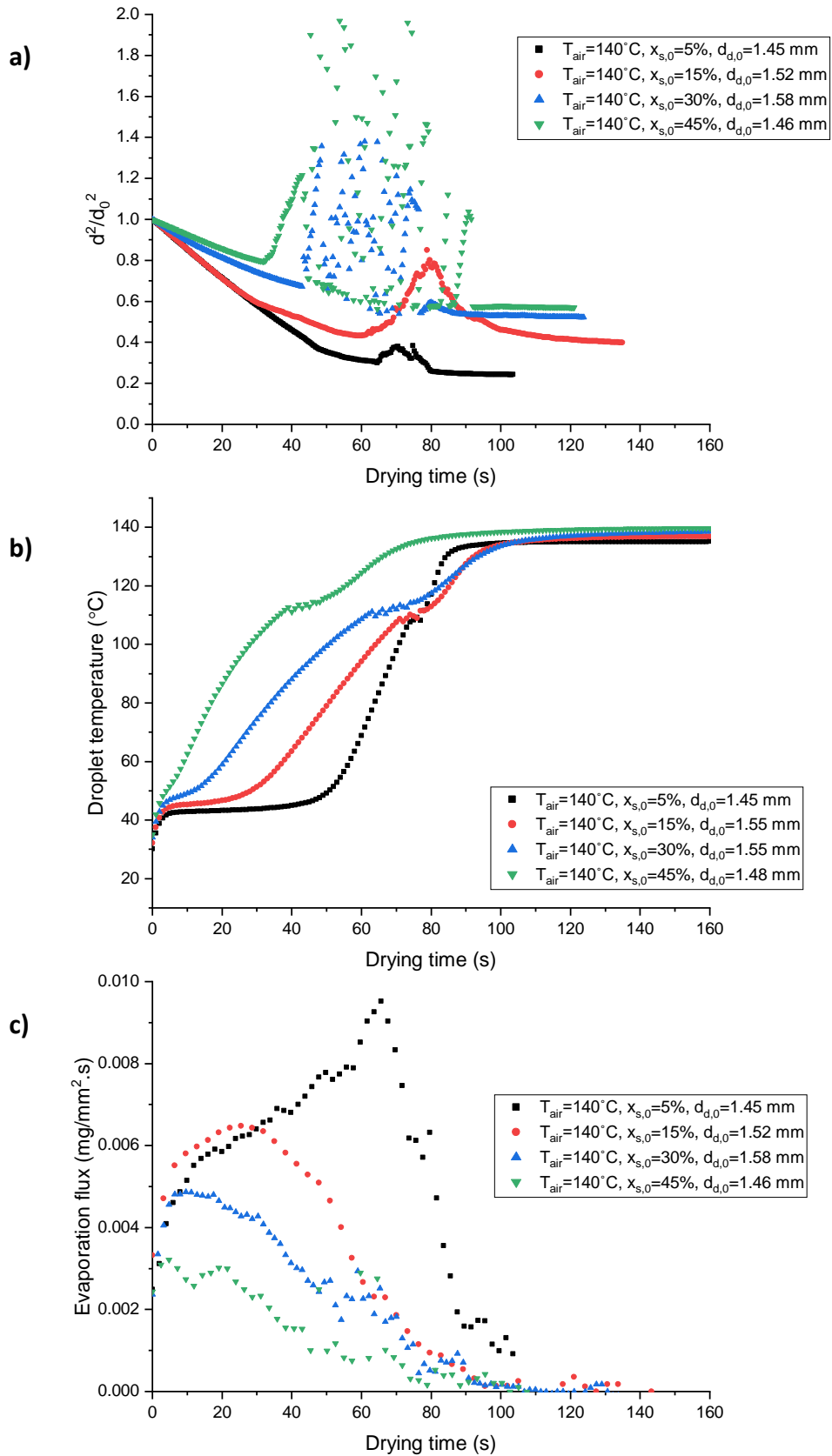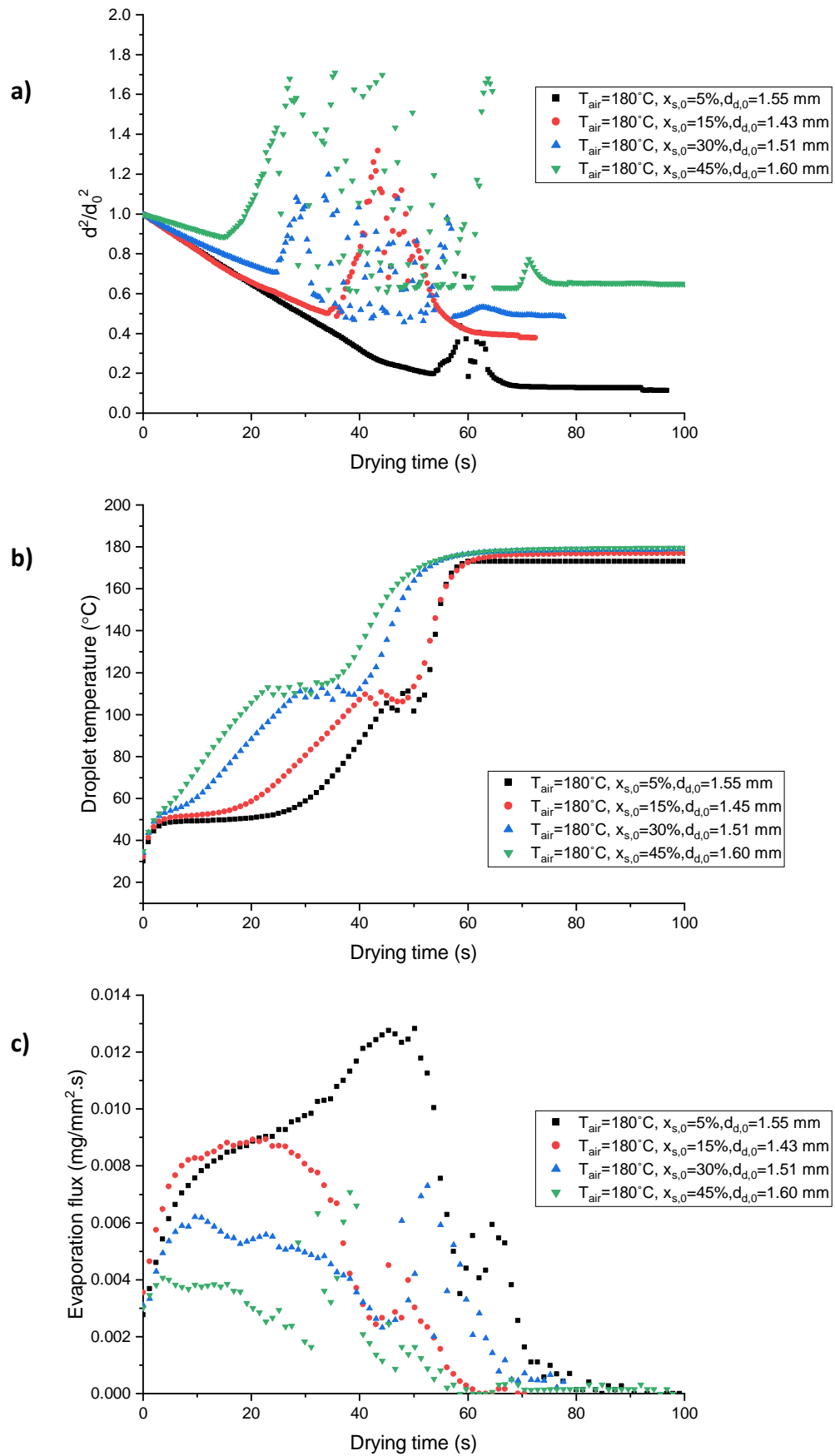
The droplet temperature profiles given in Figure 4.8 & Figure 4.9 show that drying at temperatures above boiling results in five defined stages; the heating up period, constant rate period, falling rate period, boiling stage and the final heating period. This is expected and in agreement with the drying stages established by Nešić and Vodnik (1991). Initially, the droplet dries and shrinks at the wet-bulb temperature prior to entering the boiling stage. Once the droplet enters the boiling stage, the droplet undergoes inflation/deflation cycles resulting in significant changes to the normalised surface area. The stages of drying outlined from the droplet temperature profile correspond to changes in the evaporation flux. Initially, prior to the boiling stage, the evaporation flux shows an initial increase until it reaches a maximum, corresponding to the shrinkage in the droplet size and enhanced heat and mass transfer coefficients. Afterwards, the evaporation flux decreases due to a reduction in moisture surface saturation, which in turn results in the increase in the droplet temperature to the droplet boiling temperature. Once the droplet enters the boiling stage, the evaporation flux is severely affected by the inflation/deflation cycles; the inflation of the droplet leads to lower evaporation flux due to the increase in the surface area whereas deflation results in an increase in the evaporation flux. This is expected and in agreement with equation (4.1) used to determine the evaporation flux. At the end of these inflation/deflation cycles, the particle continues to dry very slowly until the end of the drying process.

The evaporation fluxes presented in Figure 4.8 & Figure 4.9 were plotted against the water moisture content in Figure 4.10. It can be seen that with the increase in the initial solute fraction, the evaporation flux begins decreasing at higher moisture content. This is likely due to the establishment of moisture profile, which is influenced by the evaporation rate and the solute diffusion coefficient. This is better understood by the determination of Péclet number, which is presented in the next section. Figure 4.8 & Figure 4.9 also demonstrate an increase of the evaporation flux which corresponds to the boiling stage. The increase of the evaporation flux at the boiling stage is due to the liquid phase mixing caused by the rupturing action of the bubble which increases the internal mass transfer coefficient. The rupturing action of the bubble has been demonstrated by the high-speed imaging in section 4.3. It is also clear that the extent of the increase of the evaporation flux during boiling is

more pronounced at higher air temperatures (180 °C) and higher initial solid content. This is because the droplet enters the boiling stage at high moisture content with the increase in air temperature and solute concentration which increases the inflation/deflation rate as well as the inflation/deflation frequency.
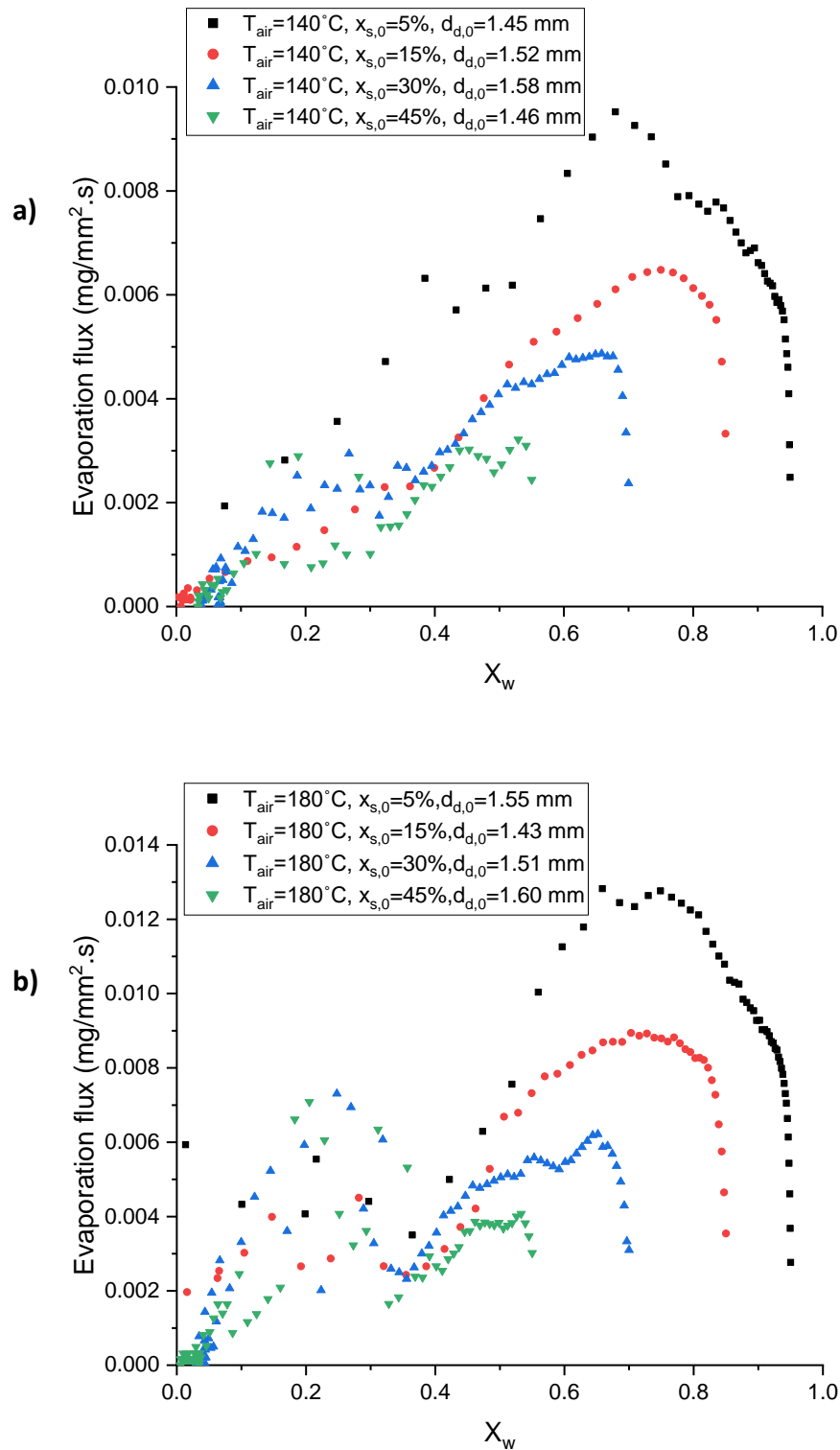
Figure 4.10 Evaporation flux versus water moisture fraction at air temperatures of (a) 140°C and (b) 180°C

4.4.2.1 Boiling onset parameters

This section focuses on the conditions at which the droplet enters the boiling stage. The plots presented in Figure 4.8 & Figure 4.9 were used to collate the diameter and moisture content at the onset of boiling. The extent of the shrinkage prior to boiling significantly depends on the initial solute concentration and air temperature. Figure 4.11a illustrates that at the same air temperature, the diameter at which the droplet enters the boiling stage is higher with higher initial solid content. This is expected as the higher the initial solid content, the less amount of water is required to be evaporated before the surface of the droplet becomes no longer saturated with moisture and thus the droplet temperature increases to the droplet boiling temperature at an early drying time. It can also be seen that at the same initial solid concentration, the increase in the air temperature from 140 ˚C to 180 ˚C results in a slight increase in the diameter at which the droplet enters the boiling stage. This is attributed to a moisture gradient within the droplet as a result of the increase in the evaporation rate associated with the increase in air temperature. The increase of the moisture gradient within the droplet with the increase in air temperature is supported by the Péclet number calculations based on the calculation method outlined in 4.4.1.2.

The mean moisture content at boiling, Figure 4.11b, shows an increase with the increase in air temperature at all initial solid concentrations. The absolute total moisture content between the boiling onset and end of boiling is higher with higher initial solid contents which result in longer total time in the boiling period, as demonstrated by the temperature profiles in Figure 4.8 & Figure 4.9. Subsequently, a higher number of inflation/deflation cycles are observed with the increase in initial solute concentration. This also explains that the increase of frequency of the inflation and deflation cycles (number of inflation/deflation cycles) with the increase in the initial solute concentration as shown in the normalised surface area plots in Figure 4.8 & Figure 4.9.
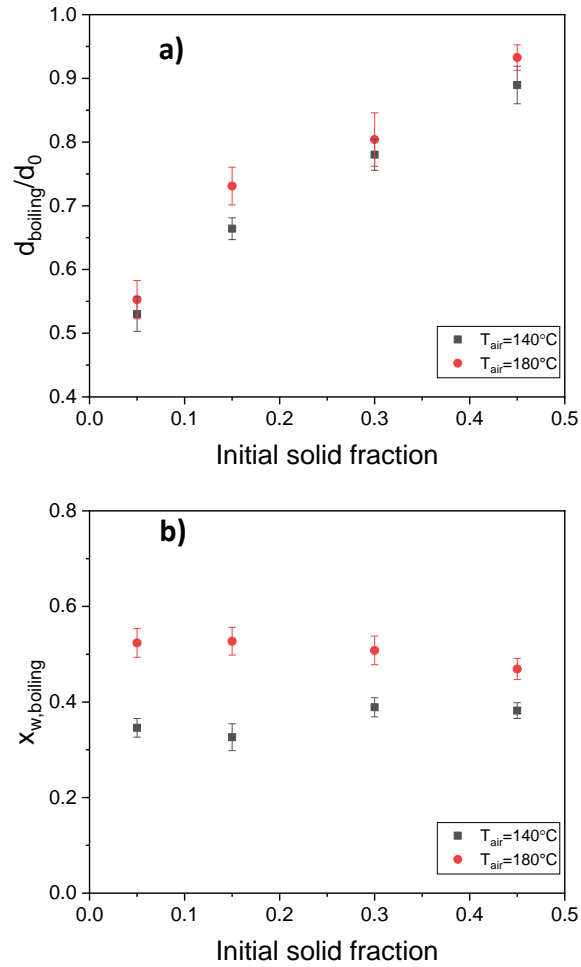
Figure 4.11 Boiling onset parameters a) relative size b) moisture fraction. Error bars were calculated based on 5 replicates at each condition. Error bars are based on the standard deviation of the mean and represent ± 1 standard deviation.
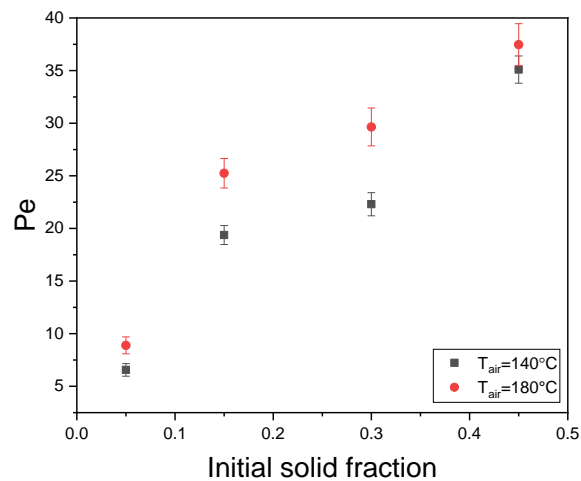
Figure 4.12 The initial Péclet number at different initial solid content at 140˚C and 180 ˚C air temperatures. Error bars were calculated based on 5 replicates at each condition. Error bars are based on the standard deviation of the mean and represent ± 1 standard deviation.
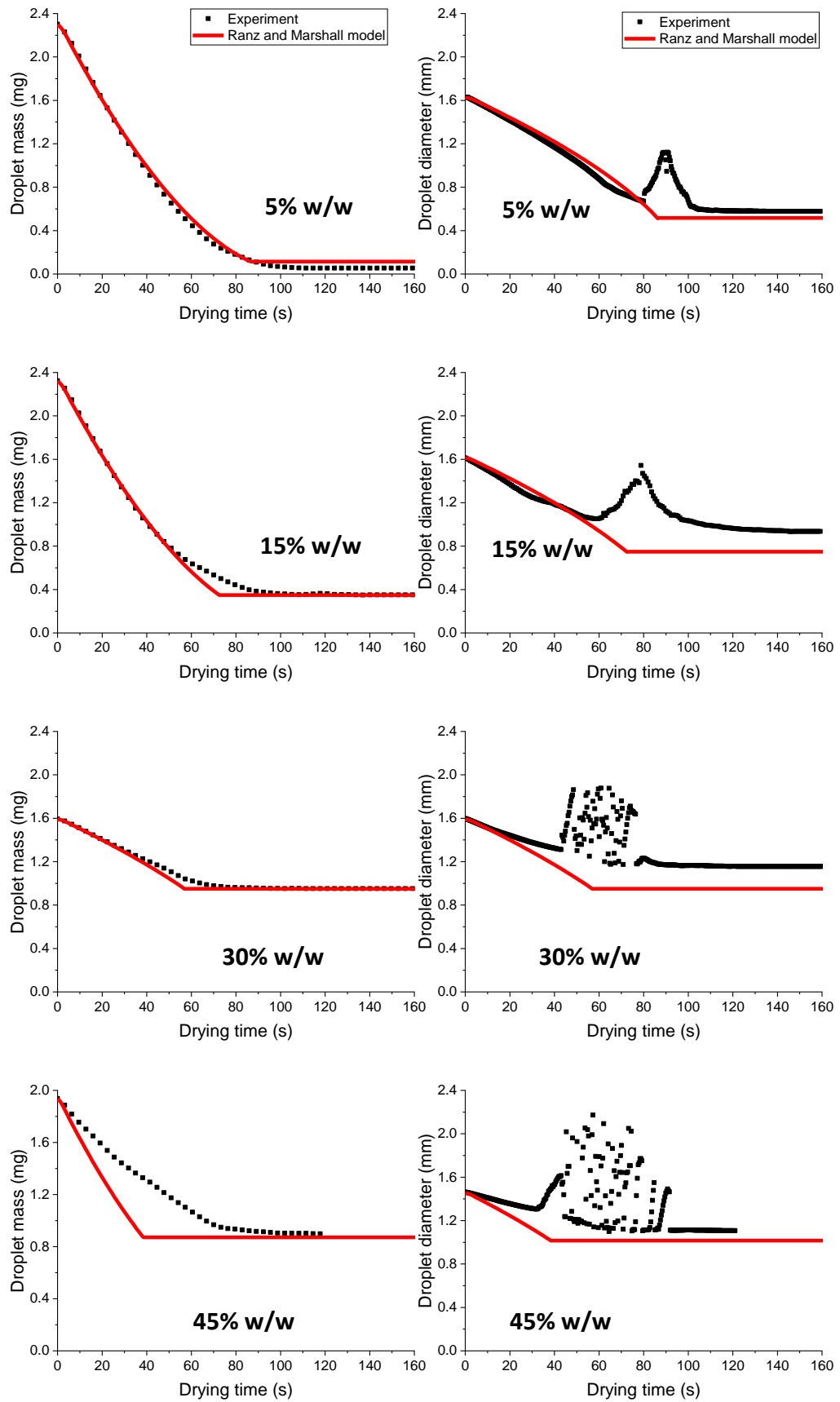
4.4.2.2 Comparison with Ranz-Marshall model

The mass and diameter measurements used to obtain the drying kinetics presented in section 4.4.2 are compared against Ranz-Marshall model. Although the Ranz-Marshall model is only applicable to drying in the constant rate period, it is helpful to compare the drying in the constant rate stage and the expected final diameters. The results of the comparisons at air temperatures of 140 and 180˚C are presented in Figure 4.13 and Figure 4.14, respectively. It can be seen that in the constant rate period, the diameter and mass measurements are similar to that predicted by the model, particularly at low solid content. The agreement demonstrates that the morphology evolution of the particle at this point has no influence on the drying behaviour, moisture transport to the surface of the droplet is unrestricted. The results suggest that the drying rate of sucrose at low solid content can be predicted by simple models based on heat and mass transfer balances.

The discrepancy between the experimental measurements and the model increase at high solid content where the experimental measurements of the reduction of the diameter and the mass loss are lower than those predicted by the model. This is due to the decrease of the evaporation rate, caused by the role of high solid content in reducing the moisture transport to the surface of the particle. The decrease in moisture transport to the surface indicates an internal mass transfer resistance and a moisture gradient within the droplet. This is in line with the Péclet number calculations in the previous section which show a Péclet number higher than 1 which increases with the increase in solute concentration, indicating a degree of solute surface enrichment at higher solute concentrations. Although the diameter measurements at high solid concentrations are slightly higher than expected, it can be seen that the particle collapses at the end of the boiling stage and no significant increase of the particle diameter is observed. This demonstrates that there is no porosity retained, which is in contrast with the silicate system, presented in Chapter 5.

Figure 4.13 Comparison of mass and diameter experimental measurements vs Ranz-Marshall Model at air temperature of 140 ˚C and v_air=0.57 m/s.
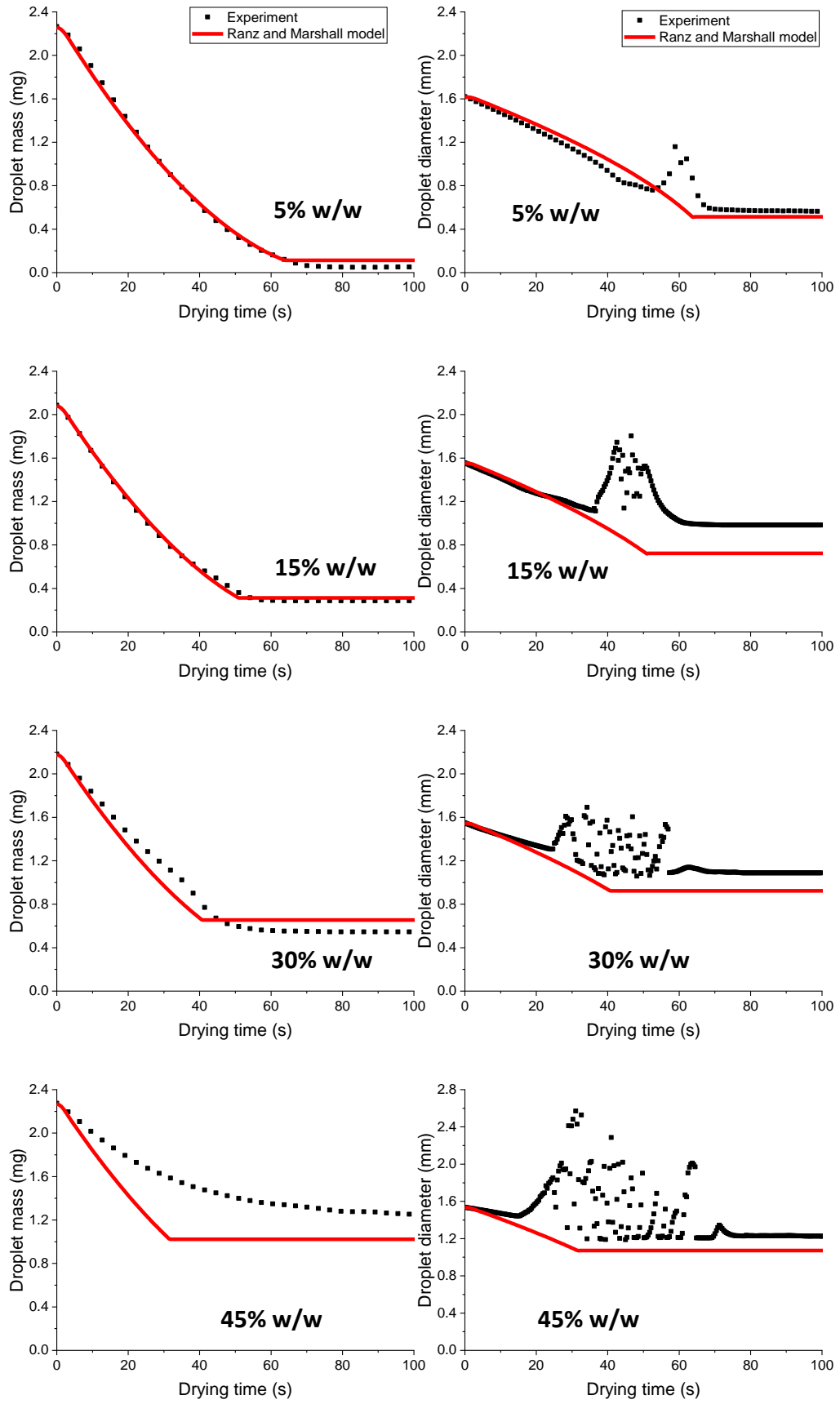
Figure 4.14 Comparison of mass and diameter experimental measurements vs Ranz-Marshall Model at air temperature of 180 ˚C and v_{air}=0.57 m/s.

4.4.3 The influence of boiling on the final size of the dried particle
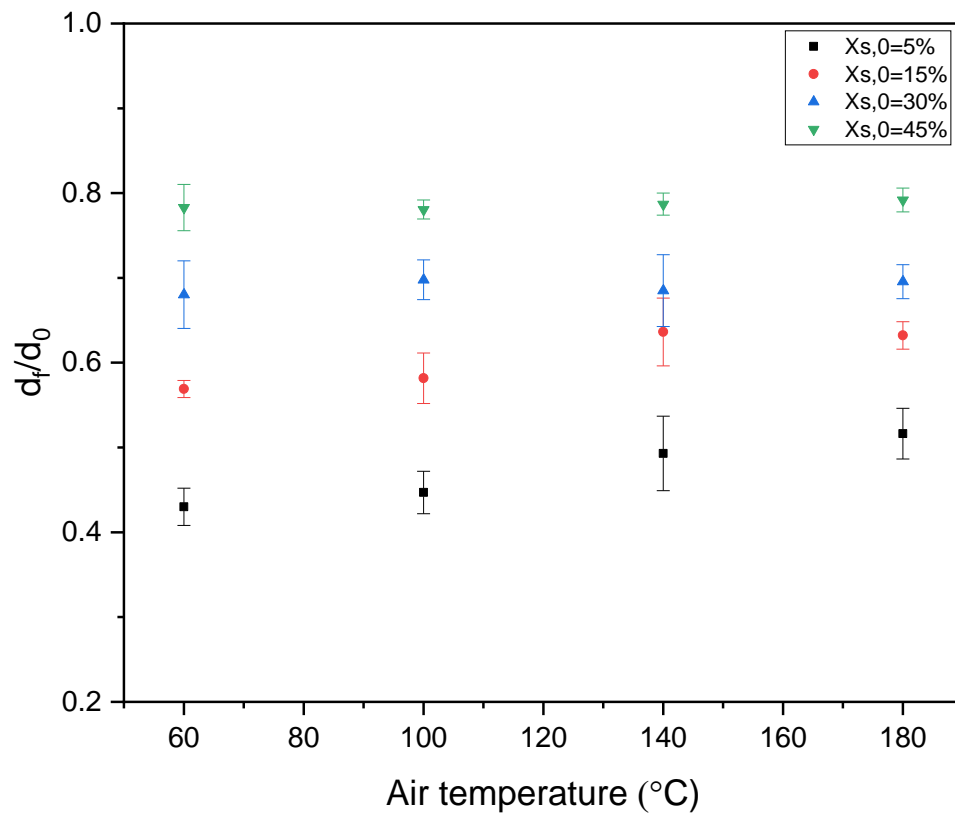
Figure 4.15 The relative size of the final dried particle at v_{air}=0.57 m/s and different air temperatures. Error bars were calculated based on 5 replicates at each condition. Error bars are based on the standard deviation of the mean and represent ± 1 standard deviation.

The final diameter of the dried particle as a function of air temperature and solute concentration is presented in Figure 4.15. It can be seen that at the same initial solid content, the increase in temperature results only in a very slight increase in the size of the dried particle. The inflation/deflation cycles during boiling resulted only on a slight increase on the size of the final dried particles as the droplet collapses at the end of inflation/deflation period and fails to maintain an inflated structure. The hypothesis behind this is that sucrose remains viscous and liquid-like during drying as shown by the morphology time series in Figure 4.1 and thus, the particle has no sufficient strength to maintain the inflation experienced during boiling. This is also supported by the viscosity data given in Table C.2 (Appendix C) measured by Telis et al. (2007), which shows a low viscosity of sucrose even at high concentrations. The viscosity of sucrose corresponding to the 0.47-0.67 solute concentration range at

which the droplet enters the boiling stage, given in Figure 4.11b, is in the range of 1.22 to 4.75 mPa at 85 ˚C as measured by Telis et al. (2007). Therefore, at such low viscosity, the droplet has little elasticity to maintain the inflated state of the particle. The limited increase of particle size when drying above boiling is in contrast with systems with higher viscosity such as maltodextrin which has been reported to show an increase of dried particle size when dried above boiling (El-Sayed et al., 1990; Alamilla-Beltran et al., 2005). It is also in contrast with silicate which is presented in Chapter 5.

4.5 Conclusion

The morphology evolution below boiling demonstrated homogenous shrinkage of the droplet and the spherical shape of the droplet was maintained till the end of the drying period. The surface of the droplet remained smooth without any instabilities or deformations. The drying kinetics of sucrose in the constant rate period demonstrated good agreement with a model based on Ranz-Marshall correlations. This suggested that the drying behaviour is unaffected by the morphology development. The particle did not form an elastic structure that hinders the shrinkage of the droplet. The influence of the concentration and air temperature on the droplet temperature profile, evaporation flux has been highlighted. The increase of initial solute concentration at the same air temperature resulted in a shorter constant rate period and early increase of the droplet temperature profile to the air temperature. This has been related to early solute surface enrichment evident by a Péclet number higher than 1, which causes a moisture a gradient and a decrease in moisture saturation at the surface.

The increase of the evaporation flux at the boiling stage has been related to the liquid phase mixing caused by the rupturing action of the bubbles, which increases the internal mass transfer coefficient. The extent of the increase of the evaporation flux during boiling was more pronounced at higher air temperatures (180 ˚C) and higher initial solid content. This was related to the moisture content at which the droplet enters the boiling stage. The droplet enters the boiling stage at high moisture

content with the increase in air temperature and solute concentration, which increases the inflation/deflation rate as well as the inflation/deflation frequency.

The total drying time at the boiling stage, based on the droplet temperature profile, increased with the rise in initial solid content. This increase was caused by early surface enrichment with the increase in initial solid content, and thus the droplet entered the boiling stage at early drying time and high moisture content. Subsequently, the absolute total moisture content between the boiling onset and end of boiling is higher with higher initial solid contents, which results in longer total time in the boiling period. The longer time at the boiling stage resulted in a higher number of inflation/deflation cycles.

Although the morphology development above boiling demonstrated inflation/deflation cycles, the particle collapses at the end of the inflation/deflation cycles, and thus it failed to retain any porosity. The failure to maintain any inflation has been related to the rheological proprieties of sucrose. Sucrose has low viscosity even with the increase in droplet temperature and solute concentrations and therefore exhibits liquid-like behaviour during boiling. The behaviour of sucrose above boiling is in contrast with materials with higher viscosity such as silicate where the inflation is maintained during boiling, and the size of the final dried particle is increased. The behaviour of silicate is investigated in detail in the next chapter.

Chapter 5 Drying of silicate/water

5.1 Introduction

Chapter 4 focused on the inflation/deflation behaviour encountered during drying of aqueous sucrose droplets. The outcome of inflation/deflation cycles resulted in particle collapse, and thus the size of the dried particles was unaffected by the boiling driven effects. This outcome was related to the rheological properties of sucrose which showed little elasticity during boiling, and thus the particle was unable to maintain an inflated state following the inflation/deflation cycles. To expand on the work conducted in Chapter 4, another system was selected to study the inflation/deflation behaviour in detail but with a different outcome to that observed with sucrose. This outcome involves inflation/deflation which results in an inflated, "puffed" final dried particle. This behaviour can cause a significant influence on the density and the size of the final dried particles, which in turn can have a significant effect on the bulk properties of the dry powder. The extent of influence is dependent on solute concentration and air temperature. Therefore, this part focuses on the drying of sodium silicate, a material used in many detergents and cleaning compounds as active alkaline builders Weldes et al. (1969) and has been reported to show puffing behaviour in a study by Walton and Mumford (1999a). A systematic study of the drying of silicate has not been conducted, particularly on the mechanism of the inflation behaviour above boiling and the effects of the drying parameters and initial solute concentration. Therefore, this part focuses on the mechanisms of drying below and above boiling with a focus on the influence of key drying parameters on the drying kinetics and the properties of the final dried particle. A particular emphasis is on the effect of boiling on the final morphology and final particle size. The link between the material properties and morphology development is also explored by using rheological properties of sodium silicate obtained from the literature.

This chapter first presents the morphology time series at different air temperatures, highlighting the key differences between drying at air temperatures below and above boiling. Then, the drying kinetics below boiling, including surface area, evaporation flux and droplet temperature history are presented, covering the link between these drying kinetics and the morphology evolution. Afterwards, this

chapter presents the drying kinetics above boiling and the effect of air temperature and solute concentration on the boiling onset parameters. The effect of boiling on the evaporation rate and evaporation flux is then discussed. This is followed by a discussion on the effect of boiling on the size and porosity of the final dried particles. The final part of this chapter investigates the structures of the final dried particles collected from the single droplet drying experiments and the lab-scale spray dryer.

5.2 Experimental work

Sodium silicate solutions were prepared from 45% sodium silicate solution supplied by Proctor and Gamble. The weight ratio of silicon oxide to sodium oxide of the solution was 1.6. Desired solutions concentrations of 6 and 17% w/w were obtained by diluting the 45% w/w concentrated solution by the addition of distilled water. To ensure complete dissolution, the solutions were left on a magnetic stirrer at 200 RPM for 3 hours.

The parameters considered in this study include air temperatures in the range of 60 ˚C -180 ˚C and initial solid contents of 6% w/w, 17% w/w and 45% w/w. The single droplet drying approach described in Chapter 3 is used at 0.57 m/s air velocity and conditions summarised in Table 5.1. Details on the experimental procedure of the single droplet drying experiments have been described in Chapter 3.

Table 5.1 Single droplet drying conditions used to dry aqueous sodium silicate droplets

Parameter	Setting
Air temperatures	60 ˚C, 100 ˚C, 140 ˚C, 180 ˚C
Initial solute concentrations	6%, 17% and 45% w/w
Air velocity	0.57 m/s
Droplet size	1.4- 1.7 mm

The solutions preparation method for spray drying was similar to the single droplet drying experiments. The liquid solutions, approximately 0.5 L in volume, were spray dried on 4M8-TriX Procept Spray dryer at the settings given in Table 5.2. The spray drying experiments were conducted with three columns set-up. The system was heated to the desired temperature and allowed to reach steady-state before turning

the pump and allowing the liquid solution to be atomised. After drying was complete, spray dried powder was collected and stored in vials for further characterisation.

Table 5.2 Spray drying settings for sodium silicate solutions

Process variable	Value
Inlet air flow	0.3 m^3/min
Nozzle airflow	16.9 l/min
Inlet feed flow rate	1.66 gram/min
Nozzle type	Two fluids nozzle
Nozzle size	0.8 mm
Solid content	5% and 15% w/w
Inlet air temperatures	100˚C, 140˚C, 180˚C

Dried particles collected from the single droplet drying were studied using a Hitachi Tabletop Microscope TM3030. The particles were removed by cutting the end of the PEEK filament holding the dried particle and depositing the particle on an SEM stub covered with adhesive tape. Analysis of spray-dried powder of silicate was also done using SEM.

5.3 Morphology evolution

The morphology evolution time series in Table 5.3 clearly shows that the drying of sodium silicate as a function of air temperature can be classified into two main categories, drying below and above boiling. Below boiling, the morphology evolution shows that the droplet goes through a shrinkage period until they form the final dried particle. The morphology of the final particle is spherical, and no notable surface deformations are observed. The lack of deformations, as opposed to those encountered in the drying of organic polymers (Pauchard and Allain, 2003a), suggests that there is no formation of any skin or solid layer that severely restricts the shrinkage or moisture diffusion. Above boiling, the droplet goes through a faster homogenous shrinkage and notably, the droplet goes through inflation/deflation cycles. The inflation experienced in these cycles is sustained at the end of drying, and puffed expanded particles are produced. The ability of silicate to maintain inflation at the end of the inflation/deflation cycles is in contrast to the behaviour of sucrose presented in the previous section where the particle collapsed at the end of the inflation/deflation cycles. This difference is attributed to the viscoelastic properties

of silicate during inflation which resists the collapse of the particle. This is discussed in more detail in part 5.5.4.

Table 5.3 Morphology development during single droplet drying of 17% w/w aqueous sodium silicate droplet at v_{air}=0.57 m/s and different air temperatures.[4]

T_{air}=60°C										
t(s)	0	20	40	60	80	100	120	140	180	280
T_d(°C)	18	29	31	35	38	43	47	50	54	58

T_{air}=100°C										
t(s)	0	15	30	45	60	75	90	105	145	175
T_d(°C)	22	42	47	53	62	70	77	83	93	96

T_{air}=140°C										
t(s)	0	20	60	89	89	104	107	118	123	138
T_d(°C)	27	64	104	113	113	128	128	132	132	134

T_{air}=180°C										
t(s)	0	20	40	59	59	63	64	69	75	145
T_d(°C)	25	79	111	126	127	132	134	153	163	167

The effect of the air temperature and the initial solute content on the drying kinetics, including surface area, droplet temperature and evaporation flux are investigated in detail in the next section. A highlight on the effect of boiling on the evaporation rate is included. The boiling onset parameters are also used to explain the drying mechanisms above boiling.

5.4 Drying kinetics of silicate below boiling

To investigate the influence of air temperature and initial solute content on the drying kinetics of sodium silicate, the normalised droplet surface area, droplet temperature and evaporation are plotted in Figure 5.1. The normalised surface area plot was done to represent the square diameter law where the squared diameter is normalised by the initial squared diameter of the droplet. For each condition, 3-5 experiments were conducted, and typical drying runs were presented. The method of the calculation of the evaporation flux has been outlined in Chapter 4.4.

---

[4] A larger size replica table with better image quality is provided in Table E.4 (Appendix E)
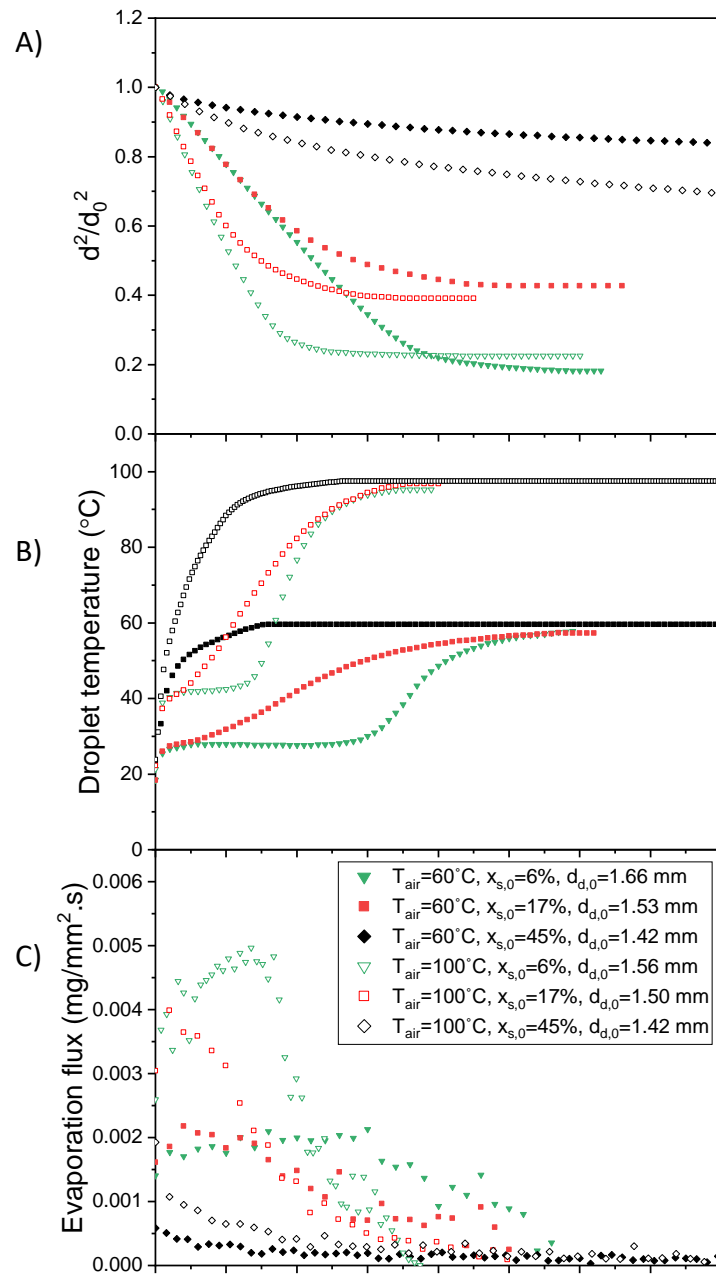
Figure 5.1 The drying kinetics as a function of time at initial mass percentages of 6% w/w, 17% w/w and 45% w/w and air temperatures of 60 and 100 ˚C (A) normalised surface area, (B) droplet temperature, (C) evaporation flux

Figure 5.1 (C) shows that the increase in air temperature and solid content affects the extent of shrinkage of the droplet and the time required to reach the final size of the dried particle. As expected, the increase in air temperature results in a faster shrinkage of the droplet due to the increase of the energy transfer to the droplet and a larger temperature gradient between the droplet surface and the hot air. This results in a higher water vapour pressure at the surface of the droplet, thereby faster

evaporation and enhanced decrease of the droplet diameter. The extent of shrinkage decreases with the increase in solute concentration, as there is a lower amount of moisture to be evaporated. The final size of the dried particles at the same solid concentration and different air temperature is similar, which suggests that the increase of air temperature from 60 ˚C to 100 ˚C causes little change to the surface structure and thus little influence on the mechanisms of shrinkage.

The evolution of the droplet temperature given in Figure 5.1 (C) shows similar stages to those defined in the literature in the study by Nešić and Vodnik (1991). At initial solid concentrations of 6% and 17% and air temperatures of 60 ˚C and 100 ˚C, the droplet temperature rises rapidly to the wet-bulb and remains constant until the moisture saturation at the surface reduces due to the decrease of moisture transport to the surface caused by the increase of the solid fraction. Subsequently, the sensible heat added to the droplet becomes higher than the heat of evaporation and therefore, the droplet temperature increases until it reaches the air temperature. The droplet temperature history can be related to the evaporation flux profile shown in Figure 5.1 (C). Initially, the evaporation flux increases, the surface is saturated with moisture and the decrease in the droplet size results in an increase in the heat and mass transfer coefficients. Afterwards, the evaporation flux undergoes a reduction which corresponds to the rise of the droplet temperature beyond the wet-bulb temperature. The lower moisture transport over time gives an indication of the decrease in surface moisture saturation due to decrease of moisture transport to the surface. The droplet temperature profile at an initial concentration of 45% w/w and air temperatures of 60 and 100 ˚C shows that the droplet skips the constant drying stage at the wet-bulb temperature. This is because high solid concentration results in reduced water activity and increased resistance to moisture transport. This is also reflected in the evaporation flux profile where the reduction in the evaporation flux is observed early in the drying time compared with lower initial solute concentrations.

The decrease of the length of the constant drying stage at the wet-bulb temperature with the increase in the solute concentration and air temperature can be related to the moisture content at which the droplet rises above the wet-bulb temperature,

shown in Figure 5.2. It can be seen that the droplet enters the falling rate period at relatively high moisture fractions. At high concentration, the droplet enters the falling rate period at a moisture fraction similar to the initial moisture fraction. The increase in air temperature also results in entering the falling stage at higher mean moisture content. This is attributed to moisture gradients within the droplet and can be explained by the calculation of the Péclet number.
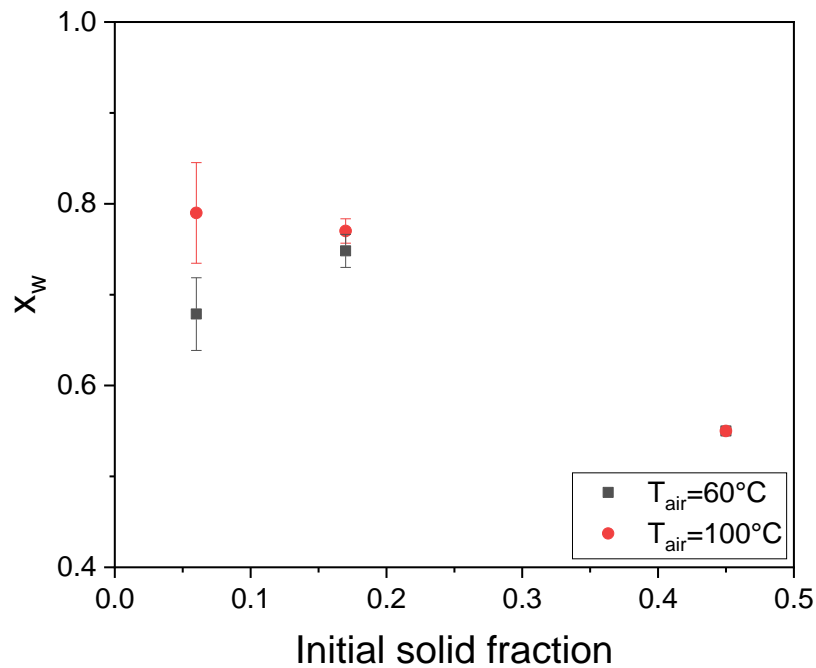

Figure 5.2 The water fraction of the particle at the end of the constant stage period, based on the end of the wet-bulb temperature, at v_{air}=0.57 m/s and different air temperature. Error bars were calculated based on 5 replicates at each condition. Error bars are based on the standard deviation of the mean and represent ± 1 standard deviation.

During drying, the evaporation of the moisture carries the solute particles to the air-water interface while diffusion motion homogenises the concentration of the particles over the droplet space. This is quantified by the dimensionless number known as Péclet number given by the following equation (Vehring et al., 2007):

$$Pe = \frac{k}{8D} \tag{5.1}$$

The Péclet number calculations are based on the initial evaporation rate in the constant rate period. The diffusion coefficients of sodium silicate were taken from an NMR study conducted by Bahlmann et al. (1997).
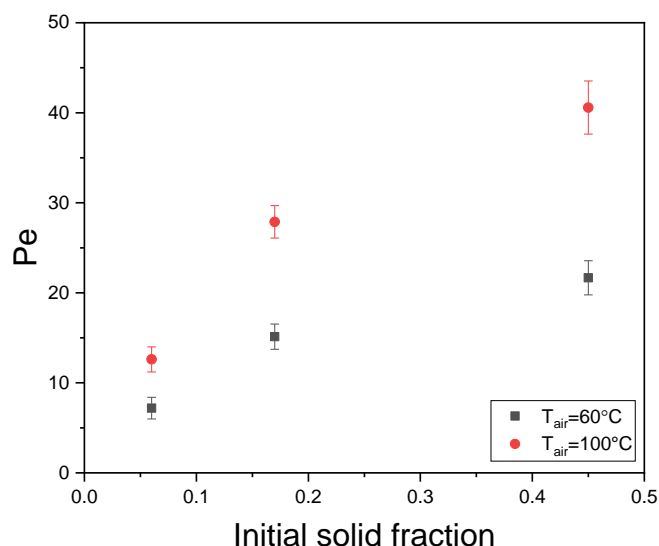
Figure 5.3 Initial Péclet number calculated based on the evaporation rate in the constant rate period Error bars were calculated based on 5 replicates at each condition. Error bars are based on the standard deviation of the mean and represent ± 1 standard deviation.

Figure 5.3 shows that the Péclet number increases at higher air temperature and solute concentration due to an increase in evaporation rate and a decrease in solute diffusion coefficient, respectively. It can be seen that the Péclet number is higher than 1 for all air temperatures and initial solid concentrations. This suggests a non-uniform solid distribution with high solid concentration at the surface and thereby a faster time for the droplet to enter the falling rate period and heat-up to the air temperature. Although the increase in air temperature results in a higher Péclet number and a higher degree of surface enrichment, the final particle size of the dried particle is unaffected, as shown in Figure 5.1 (C). This suggests that the solute surface enrichment is insufficient to lock the particle and freeze the surface area of the particle. The particle continues shrinkage even after the droplet temperature exceeds the wet-bulb temperature. This is also supported by the lack of surface deformation as shown in the morphology time series in Table 5.3, which further suggests that surface enrichment allows continued evaporation and shrinkage of the droplet. The behaviour of silicate below boiling in terms of morphology and drying kinetics is similar to sucrose, and no significant differences are observed.

5.5 Drying kinetics above boiling

Drying kinetics above boiling are presented in Figure 5.4 in a similar fashion to that below boiling for easier comparison.
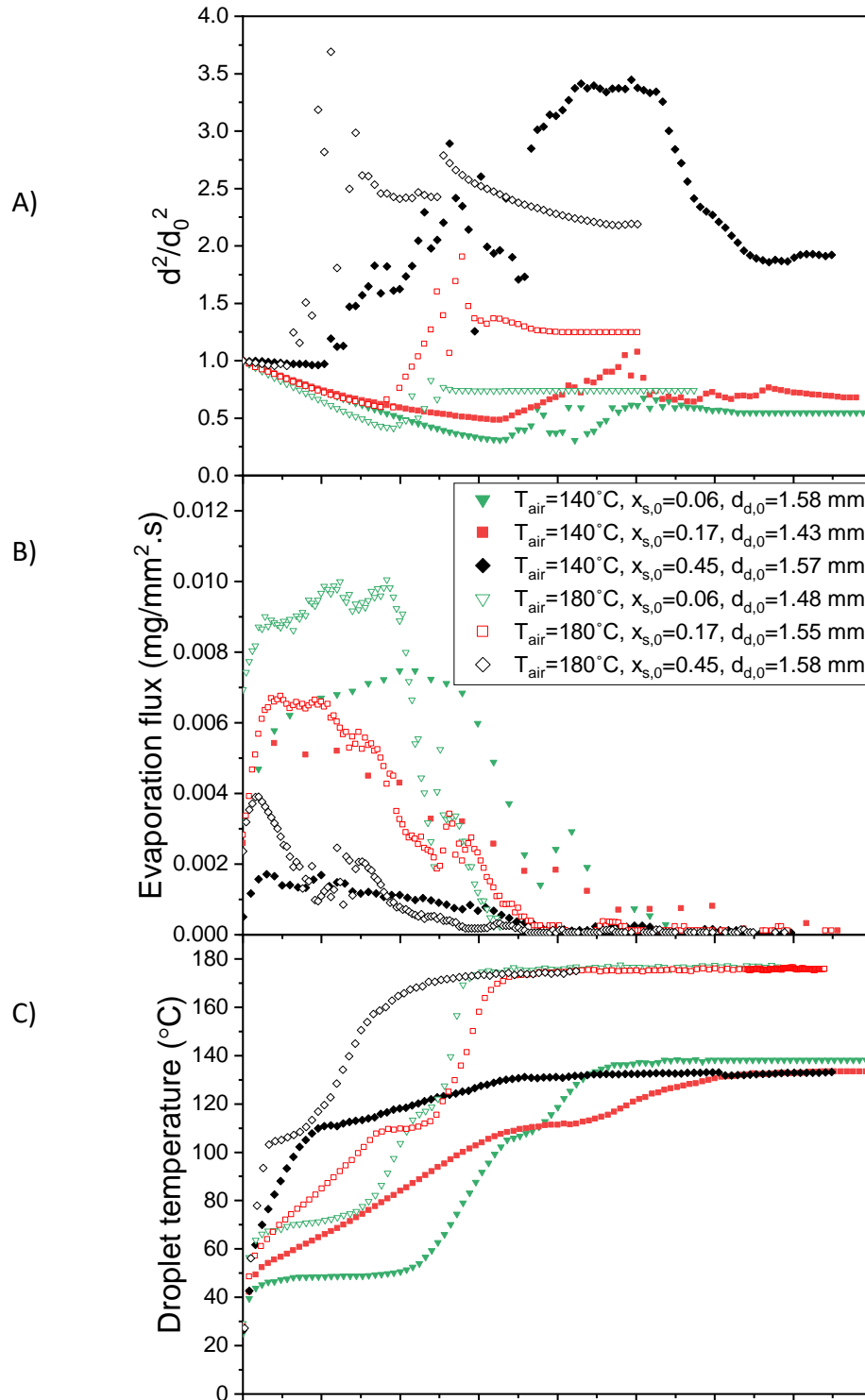

Figure 5.4 The drying kinetics as a function of time at initial mass percentages of 6%, 17% and 45% and air temperatures of 140 and 180˚ (A) normalised surface area, (B) droplet temperature (C) evaporation flux

The droplet temperature profile, Figure 5.4 (C), shows a boiling stage following the heat-up period and the constant drying stage at the wet-bulb temperature. It can be seen that the droplet experiences shrinkage prior to entering the boiling stage where the droplet goes through cycles of inflation/deflation. The extent of shrinkage prior to boiling and the timeline of entering the boiling stage are greatly affected by the air temperature and the initial solid fraction. A higher initial solid content results in a lower extent of shrinkage prior to boiling and skipping the constant drying stage at the wet-bulb temperature. This is caused by the reduction of water activity with the increase in the initial solute concentration and also by the reduction of water diffusivity to the surface of the droplet. It is also clear that the inflation/deflation cycles started earlier with higher initial solid content due to a faster increase of the droplet temperature to the droplet boiling temperature. At lower solid content, the extent of shrinkage prior to boiling is greater where the droplet remains at the wet-bulb temperature for a period of time prior to heating up to the droplet boiling temperature. It can also be seen that at the same initial solute content, the extent of shrinkage prior to boiling decreases with the increase in air temperature as is clearly evident in the case of 6% and 17% initial solute concentrations.

The evaporation flux profiles in Figure 5.4 illustrate that the initial solid concentration has a strong influence on the evaporation flux. At low initial solid concentration, it can be seen that the flux increases and remains constant for a period of time corresponding to the constant drying period at the wet-bulb temperature. Afterwards, the evaporation flux reduces due to the reduction of the moisture content at the surface of the droplet. However, at high initial solid concentration, the reduction in the evaporation flux occurs at earlier drying time, caused by the reduction of water activity with the increase in the initial solute concentration. It can also be seen that the evaporation flux is influenced by the air temperature; as expected the evaporation flux increases with the increase in air temperature. The effect of boiling on the evaporation flux and evaporation rate is studied in detail in part 5.5.2.

5.5.1 Boiling onset parameters

The parameters at the onset of boiling such as the diameter and the moisture content influence the inflation/deflation cycles and the subsequent effects of these cycles on the evaporation rate and the final size of the dried particle. Figure 5.6 (A) & (B) shows that the increase of air temperature at the same initial solute concentration results in an increase in the relative size and the moisture content at the onset of boiling. At 45% initial solid concentration, the droplet enters the boiling stage at large relative size of the droplet and a moisture content close to the initial moisture content. This can be understood by the temperature profiles, presented in Figure 5.4 (C), which show that at a high solid concentration, the droplet rises immediately to the boiling temperature indicating that the surface of the droplet is unsaturated with moisture. The increase of the mean moisture content at the onset of boiling with the increase in air temperature is strong evidence of moisture gradients within the droplet which results in an earlier reduction of surface saturation at higher mean moisture content. This is further proved by the Péclet number, shown in Figure 5.5, calculated using the initial evaporation rate and silicate diffusion coefficients obtained from Bahlmann et al. (1997). Péclet numbers higher than 1 are obtained, which suggests a non-uniform solid distribution with high solid concentration at the surface. The Péclet number increases with the increase in air temperature, caused by higher evaporation rate.
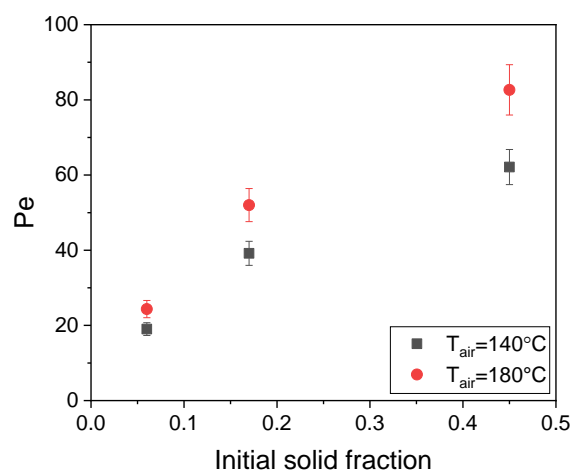

Figure 5.5 Initial Péclet number calculated based on the evaporation rate in the constant rate period. Error bars were calculated based on 5 replicates at each condition. Error bars are based on the standard deviation of the mean and represent ± 1 standard deviation.
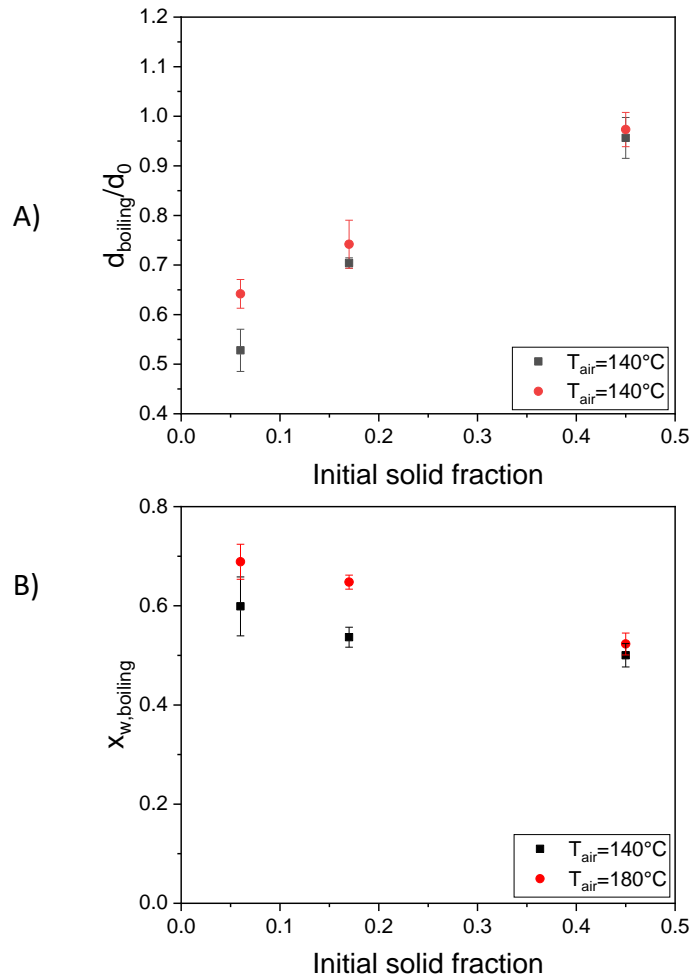
Figure 5.6 The parameters at the onset of boiling as a function of air temperature and solute concentration (A) relative size of the droplet (B) moisture content. Error bars were calculated based on 5 replicates at each condition. Error bars are based on the standard deviation of the mean and represent ± 1 standard deviation.

5.5.2 Effect of boiling on the drying rate

This section investigates the effect of boiling on the drying rate. To do this, single droplet drying runs at air temperatures of 140 ˚C and 180 ˚C are presented. For each run, the normalised surface area, evaporation rate, evaporation flux and droplet temperature profiles as a function of time are presented. Furthermore, the corresponding evaporation flux vs the moisture content is also presented.
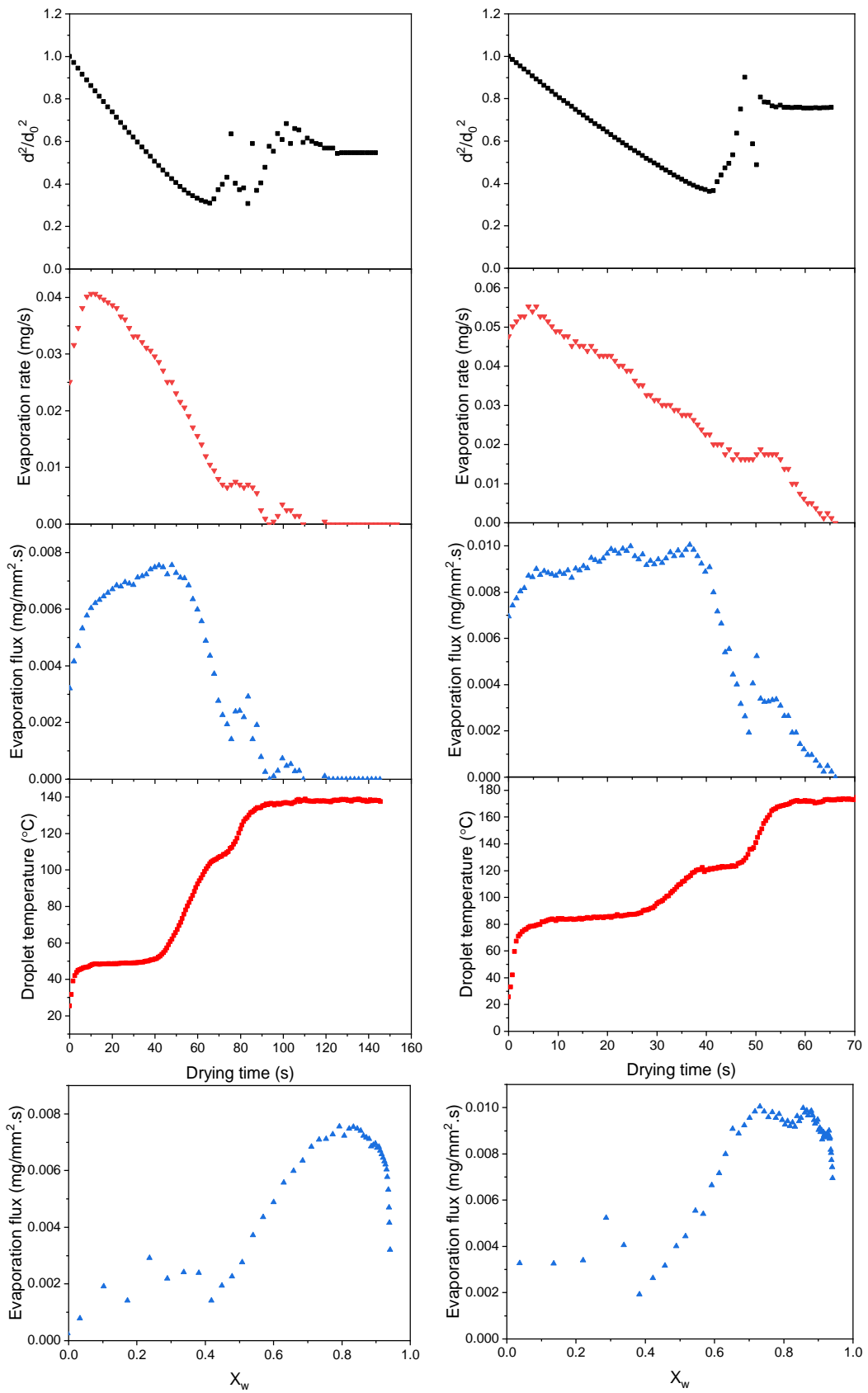
Figure 5.7 The normalised surface area, evaporation rate, droplet temperature as a function of drying time at an initial solid concentration of 6% w/w and air temperature of 140˚C (left) and 180 ˚C (right).
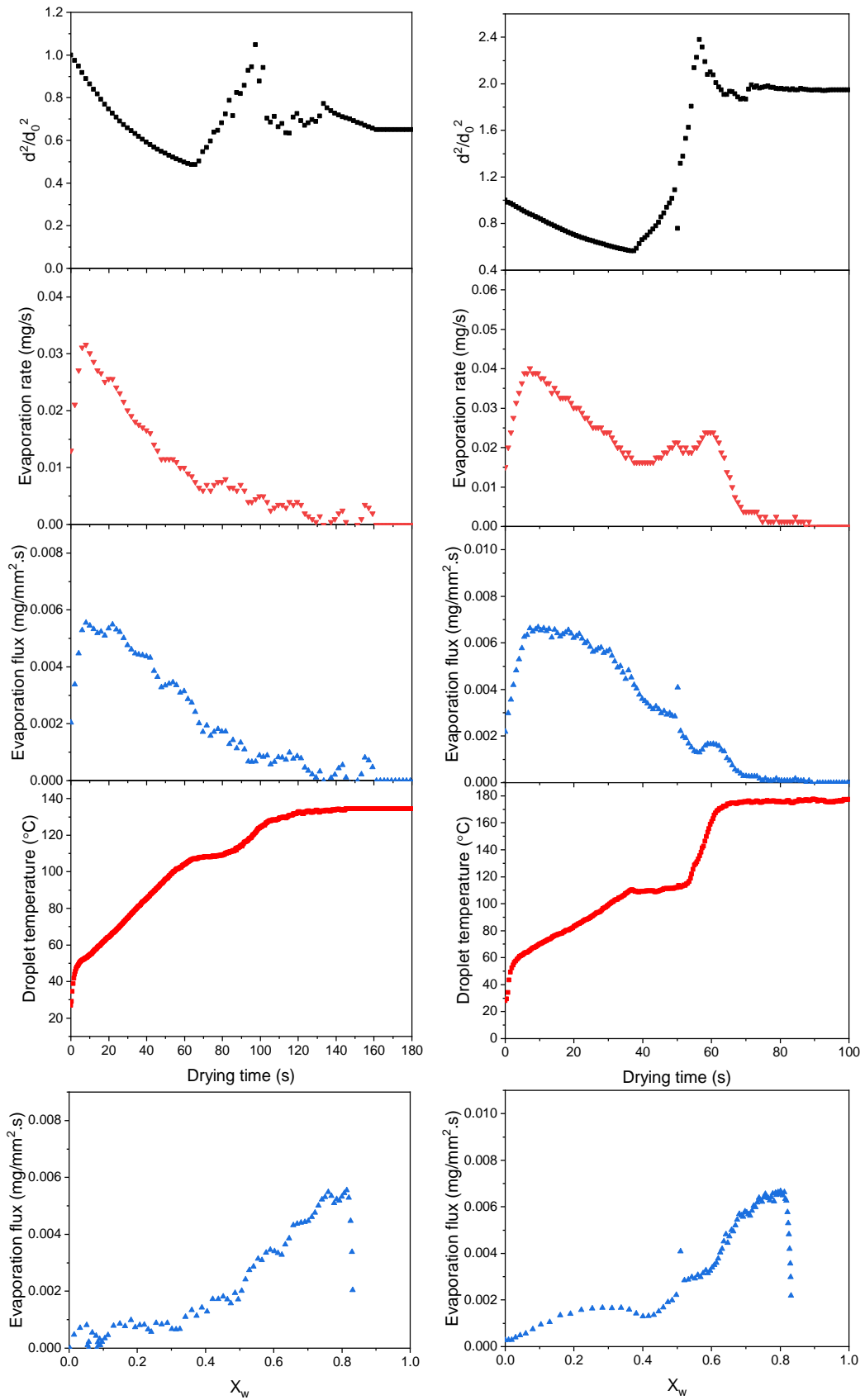
Figure 5.8 The normalised surface area, evaporation rate, droplet temperature as a function of drying time at an initial solid concentration of 17% w/w and air temperature of 140˚C (left) and 180 ˚C (right).
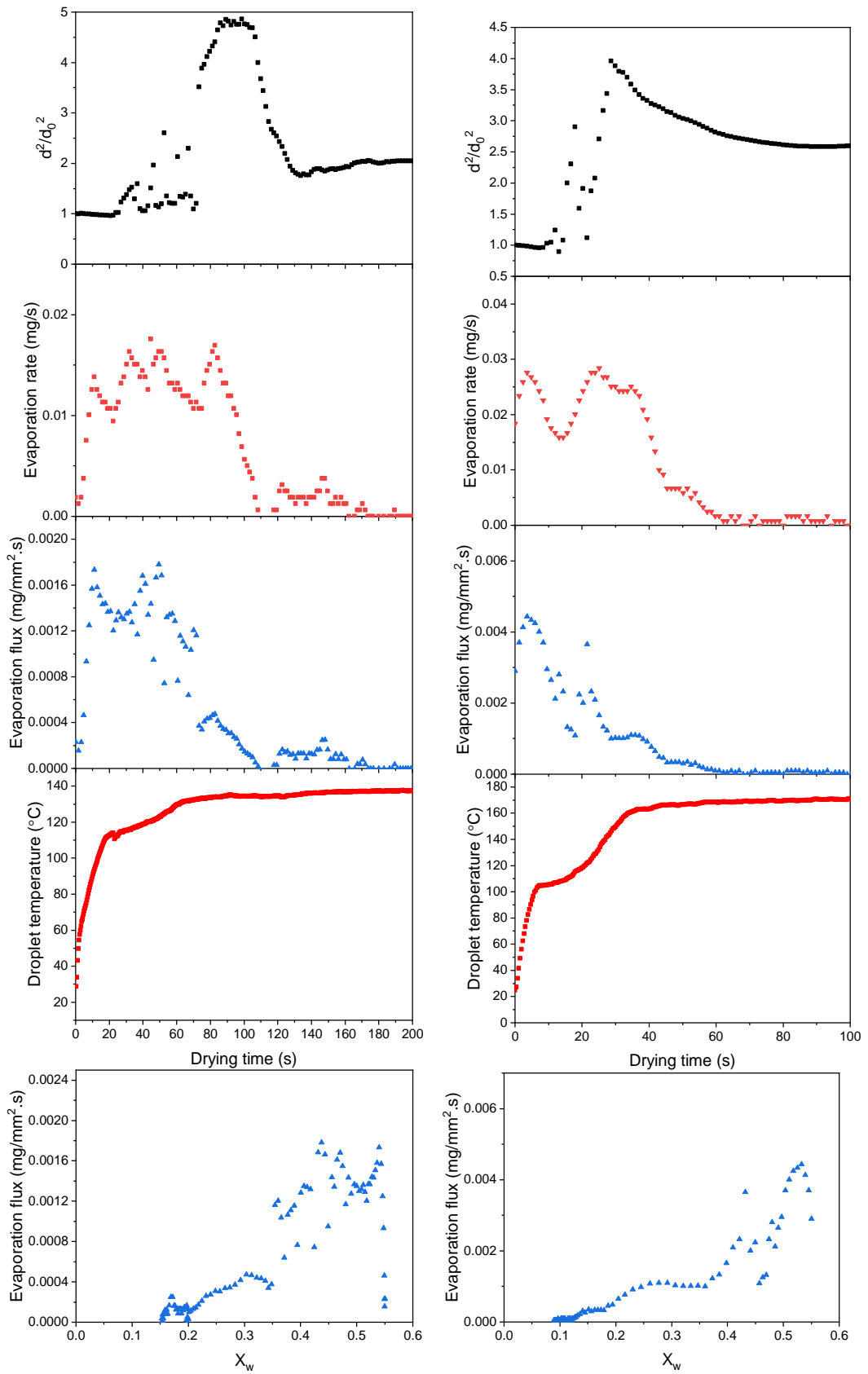
Figure 5.9 The normalised surface area, evaporation rate, droplet temperature as a function of drying time at an initial solid concentration of 45% w/w and air temperature of 140˚C (left) and 180 ˚C (right).

The results presented in Figure 5.7, Figure 5.8 and Figure 5.9 show that the evaporation rate increases during the boiling stage. This is clearly demonstrated in the case of high concentrations as the droplet enters the boiling stage with high moisture content and higher diameter and experiences a higher degree of stretching. Morphology time series showing an example of droplet stretching is presented in Figure 5.10. The morphological development including inflation increased the evaporation rate substantially and also resulted in fluctuations in the drying rate as noticed in the case of drying 45% w/w droplet at 140 ˚C (Figure 5.9). According to Hecht et al. (2000), the occurrence of inflation causes an increase in the drying rate due to the stretching of the droplet from the bubble growth occurring inside the droplet and the mixing of the droplet after the bubble bursting. The stretching of the drop causes a convective flow of the liquid towards the surface. Therefore, with the increase in the surface area, more of the drop liquid is closer to the surface than prior to the stretching. These effects of stretching result in the reduction of the internal mass transfer coefficient. The reduction in the internal mass transfer resistance is also due to liquid phase mixing caused by rupturing action of the bubbles.

Figure 5.7, Figure 5.8 and Figure 5.9 also demonstrate the effect of boiling and inflation/deflation cycles on the evaporation flux. The particle/droplet diameter increases during inflation and therefore, the evaporation flux reduces. Inflation is followed by deflation where the water vapour is released and evaporation flux increases. The fluctuations in the drying rate are more pronounced at a higher initial solute concentration as the droplet experiences a higher degree of inflation. A similar effect of inflation/deflation cycles on the evaporation flux has also been reported in another study (Tran et al., 2016a) in the case of single droplet drying of lactose/water system at air temperatures above the boiling point.
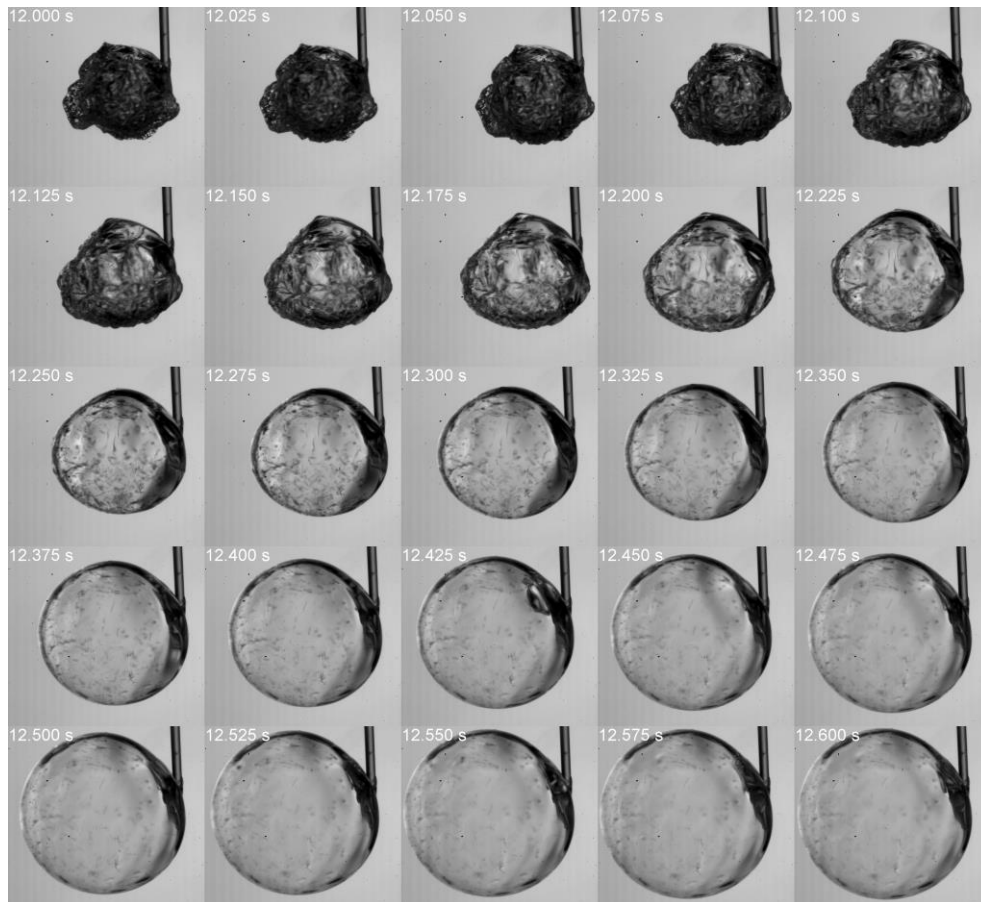
Figure 5.10 Growing behaviour of 45% silicate droplet dried at 180 ˚C, captured a using high-speed camera at 1000 frames per second. The series correspond to a starting and the ending drying time of 12 and 12.6 seconds respectively corresponding to the boiling stage shown in Figure 5.9 (right)

5.5.3 The effect of boiling on the porosity and final size of dried particles

The size of the dried particle, determined based on the images obtained during drying experiments, as a function of air temperature and initial solute concentration is given in Figure 5.11 (A). It can be seen that the increase in air temperature, below the droplet boiling temperature, from 60 and 100 ˚C causes little change in the final size. This means that in this temperature range, there is no locking or any significant change in the surface structure. On the other hand, the increase of air temperature above boiling has a significant influence on the final particle size; particles with larger diameters than the initial droplet size are produced above boiling. The extent of increase in size is largely influenced by the initial solute concentrations; higher initial solute concentrations lead to a larger final dried particle size. With the increase in initial solute concentration, the droplet enters the boiling stage at a larger relative

size as explained in 5.5.1. The effect of boiling on the final dried particles can be further investigated by determination of the porosity of the final dried particles. The porosity is calculated based on the measured mass and the diameter of the final particle according to the following equations:

$$porosity, \phi = \frac{Vmeasured - Vexpected}{Vmeasured} \qquad (5.2)$$

where,

$$Vexpected = \frac{m_{s,0}}{\rho_s} \qquad (5.3)$$

The measured volume is calculated based on the diameter of the final dried particle determined from images using ImageJ. The solid density of silicate, 2400 kg/m^3 (Weldes et al., 1969) is used in the calculations of the expected diameter. At air temperatures below boiling, Figure 5.11 (B) show that particles with low densities were obtained. This is because, at temperatures below boiling, the droplets underwent shrinkage without any hindrance from the surface structure, as explained in part 5.4. It can also be seen that there is a dramatic increase in the porosity of the dried particles with the increase of air temperature above boiling. Particles with high porosity are observed due to the inflation of particle during boiling which results in the production of puffed particles.

A) B)
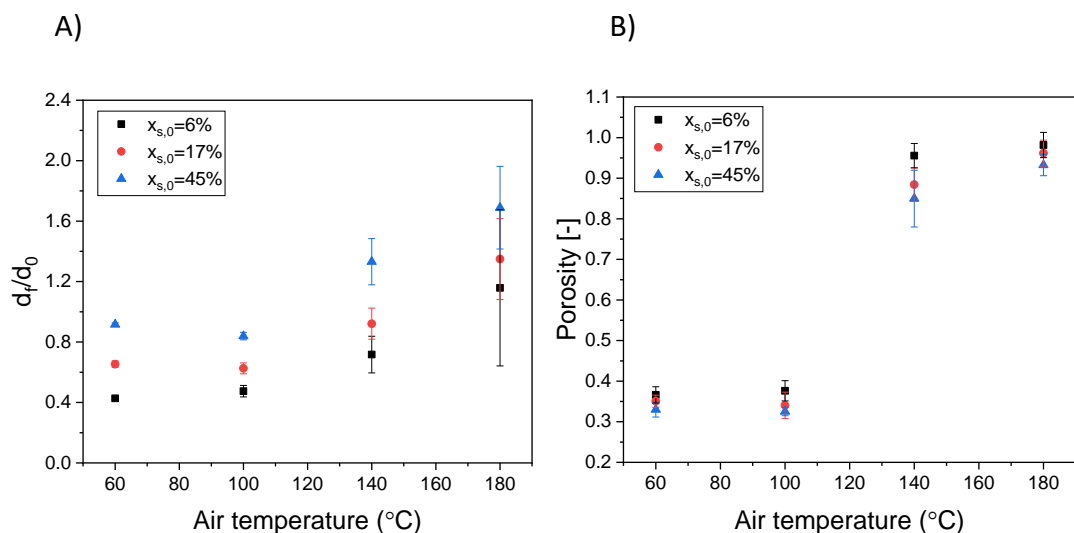
Figure 5.11 The properties of the final dried particles as a function of air temperature at different initial concentrations (A) relative final size (B) Porosity. Error bars were calculated based on 5 replicates at each condition. Error bars are based on the standard deviation of the mean and represent ± 1 standard deviation.

5.5.4 Mechanisms of inflation

The previous two parts have explained the role of boiling on the drying rate, morphology development, size and porosity of the dried particles. This part discusses the mechanisms and properties, allowing sodium silicate to undergo inflation/deflation cycles and sustain inflation at the end of these cycles forming a puffed expanded hollow particle. Figure 5.13 shows the morphology time series from the onset of boiling till the end of drying of 45% w/w silicate droplet at 180 ˚C. The expansion of the droplet during inflation cycles and the ability to sustain the inflation of the droplet is directly related to the rheological properties of the sodium silicate. The growing behaviour and lack of deflation suggest that the droplet possesses viscoelastic properties that allow inflation to be sustained. The increase of evaporation rate during inflation results in faster solidification of the droplet during the inflation period. The role of rheological properties of silicate is investigated by the inclusion of bulk rheology measurement on sodium silicate, presented in Figure 5.12, obtained from Weldes et al. (1969). Bulk rheological measurements are used due to the lack of material properties in non-equilibrium states and the inadequacy of current experimental methods to probe the process on realistic time (Vehring, 2008).
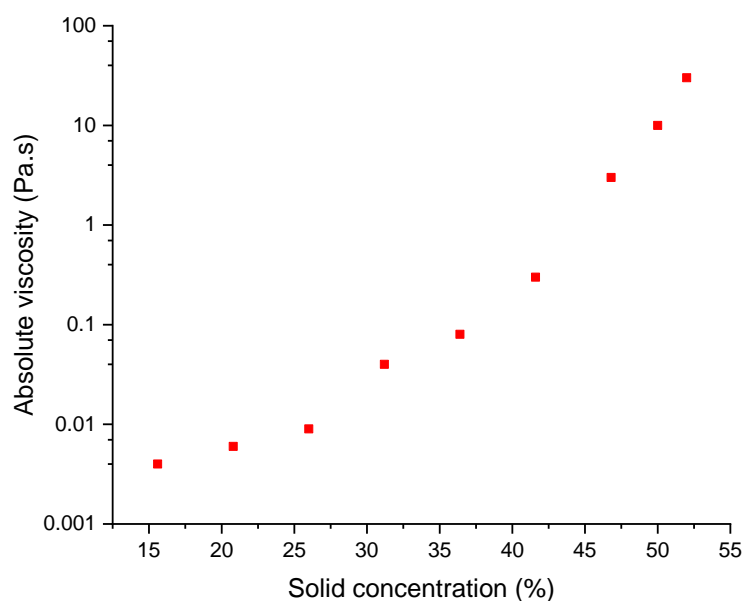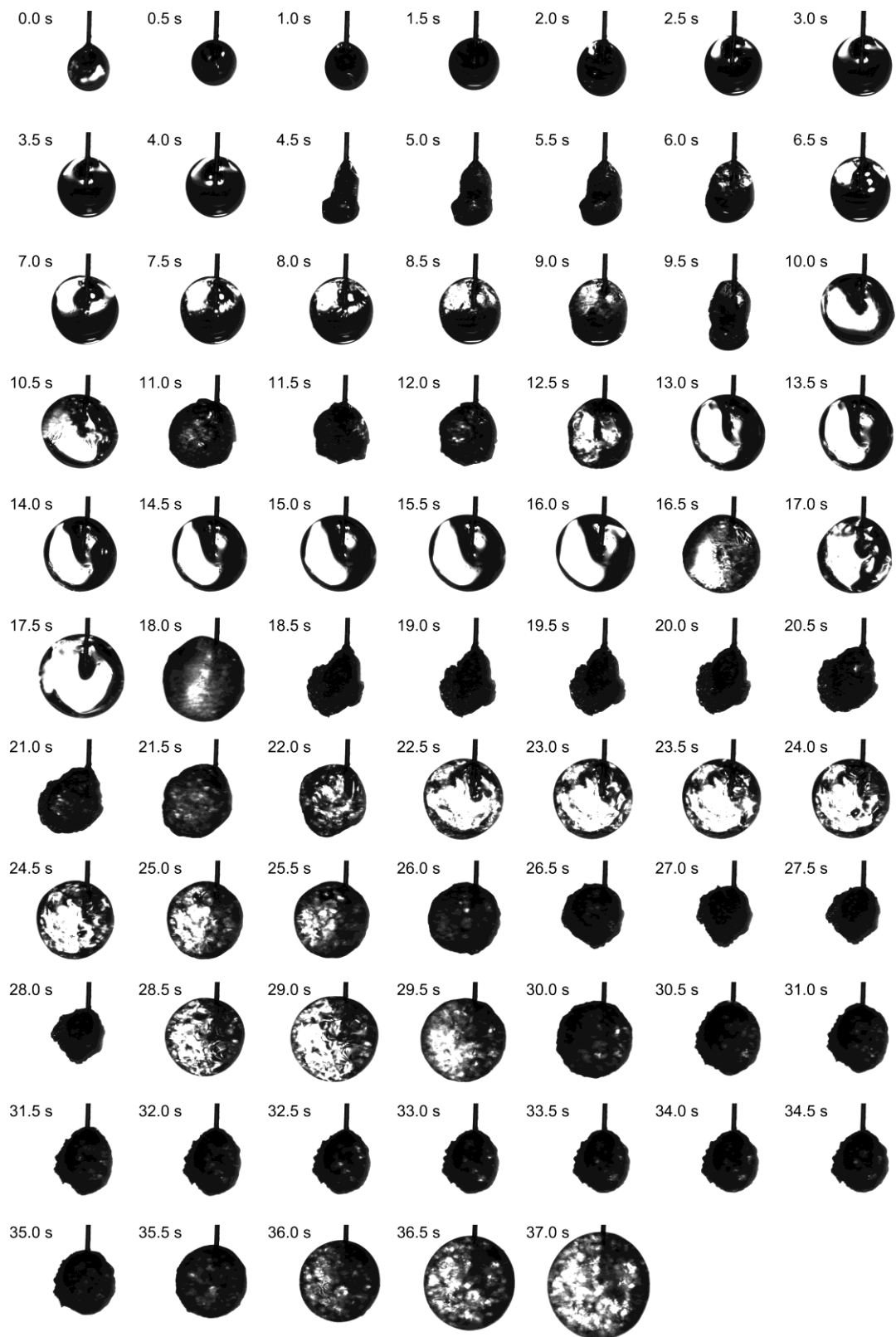

Figure 5.12 Viscosities of sodium silicate solutions as a function of concentration (Weldes et al., 1969)

Figure 5.13 Morphology time series during inflation behaviour of 45% aqueous silicate droplet at 180˚C. The annotation on the images shows the real-time of drying in seconds with respect to the onset of boiling.

The bulk rheological properties of sodium silicate can be used to give insights on the rheological properties of the droplet at the onset of boiling. The boiling onset parameters presented in part 5.5.1 shows that the droplet enters the boiling stage at solid fractions in the range of 0.3-0.5 (Figure 5.6 (A)), dependent on the air temperature and initial moisture content. This solid fraction range corresponds to viscosities in the range of 0.04-10 Pa.s (Weldes et al., 1969). At such concentration, sodium silicate begins encountering an exponential rise of the viscosity until the solution gains viscoelastic properties (Weldes et al., 1969). This is supported by the growth and surface stretching of silicate droplet, shown in Figure 5.13, which indicate a viscoelastic behaviour. It can be seen that the droplet remains expanded for a major period of drying with minor collapse cycles. This results in faster drying during boiling and particles with thin shells and high porosity are formed. The nature of inflation of silicate during boiling is very different from that encountered during drying of sucrose droplets, presented in the previous chapter. Sucrose showed more rapid inflation/deflation cycles. Unlike sucrose, drops of silicate maintain an expansion at the last stage of drying, although the surface of the bubbles collapses (Figure 5.13). The less degree of collapse indicates high viscoelastic properties and less degree of diffusivity of water than encountered when drying of sucrose. This is the reason silicate drying results in an expanded particle with large size at the end of boiling as opposed to sucrose where the particle collapses at the end of the inflation/deflation cycles, and smaller particles are formed. The extent of inflation is highly dependent on the initial solute concentration and air temperature. At the same drying conditions and initial moisture content, the extent of inflation is also stochastic from one droplet to another, illustrated by the error bars of the final diameter of the particle in Figure 5.11 (A), due to the stochastic nature of bubble nucleation.

5.6 Final morphologies

The morphologies of sodium silicate particles obtained from single droplet drying and laboratory spray drying are presented in Figure 5.14 and Figure 5.16, respectively. At low air temperatures, the SEM micrographs of the particles collected from the single droplet drying show smooth particles with spherical structures. These show high similarity to the particles collected from spray drying. The smooth appearance and sphericity of the particles are related to particle formation mechanism demonstrated by the morphology time series presented in part 5.3. The particle underwent shrinkage without any hindrance from the surface structure. Surface deformations are caused by the formation of a surface structure with elastic properties that hinders shrinkage and thus continued solvent evaporation results in surface deformations due to pressure gradients on the surface of the particles. This is not the case for silicate where the droplet underwent shrinkage for a major period of drying without any hindrance by the surface structure. At high temperatures, puffed expanded particles were collected. This is very clearly shown in Figure 5.15 where a broken particle shows a thin shell and a large internal vacuole. This is caused by the inflation of the droplet and accelerated drying which enhances the rheological properties of silicate and allowed the particle to maintain an inflated particle as discussed in part 5.5.4. It is hypothesised that these broken particles are similar to those collected from spray drying, shown in Figure 5.17.
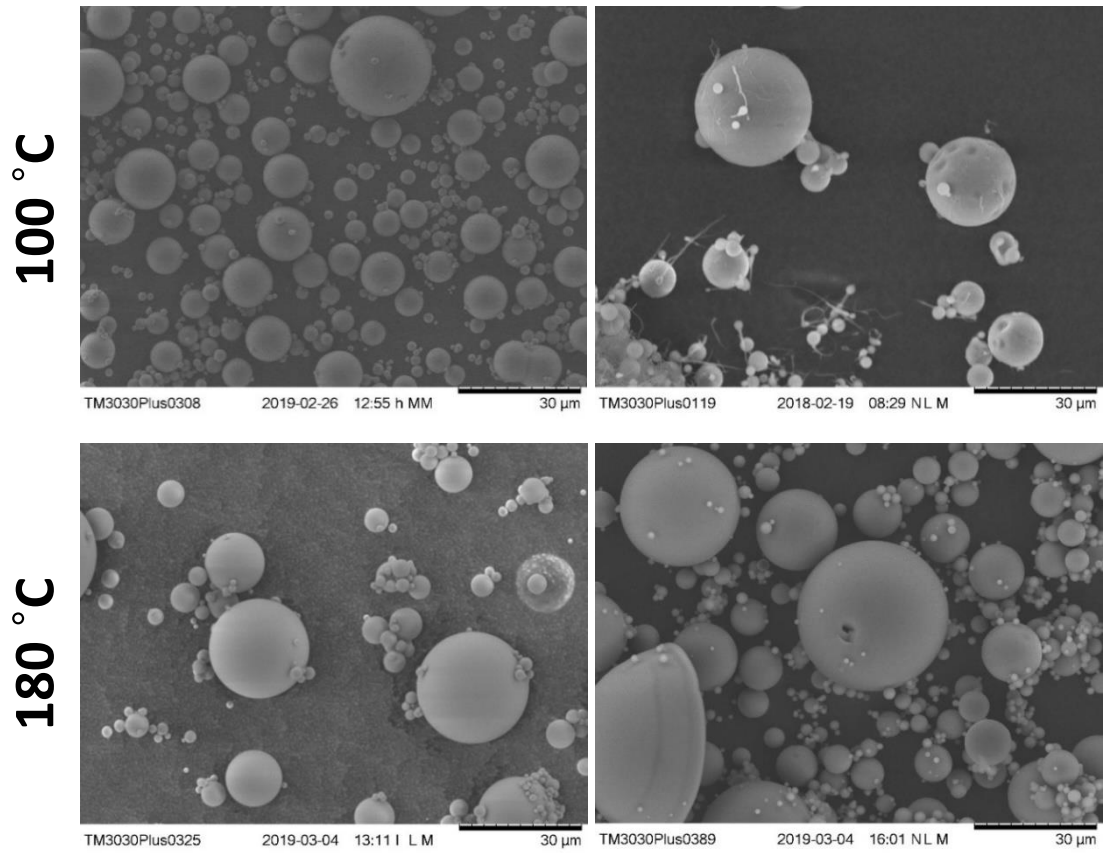
17% w/w **45 % w/w**
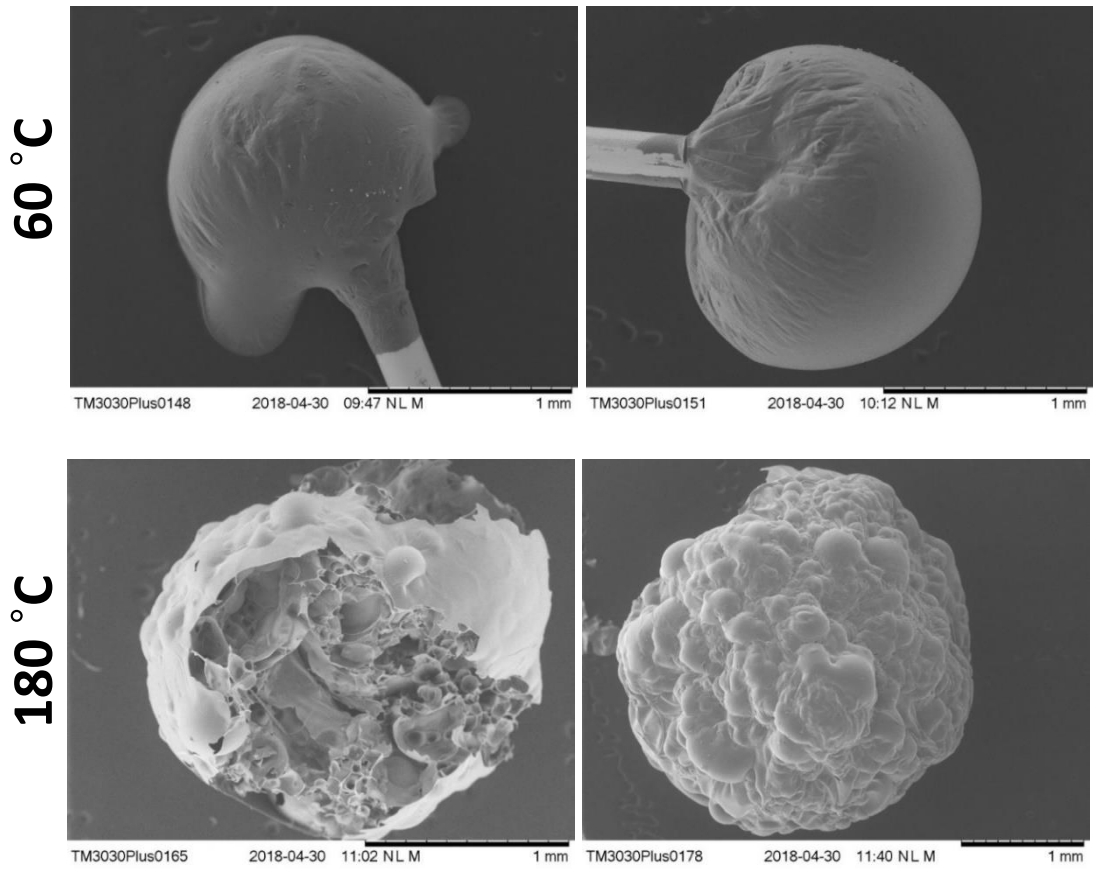
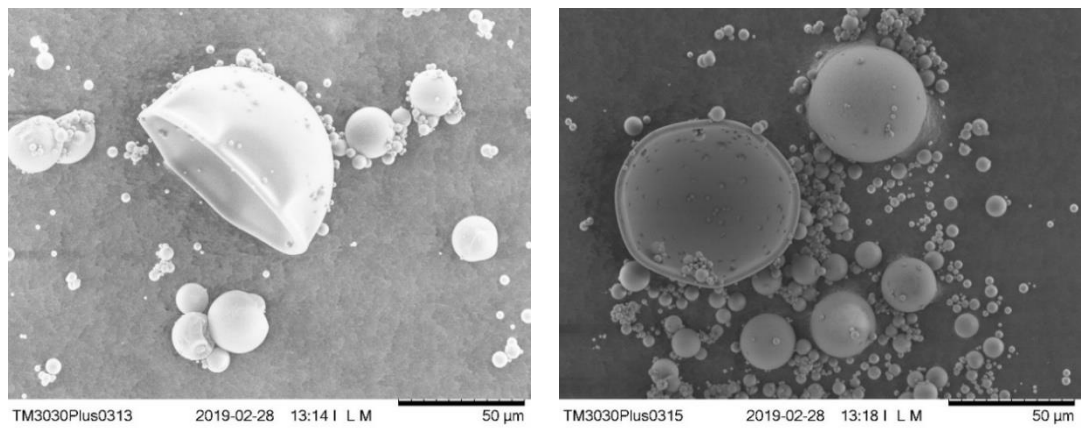Figure 5.14 SEM pictures of final dried particles collected from single droplet drying experiments
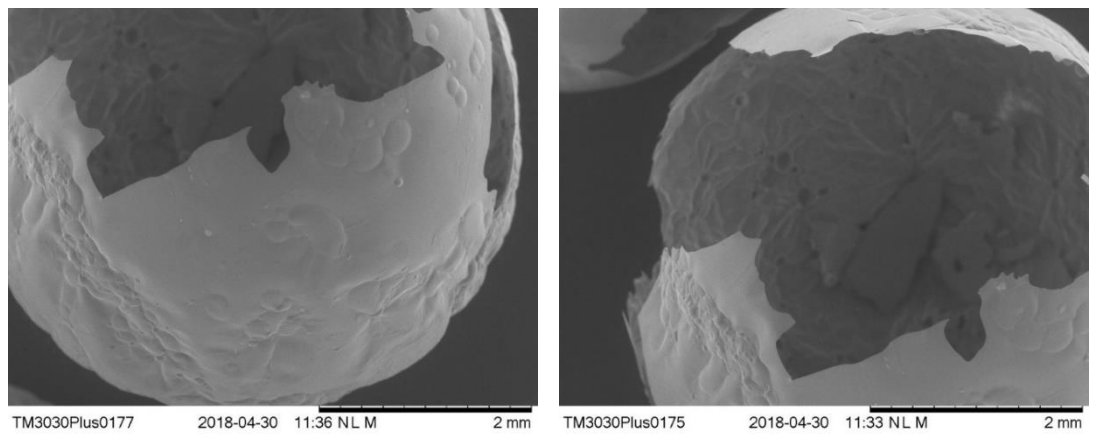
Figure 5.15 Broken particle collected from single droplet drying of 45% sodium silicate droplet at 180 ˚C

17% w/w   **45 % w/w**

100 °C

180 °C

Figure 5.16 Spray dried sodium silicate particles

Figure 5.17 Broken particles collected from spray drying of 45% sodium silicate solutions at 200 °C

5.7 Conclusion

A single droplet drying technique has been used to extensively investigate the morphology evolution and drying kinetics of single droplets of sodium silicate aqueous solutions at temperatures above and below the boiling point and different initial solute concentrations. At lower temperatures below boiling, slower drying was observed, and the particle diameter underwent shrinkage until it reached the final diameter without any significant morphological development. At higher temperatures above boiling, faster drying occurred, and inflation/deflation cycles were observed which resulted in an expanded puffed particle. The morphological development during boiling including inflation/deflation resulted in accelerated drying rate due to enhanced internal mass transfer coefficient caused by stretching of the droplet and enhanced internal mixing of the liquid. The boiling onset parameters such as size and moisture content were influenced by the air temperature and initial solute concentration. Higher initial concentration resulted in boiling at larger diameter due to rapid heating up of the droplet temperature caused by reduced water activity. Péclet number calculations showed a Péclet number higher than 1 which increased with air temperature suggesting a moisture gradient within the droplet. The moisture gradient within the droplet is further demonstrated by the increase of the mean moisture content at boiling with the increase of air temperature.

The final porosity and diameter of the dried particles were significantly influenced by the air temperatures. Drying above the boiling temperature results in a larger diameter of the final dried particles. The effect of boiling on the size of the dried particle has been linked to the mechanism of inflation, which is influenced by the rheological properties of sodium silicate. The droplet enters the boiling stage at mean solid fractions in the range of 0.3-0.5, dependent on the air temperature and initial moisture content. This solid fraction range corresponds to viscosities in the range of 0.04-10 Pa.s. This shows that the silicate droplet enters the boiling stage at very viscous liquid state, which allows the droplet to undergo and maintain inflation. The droplet remains expanded for a major period of drying with minor collapse cycles; thus, the droplet dries faster during boiling. The less degree of collapse

indicates high viscoelastic properties of the surface structure. Solidification of the surface structure upon further drying results in maintaining inflated particles and leads to the formation of puffed expanded particles with larger diameters. The nature of inflation of silicate during boiling is very different from that encountered during drying of sucrose/water droplets, presented in the previous chapter. Sucrose showed more rapid inflation/deflation cycles, suggesting a liquid-like behaviour during the boiling stage. On the other hand, silicate demonstrated the ability to maintain inflation which indicates a viscoelastic behaviour that increases with the increase in solute fraction. The behaviour above boiling is therefore largely dependent on the material properties evolution during drying.

Chapter 6 Drying of hydroxypropyl methylcellulose (HPMC)/water

6.1 Introduction

The previous two chapters covered two systems, sucrose and sodium silicate. In both these systems, the pressure generated during boiling encountered little resistance from the particle surface structure; thus, the internal vapour pressure resulted in inflation/deflation cycles. This was attributed to the nature of the surface structure of the particle at the onset of boiling. The material entered the boiling stage at a more viscous state; however, a surface structure with elastic properties was not encountered prior to the boiling stage. The literature review in 2.4 highlighted that drying skin forming materials such as proteins and polymers results in the formation of a skin layer with elastic properties which strongly influences the subsequent morphology development and the final morphology formed. This was reported in several studies in the polymer and protein solutions (Pauchard and Allain, 2003a; Arai and Doi, 2012; Both et al., 2018b). The solute concentration becomes high near the droplet surface, forming a layer with distinct rheological properties from the bulk of the initial solution. Once the skin is formed, various surface mechanical stabilities arise, caused by the drying stress due to external and internal pressure differences. Therefore, the final particle morphology obtained depends on the properties of the skin that is formed during drying. The skin formation and the subsequent drying process dictates the type of the final morphology: hollow, dimpled, folded or buckled. However, these studies were conducted at low temperatures, and the influence of boiling when drying at high temperatures has not been considered. Therefore, it is vital to include one system that exhibits these skin forming properties to expand the investigation of morphological developments encountered when drying above boiling. The interplay between skin formation and boiling is an interesting part which needs to be considered in the scope of this work. To achieve these aims, hydroxypropyl methylcellulose (HPMC), known for its film-forming properties, is selected. The selection of HPMC allows the investigation of a system that exhibits complex rheological and mechanical properties which evolve with the increase in air temperature and concentration during drying. Furthermore, HPMC was selected due to a considerable industrial interest. The unique features of HPMC such its nontoxic property, ease of handling, high biodegradability and solubility makes it desirable for a number of applications (Sakata et al., 2006). One of the major

applications of HPMC is in the pharmaceutical industry as a carrier material due to its ability to allow a slow diffusion of drugs out of the system (Siepmann and Peppas, 2001). HPMC is also used in food applications as an emulsifier, thickening and suspending agent system (Siepmann and Peppas, 2001).

The first part of this chapter investigates the morphology evolution during drying as a function of air temperature and solute concentration, with a particular focus on the role of boiling on the morphology. The differences in the morphology evolution with the increase in air temperature and solute concentration are related to the rheological and mechanical properties evolution with the increase in the droplet temperature. The morphology evolution is also used to explain the differences in the structure of the final dried particles. The drying kinetics are then presented and related to the morphology evolution. In particular, the rate of shrinkage of the droplet and evaporation flux is related to distinct morphological developments. Trends in the droplet temperature history and evaporation flux are also further explained by the determination of the Péclet number.

6.2 Experimental work

6.2.1 Solutions preparation

Hydroxypropyl methylcellulose (HPMC) solutions were prepared from Pharmacoat 603 powder, supplied by Shin-Etsu. Pharmacoat 603 is produced from hypromellose with 28.7 and 8.9 % w/w degrees of substitution of Methoxy and Hydroxypropoxyl respectively and a molecular weight of 13000 (Perfetti et al., 2011). The specifications of Pharmacoat 603 are summarised in Table 6.1.

Table 6.1 Specifications of Pharmacoat 603 used to prepare HPMC solutions (Perfetti et al., 2011)

Grade	Pharmacoat 603
Degrees of substitution % w/w	28.7 Methoxy
	8.9 Hydroxypropoxyl
Viscosity (3% solution in water at 25 ˚C)	4.5-5 mPa.s
Molecular weight	13000

6.2.2 Single droplet drying

The filament single droplet drying technique described in Chapter 3 was used to investigate the morphology evolution and drying behaviour at air temperature in the range 60 – 180 °C and across a range of initial solid concentrations. The specifications used for single droplet drying experiments are summarised in Table 5.1. The final dried particles were collected from the end of the filament for SEM characterisation.

Table 6.2 Single droplet drying conditions used to dry aqueous HPMC droplets

Parameter	Setting
Air temperatures	60 ˚C, 100 ˚C, 140 ˚C, 180 ˚C
Initial solute concentrations	5% and 15% w/w
Air velocity	0.57 m/s
Droplet size	1.4- 1.7 mm

6.2.3 Spray drying

The solutions preparation method was similar to the single droplet drying experiments. The liquid solutions, approximately 0.5 L in volume, were spray dried on 4M8-TriX Procept Spray dryer. The spray drying experiments were conducted with three columns set-up to ensure that the dry particles were collected. The system was heated to the desired temperature and allowed to reach steady-state before turning the pump and allowing the liquid solution to be atomised.

Table 6.3 Spray drying settings

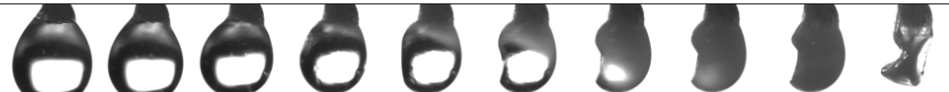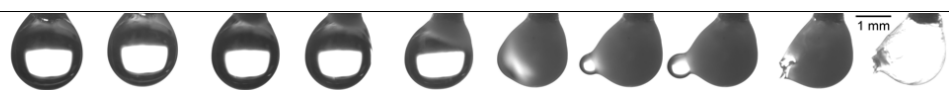| Process variable	Value
Inlet air flow (m³/min)	0.3
Nozzle air flow (l/min)	16.9
Nozzle size	0.8 mm
Solid content (w/w)	5% and 15% w/w
Inlet air temperatures	100˚C, 140˚C, 180˚C

6.2.4 Microscopy

Dried particles collected from the single droplet drying were studied using a Hitachi Tabletop Microscope TM3030. The particles were removed by cutting the end of the PEEK filament holding the dried particle and depositing the particle on an SEM stub covered with adhesive tape. Analysis of spray-dried powder of HPMC was also done using SEM.

6.3 Morphology evolution and structure of final dried particles
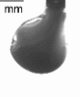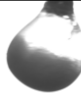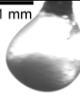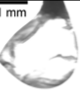
The particle morphology evolution and the droplet temperature as a function of drying time at different air temperatures are given in Table 6.4 & Table 6.5. The morphology time series presented represent the typical behaviour based on 3-5 single droplet drying runs. The final morphologies of the dried particles collected from these single droplet drying experiments are shown in Figure 6.1 & Figure 6.2. It can be seen that the morphology evolution is strongly dependent on the air temperature: low air temperatures lead to buckled particles while high air temperatures result in spherical particles with smooth surfaces. The mechanisms of drying at low air temperature and high air temperatures are analysed in detail in this section to explain the reason behind the drastic differences in morphology with the increase in air temperature.

Table 6.4 Morphology development during single droplet drying of HPMC with 5% initial solid concentration v_{air}=0.57 m/s and different air temperatures, the air is passing from right to left. [5]

T_{air}=60°C										1 mm
t(s)	0	51	101	106	115	122	129	146	162	260
T_d(°C)	17	30	36	37	39	41	42	44	46	63

T_{air}=100°C										1 mm
t(s)	0	24	45	51	54	60	72	79	107	151
T_d(°C)	34	47	56	59	60	64	72	75	84	99

T_{air}=140°C										1 mm
t(s)	0	14	26	32	35	38	43	79	86	106
T_d(°C)	46	58	70	77	82	87	93	120	122	138

T_{air}=180°C										1 mm
t(s)	0	6	11	13	15	18	37	53	63	79
T_d(°C)	53	73	82	86	91	98	123	163	178	180

---

[5] A larger size replica table with better image quality is provided in Table E.5 (Appendix E)

Table 6.5 Morphology development during single droplet drying of HPMC with 15% initial solid concentration v_{air}=0.57 m/s and different air temperatures, air is passing from right to left. [6]

T_{air}=60°C										1 mm
t(s)	0	31	49	59	67	78	89	106	132	214
T_d(°C)	17	34	38	41	42	44	45	47	48	57

T_{air}=100°C										1 mm
t(s)	0	9	27	29	31	35	39	50	91	214
T_d(°C)	40	52	68	70	71	74	76	81	87	100

T_{air}=140°C										1 mm
t(s)	0	10	11	13	15	17	19	78	103	119
T_d(°C)	26	69	72	77	82	86	93	127	137	138

T_{air}=180°C										1 mm
t(s)	0	3	4	5	7	8	35	39	56	69
T_d(°C)	25	60	70	78	85	91	163	169	176	178

5% w/w   15% w/w

A)   B)
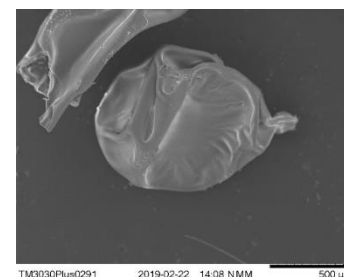
C)   D)

Figure 6.1 Morphology of the final dried HPMC particles collected from the single droplet drying experiments at different temperatures (A) 5% w/w, T_{air}=60 °C (B) 15% w/w, T_{air} =60 °C (C) 5% w/w, T_{air} =100 °C (D).

---

[6] A larger size replica table with better image quality is provided in Table E.6 (Appendix E)
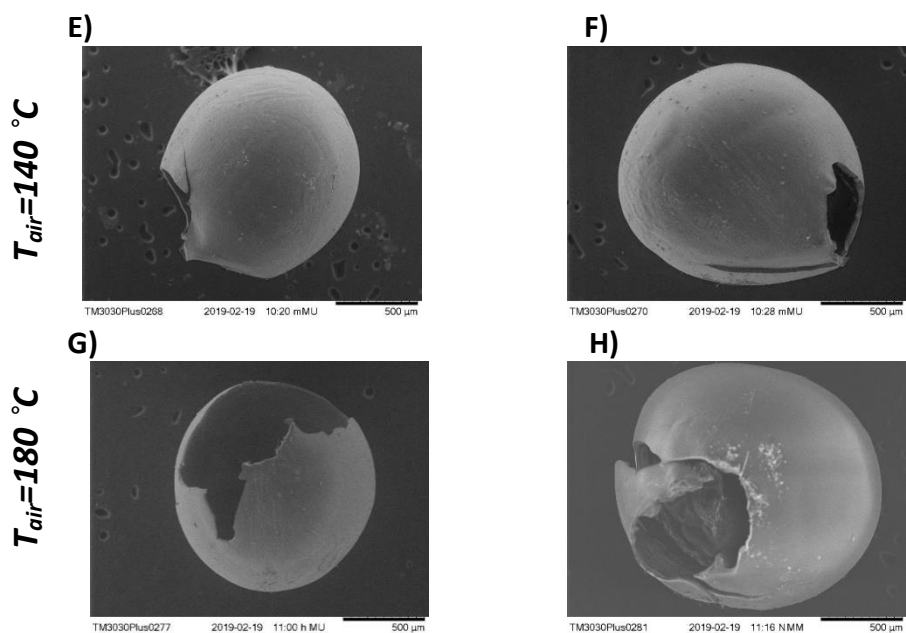
Figure 6.2 Morphology of the final dried HPMC particles collected from the single droplet drying experiments at different temperatures (E) 5% w/w, T_{air} =140˚C (F) 15% w/w, T_{air} =140˚C (G) 5% w/w, T_{air} =180˚C (H) 15% w/w, T_{air} =180˚C

At 60 ˚C, the morphology evolution and final morphology are significantly influenced by the initial solid content. At low solid content (5%), shrinkage is followed by bending and vacuole formation on the downstream side of the airflow as can be seen in the morphology evolution given in Table 6.4 as well as the final morphology in Figure 6.1 (A). The location of this vacuole is on the downstream side of the airflow as the modulus of the skin layer is minimal due to lower local evaporation. On the other hand, at higher solid content, the droplet undergoes surface deformations which begin on the left side of the airflow and spread throughout the whole droplet surface. The deformations of the droplet are caused by the change of the rheological properties at the surface due to the increase in solute concentration which gives the surface of the particle sufficient strength to counter shrinkage. However, the interior of the particle still contains moisture and the removal of this moisture from the particle through the skin can cause a pressure gradient on the skin. This has also been reported in a study by Arai and Doi (2012) which was conducted on the drying of polymers where an inward bend of the surface was observed. It was related to continued solvent evaporation after skin formation which creates a lower pressure under the skin, thus exerting a stress on the skin after skin formation.

The strength of the developed skin determines the extent to which the skin can resist the difference between internal pressure and atmospheric pressure and subsequently the type of morphology produced (Vehring, 2008; Both et al., 2018a). Weak skin can buckle and bend leading to wrinkled buckled particle while particles with fully rigid skin will not bend and will develop defect at the lowest point of the skin and a vacuole is formed at this point. The occurrence of surface instabilities such as buckling and invaginations has been reported in previous studies in the evaporation of polymers solutions (dextran) (Pauchard and Allain, 2003a; Sugiyama, 2006; Pauchard and Allain, 2003b; Pauchard and Allain, 2003c) as well as colloidal systems (Tsapis et al., 2005; Sugiyama, 2006). In all these studies, it has been hypothesised that these instabilities occur due to skin formation on the surface of the droplet, which impedes evaporation of moisture and shrinkage of the droplet. However, the effect of air temperature on buckling has not been investigated in previous studies. The internal pressure can also play a role in the final morphology developed, particularly the increase of the internal pressure due to boiling when drying at temperatures above the droplet boiling point.

With the increase in air temperature to a 100 ˚C, the morphology evolution time series show a distinct clouding of the droplet. This is shown in Table 6.4 at 100 ˚C air temperature at the drying time from 54 to 107 seconds and in Table 6.5 at drying time from 29 to 91 seconds. This clouding is an indication of the phase separation of the polymer and water, which is consistent with the two phases having different refractive indexes and thus scattering the light (Yoo and Um, 2013). HPMC undergoes sol-gel transition due to phase separation of the polymer and the water, which results in a change of rheological properties of the surface from viscous to elastic. The formation of gels from aqueous solutions of methylcellulose upon heating has been reported in a few studies (Heymann, 1935; Sarkar, 1979; Bajwa et al., 2009). The gelation of HPMC occurs at temperatures in the range of 60-65 ˚C (Bajwa et al., 2009). The phase separation is induced by associations between hydrophobic rich areas of the polymer chain. In solutions at low temperatures, the polymer is a random coil with few polymer-polymer interactions. The solute-solvent interactions protect the hydrated polymer molecules against agitation. However, upon increasing the temperature, polymer molecules lose their water hydration, and

polymer-polymer associations occur between the hydrophobic methyl side groups. This results in a macroscopic phase separation which is seen as the insolubility of the gel or polymer precipitate. This is accompanied by a rise in viscosity and a rapid increase in the dynamic storage modulus G' (Bajwa et al., 2009; Sarkar, 1979). The gelation effects on the droplets with low solid content experience an inward bending of the droplet at the left side of the airflow; however, the vacuole formation is not observed. This is strongly related to the gelation of the droplet which occurs after the bending of the droplet as can be seen in morphology time-series in Table 6.4. The gelation of the droplet gives sufficient strength to resist the vacuole formation. At higher solid content, although the droplet undergoes gelation, similar morphology evolution and final morphology are seen to that produced at 60 ˚C; surface deformations and buckled dried particles are produced.

The increase of air temperature to 140 ˚C and 180 ˚C resulted in a significant change in the surface/external morphology. For low and high solid content, no surface deformations were observed and smooth spherical particles were produced. The SEM micrographs of the final morphology, Figure 6.2 (E), (F), (G) & (H) clearly show that these particles have hollow internal morphology. The drastic change in external morphology as compared to low temperatures is thought to be related to two factors (a) rapid gelation and the influence of the air temperature on the strength of the gelled skin, and (b) higher internal pressure due to the vapour generated during boiling which acts as resistance force to the inward pressure gradient. Higher air temperature results in faster drying which causes the droplet to cross the phase boundary into a gelled region as it can be seen from the droplet drying trajectory superimposed on the phase diagram of HPMC in Figure 6.3. Drying at high temperatures also leads to boiling within the droplet as is evident from the droplet temperatures profile, presented in section 6.4 in Figure 6.4 (A) and Figure 6.5 (A), which show a clear boiling stage (the characteristic "step" during which the droplet is at constant temperature, close to the boiling point of water). During this boiling stage, an additional driving force is introduced due to the vapour pressure inside the droplet which resists the inward pressure gradient on the skin. This is very clearly seen in the case of 5% solid content and air temperatures of 140 ˚C, Table 6.4. The particle initially begins bending inwards at the left side of the airflow, but as the

droplet reaches boiling, the particle expands and regains a spherical shape. However, this pressure build-up within the drop is insufficient to overcome the elasticity of the skin. Unlike the inflation/deflation cycles observed during drying of sucrose and silicate presented in Chapter 4 & Chapter 5, boiling did not cause any inflation/deflation cycles when drying HPMC droplets above the boiling point. This is evident from the morphology time series in Table 6.4 as well as the diameter history of the droplet given in Figure 6.4. This is an indication of the skin strength to suppress any inflation and deflation cycles. This is attributed to the skin formation and its response to the pressure build-up: the droplet is not flexible enough to allow for inflation/deflation. However, in some cases, a bubble protrudes from the opposite side of airflow and ruptures at the opposite side of the airflow, the point of the skin with the lowest strength.
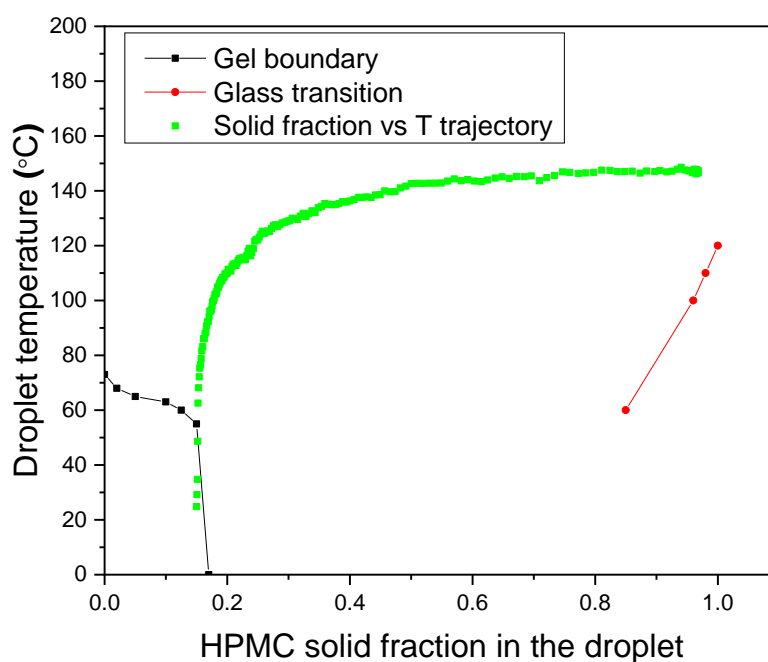
Figure 6.3 The drying trajectory, droplet solid fraction vs droplet temperature, superimposed on HPMC phase diagram. The drying trajectory data was collected from a single droplet of 15% w/w HPMC at 180 ˚C. Gel boundary, as well as the sol-gel boundary, were extracted from data given in Silva et al. (2008) and Bajwa et al. (2009). Glass transition boundary was extracted from Perfetti et al. (2011)

Thermal gelation properties such as gel strength, rate of gelation and gel point are hypothesised to play a key role in the morphology evolution and subsequently, the final structure. These properties are significantly influenced by air temperature and solid concentration. Higher temperatures leads to rapid gelation, which is thought

to give a stronger skin that can resist surface deformations. Sarkar (1995) conducted oscillatory shear mode rheology experiments for aqueous solutions of HPMC by raising the solution temperature as quickly as possible to the desired temperature and measuring the increase in the storage modulus as a function of time. From these experiments, the maximum rate of gelation and the final storage modulus of the gel, G'f, for methylcellulose were related to various parameters according to the following models:

$$\frac{dG'}{dt} = KC^{3.3}T^{4.0}(\%MeO)^{3.4}(M_w)^{0.5} \tag{6.1}$$

$$G'_f = KC^{2.9}T^{0.3}(\%MeO)^{6}(M_w)^{0.8} \tag{6.2}$$

Where

C, T, $(\%\mathrm{MeO})$, M_w are the concentration in wt% the temperature in ˚C, the methoxyl content and the molecular weight respectively.

Equation (6.1) shows that the rate of gelation is related to the fourth power of temperature and third power of concentration. This corresponds well with the timeline of gelation in the morphology time series shown in Table 6.4 and Table 6.5, which shows that gelation onset timeline becomes shorter with the increase in air temperature and initial solute concentration. Further quantitative data on the time of gelation is given in and is discussed further in section 6.4.1. The storage modulus of the gel is related to the third power of temperature, which is consistent with the lack of surface deformations with the increase in air temperature. Hydroxypropyl methylcellulose also exhibits similar gelation behaviour with G'f related to nearly the third power of concentration. This has also been reported in another study by Silva et al. (2008) where the absolute value of modulus becomes higher with increasing HPMC content as evident from the storage, loss and the complex viscosity modulus recorded at concentrations of 1%, 2% 5% and 10% in the temperature range of 20 ˚C to 90 ˚C. It can be concluded that the initial solid concentration, as well as the air temperature, plays a role in the skin formation, skin formation properties and the resistance of the droplet to surface deformations, high initial solid concentration and air temperatures is hypothesised to lead to a stronger skin which in turn resists the surface deformations particularly at high temperatures.

6.4 Drying kinetics

In this section, the drying kinetics, including normalised surface area, droplet temperature and evaporation flux are presented. These drying kinetics are interdependent, and therefore they are presented together in Figure 6.4 & Figure 6.5 for air temperatures in the range of 60 ˚C to 180 ˚C and initial solute concentrations of 5% and 15% w/w. The influence of the air temperature and initial solute concentration on the surface area, evaporation flux and droplet temperature history are discussed in detail with particular focus on the effect of air temperature and initial solute concentration on locking, gelation and boiling. Evaporation flux was determined from mass loss measurements recorded using the microbalance and diameter measurements calculated from the measured projected area from the images.

6.4.1 Particle locking

The normalised surface area, shown in Figure 6.4 (A), is significantly affected by the initial solute concentration and the air temperature. At low solid concentration, 5% w/w, Figure 6.4 (A) demonstrate that faster shrinkage is encountered with the increase in air temperature. On the other hand, at high initial solute concentration, 15% w/w, the increase of air temperature results in a significant reduction in the extent of shrinkage, Figure 6.5 (A). In this study, the time when the shrinkage ceases is defined as the locking time and occurs when the surface of the droplet possesses sufficient strength to counter shrinkage and freezes the surface area of the droplet. Continued evaporation post locking results in a pressure gradient on the skin, which can result in surface deformations. Locking can also be influenced by gelation which occurs when the droplet temperature exceeds gelation temperature, 60-65 ˚C (Bajwa et al., 2009). Gelation causes a rise in viscosity and a rapid increase in the dynamic storage modulus G' (Bajwa et al., 2009; Sarkar, 1979) and therefore influences the particle size and time at locking. Therefore, the time of locking, gelation onset and full gelation need to be investigated to reveal the effects of the air temperature and initial solute concentration. Locking time is determined based on the morphology time series as the start of the morphology development onset such as bending, surface deformations of the droplet (refer to morphology time

series in Table 6.4 and Table 6.5). The onset of gelation and full gelation are also based on the morphology time series as the time of the first appearance of clouding and time at which the whole droplet becomes fully cloudy respectively. To reduce error from random variation, the results of 3-5 drying runs were used in the determination of the time of locking and gelation.
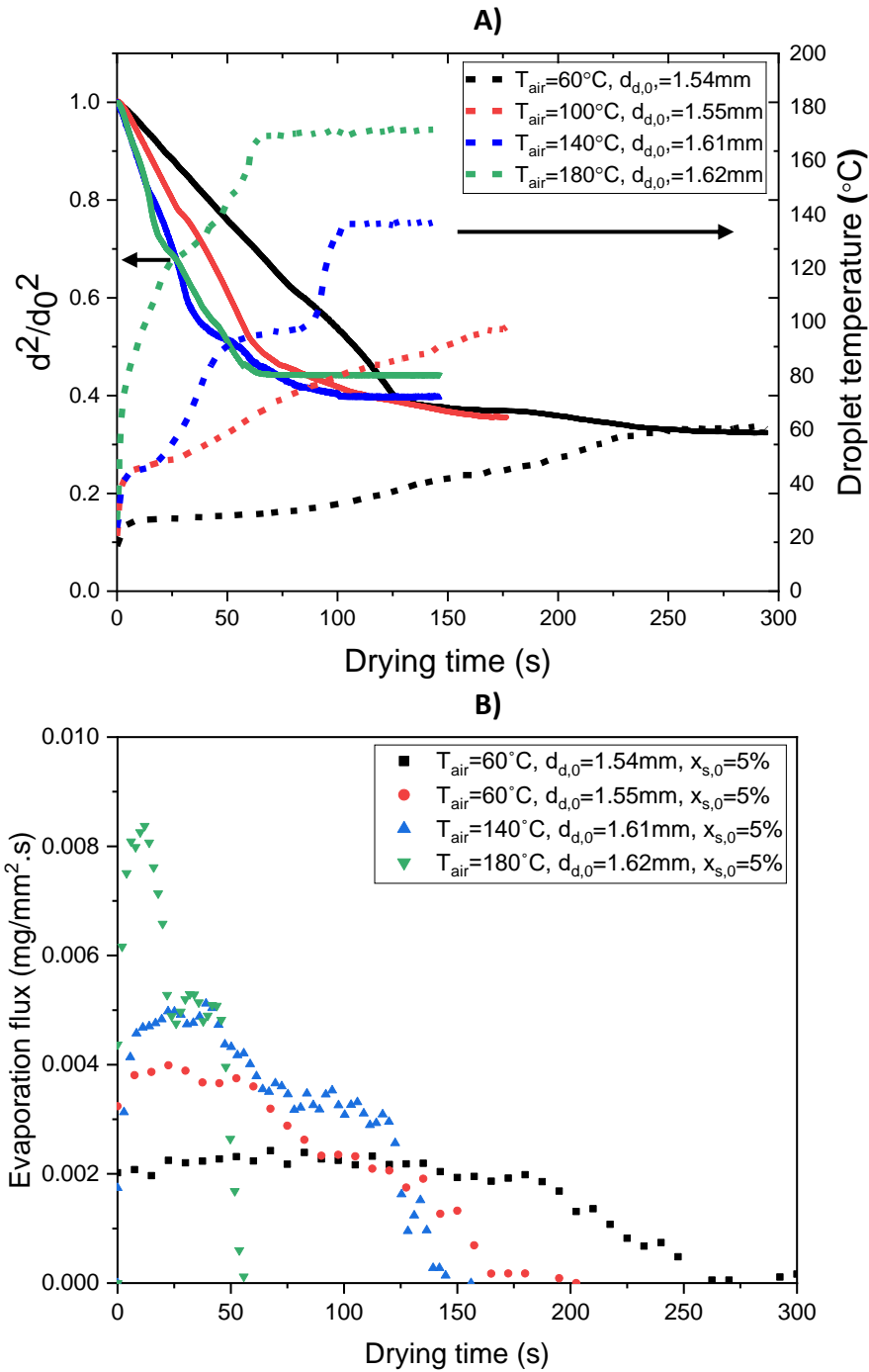
Figure 6.4 Drying kinetics measurements of HPMC at air temperatures of 60 ˚C, 100 ˚C, 140 ˚C and 180 ˚C and 5% initial concentration (A) Normalised surface area (solid line) and temperature history (dashed) (B) Evaporation flux versus drying time.
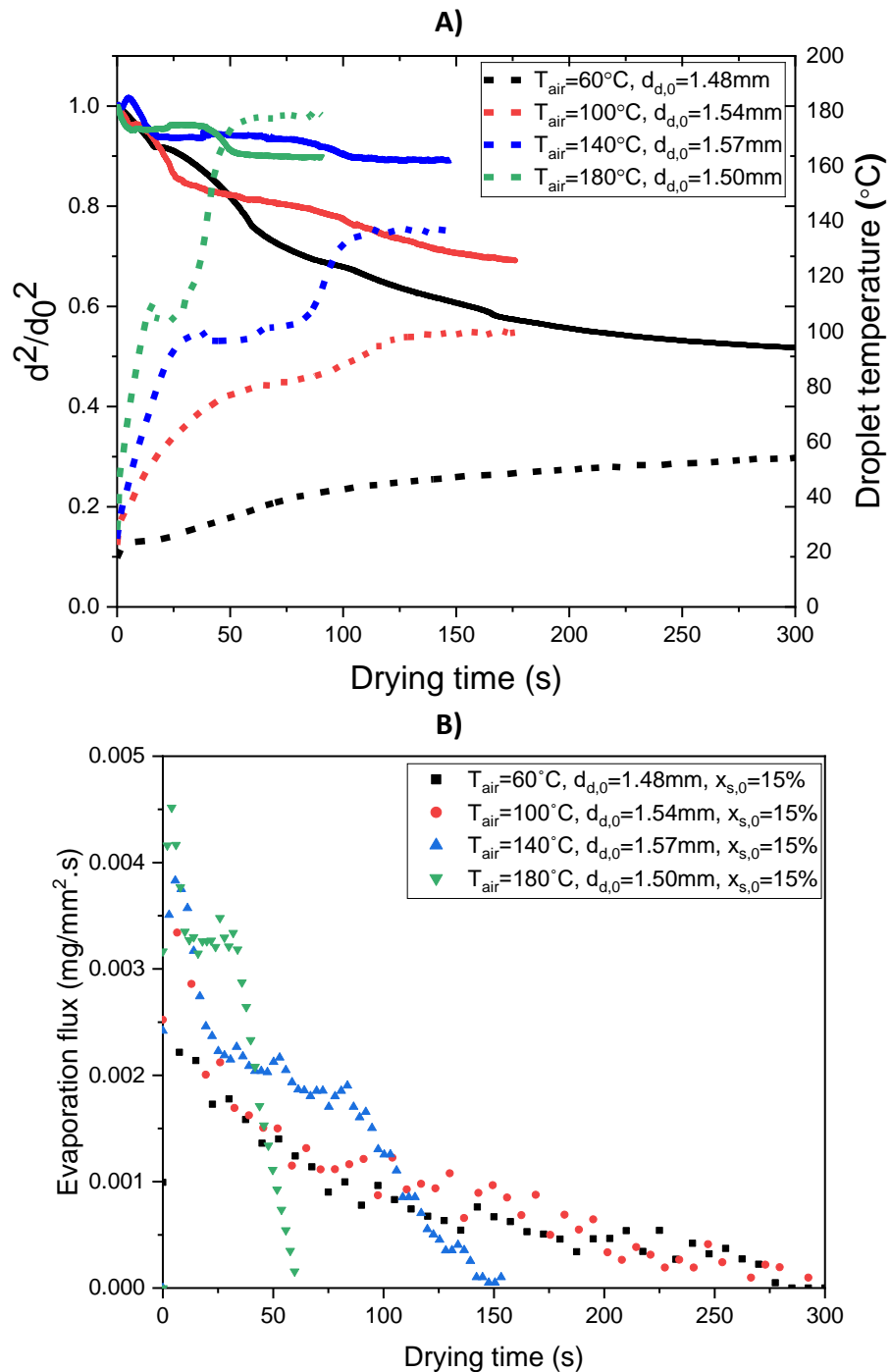
Figure 6.5 Drying kinetics measurements of HPMC at air temperatures of 60 ˚C, 100 ˚C, 140 ˚C and 180 ˚C and 15% initial concentration(A) Normalised surface area (solid line) and temperature history (dashed) (B) Evaporation flux versus drying time.

Figure 6.6 and Figure 6.7 show that the time and diameter at locking significantly decrease with the increase in air temperature. At air temperature of 60 °C, below the gelation temperature, locking occurs at small particle size compared with higher air temperatures. This can be related to the droplet temperature history. Figure 6.4 (A) shows that at air temperatures of 60 ˚C, the droplet displays an initial period of

constant rate drying at the wet-bulb temperature which corresponds to a relatively constant evaporation flux as demonstrated by the evaporation flux in Figure 6.4 (B). In this stage, the surface remains saturated with moisture, and the evaporation is controlled by the diffusion of water from the surface of the droplet to the air. This constant evaporation flux at the wet-bulb temperature allows the droplet to undergo shrinkage and hence locking occurs at smaller particle size. The point of the reduction of the evaporation flux corresponds with the increase of the droplet temperature beyond the wet-bulb temperature. The reasoning behind this late reduction in the evaporation flux is related to surface enrichment and explained in detail in parts 6.4.2 & 6.4.3. After locking, the particle is subjected to severe degree of bending and surface deformations, as shown by the morphology time series in Table 6.4 and Table 6.5. These deformations result in a reduction of the final particle size compared to the particle size at locking as demonstrated by Figure 6.7 which shows that at 60 ˚C air temperature, the final size of the dried particle is much lower than the size at locking for both 5% and 15% initial concentrations.

At air temperatures above the gelation temperature, the size of the dried particle and the size at locking depend on the relative timeline of gelation and locking. In the cases of drying of 5% w/w at 100 ˚C and 140 ˚C air temperatures and 15% w/w at 100 ˚C air temperature, it can be seen that locking precedes gelation which means skin formation occurred earlier than full gelation. The morphology time series in Table 6.4 (T_{air}=100 ˚C, drying time=51-60 seconds) and Table 6.5 (T_{air}=100 ˚C, drying time=27-29 seconds) show that the droplet locks and undergoes bending and deformations prior to gelation. This results in a smaller final particle size compared to that at locking. These differences in the timeline of locking and gelation can be understood by investigating the droplet temperature history of the droplet and the evaporation flux. For the droplet to undergo gelation, it must exceed gelation temperature, 60-65 ˚C (Bajwa et al., 2009). At 5% solid concentration and air temperatures of 100 ˚C and 140 ˚C, Figure 6.4 (A) shows that the droplet displays a constant drying stage at a wet-bulb temperature below gelation temperature. The increase of the air temperature above wet-bulb temperature corresponds to the reduction in evaporation flux, Figure 6.4 (B). The drying at the wet-bulb temperature results in delayed gelation and the droplet experiences shrinkage. This is due to a

137

lower rate of heating allowing the skin formation and deformations to occur prior to full gelation of the droplet.

The gelation time and locking occur simultaneously at early drying time in the case of 5% w/w at 180 °C and 15% at 140 °C and 180 °C. Locking occurs at large size of the droplet almost similar to the size of the initial droplet. This is due to the rapid rate of heating and the skipping of the constant drying stage at the wet-bulb temperature as shown from the droplet temperature history in Figure 6.4 (A) and Figure 6.5 (A). The skipping of the constant drying stage at the wet-bulb temperature corresponds to an instantaneous reduction of the evaporation flux at early drying time, as shown in Figure 6.4 (B) and Figure 6.5 (B). The increase in air temperature resulted in simultaneous full gelation and skin formation due to the rapid rate of heating. The size at locking is similar to the size of the final dried particle. This can be related to the rapid gelation which causes a sharp rise in viscosity and results in freezing the droplet surface and resisting any surface deformations. It is also related to boiling driven effects which also act as a resisting force to surface deformations and bending of the droplet.

Figure 6.4 (A) and Figure 6.5 (A) show that at both low and high solid concentrations, the normalised surface area remains unchanged during the boiling stage. This has been explained by the morphology time series which demonstrate that gelation precedes the boiling stage and thus the droplet enters the boiling stage at a gelled state. Gelation causes a rise in viscosity and a rapid increase in the dynamic storage modulus G' (Bajwa et al., 2009; Sarkar, 1979) and provides sufficient strength to suppress any effects of the vapour pressure on the surface area. In some cases, the droplet underwent a secondary bubble growth and rupture in the downstream side of the air stream, as shown in the morphology time series of 5% w/w at 180 °C in Table 6.4. This is caused by the direction of the airflow, which results in the lower modulus of the skin formed on the downstream side of the airflow due to lower local evaporation rate. Figure 6.7 shows that the final particle size is smaller than the initial droplet diameter for air all temperatures above boiling. Boiling fails to result in an increase of the droplet diameter above the diameter of locking or initial size of the droplet. This further demonstrates that the puffing behaviour which has been

reported in the previous chapter to cause an increase of the surface area is not observed for HPMC related to the formation of a skin with high elastic modulus.
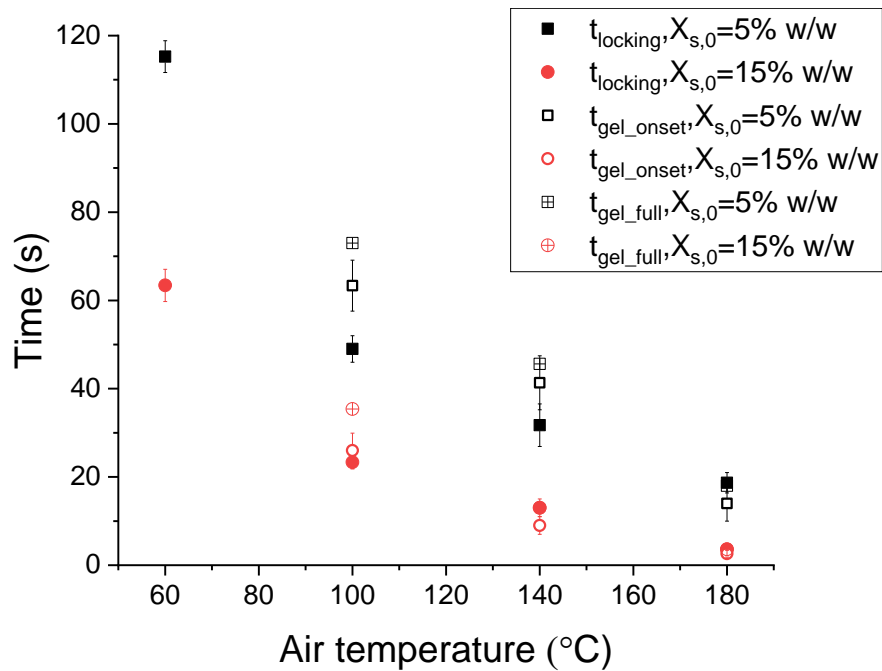
Figure 6.6 Time of locking (solid), gelation onset (open), full gelation (centre) as function of air temperature and initial solute concentrations of 5% w/w (square) and 15% w/w (circle). Error bars were calculated based on 5 replicates at each condition. Error bars are based on the standard deviation of the mean and represent ± 1 standard deviation.
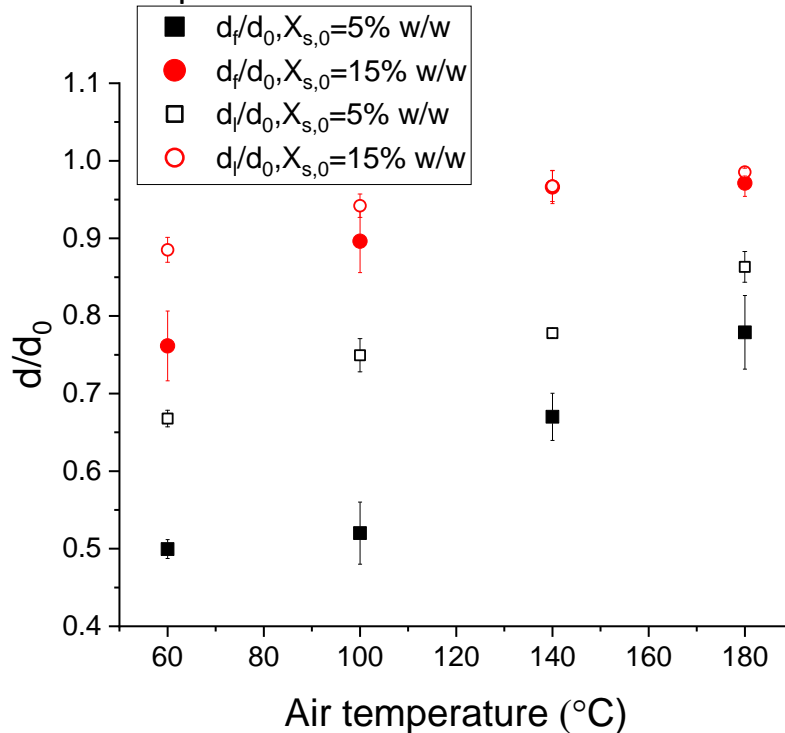
Figure 6.7 The relative size of the HPMC particles at locking (open) and the relative size of the final dried particles (solid) at v_{air}=0.57 m/s and different air temperatures. Error bars were calculated based on 5 replicates at each condition. Error bars are based on the standard deviation of the mean and represent ± 1 standard deviation.

6.4.2 Evaporation flux versus moisture content

The effect of the air temperature on the droplet temperature history, particularly on the length of the constant stage at the wet-bulb temperature, has been related to the reduction of the evaporation flux in the previous section. It was shown that a constant evaporation flux is obtained at the wet-bulb temperature and the reduction of the evaporation flux corresponds with the increase of the droplet temperature beyond the wet-bulb temperature. This is further investigated by the presentation of evaporation flux versus the moisture content presented in Figure 6.8 (A) & (B). Figure 6.8 (A) shows that drying at 60 °C results in a lower evaporation flux compared with higher air temperature which is maintained for a period of drying until it reduces later at lower mean moisture content. Lower evaporation rate delays solute surface enrichment and allows moisture transport to the surface of the droplet. With the increase in air temperature, the reduction in evaporation flux occurs at higher mean moisture content, Figure 6.8 (A), and thus the increase in droplet temperature beyond wet-bulb temperature occurs at an early drying time. This is due to the increase in the evaporation rate which results in early solute surface enrichment and the decrease of moisture transport to the surface. This is clearly shown at 180 °C air temperature where the reduction in evaporation flux occurs instantly at a mean moisture content close to the initial moisture content. The evaporation flux is very high resulting in an instantaneous solute surface enrichment and a reduction of moisture transport to the surface of the droplet. At high solid concentration, the droplet temperature profile presented in the previous section in Figure 6.5 (A) shows that the constant stage is only encountered briefly at 60 °C air temperature and drying at higher air temperatures resulted in skipping the constant drying stage at the wet-bulb temperature. This is strongly related to an instantaneous early reduction in the evaporation flux at high moisture content as shown in Figure 6.8 (B). This occurs because the high evaporation flux encountered at these air temperatures resulted in early solute surface enrichment and a reduction of the moisture transport to the surface. This theory of surface enrichment is investigated further by the determination of the Péclet number.
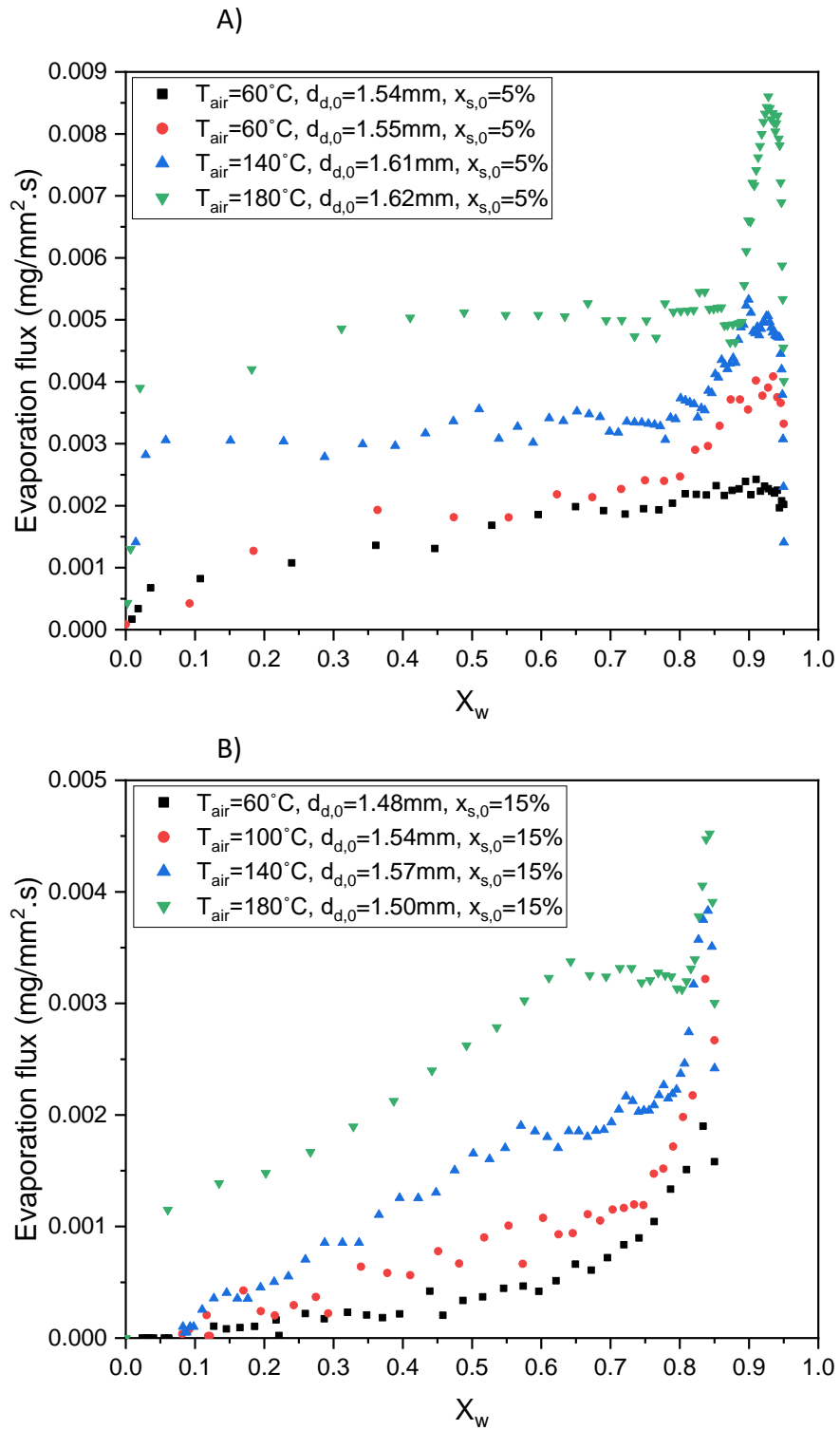
Figure 6.8 The evaporation flux vs the moisture fraction at different air temperatures and at (A) 5% initial solute concentration (B) 15% w/w initial solute concentration

6.4.3 Determination of the Péclet number

The relationship between air temperature, solute concentration and the constant drying stage at the wet-bulb temperature can be explored further by the determination of the Péclet number. The Péclet number gives the ratio of the evaporation rate to the diffusion motion of the solute. A Péclet number higher than 1 indicates a degree of solute surface enrichment (Vehring et al., 2007). The diffusion coefficient of the HPMC is not available from the literature. Therefore, an estimation is made using the Stokes-Einstein equation as follows:

$$D = \frac{k_B T}{6\pi\eta r_H}$$
(6.3)

where,

k_B is the Boltzmann's constant

T is the absolute temperature

η is the viscosity of the solvent

r_H is the hydrodynamic radius of the solute

The hydrodynamic radius, r_H, is measured to be 60 nm using dynamic light scattering (Bodvik et al., 2012). The diffusion coefficient of HPMC is calculated using the Stokes-Einstein equation at the wet-bulb temperature to be 4.6×10^{-12} m^2/s. It should be noted that the Stokes-Einstein equation fails to account for the effect of the increased solute concentration on the diffusion coefficient. Therefore, the value of the diffusion coefficient from Stokes-Einstein, 4.6×10^{-12} m^2/s, is used for the calculations of Péclet number at 5% w/w and 15% w/w initial solute concentrations. The Péclet number is determined using the evaporation rate in the initial stage of drying based on the diameter measurements shown in Figure 6.4 (A) and Figure 6.5 (A).
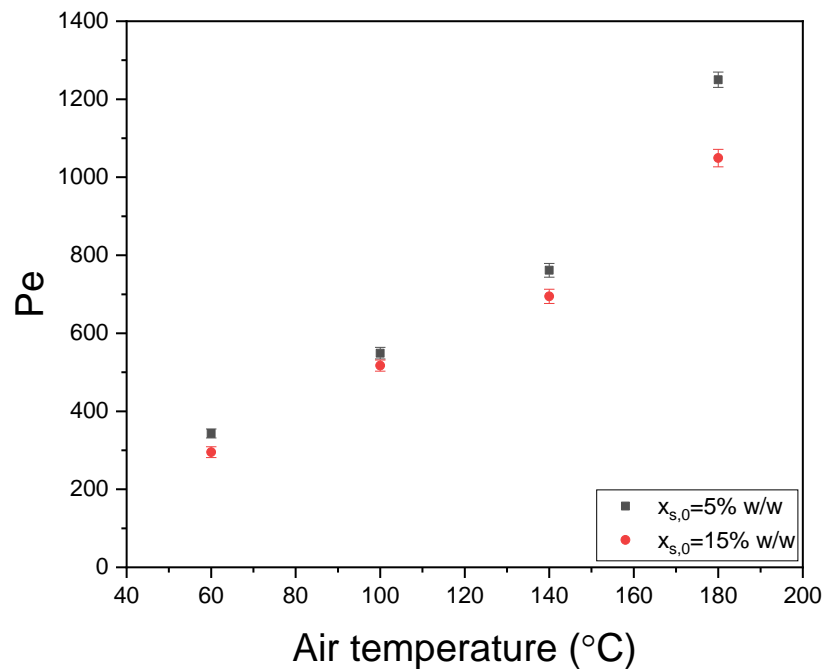
Figure 6.9 Péclet **number determined using the initial evaporation rate at different air temperatures and 5%w/w and 15% w/w initial solute concentrations. Error bars were calculated based on 5 replicates at each condition. Error bars are based on the standard deviation of the mean and represent ± 1 standard deviation.**

Figure 6.9 shows that the Péclet number is significantly higher than 1 for all air temperatures and initial solute concentrations, suggesting solute surface enrichment. It is also clear that the Péclet number increases with the air temperature due to the increase in the evaporation rate. The Péclet number is also lower at higher solute concentration. This is due to the use of the same diffusion coefficient for the calculations of the Péclet number. At 15% initial solute concentration, the diffusion coefficient is likely to be much lower than that determined using the Stokes-Einstein equation. Therefore, it is expected that the Péclet number at 15% solid concentration to be much higher than that calculated in Figure 6.9 should accurate measurements of the diffusion coefficient be used. Nonetheless, the Péclet number values shown in Figure 6.9 suggest a high degree of surface enrichment, which increases with the increase in air temperature. This solute surface enrichment reduces the moisture transport to the surface and thus results in an early reduction in evaporation flux and reducing the timeline of the initial drying stage in agreement with the temperature and evaporation flux profiles. The theory of solute surface

enrichment is also supported by the mean moisture content at the moment of locking, shown in Figure 6.10.
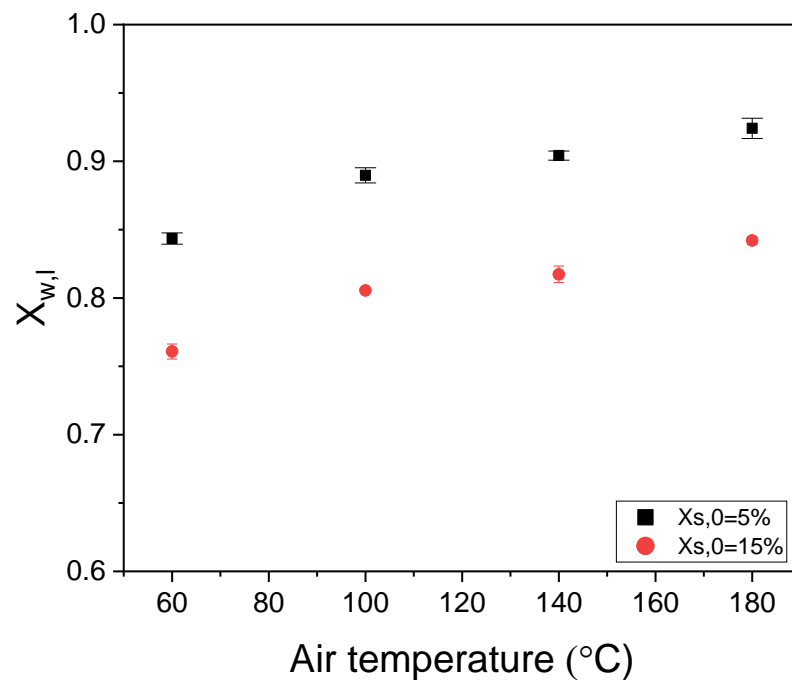
Figure 6.10 The water fraction of the particle at the moment of locking at v_{air}=0.57 m/s and different air temperatures. Error bars are based on 3-5 repeats at each condition. Error bars were calculated based on 5 replicates at each condition. Error bars are based on the standard deviation of the mean and represent ± 1 standard deviation.

Figure 6.10 shows that mean moisture content at locking increases with the increase in air temperature at the same initial solid content. The increase of the mean moisture content at locking with the increase in air temperature is due to the increase of evaporation rate which in turns results in early solute surface enrichment as explained by the Péclet number calculations shown in Figure 6.9. At 180 ˚C air temperatures, locking occurs at very high moisture content, close to the initial moisture content. This is because, with the increase in air temperature, the solute surface concentration at the surface increases more rapidly which results in a reduction in surface moisture saturation and rapid increase in droplet temperature exceeding gelation temperature. It must be emphasised that this study gives the average water content, whereas locking is mainly influenced by the water content at the surface rather than the average water content. Although it would be extremely useful to measure the water concentration at the surface, it is not possible with the

current set-up of the drying apparatus, and the author is unaware of any previous studies in the literature where such measurements have been conducted.

6.5 Final morphologies single droplet drying vs spray drying

A)

B)

C)

D)
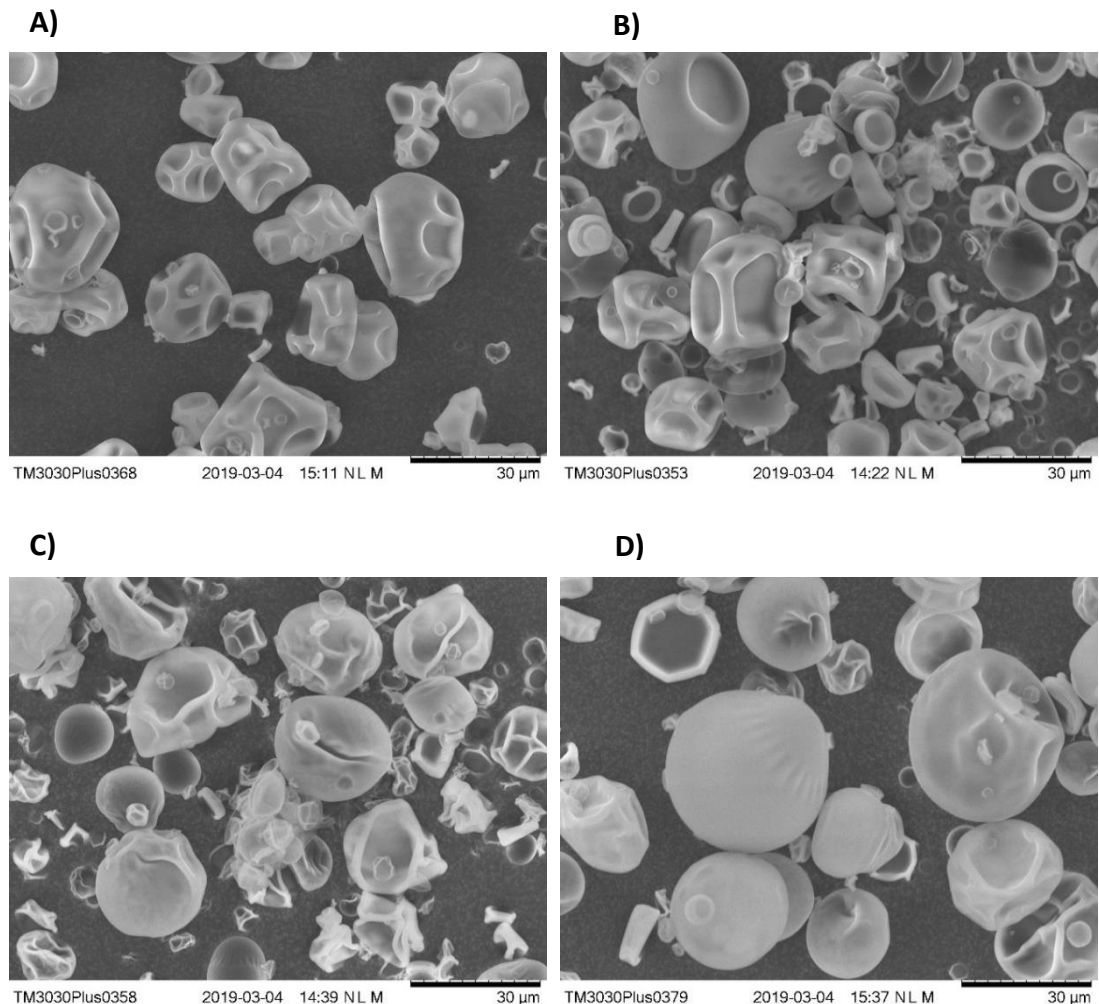
Figure 6.11 SEM pictures of spray-dried HPMC particles (5% w/w, T_{inlet}=100˚C, $T_{chamberout}$=60 ˚C (B) 15% w/w, T_{inlet}=100˚C, $T_{chamberout}$=60 ˚C (C) 5% w/w, T_{inlet}=200˚C, $T_{chamberout}$=130 ˚C (D) 15% w/w, T_{inlet}=200˚C, $T_{chamberout}$=130 ˚C.

The morphologies collected from the lab-scale spray dryer are shown in Figure 6.11. Details on the spray drying conditions have been presented in Table 6.3. At low air temperatures, the morphologies collected from spray drying show particles with buckled morphologies and deformed surfaces at high and low solid content. This is highly similar to the particles collected from the single droplet drying rig shown in Figure 6.2. At high air temperatures, the morphologies collected from spray drying show deformed particles as well as spherical particles with smooth surfaces. The

145

different types of structures are due to the different drying trajectories the droplets encounter in the spray dryer. The particles with smooth surfaces are similar to the ones seen in the single droplet drying rig, and the mechanism behind this formation has been related to rapid gelation and boiling effects as explained in Part 6.3. Overall, particles collected from the spray drying show high similarities to the particles collected from the single droplet drying rig. This shows that regardless of the droplet generation system and the scale, similar drying mechanism are observed in the spray dryer which proves the usefulness of the single droplet drying technique described in this work, to closely investigate the mechanisms governing the morphology evolution and the formation of the final structures.

6.6 Conclusion

This chapter has investigated the influence of the air temperature and initial solid content on the drying behaviour and final morphology of hydroxypropyl methylcellulose. It has highlighted the significant influence of heat-induced gelation on locking, evaporation rate and ultimately the final size as well as the external and internal structure of the final dried particles. Drying at temperatures above the gelation temperature resulted in heat-induced gelation which caused a sharp rise in the viscosity of the particle and thus resulted in a low extent of shrinkage and locking at an early drying time. This effect was more pronounced at higher solid content. The strength of the skin was also influenced by the air temperature, which is evident from the morphology evolution time series. Droplets dried at low air temperatures resulted in the formation of a weak skin that endured deformations. The deformations were related to continued solvent evaporation after skin formation which creates a lower pressure under the skin, thus exerting stress on the skin, which eventually results in bending and deformations. At high air temperatures, rapid gelation at the start of drying is thought to result in the formation of a stronger gelled skin which resisted the deformations and spherical particles with smooth surfaces were produced. It was also hypothesised that the vapour pressure associated with boiling plays a role in altering the internal and external pressure differences on the particle surface and thus causing expansion and inhibition of surface deformations.

146

The normalised surface area remains unchanged during the boiling stage and boiling driven effects caused no inflation or deflation of the droplet. This has been explained by the morphology time series which demonstrate that gelation precedes the boiling stage and thus the droplet enters the boiling stage at a gelled state. This gelation causes a rise in the viscosity and the dynamic storage modulus G' of the skin (Bajwa et al., 2009; Sarkar, 1979) and provides sufficient strength to suppress any effects of the vapour pressure on the surface area. The behaviour of HPMC above boiling is different from that demonstrated by sucrose and silicate, which exhibited inflation/deflation cycles. Drying of HPMC resulted in skin formation and heat-induced gelation which suppressed boiling driven effects. The differences in behaviour highlight the role of the evolution of material properties on the morphology behaviour, particularly above boiling.

The significant influence of the skin properties on the final structure offers an opportunity to manipulate the properties of the skin, for example by the use of plasticisers, to influence the morphology evolution and ultimately the structure of the final dried particles.

The structures produced from the single droplet drying showed high similarities with structures produced from spray drying, which proves the usefulness of the single droplet drying technique to understand the drying mechanisms resulting in certain morphologies.

Chapter 7 Drying behaviour of HPMC – water-acetone system

7.1 Introduction

Extensive work on the drying of aqueous HPMC droplets in the previous chapter has demonstrated that the morphology evolution, as well as the drying behaviour, is dominated by the skin formation and its elastic properties which is enhanced by heat-induced gelation. Drying at lower air temperatures resulted in buckled morphologies due to skin formation followed by continued solvent evaporation. The deformations were related to continued solvent evaporation after skin formation, which creates a lower pressure under the skin, thus exerting stress on the skin and eventually results in bending and deformations. At high air temperatures (140 °C and 180 °C), rapid gelation at the start of drying is thought to result in the formation of a stronger gelled skin which resisted the deformations and spherical particles with a smooth surface were produced. However, the properties of the gelled skin prevented any effects of boiling on the expansion of the droplet surface area. One of the objectives of this thesis was to explore the link of the drying behaviour and morphology evolution to the material properties, particularly at high temperatures. The morphological development studies conducted on materials with skin forming properties including polymers (Pauchard and Allain, 2003c), proteins (Bouman et al., 2016; Both et al., 2018b; Sadek et al., 2015) were conducted at low air temperatures. Therefore, this chapter investigates the potential of manipulating the skin properties to change the structure of the final dried particles and the morphology evolution during boiling. This is done by the addition of acetone which influences the drying kinetics including the boiling point as well as the mechanical properties and rheological properties of HPMC. Therefore, an investigation at a wide range of conditions, mainly air temperature, is required.

The first part of this chapter includes an investigation of the effects of the addition of acetone on the morphology evolution, particularly focusing on the response of the skin to the subsequent drying. The effect on the final morphology is also investigated by characterisation of the final dried particles using SEM. The morphological developments are compared to the morphological developments encountered during drying of aqueous HPMC droplets and other materials with skin forming properties established in the literature. The second part of this chapter

investigates the effects of the addition of acetone on the drying kinetics with an emphasis on the effect of boiling. Finally, the drying metrics, including the final size and size at locking, are investigated with a focus on the effect of air temperature and initial solute concentration.

7.2 Experimental work

HPMC is insoluble in acetone; therefore, this required the use of a mixture of acetone and water to increase HPMC solubility. In this study, a mixture containing 70 w/w acetone and 30% w/w water was used to prepare HPMC solutions at concentrations of 5% and 15% w/w. Pharmacoat 603 powder was used as the solute in the solutions. Specifications of Pharmacoat 603 has been described in 6.2.1. The solutions were left overnight on a magnetic stirrer, and the beakers were fully enclosed to ensure no evaporation of acetone. The single droplet drying apparatus described in Chapter 3 was used to conduct single droplet drying experiments at the conditions summarised in Table 7.1. The final dried particles collected from single droplet drying experiments were also characterised using SEM.

Table 7.1 Single droplet drying conditions used to dry HPMC-acetone-water solutions
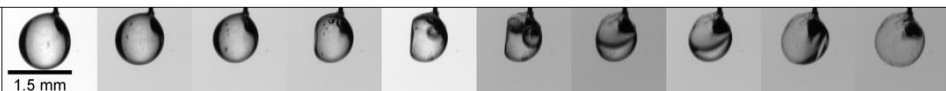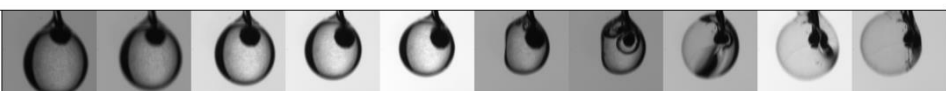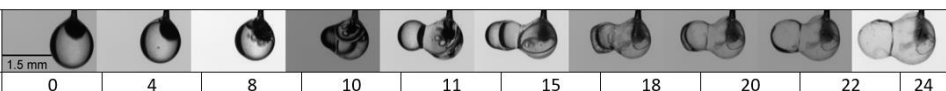
Parameter	Setting
Air temperatures	60 ˚C, 100 ˚C, 140 ˚C, 180 ˚C
Initial solute concentrations	5%, 15% w/w
Air velocity	0.57 m/s
Droplet size	1.4- 2 mm
Solvent mixture	(70 % w/w Acetone, 30% w/w water)

7.3 Results
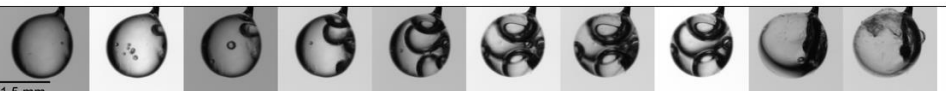
In this results section, first, the morphology evolution and the morphology of dried particles are presented, and the effect of air temperature and solute concentration is discussed. Typical morphology behaviour is selected based on 3-5 experimental repeats. The morphology development time series are used to investigate closely the effect of skin formation on the subsequent drying below and above boiling. The drying kinetics are then presented and related to the morphology development. The drying kinetics are used to investigate closely the effect of skin formation and boiling on the evaporation flux.

7.3.1 Morphology evolution during drying

Table 7.2: Morphology development of single droplets containing 5% w/w HPMC in a mixture of acetone and water with weight percentages of 70% w/w and 30% w/w respectively at v_{air} =0.57 m/s and different air temperatures. The direction of airflow is from right to left. [7]

T_{air}=60°C										
t(s)	0	11	29	34	39	50	58	67	81	129
T_d (°C)	5	26	35	37	39	42	44	45	48	61

T_{air}=100°C										
t(s)	0	4	10	14	19	26	33	36	42	54
T_d (°C)	35	48	59	63	69	75	84	85	87	105

T_{air}=140°C										
t(s)	0	7	13	20	23	30	35	42	47	54
T_d (°C)	9	46	62	71	75	71	89	122	135	136

T_{air}=180°C										
t(s)	0	4	8	10	11	15	18	20	22	24
T_d (°C)	14	62	85	88	92	125	167	176	177	177

Table 7.3: Morphology development of single droplets containing 15% w/w HPMC in a mixture of acetone and water with weight percentages of 70% w/w and 30% w/w respectively at v_{air}=0.57 m/s and different air temperatures.[8]

T_{air}=60°C										
t(s)	0	4	8	12	15	22	32	47	65	122
T_d (°C)	16	32	39	42	44	46	49	51	54	60

T_{air}=100°C										
t (s)	0	7	13	16	22	30	37	42	51	68
T_d (°C)	17	57	64	66	69	72	73	75	76	102

T_{air}=140°C										
t(s)	0	6	9	10	11	14	21	27	36	44
T_d (°C)	21	71	74	75	77	79	98	112	137	138

T_{air}=180°C										
t(s)	0	5	6	7	12	13	14	19	21	30
T_d (°C)	21	78	82	85	101	106	111	134	148	175

---

[7] A larger size replica table with better image quality is provided in Table E.7 (Appendix E)

[8] A larger size replica table with better image quality is provided in Table E.8 (Appendix E)
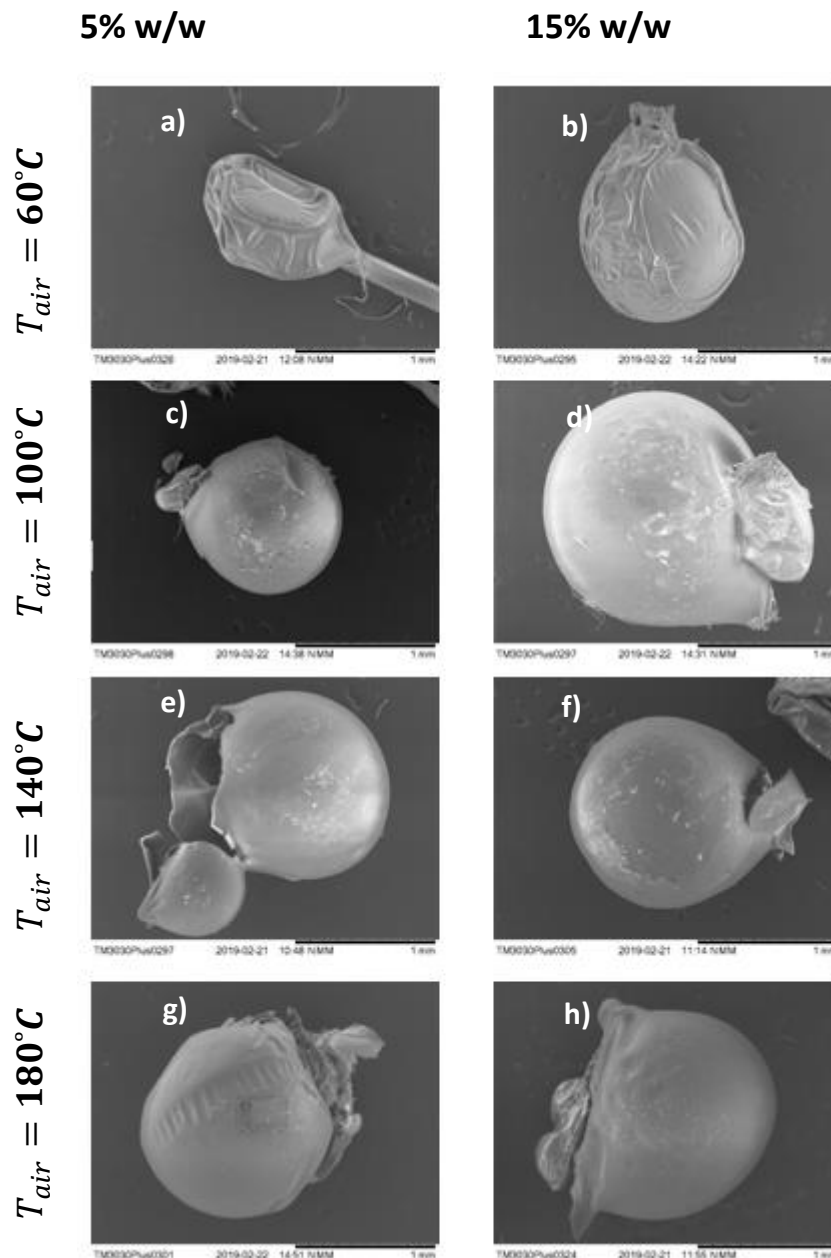
Figure 7.1 Morphology of the final dried HPMC particles collected from the single droplet drying experiments at different temperatures (a) 5% w/w, T_{air}=60 ˚C (b) 15% w/w, T_{air}=60 ˚C (c) 5% w/w, T_{air}=100 ˚C (d) 15% w/w, T_{air}=100 ˚C (e) 5% w/w, T_{air}=140 ˚C (f) 15% w/w, T_{air}=140 ˚C (g) 5% w/w, T_{air}=180 ˚C (h) 15% w/w, T_{air}=180 ˚C.

The morphology time series in Table 7.2 and Table 7.3 show that at air temperature below boiling, 60 ˚C, the droplet goes through a shrinkage period where the droplet decreases in size without enduring any surface deformations. At the end of this period, the droplet undergoes bending on the downstream side of the droplet followed by some deformations on the surface of the particle. The bending of the droplet on the downstream side of the airflow is attributed to the weak skin caused

by lower local evaporation. The SEM micrographs, shown in Figure 7.1, demonstrate that the particles collected at 60 ˚C air temperature show surface deformations. The deformations can be attributed to continued solvent evaporation after skin formation, which creates a lower pressure under the skin, thus exerting a stress on the skin (Arai and Doi, 2012). At higher initial solid concentration, 15% w/w, it can be seen that shrinkage ceases early on during drying (refer to Table 7.3, 60 ˚C air temperature). This is due to the early skin formation which is enhanced by the increase in solute content. Deformations of drying of materials with skin forming properties are expected and have been demonstrated during drying of polymers (Pauchard and Allain, 2003c) and proteins (Both et al., 2018b). The deformations are also similar to the case of drying of aqueous HPMC droplets at air temperatures of 60 ˚C and 100 ˚C presented in Chapter 6 in Table 6.4 and Table 6.5.
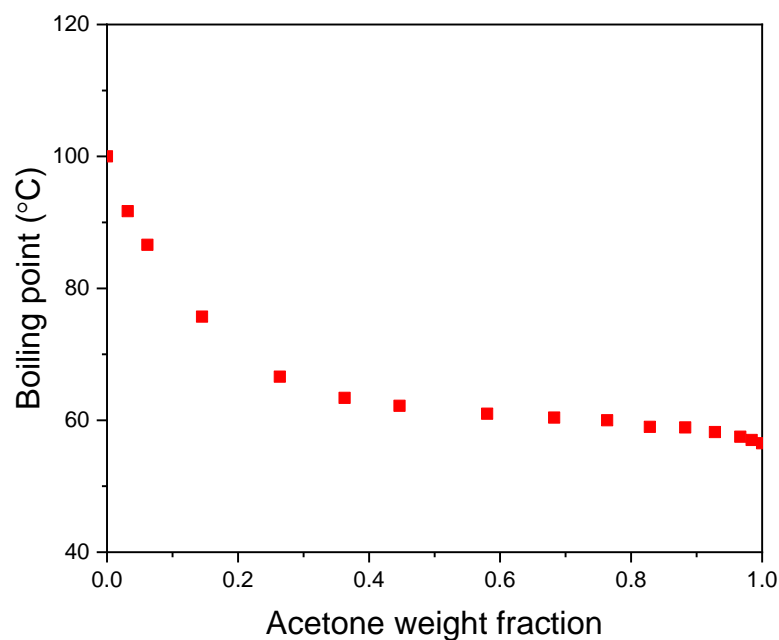
Figure 7.2 Boiling point of acetone/water mixture as a function of acetone weight fraction (Thomas and McAllister, 1957)

Drying at air temperatures of 100 ˚C, 140 ˚C and 180 ˚C is above the boiling point of the 70/30 % w/w acetone/water mixture used in this study. This is evident from the boiling point of the mixtures of acetone/water shown in Figure 7.2. The mixture used in this study involved weight percentages of 70%/30% w/w of acetone and water respectively, which corresponds to a boiling point of 62 ˚C. The boiling point is expected to increase with the addition of HPMC solute. Table 7.2 and Table 7.3

demonstrate that drying at air temperatures of 100 ˚C, 140 ˚C and 180 ˚C results in boiling, which aids in resisting the deformation of the skin. The vapour pressure due to boiling introduces a new factor force on the skin where it resists the pressure difference acting on the skin. This is clearly shown in Table 7.2 at 100 ˚C and 140 ˚C air temperatures where the bending of the droplet on the downstream of the droplet occurs at times from 14-19 s and 13-19 s for 100 ˚C and 140 ˚C respectively. Once the droplet reaches boiling, the vapour pressure resists these deformations applied on the skin. The droplet also shows an inflation corresponding to the boiling stage. The nature of the inflation included a sustained increase in the surface area without any noticeable deflation cycles (refer to Table 7.2). Homogenous inflation of the droplet is observed at 100 ˚C and 140 ˚C at 5% w/w and 100 ˚C at 15% w/w (Table 7.3). The ability of the vapour pressure to force expansion of the skin indicates the skin has a plasticised nature with weakened mechanical properties. Table 7.2 and Table 7.3 also demonstrate that at 5% w/w at 180 ˚C and 15% w/w at 140 ˚C and 180 ˚C, the droplet undergoes a very significant partial inflation in the direction of airflow. This is due to the nature the heterogeneous skin layer formed on the droplet surface caused by the direction of airflow. The upstream side of the droplet forms a skin instantly with stronger mechanical properties due to higher degree of evaporation. On the other hand, the skin formed on the downstream of the droplet is weakened with lower modulus, and therefore the droplet expands in the direction with the least resistance. The SEM micrographs, Figure 7.1, demonstrate that dried particles above boiling possess puffed hollow structures with smooth appearance.

The expansion and inflation of the droplet in the case of drying HPMC using acetone and water mixture as a solvent is different from the behaviour observed when drying aqueous HPMC droplets. Drying of aqueous HPMC droplets results in the formation of skin with higher elastic modulus, which suppressed the effect of the boiling and thus had insignificant influence on the surface area during boiling. The contrast in behaviour is due to the role of acetone in changing the mechanical properties of HPMC. Previous studies have reported that plasticisers including glycerol and Polyethylene glycol (PEG) (Aulton et al., 1981) and Sorbitol (Somashekarappa et al., 2013) result in a breakdown of the HPMC polymer network which in turn causes the increase in the elongation and decrease in the tensile strength and modulus of

elasticity of dried HPMC films. It is expected that acetone results in similar mechanical changes to the properties of the HPMC which explains the occurrence of inflation. Furthermore, a vital effect of the addition of acetone is the prevention of sol-gel transition which was reported in the drying of aqueous HPMC droplets. The morphology time series, Table 7.2 and Table 7.3, show no cloudiness which demonstrates the prevention of sol-gel transition. This is a direct influence of acetone which prevents gelation when added in considerable quantities (30%) into HPMC (Heymann, 1935). Boiling driven effects on the drying kinetics including droplet temperature profile and evaporation flux are further investigated in the next section

7.3.2 Drying kinetics

The measurements of the drying kinetics of solutions made with organic solvents are more challenging than the drying of aqueous solutions. Repeatability is much harder to obtain due to the fast nature of evaporation, the difficulty of droplet handling, error arising from evaporation before turning the airflow. Furthermore, at air temperature above boiling, the droplet enters the boiling stage and extent of inflation is highly stochastic. Therefore, repeats of individual droplet drying runs at the same conditions are presented rather than averages. Although several errors arise from the use of solvents, this study is very useful in highlighting the potential of manipulating the skin mechanical and rheological properties to alter the final structure of the dried particles as well as the drying behaviour above boiling. It should be noted that the diameter, mass measurements presented in this chapter are taken from the same run using PEEK filament. Temperature measurements are taken from a separate run with a type K thermocouple.

This section focuses on the relation between the drying kinetics, particularly surface area, droplet temperature and evaporation flux. The drying kinetics are related to the morphological developments presented in the previous section to highlight the influence of skin formation and boiling on the droplet surface area and evaporation flux. The drying kinetics are divided into two parts; drying kinetics below boiling at 60 ˚C air temperature and drying kinetics above boiling at air temperatures of 100 ˚C, 140 ˚C, 180 ˚C.

7.3.2.1 Drying kinetics below boiling

5% w/w   **15% w/w**

Figure 7.3 Normalised surface area, normalised mass, evaporation flux and droplet temperature vs drying time at 60˚C air temperature with 5% and 15% w/w initial solute concentrations[9].

The temperature profiles, shown in Figure 7.3, clearly demonstrate that the droplets skip the constant rate drying stage at the wet-bulb temperature at both 5% and 15%

---

[9] Diameter, mass and evaporation flux are taken from the same run whilst temperature measurements are taken from a separate run with type K thermocouple.

w/w initial solid content. This shows disagreement with temperature profiles expected and established in the literature in studies by Nešić and Vodnik (1991). It is also in contrast with the case of drying of aqueous HPMC droplets at 60 ˚C air temperature, presented in Chapter 6, which resulted in drying at the wet-bulb temperature. The skipping of the wet-bulb temperature can be explained by the high initial evaporation flux, Figure 7.3, caused by the preferential evaporation of acetone due to its high volatility compared with water. The high evaporation flux results in early surface enrichment and hindering of moisture transport to the surface. The large hydrodynamic radius of the HPMC molecule, 60 nm (Bodvik et al., 2012), also indicates slow diffusion of the solute and hence enhances early surface enrichment. The temperature profiles also show no boiling stage was observed as the drying air temperature of 60 ˚C is below the droplet boiling point.

The high evaporation flux encountered in the initial stage in the drying of 5% w/w, Figure 7.3, corresponds to the initial linear decrease in the normalised surface area plot due to shrinkage of the droplet. Once the linear shrinkage period ceases, it is followed by partial bending from the downstream side of the airflow. This is evident from the morphology time series given in Table 7.2 (T_{air}=60˚C and drying time= 81 seconds). The surface area plot demonstrates that the extent of shrinkage at 15% w/w initial solute concentration is less than at lower solid concentration (5%). This is expected and is due to the formation of the skin layer at earlier drying time at higher solute concentrations, which resists shrinkage. The normalised surface after skin formation exhibit differences at the same drying conditions due to the nature of the deformations and the bending of the droplet surface. The timeline of these deformations corresponds to a reduction in the evaporation flux as the formation of the skin hinders the moisture transport to the surface of the droplet. In conclusion, the morphology, as well as the drying kinetics, show a high similarity to that encountered in the case of drying aqueous HPMC and similar polymer systems in the literature (Pauchard and Allain, 2003c); the shrinkage is hindered by the skin formation which results in surface deformations and bending. The disagreement in the droplet temperature profile, skipping of drying at the wet-bulb temperature, has been attributed to high initial evaporation flux due to preferential evaporation of acetone.

7.3.2.2 Drying kinetics above boiling

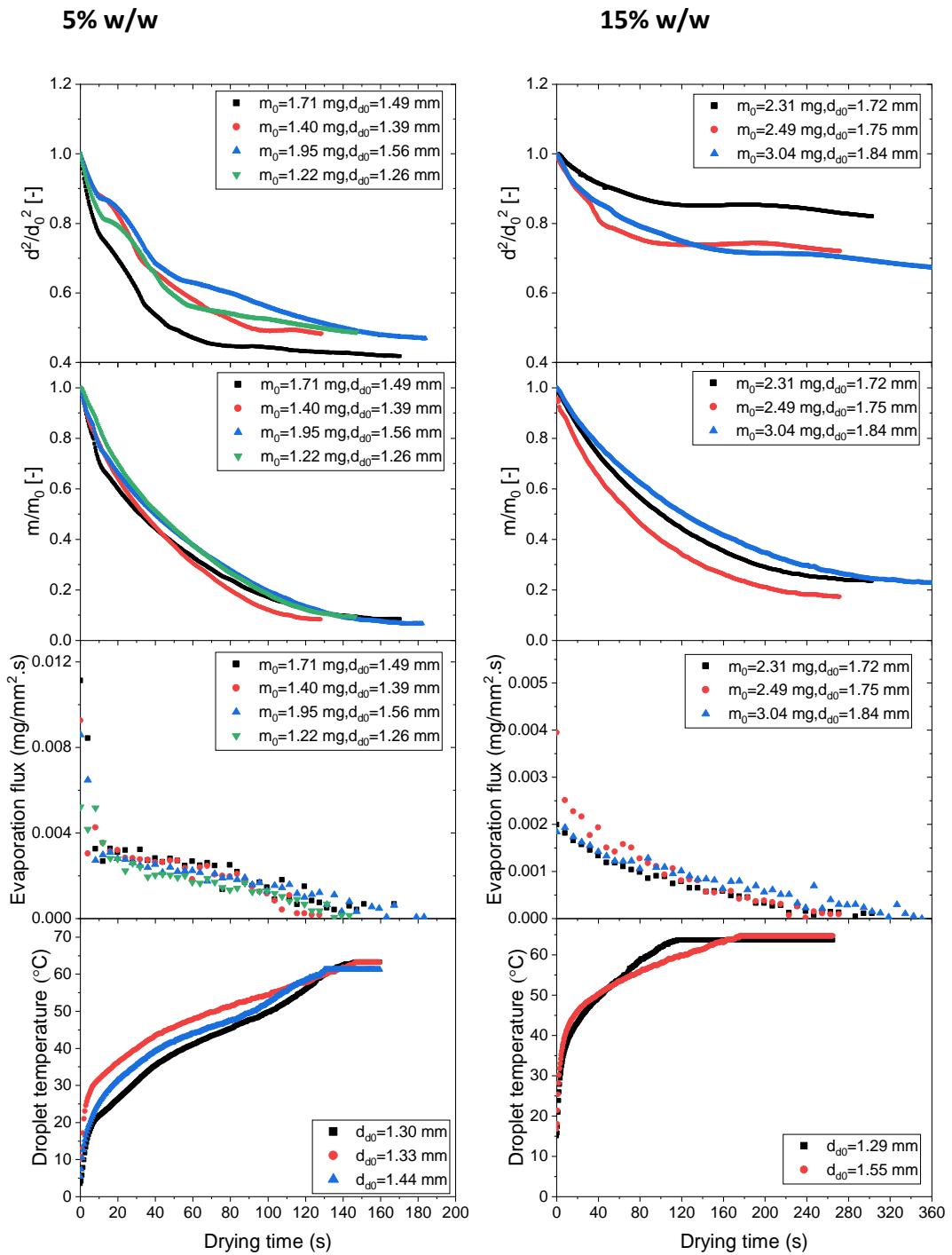**5% w/w**   **15% w/w**
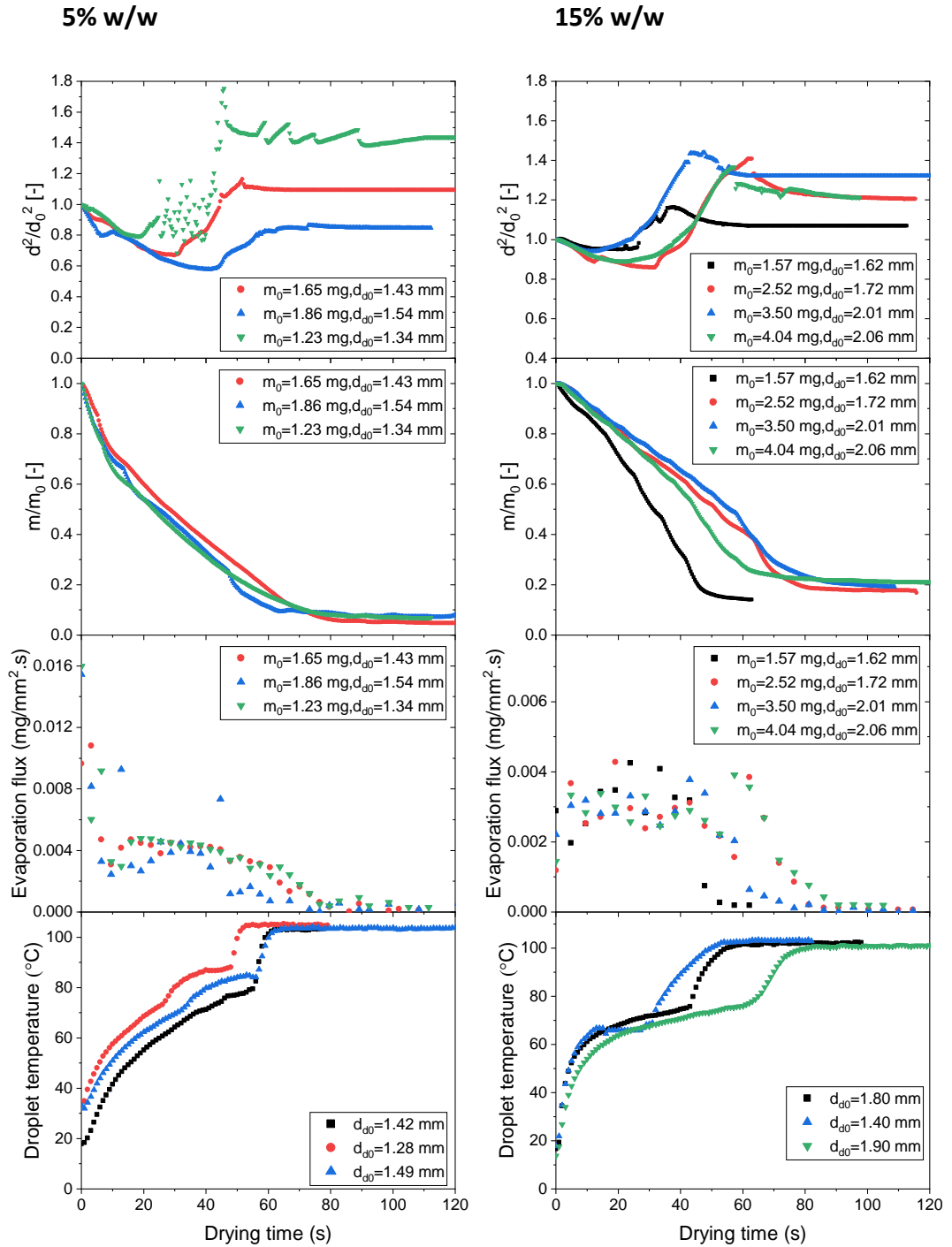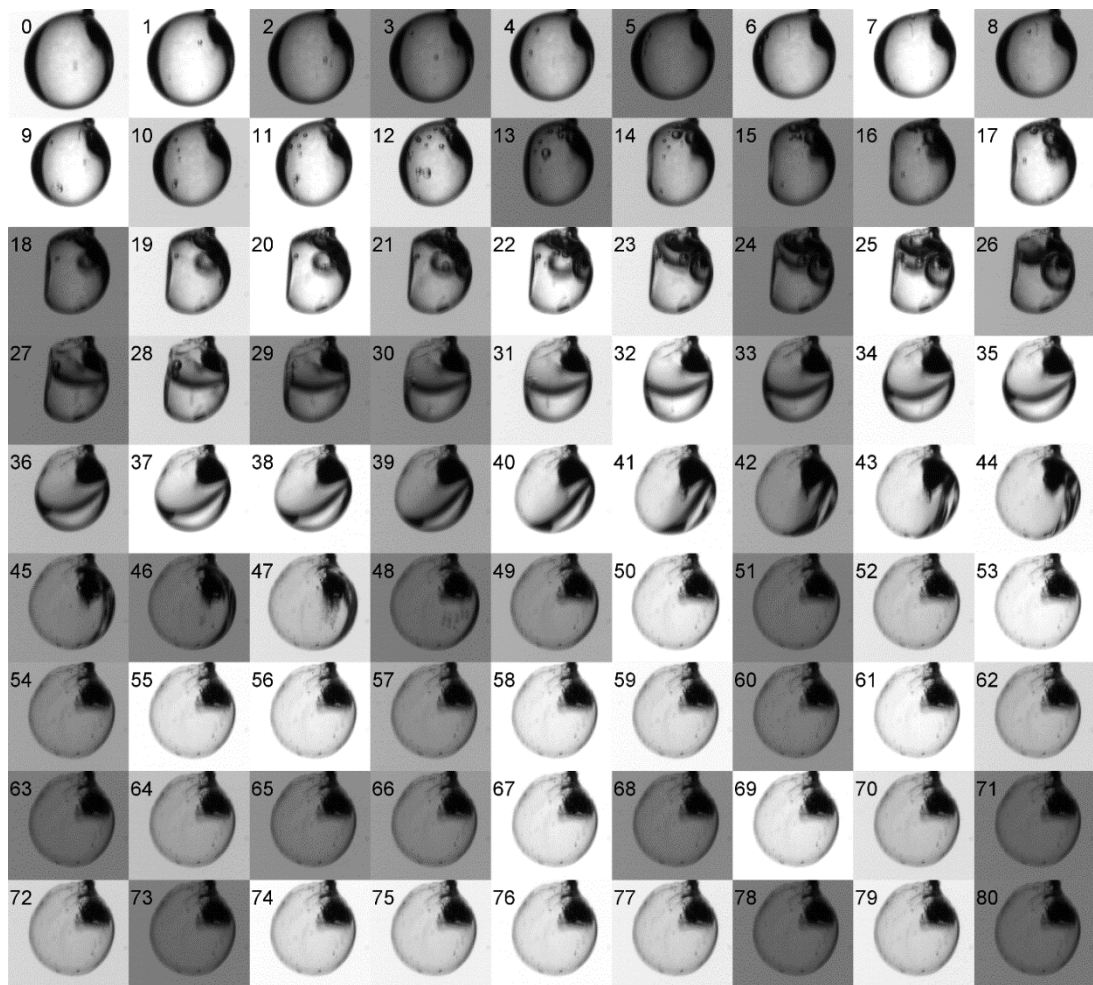

Figure 7.4 Normalised surface area, normalised mass, evaporation flux and droplet temperature vs drying time at 100˚C air temperature at 5% and 15% w/w initial solute concentrations[10].

---

[10] *Note: the scattering observed in the third run of 5% w/w ($d_{d,0}$= 1.34 mm) is due to secondary bubble growth and collapse rather than inflation/deflation cycles.*

Figure 7.4 demonstrates that at 100 °C air temperature, a boiling stage exists at the droplet temperatures in the range of 65-85 °C. The use of the acetone/water mixture decreases the boiling point of the droplet. Similar to below boiling, a high evaporation flux is established in the early stage of drying which has been related to preferential drying of acetone. In all drying repeats, an increase in the surface area is encountered which is driven by boiling as demonstrated by the morphology time series shown in Table 7.2 & Table 7.3. The boiling driven effects result in a homogenous increase in size and growth rather than inflation and collapse. This is demonstrated by a series of frames collected every 1 second, Figure 7.5. This behaviour of growth in surface area without collapse is in contrast with materials with low viscosity such as sucrose presented in Chapter 4, which exhibited inflation/deflation cycles due to liquid-like behaviour during boiling. The difference in behaviour is attributed to the skin forming properties of HPMC which exhibits a solid-like behaviour pre and during boiling. This is evident by the deformations (mainly bending) of the droplet surface prior to expansion of the droplet, Figure 7.5 (bending starting at frame number 15), indicating that the surface structure possesses some degree of solid-like behaviour. Therefore, the vapour pressure results only in growth behaviour and the droplet solidifies with further drying and results in the formation of "puffed" expanded particle as demonstrated by the final SEM micrographs shown in Figure 7.1. The behaviour of inflation displayed for skin forming properties is reported here for the first time. This behaviour is in contrast to the morphology evolution observed for aqueous HPMC droplets where boiling driven effects resulted in resistance of surface deformations and the formation of hollow morphologies with little expansion of the surface, owning to enhanced mechanical properties of the skin.

The effect of boiling on the evaporation flux can be investigated by correlating the point of the increase in the surface area with the evaporation flux. Figure 7.4 shows that the evaporation flux for 5% w/w initial solute concentration is on a decreasing trend as the droplets enter the boiling stage. However, as the droplet enters the boiling stage, the flux increases and is maintained with the increase in surface area. Vapour pressure is generated due to the high moisture within the droplet during boiling and bubbling within the droplet is thought to result in internal mixing of the

droplet even without a deflation cycle. It is hypothesised that the stretching of the droplet and the internal bubbling results in mixing of the droplet and distorting the established moisture gradients within the droplet and thus decreasing the internal mass transfer resistance. Therefore, a high evaporation flux is maintained even after the skin has formed on the surface. This behaviour is in contrast with drying below boiling at 60 ˚C (discussed in 7.3.2.1) where the skin formation resulted in a reduction in the evaporation flux.

Figure 7.5 Growth behaviour of 5% w/w HPMC droplet (in acetone water) following surface bending at 100˚C air temperature. Frames displayed are at a rate of 1 frame per second.

The effects of boiling on eliminating the surface deformations and the increase in evaporation rate are new findings and can further expand the understanding of drying skin forming materials such as polymers at high air temperatures. Further investigation is conducted at higher air temperatures, 140 ˚C and 180 ˚C in Figure 7.6 and Figure 7.7 respectively
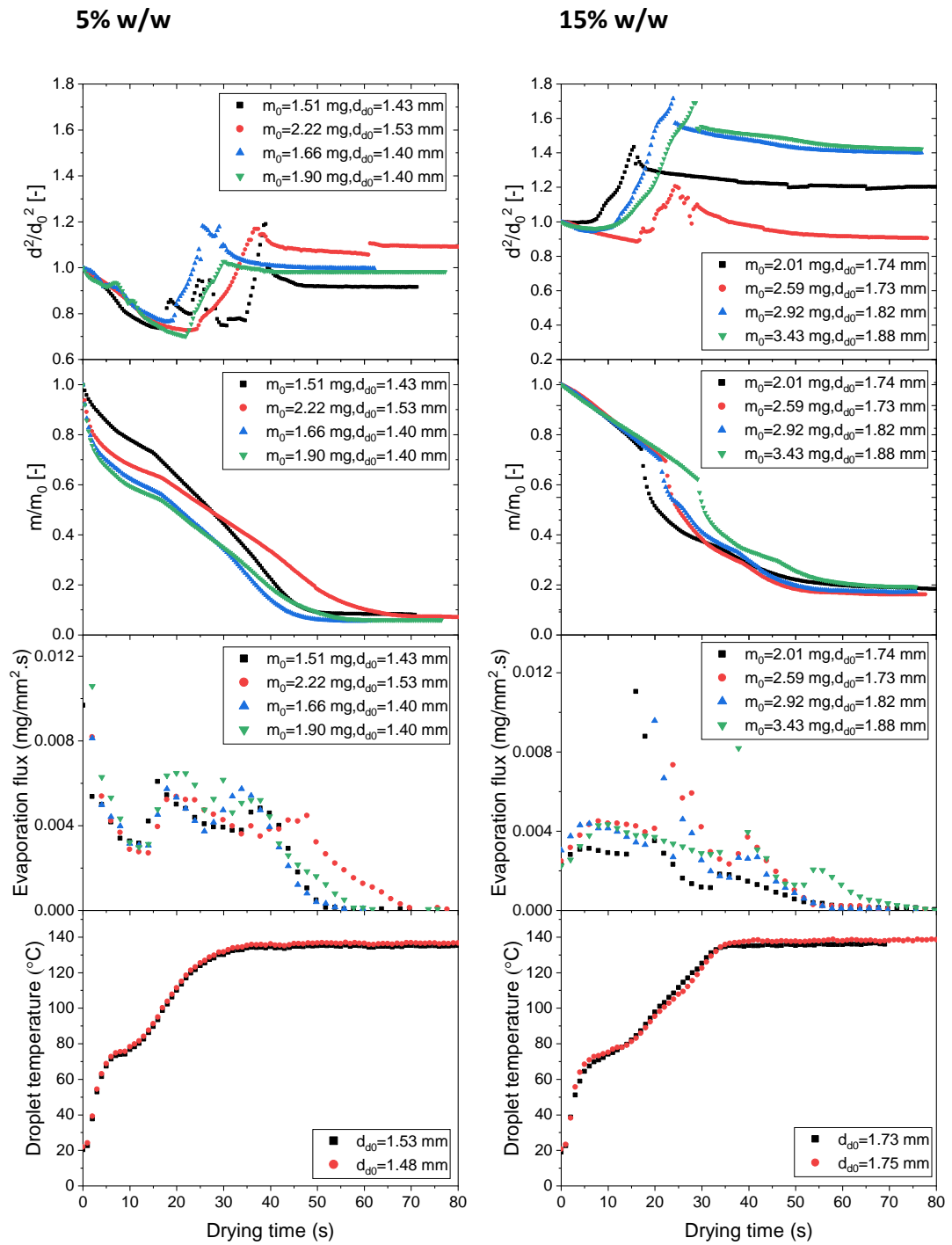
160

Figure 7.6 Normalised surface area, normalised mass, evaporation flux and droplet temperature vs drying time at 140˚C air temperature at 5% and 15% w/w initial solute concentrations.
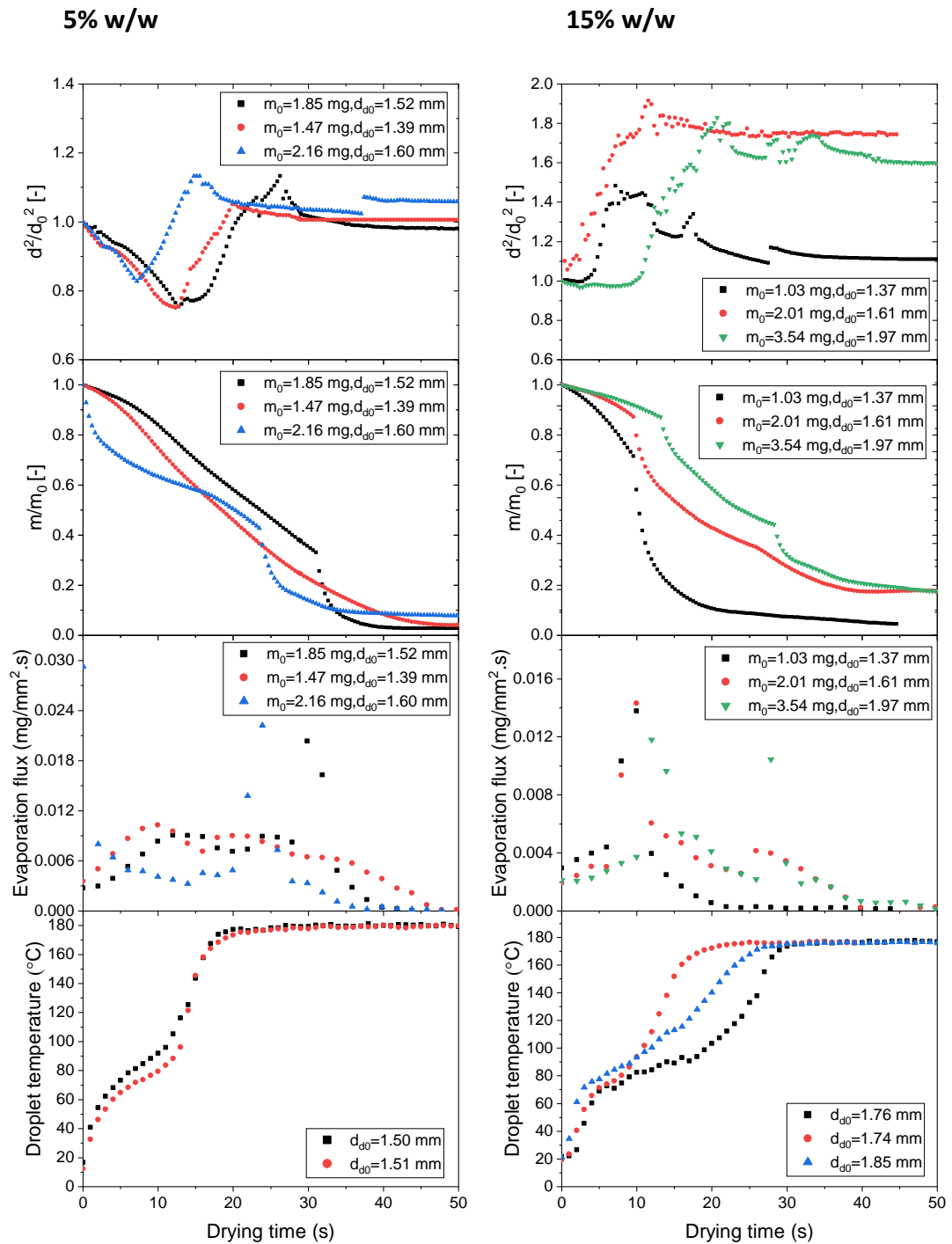
Figure 7.7 Normalised surface area, normalised mass, evaporation flux and droplet temperature vs drying time at 180˚C air temperature at 5% and 15% w/w initial solute concentrations.

The normalised surface area in Figure 7.6 and Figure 7.7 demonstrate that the shrinkage pre-boiling is highly dependent on the initial solute concentrations. At 5% initial solute concentration, the normalised surface show shrinkage of the droplet prior to entering the boiling stage. As the droplet enters the boiling stage, the

normalised surface area increases corresponding to a boiling stage of the droplet. At 15% w/w, the droplet undergoes little shrinkage and enters the boiling stage at a diameter close to the initial droplet diameter due to rapid surface enrichment related to the high initial solid content and high evaporation flux due to preferential drying of acetone. A significant increase in the surface area occurs due to inflation in the direction of airflow, as demonstrated by the morphology time series in Table 7.2 and Table 7.3. The surface area should be taken with caution due to the assumption of sphericity in the calculations of the effective diameter. The extreme degree of inflation, in the direction of airflow, observed at 140 ˚C and 180 ˚C air temperatures is due to the heterogonous properties of the skin; the skin formed on the downstream side of the airflow possesses lower modulus due to lower local evaporation.

The degree of the influence of the boiling on the evaporation flux is more significant with the increase in air temperature. Figure 7.6 and Figure 7.7 demonstrate that the increase in surface area corresponds to an increase in mass loss and evaporation flux. The trend is very clearly shown for 15% w/w at 140 ˚C and 180 ˚C. The boiling driven effects accelerate the evaporation flux and mass loss. This could be due to the droplet entering the droplet stage at higher initial moisture content, as demonstrated in Figure 7.8. The increase in moisture content at boiling is due to rapid heat-up of the droplet caused by an increase in surface enrichment with the rise in evaporation flux. The increase in moisture content at boiling is hypothesised to result in a greater extent of bubble nucleation within the droplet, leading to internal mixing of the droplet, decreasing the moisture gradients within the droplet and thus increasing the internal mass transfer. The increase of the evaporation flux due to boiling even with skin formation is a major difference to that below boiling. Drying below boiling showed decrease in evaporation flux after skin formation which hindered moisture evaporation.
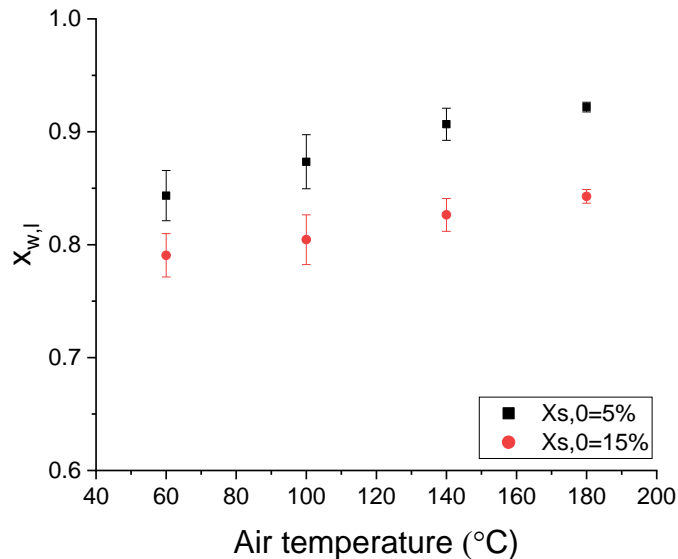
Figure 7.8 Moisture content at locking at air temperatures of 60 ˚C, 100 ˚C, 140 ˚C, 180˚C and initial solute concentrations of 5% and 15% w/w. Error bars were calculated based on 5 replicates at each condition. Error bars are based on the standard deviation of the mean and represent ± 1 standard deviation.

7.3.3 Influence of air temperature and solute concentration on the final dried particle size

The morphology evolution time series in Table 7.2 and Table 7.3 as well as the final SEM micrographs, Figure 7.1, show that the droplet experiences deformations below boiling, at 60 ˚C air temperature. This is a clear indication of locking where the moisture trapped within the skin is evaporated through the skin, causing surface deformations. Based on the morphology time series, the diameter at locking was determined based as the diameter at the deformations onset. At higher air temperature above boiling, the droplet locks right before it enters the boiling stage and the conditions of boiling are taken as locking due to small timeline between locking and boiling. The normalised diameter at locking and the normalised final dried particle diameters are given in Figure 7.9.

Figure 7.9 illustrates that the final size of the dried particle is largely affected by the air temperature and governed by whether the drying air temperature is below or above boiling. At temperatures below boiling, the final size of the dried particle is lower than the size of the droplet at locking due to deformations caused by continued evaporation after skin formation. Locking occurs at relatively large particle size for higher initial solute concentration due to early skin formation. At temperatures above boiling, the final size of the dried particle is higher than the size

164

of the particle at locking due to boiling driven effects which results in expansion of the droplet surface. At lower initial solute concentration, the extent of shrinkage below boiling is larger as the skin formation is delayed. This extent of shrinkage decreases as the air temperature increases due to the increase in evaporation rate, which results in earlier locking. On the other hand, it can be seen that droplet enters boiling at larger diameter at higher initial solute concentrations, locking occurs almost instantly due to the rapid increase in surface solute concentration.
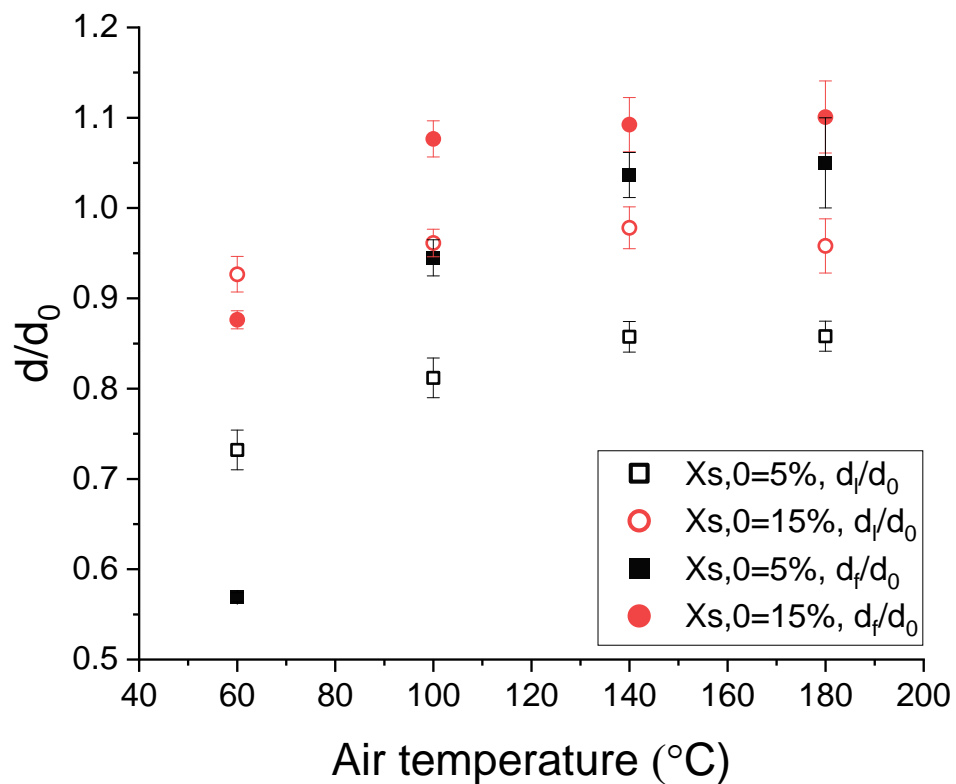
Figure 7.9 The final size of the dried particle (solid) and the size of the particle at locking (open) at 5% and 15% w/w initial concentrations and different air temperatures. Error bars were calculated based on 5 replicates at each condition. Error bars are based on the standard deviation of the mean and represent ± 1 standard deviation.

The drying kinetics plots given in this section show that the variability of measurements increases, and repeatability of the data becomes highly dependent on the initial mass, particularly at high air temperatures. A high degree of repeatability is obtained for similar droplet sizes, for example, the repeatability of the temperature data at 5% and 15% w/w and 140 ˚C air temperature (Figure 7.6). Although the repeatability of the drying data is highly dependent on the initial mass and influenced by the fast evaporation, the trends of the increase in evaporation flux

during boiling occur for all repeated runs. Therefore, the results obtained in this section can be applied to other materials with similar skin forming properties. The addition of organic solvents and drying above boiling can result in enhanced evaporation rate, resistance to surface deformations and driving change in morphology to the formation of hollow expanded particles with a smooth appearance.

7.4 Conclusion

This chapter has revealed new insights into the influence of the organic solvents on the morphology evolution, particle formation, and the drying behaviour of HPMC at a wide range of air temperatures. At air temperatures below boiling temperature, a skin forms on the particle which deforms as a result of continued solvent evaporation. The final dried particles showed deformed, buckled morphologies similar to the drying of aqueous HPMC. This behaviour at lower temperatures shows similarities with the literature on drying of polymer and proteins where the skin forms early during drying due to solute surface enrichment and results in surface mechanical instabilities. However, the use of solvents results in faster evaporation and differences in the expected drying kinetics. Notably, the droplet shows skipping of the constant drying rate period at the wet-bulb temperature. This has been attributed to early fast evaporation caused by preferential evaporation of acetone owing to its high volatility. The high evaporation flux resulted in early surface enrichment which halted surface moisture saturation, causing the skipping of the constant rate period at the wet-bulb temperature.

New findings into the effect of the skin on the final structure were revealed at high air temperatures above the boiling point. Boiling driven effects result in resistance to the bending and deformations and a clear shift in external morphology where the dried particles exhibited smooth appearance with a puffed hollow structure. Inflation of the particle and increase of the particle surface area during boiling were reported. This has been attributed to the role of acetone in the breakdown of the HPMC polymer network causing a decrease in the modulus of elasticity of HPMC. Additionally, the drying of HPMC in solvents prevented the occurrence of gelation, which further contributed to lowering the mechanical strength of the skin. The

combined effect of acetone on the mechanical properties of HPMC resulted in an expansion of the droplet and continued the increase of the surface area during boiling. However, the skin still exhibited a degree of elasticity which prevented inflation/deflation cycles demonstrating the significant contrast in behaviour with materials of low viscosity such as sucrose which exhibited rapid inflation/deflation cycles above boiling.

The effect of boiling on the drying kinetics was very significant and included an increase in the surface area and enhanced mass loss. The nature of inflation included a sustained increase in the surface area without any noticeable deflation cycles. The addition of acetone and drying above boiling can result in enhanced evaporation rate, resistance to surface deformations, and driving change in morphology to the formation of hollow expanded particles with a smooth appearance. The results obtained in this section can be applied to other materials with similar skin forming properties. The work in this chapter is the first study using multicomponent solvents and solids in the temperature range above the boiling point of the solution. However, the drying kinetics with the use of solvents are more complex to analyse in this high range of air temperatures due to the complexity of characterising multicomponent solvent mixtures and the lack of physical properties, making modelling studies of these systems more challenging.

Chapter 8 Conclusion and future work

8.1 Overall conclusions

The novelty of the work in this thesis involved the development of a highly accurate single droplet apparatus which incorporated a direct mass measurement method (a microbalance with a resolution of 6 digit to a gram), compared with recent similar apparatuses where the mass is measured indirectly using infrared spectrometer (Tran et al., 2016a). Further significant novel elements of this work involve the consideration of three systems which resulted in a comprehensive study of drying above boiling. In particular, the consideration of a film-forming system (HPMC) showed interesting results where the skin formed suppressed the effect of boiling on the size and the morphology of the final dried particle. The novelty of this work was further expanded by using a mixture of organic solvent/water, which showed interesting insights on the effect of the higher vapour pressure on altering the pressure differences on the droplet surface and consequently an increase in the particle size. However, the use of organic solvents has costs implications, which must be considered. The industrial relevance of the work in this thesis was demonstrated using a lab-scale spray dryer which showed a good agreement with the properties of the particles collected from single droplet drying experiments.

Validation of the single droplet drying apparatus by the drying of pure water droplets demonstrated very good accuracy and reproducibility at the range of conditions used; 25-180 °C air temperature, 1.4-2 mm droplet size, 1- 3 mg droplet weight, and 0-0.57 m/s air velocity. A robust method for mass loss calculations was devised using a microbalance with a resolution of six decimal places to a gram. The advantages of the single droplet drying apparatus have been highlighted; reducing the calibration effort by the use of calibration-free telecentric lens and balance for mass loss measurements, and reduction of heat conduction error by the use of PEEK (Polyether Ether Ketone) filament with low heat conductivity.

The advantages of the single droplet drying apparatus have allowed for a systematic study of three systems, sucrose, sodium silicate and HPMC at a wide range of air temperatures and initial solute concentrations. The selection of these three systems was due to the dominant influence of the composition on the boiling driven effects which necessitated the investigation of systems of different properties (low

viscosity, high viscosity and systems of film-forming properties). The systematic study on the three selected systems at a wide range of air temperatures and a selection of initial solute concentrations has allowed mapping the drying behaviour below and above the boiling point. From this study, maps on the conditions of boiling onset (size and moisture) and final dried particle metrics such as size and porosity were constructed. The work also benefited from the use of a lab-scale spray dryer for a comparison of structures with single droplet drying experiments.

The first system considered, sucrose, exhibited inflation/deflation cycles above boiling. This system had been investigated in previous studies; however, this work has allowed the mapping of the drying behaviour at different air temperatures and initial solute concentrations. The measurements of drying at the constant rate stage demonstrated agreements with a model based on Ranz-Marshall Correlations, particularly at low air temperature and low solute content. The morphology development at this stage had little effect on the drying rate. Above boiling, it was demonstrated that the particle collapses at the end of the inflation/deflation cycles and fails to retain any porosity. At the same initial solid content, the increase in air temperature above boiling results in a limited increase in the final dried particle size. This has been attributed to the low viscosity of sucrose even with the increase in concentration and temperature, and thus the particle is unable to maintain any degree of inflation. High-speed imaging showed rapid inflation/deflation cycles with bubble outbreak suggesting a liquid-like behaviour. The inflation/deflation cycles encountered during drying resulted in an increase in the evaporation flux due to the stretching and collapse of the droplet which results in enhanced mixing and increase of internal mass transfer coefficient. The boiling onset parameters such as size and moisture have been established, and the relationship to inflation/deflation frequency and inflation/deflation rate was investigated. A higher initial solid content and air temperature results in entering the boiling stage at a high moisture content which results in a longer drying period at the boiling temperature and a more violent inflation/deflation cycles. Similar systems with a lower viscosity which remain liquid-like with the increase in concentration and temperature are expected to display similar drying behaviour above boiling.

The second system investigated in this study, sodium silicate, also exhibited inflation/deflation cycles above boiling; however, remarkably boiling resulted in a significant increase in the final particle size and porosity. The dried particles demonstrated hollow expanded structures with thin shells. Larger dried particles were obtained for higher initial solid content, and higher air temperature as the droplets enter the boiling stage with higher absolute moisture content and experience a higher degree of inflation. The final particle size showed significant variability for the same initial solid content and at the same drying conditions caused by the stochastic nature of inflation. The behaviour of sodium silicate below boiling demonstrated shrinkage without surface deformations, thereby the formation of particles with smooth surfaces. The final size and porosity remained unchanged with the increase in air temperature from 60 ˚C to 100 ˚C, indicative of no locking and little influence of the increase of air temperature in this range on the structure of the particle and the extent of shrinkage. The structures collected from the single droplet drying were highly similar to those produced from spray drying which demonstrates the usefulness of this single droplet drying technique for morphology studies and the limited effect of the intrusion nature of the filament on the morphology development.

The behaviour of maintained inflation and lack of deflation of silicate is in contrast to that exhibited by sucrose. The difference in behaviour was related to the viscoelastic behaviour of silicate during boiling and reflects the importance of rheo-mechanical properties evolution during drying. The morphology development of silicate demonstrated that the droplets enter the boiling stage with high viscosity but with liquid-like behaviour. However, with continued drying, silicate gains further viscoelastic properties which help in maintaining a degree of inflation. Silicate exhibits similar behaviour to systems in the literature such as maltodextrin (El-Sayed et al., 1990) and lactose (Tran et al., 2016a). These systems show a significant increase in the final size and porosity when dried above boiling which would cause significant changes in the final powder properties.

The third system considered in this work, HPMC, is a film-forming material which forms a skin during drying. The drying kinetics showed a significant difference to the

expected drying history; for example, the droplet temperature profile exhibited skipping of the wet-bulb stage and rapid heat-up to the air temperature or the boiling point. Further, the particles showed limited shrinkage with the increase in air temperature and solute concentration. This was shown to be due to heat-induced gelation. Heat-induced gelation also resulted in a significant influence on the drying behaviour; a reduction in the evaporation flux and the degree of shrinkage. The interdependency of these factors; skin formation, heat gelation, shrinkage and drying rate further added to the complexity of understanding the drying behaviour of HPMC. Below boiling, a skin formed on the particle surface which was subjected to deformations and bending. The deformations were related to continued solvent evaporation after skin formation, which creates a lower pressure under the skin, thus exerting stress on the skin which eventually results in bending and deformations. At high air temperatures (140 and 180 ˚C), rapid gelation at the start of drying is thought to result in the formation of a stronger gelled skin which resisted the deformations and spherical particles with a smooth surface were produced. It was also hypothesised that the vapour pressure associated with boiling plays a role in altering the internal and external pressure differences on the particle surface and thus causing expansion and inhibition of surface deformations. Furthermore, the formation of skin above boiling resulted in suppressing effects of boiling and inhibited inflation/deflation cycles as opposed to sucrose and silicate. Systems with comparable film-forming properties and strengths of skin are expected to exhibit similar behaviours above boiling.

The influence of the skin properties on the outcome of boiling was further investigated by the use of acetone in the preparation of HPMC solutions. Acetone results in the breakdown of the polymer network and altering the mechanical properties such as elongation and modulus of elasticity. The results from the single droplet drying experiments showed an expansion of the surface area of the droplet and increase of the particle size during boiling. However, inflation/deflation cycles were not observed, which was related to the solid-like behaviour of the skin resulting in resistance to deflation and slow increase in the surface area. The role of the addition of organic solvents in changing the skin properties is an attractive option to manipulate the drying behaviour and the structure of the final dried particles. It

demonstrates that the behaviour above boiling can be manipulated by a change of the mechanical and rheological properties as well as the boiling point and the internal vapour pressure.

The systematic drying study using three different compositions has furthered our understanding of the various behaviours obtained during drying at temperatures above the boiling. The effect of drying above boiling on the morphology development and evaporation rate was significantly dependent on the evolution of the rheological and mechanical properties with the increase in the air temperature and solute concentration. Simple systems such as sucrose which exhibits little rheological and mechanical changes with the increase in droplet temperature and concentration go through inflation/deflation cycles. However, the particle collapses at the end of inflation/deflation, thereby the final structure and size of the dried particle are similar to those obtained below boiling. Systems which exhibit an increase in the viscosity during drying without the formation of an elastic shell/skin allow the droplet to experience inflation/deflation cycles with less degree of collapse. The mechanisms of inflation/deflation cycles can also give insights into the subsequent morphology formed. Rapid inflation/deflation cycles suggest a liquid-like behaviour and the particles fail to retain any porosity at the end of the boiling stage. One the other hand, inflation with less degree of deflation suggests an increase of viscoelastic properties and the particles are more likely to retain porosity. The class of materials showing a drastic change in rheo-mechanical properties with the increase in air temperature and the formation of a skin layer are more complex to predict. This is due to the significant influence of skin formation on the evaporation rate and morphology development. In addition, phase changes such as gelation can occur and cause a change in the rheological properties. The outcome of boiling for this class of materials is dependent on the skin properties; the formation of a skin with strong mechanical properties can inhibit the occurrence of inflation/deflation cycles.

8.2 Wider scientific and industrial context of this work

The work conducted in this thesis can be put in a wider context by understanding recent advances to improve powder properties by enhancing particle functionalities. The industrial context of this work comes from the recent shift of spray drying as well as other drying processes from the focus on minimising capital costs and energy input to delivering specific product performance with enhanced properties (Walton, 2000). Many bulk powder and particulate properties such as powder flowability, particle size and particle friability, were found to be directly related to morphological structure (Walton, 2000). The ability to control these characteristics is a huge advantage of spray drying over other drying methods, particularly when processing high performance, high cost and low-volume consumer products (Walton, 2000).

Great potential for use in various applications could be achieved with morphological control including pharmaceuticals, detergents, electronics and catalysts (Iskandar, 2009). In the pharmaceutical industry, spray drying has demonstrated great potential to manipulate the properties of the final powder. For example, Steckel and Brandes (2004) demonstrated that spray drying can be used to produce low density particles for pulmonary delivery which had a potential to enhance dispersibility properties of the powder properties (Steckel and Brandes, 2004). Rabbani and Seville (2005) demonstrated the influence of formulation components on the aerosolisation properties of spray-dried powders. Benjasirimongkol et al., (2019) investigated the effect of formulations and spray drying process conditions on physical properties of resveratrol spray-dried emulsions. They demonstrated that the production of hollow active pharmaceutical ingredients resulted in an enhancement in dissolution and inhaled delivery. Further study by Nair et al. (2019) used a quality by design approach for the optimization of the spray drying process used in the drying of risperidone nanosuspension. In this study, the spray drying of Risperidone (RIS) nanosuspension was optimised to achieve lower particle size, higher yield and good compressibility of spray-dried powder using quality by design approach. Furthermore, Ekdahl et al. (2019) demonstrated the capability of tuning spray drying conditions to produce particles with desired properties using amorphous solid dispersions, ASDs. ASDs were engineered using the spray-drying process to influence

mechanical and flow properties critical to tableting. It was shown that by tuning spray drying conditions, ASD particles with a wide range of particle sizes, densities, and particle morphologies (intact, collapsed, and fractured hollow spheres) can be produced.

In food applications, spray drying can also be used to manipulate the properties of the final powder. For example, the particle size and density in spray drying were related to the effects of carbohydrate properties (Elversson and Millqvist-Fureby, 2005). It was found that larger particles were produced by either increasing the droplet size and concentration feed solution; or decreasing the solubility of the solute. Furthermore, the apparent particle density was found to be decreasing with the feed concentration. Souza et al. (2009) investigated the influence of spray drying conditions on the physical properties of dried pulp tomato. It was demonstrated the best spray drying conditions to produce lower moisture content and higher apparent density tomato powder were at an inlet air temperature of 200 °C (Souza et al., 2009). Wang and Selomulya (2019) demonstrated that spray drying strategy can be used for the encapsulation of bioactive peptide powders for food applications. It was demonstrated that depending on the particle morphology and type of concentrate (crystalline or emulsified carotenoids), the encapsulation efficiency can be increased from 43 to 88%. The increase in encapsulation efficiency resulted in significant differences in carotenoid stability during subsequent storage.

The work done on this thesis has focused on systems with higher viscosity and with a resemblance to "real" industrial drying systems. It added our understanding of the effect of the air temperature and composition on the final density, size and morphology of the final dried particle. The new knowledge used can be utilised to enhance the design of spray drying based on an engineering approach. It has been demonstrated that drying at high temperatures above boiling can vastly change the density and size of the final particle which can have a significant impact on powder properties and thus post-drying powder processing. Comparisons with lab-scale spray drying offered the opportunity to probe the usefulness of the single droplet drying technique and demonstrate usefulness to industrial applications.

The wider scientific interest of this work involves the need for an understanding of particle formation from droplet drying including the stages of particle drying and the influence of process conditions and composition on the properties of the final particle. An understanding of the particle formation can consequently be used to predict the properties of the particles formed and thus the final powder characteristics such as density and flowability. Understanding of the particle formation kinetics can also be implemented in spray drying models and be used as a basis to explain pilot plant trials. Particle formation studies including those by Walton and Mumford (1999a), Hecht et al. (2000) and (Tran et al., 2016a) have been conducted using single droplet drying methods and revealed insights on the influence of the drying behaviour on the final morphology. Remarkably, it has been revealed that drying at high temperatures can lead to boiling and thus have a significant effect on the drying rate and morphology evolution (Walton and Mumford (1999a). However, the literature review (section 2.6) demonstrated that limited studies have conducted at air temperature above boiling, particularly systematic studies where a range of compositions, air temperatures and initial concentration are lacking. The work in this thesis has provided systematic studies where various routes of drying above boiling were examined and the influence of composition, air temperature and choice of solvent were investigated. It has highlighted the effect of boiling on the drying rate (measured using a direct mass measurement method), the final particle size and density. This work has consequently enhanced our understanding of the particle formation kinetics above the boiling point and in cases where different mechanisms of skin formation are encountered (strong case formation). It has expanded on the work done by Walton and Mumford (1999a) with systems that do not fully fit in the regime i.e. skin forming materials such as HPMC that don't endure any changes after boiling due to formation of rigid skin enhanced by phase transitions. Furthermore, this study has highlighted the influence of the evolution of morphology on the drying rate by monitoring closely the drying rate pre and post boiling as well as pre and post skin formation. Moreover, the role of the composition on the differences in particle formation and consequently on the final size and density have been highlighted and quantified. The drying kinetics and morphology evolution data collected from this work can be

integrated into CFD and drying models to account for particle morphology changes—inflation/deflation model. The data collected can also be used to validate current single droplet drying models.

8.3 Future work

The suggested future work is summarised in the following:

1- Monodisperse spray drying

Although this study has used a lab-scale spray dryer for comparison of structures from spray drying and single droplet drying experiments, the bi-fluid nozzle used produce polydisperse droplets which make the evaluation of the initial droplet size and final dried particle size more challenging. The use of monodisperse nozzles allows the measurement of the initial droplet size and therefore, the increase in size and porosity of the final particles with the increase in air temperature and initial solute concentration can be investigated. The results obtained can be compared with the final size and porosity maps obtained in this work from the singe droplet drying experiments. The monodisperse spray drying can also reduce the variability of the final spray-dried structures caused by different drying trajectories, observed in the case of spray drying of HPMC, and therefore enhances the comparison of structures between single droplet drying and spray drying.

2- Material properties measurements

The material properties measurements can include offline mechanical measurements of dried films using Dynamic mechanical analysis (DMA), Atomic force microscopy (AFM) and Nanoindentation. The moisture at the onset of boiling and locking conditions obtained from the single droplet drying experiments can be used as the start point of these measurements. These measurements are very challenging, particularly at the boiling point temperatures and low moisture contents.

3- Validation of single droplet drying models

The work in this thesis involved the measurement of drying kinetics at a large range of air temperatures and solute concentrations. These drying kinetics can

be used to validate existing single droplet drying models. The validation of the models would be very useful for highlighting the limitations of the current models in predicting the drying rate particularly during boiling where the morphological developments have been shown to have a dominant influence on the drying rate.

References

Adhikari, B., Howes, T. & Bhandari, B. R. 2007. Use of solute fixed coordinate system and method of lines for prediction of drying kinetics and surface stickiness of single droplet during convective drying. *Chemical Engineering and Processing: Process Intensification,* 46**,** 405-419.

Adhikari, B., Howes, T., Bhandari, B. R. & Troung, V. 2004. Effect of addition of maltodextrin on drying kinetics and stickiness of sugar and acid-rich foods during convective drying: experiments and modelling. *Journal of Food Engineering,* 62**,** 53-68.

Alamilla-Beltran, L., Chanona-Perez, J. J., Jimenez-Aparicio, A. R. & Gutierrez-Lopez, G. F. 2005. Description of morphological changes of particles along spray drying. *Journal of Food Engineering,* 67**,** 179-184.

Arai, S. & Doi, M. 2012. Skin formation and bubble growth during drying process of polymer solution. *Eur Phys J E Soft Matter,* 35**,** 57.

Aulton, M.E., Abdul-Razzak, M.H. and Hogan, J.E., 1981. The mechanical properties of hydroxypropylmethylcellulose films derived from aqueous systems Part 1: the influence of plasticisers. *Drug Development and Industrial Pharmacy*, 7(6), pp.649-668.

Bahlmann, E.F., Harris, R., Rockliffe, J. and Smith, E., 1997. Silicon-29 NMR self-diffusion and chemical-exchange studies of concentrated sodium silicate solutions. *Journal of the Chemical Society, Faraday Transactions*, 93(1), pp.93-98.

Bajwa, G. S., Sammon, C., Timmins, P. & Melia, C. D. 2009. Molecular and mechanical properties of hydroxypropyl methylcellulose solutions during the sol:gel transition. *Polymer,* 50**,** 4571-4576.

Baldwin, K.A., Granjard, M., Willmer, D.I., Sefiane, K. and Fairhurst, D.J., 2011. Drying and deposition of poly (ethylene oxide) droplets determined by Peclet number. *Soft Matter*, 7(17), pp.7819-7826.

Bellinghausen, R. 2019. Spray drying from yesterday to tomorrow: An industrial perspective. *Drying Technology,* 37**,** 612-622.

Benjasirimongkol, P., Piriyaprasarth, S. & Sriamornsak, P. Effect of Formulations and Spray Drying Process Conditions on Physical Properties of Resveratrol Spray-Dried Emulsions. Key Engineering Materials, 2019. Trans Tech Publ, 246-251.

Bertrand, G., Filiatre, C., Mahdjoub, H., Foissy, A. and Coddet, C., 2003. Influence of slurry characteristics on the morphology of spray-dried alumina powders. *Journal of the European Ceramic Society*, 23(2), pp.263-271.

Bodvik, R., Karlson, L., Edwards, K., Eriksson, J., Thormann, E. and Claesson, P.M., 2012. Aggregation of modified celluloses in aqueous solution: Transition from methylcellulose to hydroxypropylmethylcellulose solution properties induced by a low-molecular-weight oxyethylene additive. *Langmuir*, 28(38), pp.13562-13569.

Both, E.M., Siemons, I., Boom, R.M. and Schutyser, M.A.I., 2019. The role of viscosity in morphology development during single droplet drying. *Food Hydrocolloids*, 94, pp.510-518.

Both, E. M., Karlina, A. M., Boom, R. M. & Schutyser, M. a. I. 2018a. Morphology development during sessile single droplet drying of mixed maltodextrin and whey protein solutions. *Food Hydrocolloids,* 75**,** 202-210.

Both, E. M., Nuzzo, M., Millqvist-Fureby, A., Boom, R. M. & Schutyser, M. a. I. 2018b. Morphology development during single droplet drying of mixed component formulations and milk. *Food Res Int,* 109**,** 448-454.

Bouman, J., Venema, P., De Vries, R. J., Van Der Linden, E. & Schutyser, M. a. I. 2016. Hole and vacuole formation during drying of sessile whey protein droplets. *Food Research International,* 84**,** 128-135.

Boynton, W.P. and Brattain, W.H., 1929. Interdiffusion of gases and vapors. *International Critical Tables*, *5*, pp.62-63.

Charlesworth, D.H. and Marshall, W.R., 1960. Evaporation from drops containing dissolved solids. *AIChE Journal*, *6*(1), pp.9-23.

Chen, X., Boyko, V., Rieger, J., Reinhold, F., Reck, B., Perlich, J., Gehrke, R. and Men, Y., 2012. Buckling-induced structural transition during the drying of a polymeric latex droplet on a solid surface. *Soft Matter*, *8*(48), pp.12093-12098.

Chen, X. D. & Lin, S. X. Q. 2005. Air drying of milk droplet under constant and time-dependent conditions. *AIChE Journal,* 51**,** 1790-1799.

Chen, X. D. & Mujumdar, A. S. 2009. *Drying technologies in food processing*, John Wiley & Sons.

Chen, X. D. & Xie, G. Z. 1997. Fingerprints of the Drying Behaviour of Particulate or Thin Layer Food Materials Established Using a Reaction Engineering Model. *Food and Bioproducts Processing,* 75**,** 213-222.

Cheong, H.W., Jeffreys, G.V. and Mumford, C.J., 1986. A receding interface model for the drying of slurry droplets. *AIChE Journal*, *32*(8), pp.1334-1346.

Chindapan, N., Niamnuy, C. and Devahastin, S., 2018. Physical properties, morphology and saltiness of salt particles as affected by spray drying conditions and potassium chloride substitution. *Powder technology*, *326*, pp.265-271.

Chow, A. H., Tong, H. H., Chattopadhyay, P. & Shekunov, B. Y. J. P. R. 2007. *Particle engineering for pulmonary drug delivery*. 24**,** 411-437.

Davis, E.J., Ravindran, P. and Ray, A.K., 1981. Single aerosol particle studies. *Advances in Colloid and Interface Science*, *15*(1), pp.1-24.

Edmund Optics. 2019. *The Advantages of Telecentricity* [Online]. Available: https://www.edmundoptics.com/resources/application-notes/imaging/advantages-of-telecentricity/ [Accessed].

Ekdahl, A., Mudie, D., Malewski, D., Amidon, G. and Goodwin, A., 2019. Effect of Spray-Dried Particle Morphology on Mechanical and Flow Properties of Felodipine in PVP VA Amorphous Solid Dispersions. *Journal of pharmaceutical sciences*, *108*(11), pp.3657-3666.

Ekdawi-Sever, N., De Pablo, J. J., Feick, E. & Von Meerwall, E. 2003. Diffusion of sucrose and α, α-trehalose in aqueous solutions. *The Journal of Physical Chemistry A,* 107**,** 936-943.

El-Sayed, T.M., Wallack, D.A. and King, C.J., 1990. Changes in particle morphology during drying of drops of carbohydrate solutions and food liquids. 1. Effect of composition and drying conditions. *Industrial & Engineering Chemistry Research*, *29*(12), pp.2346-2354.

Elversson, J. and Millqvist-Fureby, A., 2005. Particle size and density in spray drying—effects of carbohydrate properties. *Journal of pharmaceutical sciences*, *94*(9), pp.2049-2060.

Emerson. 2008. *Instruction Manual Platform for NGA 2000* [Online]. Available: https://www.emerson.com/documents/automation/manual-nga-2000-platform-hardware-3rd-ed-rosemount-en-70110.pdf [Accessed].

Fäldt, P. and Bergenståhl, B., 1994. The surface composition of spray-dried protein—lactose powders. *Colloids and Surfaces A: Physicochemical and Engineering Aspects*, *90*(2-3), pp.183-190.

Fäldt, P. and Bergenståhl, B., 1996. Spray-dried whey protein/lactose/soybean oil emulsions. 1. Surface composition and particle structure. *Food Hydrocolloids*, *10*(4), pp.421-429.

Frossling, N., 1938. Uber die Verdunstung Fallernder Tropfen. *Gerlands Beitr. Geophys.*, *52*, pp.170-216.

Fu, F.-L. Mi, T.-B. Wong, S.-S. Shyu, Y.J., 2001. Characteristic and controlled release of anticancer drug loaded poly (D, L-lactide) microparticles prepared by spray drying technique. *Journal of microencapsulation*, *18*(6), pp.733-747.

Fu, N., Woo, M. W. & Chen, X. D. 2012a. Single Droplet Drying Technique to Study Drying Kinetics Measurement and Particle Functionality: A Review. *Drying Technology,* 30**,** 1771-1785.

Fu, N., Woo, M.W., Moo, F.T. and Chen, X.D., 2012. Microcrystallization of lactose during droplet drying and its effect on the property of the dried particle. *Chemical Engineering Research and Design*, *90*(1), pp.138-149.

Fuchs, N., 1934. Über die Verdampfungsgeschwindigkeit kleiner Tröpfchen in einer Gasatmosphäre. *Physikalische zeitschrift der Sowjetunion*, *6*, pp.224-243.

Fyhr, C. & Kemp, I. C. 1998. Comparison of different drying kinetics models for single particles. *Drying Technology,* 16**,** 1339-1369.

Gaiani, C., Ehrhardt, J.J., Scher, J., Hardy, J., Desobry, S. and Banon, S., 2006. Surface composition of dairy powders observed by X-ray photoelectron spectroscopy and effects on their rehydration properties. *Colloids and Surfaces B: Biointerfaces*, *49*(1), pp.71-78.

Gamble, J.F., Terada, M., Holzner, C., Lavery, L., Nicholson, S.J., Timmins, P. and Tobyn, M., 2016. Application of X-ray microtomography for the characterisation of hollow polymer-stabilised spray dried amorphous dispersion particles. *International journal of pharmaceutics*, *510*(1), pp.1-8.

Goodfellow. 2018. *Polyetheretherketone - online catalogue source - supplier of research materials in small quantities* [Online]. Available: http://www.goodfellow.com/E/Polyetheretherketone.html [Accessed].

Gouaou, I., Shamaei, S., Koutchoukali, M.S., Bouhelassa, M., Tsotsas, E. and Kharaghani, A., 2019. Impact of operating conditions on a single droplet and spray drying of hydroxypropylated pea starch: Process performance and final powder properties. *Asia-Pacific Journal of Chemical Engineering*, *14*(1), p.e2268.

Gregson, F.K.A., Robinson, J.F., Miles, R.E.H., Royall, C.P. and Reid, J.P., 2018. Drying Kinetics of Salt Solution Droplets: Water Evaporation Rates and Crystallization. *The Journal of Physical Chemistry B, 123*(1), pp.266-276.

Groenewold, C., Möser, C., Groenewold, H. and Tsotsas, E., 2002. Determination of single-particle drying kinetics in an acoustic levitator. *Chemical Engineering Journal*, *86*(1-2), pp.217-222.

Haas, K., Obernberger, J., Zehetner, E., Kiesslich, A., Volkert, M. and Jaeger, H., 2019. Impact of powder particle structure on the oxidation stability and color of encapsulated crystalline and emulsified carotenoids in carrot concentrate powders. *Journal of Food Engineering*, *263*, pp.398-408.

Handscomb, C. S., Kraft, M. & Bayly, A. E. 2009. A new model for the drying of droplets containing suspended solids. *Chemical Engineering Science,* 64**,** 628-637.

Hecht, J. P. 1999. *Influence of the development of drop morphology on drying rates and loss rates of volatile components during drying*, University of California, Berkeley.

Hecht, J.P. and King, C.J., 2000. Spray drying: influence of developing drop morphology on drying rates and retention of volatile substances. 1. Single-drop experiments. *Industrial & engineering chemistry research*, *39*(6), pp.1756-1765.

Henderson-Sellers, B., 1984. A new formula for latent heat of vaporization of water as a function of temperature. *Quarterly Journal of the Royal Meteorological Society*, *110*(466), pp.1186-1190.

Henrion, P.N., 1964. Diffusion in the sucrose+ water system. *Transactions of the Faraday Society*, *60*, pp.72-74.

Heymann, E. 1935. Studies on sol-gel transformations. I. The inverse sol-gel transformation of methylcellulose in water. *Transactions of the Faraday Society,* 31**,** 846-864.

Hirschmüller, H. 1953. Physical properties of sucrose. *Principles of sugar technology.* Elsevier.

Iler, K. R. 1979. The chemistry of silica. *Solubility, Polymerization, Colloid and Surface Properties and Biochemistry of Silica*.

Iskandar, F., 2009. Nanoparticle processing for optical applications–A review. *Advanced Powder Technology*, *20*(4), pp.283-292.

Kastner, O., Brenn, G., Rensink, D. and Tropea, C., 2001. The acoustic tube levitator–a novel device for determining the drying kinetics of single droplets. *Chemical Engineering & Technology: Industrial Chemistry-Plant Equipment-Process Engineering-Biotechnology*, *24*(4), pp.335-339.

Kawakami, K., Sumitani, C., Yoshihashi, Y., Yonemochi, E. and Terada, K., 2010. Investigation of the dynamic process during spray-drying to improve aerodynamic performance of inhalation particles. *International journal of pharmaceutics*, *390*(2), pp.250-259.

Keey, R.B. and Suzuki, M., 1974. On the characteristic drying curve. *International Journal of Heat and Mass Transfer*, *17*(12), pp.1455-1464.

Keey, R. B. 1992. Drying of Loose and Particulate Materials. *Drying Technology,* 10**,** 1139-1141.

Kim, E.H.J., Chen, X.D. and Pearce, D., 2002. Surface characterization of four industrial spray-dried dairy powders in relation to chemical composition, structure and wetting property. *Colloids and surfaces B: Biointerfaces*, *26*(3), pp.197-212.

Kim, E.H.J., Dong Chen, X. and Pearce, D., 2003. On the mechanisms of surface formation and the surface compositions of industrial milk powders. *Drying Technology*, *21*(2), pp.265-278.

Kincaid, D.C. and Longley, T.S., 1989. A water droplet evaporation and temperature model. *Transactions of the ASAE*, *32*(2), pp.457-0462.

Kinzer, G.D. and Gunn, R., 1951. The evaporation, temperature and thermal relaxation-time of freely falling waterdrops. *Journal of Meteorology*, *8*(2), pp.71-83.

Koç, B., Sakin-Yılmazer, M., Kaymak-Ertekin, F. & Balkır, P. 2014. Physical properties of yoghurt powder produced by spray drying. *Journal of food science and technology,* 51**,** 1377-1383.

Langrish, T.A.G., 2007. New engineered particles from spray dryers: Research needs in spray drying. *Drying Technology*, *25*(6), pp.971-983.

Langstroth, G.O., Diehl, C.H.H. and Winhold, E.J., 1950. The evaporation of droplets in still air. *Canadian Journal of Research*, *28*(6), pp.580-595.

Lin, J.-C. & Gentry, J. W. 2003. Spray Drying Drop Morphology: Experimental Study. *Aerosol Science and Technology,* 37**,** 15-32.

Lin, S. X. Q. & Chen, X. D. 2007. The reaction engineering approach to modelling the cream and whey protein concentrate droplet drying. *Chemical Engineering and Processing-Process Intensification,* 46**,** 437-443.

Lintingre, E., Lequeux, F., Talini, L. & Tsapis, N. 2016. Control of particle morphology in the spray drying of colloidal suspensions. *Soft Matter,* 12**,** 7435-44.

Maa, Y.F., Costantino, H.R., Nguyen, P.A. and Hsu, C.C., 1997. The effect of operating and formulation variables on the morphology of spray-dried protein particles. *Pharmaceutical development and technology*, *2*(3), pp.213-223.

Maa, Y.F., Nguyen, P.A.T. and Hsu, S.W., 1998. Spray-drying of air–liquid interface sensitive recombinant human growth hormone. *Journal of pharmaceutical sciences*, *87*(2), pp.152-159.

Maki, K.L. and Kumar, S., 2011. Fast evaporation of spreading droplets of colloidal suspensions. *Langmuir*, *27*(18), pp.11347-11363.

Manukyan, S., Sauer, H.M., Roisman, I.V., Baldwin, K.A., Fairhurst, D.J., Liang, H., Venzmer, J. and Tropea, C., 2013. Imaging internal flows in a drying sessile polymer dispersion drop using Spectral Radar Optical Coherence Tomography (SR-OCT). *Journal of colloid and interface science*, *395*, pp.287-293.

Marín, Á.G., Gelderblom, H., Lohse, D. and Snoeijer, J.H., 2011. Order-to-disorder transition in ring-shaped colloidal stains. *Physical review letters*, *107*(8), p.085502.

Masters, K. 1991. Handbook of Spray Drying. Longman, New York.

Maury, M., Murphy, K., Kumar, S., Mauerer, A. and Lee, G., 2005. Spray-drying of proteins: effects of sorbitol and trehalose on aggregation and FT-IR amide I spectrum of an immunoglobulin G. *European journal of pharmaceutics and biopharmaceutics*, *59*(2), pp.251-261.

Meerdink, G. & Vantriet, K. 1995. Modeling segregation of solute material during drying of liquid foods. *Aiche Journal,* 41**,** 732-736.

Mettler Toledo. 2019. *Laboratory_Weighing_Solutions* [Online]. Available: https://www.mt.com/gb/en/home/products/Laboratory_Weighing_Solutions/Micro_Ultra_Balances/XPR_MicroBalance/XPR2U.html [Accessed].

Mezhericher, M., Levy, A. & Borde, I. 2010. Theoretical Models of Single Droplet Drying Kinetics: A Review. *Drying Technology,* 28**,** 278-293.

Moghbeli, S., Jafari, S.M., Maghsoudlou, Y. and Dehnad, D., 2019. Influence of pectin-whey protein complexes and surfactant on the yield and microstructural properties of date powder produced by spray drying. *Journal of food engineering*, *242*, pp.124-132.

Mondragon, R., Hernandez, L., Enrique Julia, J., Carlos Jarque, J., Chiva, S., Zaitone, B. & Tropea, C. 2011. Study of the drying behavior of high load multiphase droplets in an acoustic levitator at high temperature conditions. *Chemical Engineering Science,* 66**,** 2734-2744.

Mondragon, R., Jarque, J. C., Julia, J. E., Hernandez, L. & Barba, A. 2012. Effect of slurry properties and operational conditions on the structure and properties of porcelain tile granules dried in an acoustic levitator. *Journal of the European Ceramic Society,* 32**,** 59-70.

Mosén, K., Bäckström, K., Thalberg, K., Schaefer, T., Kristensen, H.G. and Axelsson, A., 2005. Particle formation and capture during spray drying of inhalable particles. *Pharmaceutical development and technology*, *9*(4), pp.409-417.

Mu, L. and Feng, S.S., 2001. Fabrication, characterization and in vitro release of paclitaxel (Taxol®) loaded poly (lactic-co-glycolic acid) microspheres prepared by spray drying technique with lipid/cholesterol emulsifiers. *Journal of Controlled Release*, *76*(3), pp.239-254.

Nair, A., Khunt, D. and Misra, M., 2019. Application of quality by design for optimization of spray drying process used in drying of risperidone nanosuspension. *Powder technology*, *342*, pp.156-165.

Nandiyanto, A.B.D. and Okuyama, K., 2011. Progress in developing spray-drying methods for the production of controlled morphology particles: From the nanometer to submicrometer size ranges. *Advanced Powder Technology*, *22*(1), pp.1-19.

Nešić, S. and Vodnik, J., 1991. Kinetics of droplet evaporation. Chemical Engineering Science, 46(2), pp.527-537.

Okuzono, T., Ozawa, K. & Doi, M. 2006. Simple model of skin formation caused by solvent evaporation in polymer solutions. *Phys Rev Lett,* 97**,** 136103.

Paramita, V., Iida, K., Yoshii, H. & Furuta, T. 2010. Effect of Additives on the Morphology of Spray-Dried Powder. *Drying Technology,* 28**,** 323-329.

Patel, K. C. & Chen, X. D. 2008. Surface-Center Temperature Differences Within Milk Droplets During Convective Drying and Drying-Based Biot Number Analysis. *Aiche Journal,* 54**,** 3273-3290.

Patel, K.C., Chen, X.D., Lin, S.X. and Adhikari, B., 2009. A composite reaction engineering approach to drying of aqueous droplets containing sucrose, maltodextrin (DE6) and their mixtures. *AIChE Journal*, *55*(1), pp.217-231.

Pauchard, L. and Allain, C., 2003a. Buckling instability induced by polymer solution drying. *EPL (Europhysics Letters)*, *62*(6), p.897.

Pauchard, L. & Allain, C. 2003b. Mechanical instability induced by complex liquid desiccation. *Comptes Rendus Physique,* 4**,** 231-239.

Pauchard, L. & Allain, C. 2003c. Stable and unstable surface evolution during the drying of a polymer solution drop. *Phys Rev E Stat Nonlin Soft Matter Phys,* 68**,** 052801.

Pauchard, L. & Couder, Y. 2004a. Invagination during the collapse of an inhomogeneous spheroidal shell. *Europhysics Letters (EPL), 66,* 667-673.

Pauchard, L. & Couder, Y. 2004b. Invagination during the collapse of an inhomogeneous spheroidal shell. *Europhysics Letters, 66,* 667-673.

Perdana, J., Fox, M. B., Schutyser, M. a. I. & Boom, R. M. 2011. Single-Droplet Experimentation on Spray Drying: Evaporation of a Sessile Droplet. *Chemical Engineering & Technology, 34,* 1151-1158.

Perfetti, G., Alphazan, T., Wildeboer, W. J. & Meesters, G. M. H. 2011. Thermo-physical characterization of Pharmacoat® 603, Pharmacoat® 615 and Mowiol® 4-98. *Journal of Thermal Analysis and Calorimetry, 109,* 203-215.

Power, R. M., Simpson, S. H., Reid, J. P. & Hudson, A. J. 2013. The transition from liquid to solid-like behaviour in ultrahigh viscosity aerosol particles. *Chemical Science, 4,* 2597.

Price, H. C., Mattsson, J. & Murray, B. J. 2016. Sucrose diffusion in aqueous solution. *Phys Chem Chem Phys, 18,* 19207-16.

Qi Lin, S. X. & Chen, X. D. 2002. Improving the Glass-Filament Method for Accurate Measurement of Drying Kinetics of Liquid Droplets. *Chemical Engineering Research and Design, 80,* 401-410.

Rabbani, N.R. and Seville, P.C., 2005. The influence of formulation components on the aerosolisation properties of spray-dried powders. *Journal of controlled release*, *110*(1), pp.130-140.

Rampp, M., Buttersack, C. & Lüdemann, H.-D. 2000. c, T-dependence of the viscosity and the self-diffusion coefficients in some aqueous carbohydrate solutions. *Carbohydrate Research, 328,* 561-572.

Ranz, W.E. and Marshall, W.R., 1952. Evaporation from drops. *Chem. eng. prog*, *48*(3), pp.141-146.

Ranz, W. E. & Marshall, W. R. 1952b. EVAPORATION FROM DROPS .1. *Chemical Engineering Progress, 48,* 141-146.

Ranz, W. E. & Marshall, W. R. 1952c. EVAPORATION FROM DROPS .2. *Chemical Engineering Progress, 48,* 173-180.

Rogers, S., Wu, W. D., Lin, S. X. Q. & Chen, X. D. 2012. Particle shrinkage and morphology of milk powder made with a monodisperse spray dryer. *Biochemical Engineering Journal, 62,* 92-100.

Sadek, C., Pauchard, L., Schuck, P., Fallourd, Y., Pradeau, N., Le Floch-Fouéré, C. & Jeantet, R. 2015. Mechanical properties of milk protein skin layers after drying: Understanding the mechanisms of particle formation from whey protein isolate and native phosphocaseinate. *Food Hydrocolloids, 48,* 8-16.

Sadek, C., Schuck, P., Fallourd, Y., Pradeau, N., Jeantet, R. & Le Floch-Fouéré, C. 2016. Buckling and collapse during drying of a single aqueous dispersion of casein micelle droplet. *Food Hydrocolloids, 52,* 161-166.

Sadek, C., Schuck, P., Fallourd, Y., Pradeau, N., Le Floch-Fouéré, C. & Jeantet, R. 2014. Drying of a single droplet to investigate process–structure–function relationships: a review. *Dairy Science & Technology, 95,* 771-794.

Sadek, C., Tabuteau, H., Schuck, P., Fallourd, Y., Pradeau, N., Le Floch-Fouere, C. & Jeantet, R. 2013. Shape, shell, and vacuole formation during the drying of a single concentrated whey protein droplet. *Langmuir, 29,* 15606-13.

Sakata, Y., Shiraishi, S. & Otsuka, M. 2006. A novel white film for pharmaceutical coating formed by interaction of calcium lactate pentahydrate with

hydroxypropyl methylcellulose. *International journal of pharmaceutics,* 317**,** 120-126.

Samborska, K., Witrowa-Rajchert, D. and Gonçalves, A., 2005. Spray-drying of α-amylase—The effect of process variables on the enzyme inactivation. *Drying Technology*, *23*(4), pp.941-953.

Sano, Y. and Keey, R.B., 1982. The drying of a spherical particle containing colloidal material into a hollow sphere. *Chemical Engineering Science*, *37*(6), pp.881-889.

Sarkar, N. 1979. Thermal gelation properties of methyl and hydroxypropyl methylcellulose. *Journal of applied polymer science,* 24**,** 1073-1087.

Sarkar, N. 1995. Kinetics of thermal gelation of methylcellulose and hydroxypropylmethylcellulose in aqueous solutions. *Carbohydrate Polymers,* 26**,** 195-203.

Sartorius Ag. 2019. *Laboratory weighing laboratory balances* [Online]. Available: https://www.sartorius.com/shop/ww/en/usd/applications-laboratory-weighing-laboratory-balances/cubis®-micro-balance/p/MSE6.6S-000-DM [Accessed].

Schiffter, H. & Lee, G. 2007a. Single-droplet evaporation kinetics and particle formation in an acoustic levitator. Part 1: evaporation of water microdroplets assessed using boundary-layer and acoustic levitation theories. *J Pharm Sci,* 96**,** 2274-83.

Schiffter, H. and Lee, G., 2007. Single-droplet evaporation kinetics and particle formation in an acoustic levitator. Part 1: Evaporation of water microdroplets assessed using boundary-layer and acoustic levitation theories. *Journal of Pharmaceutical Sciences*, *96*(9), pp.2274-2283.

Schneider, C.A., Rasband, W.S. and Eliceiri, K.W., 2012. NIH Image to ImageJ: 25 years of image analysis. *Nature methods*, *9*(7), p.671.

Schutyser, M. a. I., Both, E. M., Siemons, I., Vaessen, E. M. J. & Zhang, L. 2018. Gaining insight on spray drying behavior of foods via single droplet drying analyses. *Drying Technology***,** 1-10.

Schutyser, M. a. I., Perdana, J. & Boom, R. M. 2012. Single droplet drying for optimal spray drying of enzymes and probiotics. *Trends in Food Science & Technology,* 27**,** 73-82.

Selvamuthukumaran, M. 2019. *Handbook on Spray Drying Applications for Food Industries*, CRC Press.

Siepmann, J. & Peppas, N. 2001. Modeling of drug release from delivery systems based on hydroxypropyl methylcellulose (HPMC). *Advanced drug delivery reviews,* 64**,** 163-174.

Silva, S. M., Pinto, F. V., Antunes, F. E., Miguel, M. G., Sousa, J. J. & Pais, A. A. 2008. Aggregation and gelation in hydroxypropylmethyl cellulose aqueous solutions. *J Colloid Interface Sci,* 327**,** 333-40.

Singh, S., Singh, S.K., Chauhan, M.G., Kumar, B., Pandey, N.K., Kaur, B., Kumar, A., Mohanta, S., Gulati, M., Wadhwa, S. and Yadav, A.K., 2019. Quality by Design-based Optimization of Formulation and Process Variables for Controlling Particle Size and Zeta Potential of Spray Dried Incinerated Copper Nanosuspension. *Recent Innovations in Chemical Engineering (Formerly Recent Patents on Chemical Engineering)*, *12*(3), pp.248-260.

Somashekarappa, H., Prakash, Y., Hemalatha, K., Demappa, T. and Somashekar, R., 2013. Preparation and characterization of HPMC/PVP blend films plasticized with sorbitol. *Indian Journal of Materials Science*, *2013*.

Souza, A.S., Borges, S.V., Magalhães, N.F., Ricardo, H.V., Cereda, M.P. and Daiuto, E.R., 2009. Influence of spray drying conditions on the physical properties of dried pulp tomato. *Food Science and Technology*, *29*(2), pp.291-294.

Stanford, M.K., Eylon, D. and DellaCorte, C., 2004. Effect of particle morphology on flow characteristics of a composite plasma spray powder. *Journal of Thermal Spray Technology*, *13*(4), pp.586-592.

Steckel, H. and Brandes, H.G., 2004. A novel spray-drying technique to produce low density particles for pulmonary delivery. *International journal of pharmaceutics*, *278*(1), pp.187-195.

Stunda-Zujeva, A., Irbe, Z. and Berzina-Cimdina, L., 2017. Controlling the morphology of ceramic and composite powders obtained via spray drying–a review. *Ceramics International*, *43*(15), pp.11543-11551.

Sugiyama, Y., Larsen, R., Kim, J. And Weitz, D. 2006. Buckling and Crumpling of Drying Droplets of Colloid-Polymer Suspensions. *Langmuir,* 22**,** 6024-6030.

Sunkel, J.M. and King, C.J., 1993. Influence of the development of particle morphology upon rates of loss of volatile solutes during drying of drops. *Industrial & engineering chemistry research*, *32*(10), pp.2357-2364.

Swindells, J.F., Snyder, C.F., Hardy, R.C. and Golden, P.E., 1958. *Viscosities of sucrose solutions at various temperatures: Tables of recalculated values* (Vol. 440). US Department of commerce, National Bureau of standards.

Telis, V., Telis-Romero, J., Mazzotti, H. & Gabas, A. 2007. Viscosity of aqueous carbohydrate solutions at different temperatures and concentrations. *International Journal of food properties,* 10**,** 185-195.

Thomas, K.T. and McAllister, R.A., 1957. Densities of liquid-acetone-water solutions up to their normal boiling points. *AIChE Journal*, *3*(2), pp.161-164.

Threlfall-Holmes, P. N. 2009. *Spray dryer modelling.* Heriot-Watt University.

Tran, T. T. H., Avila-Acevedo, J. G. & Tsotsas, E. 2016a. Enhanced methods for experimental investigation of single droplet drying kinetics and application to lactose/water. *Drying Technology,* 34**,** 1185-1195.

Tran, T. T. H., Jaskulski, M., Avila-Acevedo, J. G. & Tsotsas, E. 2016b. Model parameters for single-droplet drying of skim milk and its constituents at moderate and elevated temperatures. *Drying Technology,* 35**,** 444-464.

Tran, T. T. H., Jaskulski, M. & Tsotsas, E. 2017. Reduction of a model for single droplet drying and application to CFD of skim milk spray drying. *Drying Technology,* 35**,** 1571-1583.

Tsapis, N., Dufresne, E. R., Sinha, S. S., Riera, C. S., Hutchinson, J. W., Mahadevan, L. & Weitz, D. A. 2005. Onset of buckling in drying droplets of colloidal suspensions. *Phys Rev Lett,* 94**,** 018302.

Vehring, R. 2008. Pharmaceutical particle engineering via spray drying. *Pharm Res,* 25**,** 999-1022.

Vehring, R., Foss, W. R. & Lechuga-Ballesteros, D. 2007. Particle formation in spray drying. *Journal of Aerosol Science,* 38**,** 728-746.

Verderber PA, Judson King C. Measurehent of instantaneous rates of loss of voiatile compounds during drying of drops. *Drying Technology*. 1992 Sep 1;10(4):875-91.

El-Sayed, T.M., Wallack, D.A. and King, C.J., 1990. Changes in particle morphology during drying of drops of carbohydrate solutions and food liquids. 1. Effect of composition and drying conditions. *Industrial & Engineering Chemistry Research*, *29*(12), pp.2346-2354.

Walters, R.H., Bhatnagar, B., Tchessalov, S., Izutsu, K.I., Tsumoto, K. and Ohtake, S., 2014. Next generation drying technologies for pharmaceutical applications. *Journal of pharmaceutical sciences*, *103*(9), pp.2673-2695.

Walton, D.E. and Mumford, C.J., 1999a. The morphology of spray-dried particles: the effect of process variables upon the morphology of spray-dried particles. *Chemical Engineering Research and Design*, *77*(5), pp.442-460.

Walton, D.E. and Mumford, C.J., 1999b. Spray dried products—characterization of particle morphology. *Chemical Engineering Research and Design*, *77*(1), pp.21-38.

Walton, D.E., 2000. The morphology of spray-dried particles a qualitative view. *Drying Technology*, *18*(9), pp.1943-1986.

Wang, H., Sun, Y., Li, Y., Tong, X., Regenstein, J.M., Huang, Y., Ma, W., Sami, R., Qi, B. and Jiang, L., 2019. Effect of the condition of spray-drying on the properties of the polypeptide-rich powders from enzyme-assisted aqueous extraction processing. *Drying Technology*, pp.1-11.

Wang, W., Dufour, C. and Zhou, W., 2015. Impacts of spray-drying conditions on the physicochemical properties of soy sauce powders using maltodextrin as auxiliary drying carrier. *CyTA-Journal of Food*, *13*(4), pp.548-555.

Wang, Y. and Selomulya, C., 2019. Spray drying strategy for encapsulation of bioactive peptide powders for food applications. *Advanced Powder Technology*.

Weldes, H. H., Lange, K. R. J. I. & Chemistry, E. 1969. Properties of soluble silicates. 61**,** 29-44.

Wu, W.D., Patel, K.C., Rogers, S. and Chen, X.D., 2007. Monodisperse droplet generators as potential atomizers for spray drying technology. *Drying Technology*, *25*(12), pp.1907-1916.

Wulsten, E., Kiekens, F., Van Dycke, F., Voorspoels, J. & Lee, G. 2009. Levitated single-droplet drying: case study with itraconazole dried in binary organic solvent mixtures. *Int J Pharm,* 378**,** 116-21.

Yarin, A.L., Brenn, G., Kastner, O., Rensink, D. and Tropea, C., 1999. Evaporation of acoustically levitated droplets. *Journal of Fluid Mechanics*, *399*, pp.151-204.

Yoo, Y. J. & Um, I. C. 2013. Examination of thermo-gelation behavior of HPMC and HEMC aqueous solutions using rheology. *Korea-Australia Rheology Journal,* 25**,** 67-75.

Zografos, A.I., Martin, W.A. and Sunderland, J.E., 1987. Equations of properties as a function of temperature for seven fluids. *Computer Methods in Applied Mechanics and Engineering*, *61*(2), pp.177-187.

Appendix A LabVIEW codes

Appendix A.1 Code for mass flow controller
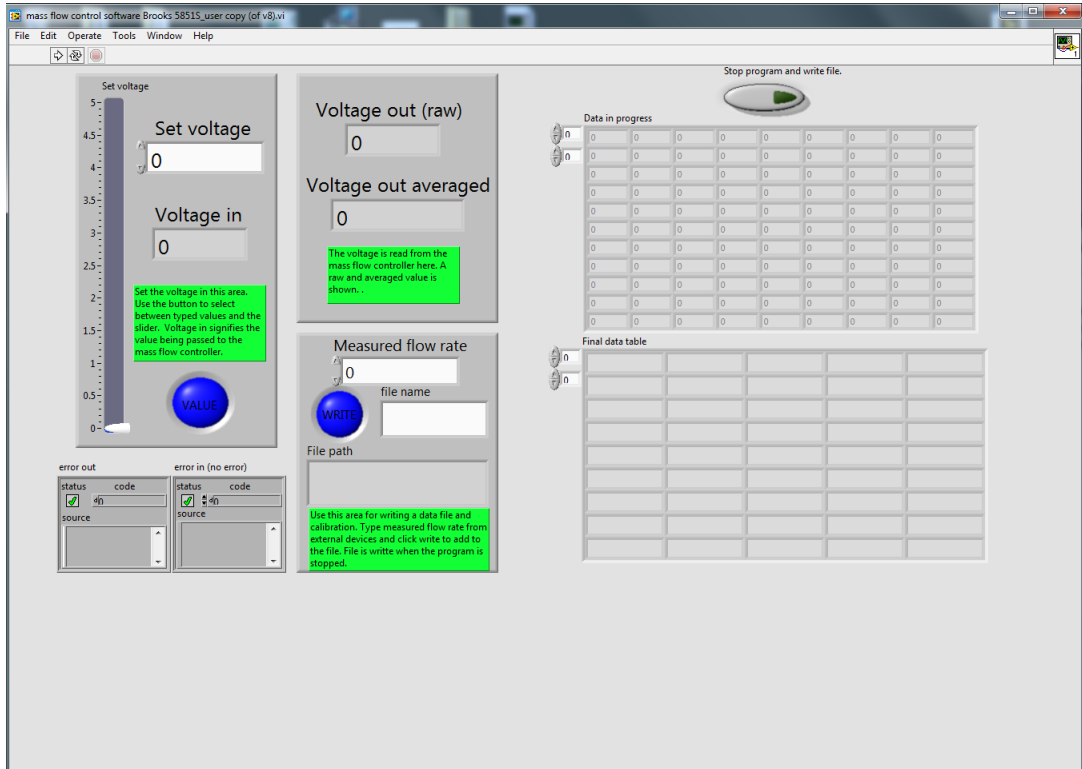
Figure A.1 The front panel view of the LabVIEW code to control the volumetric flow rate using the mass flow controller

Appendix A.2 Codes for data logging and synchronisation
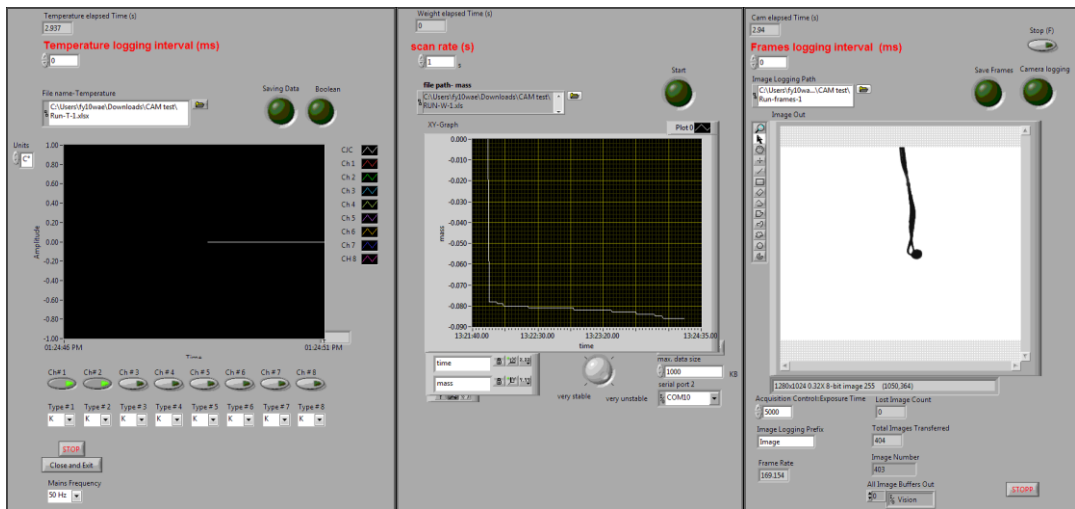
Figure A.2 Front panel view of the LabVIEW code to synchronise logging of temperature, mass and frames
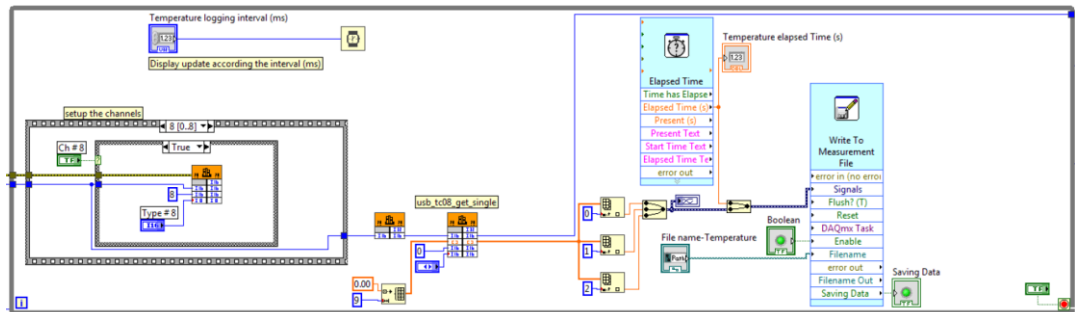
Figure A.3 LabVIEW code to measure droplet temperature
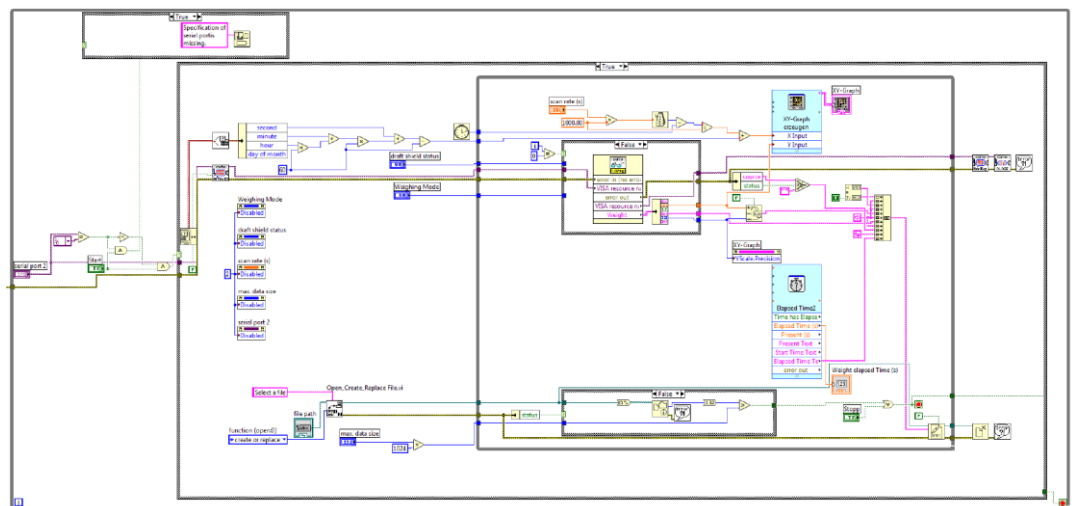
Figure A.4 LabVIEW code to log data from the analytical microbalance
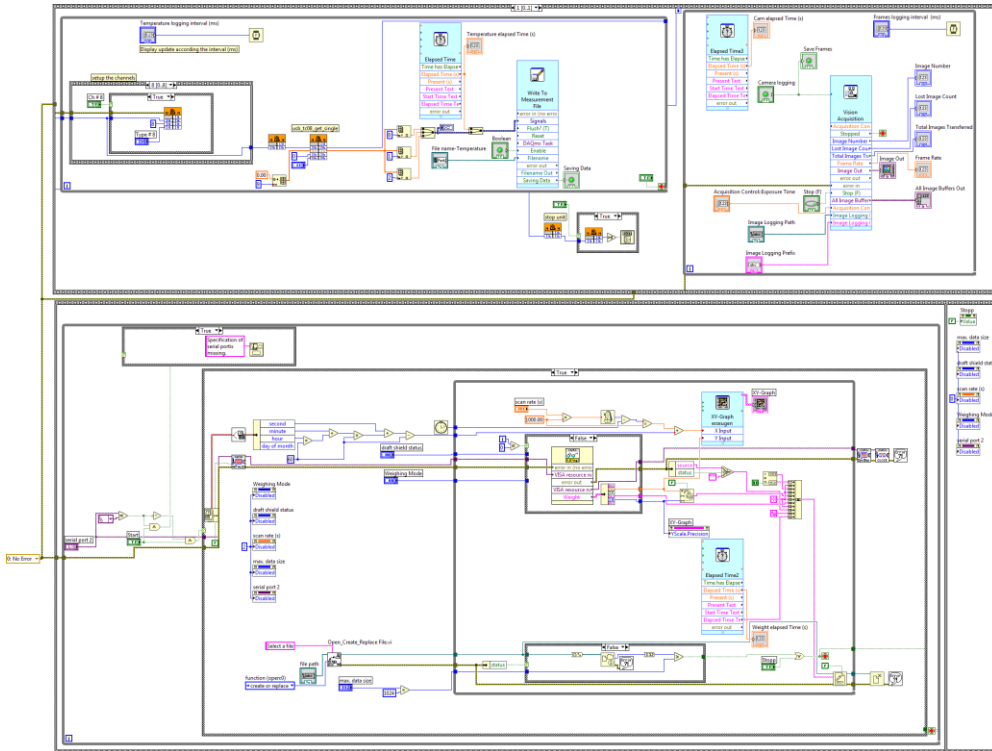
Figure A.5 Merged code to synchronise the logging of temperature, mass and frames
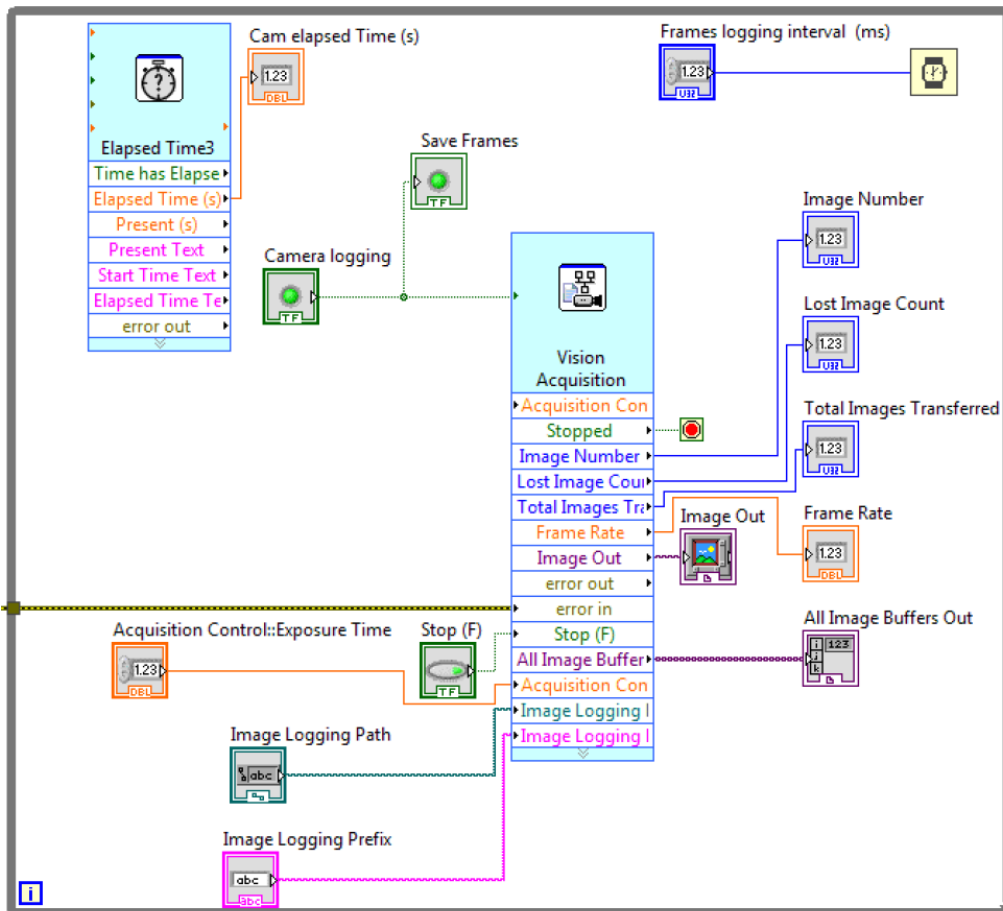
Figure A.6 LabVIEW code to capture images from the USB3 camera

Appendix B Single droplet apparatus validation

Appendix B.1 Validation at T_{air}=25 ˚C
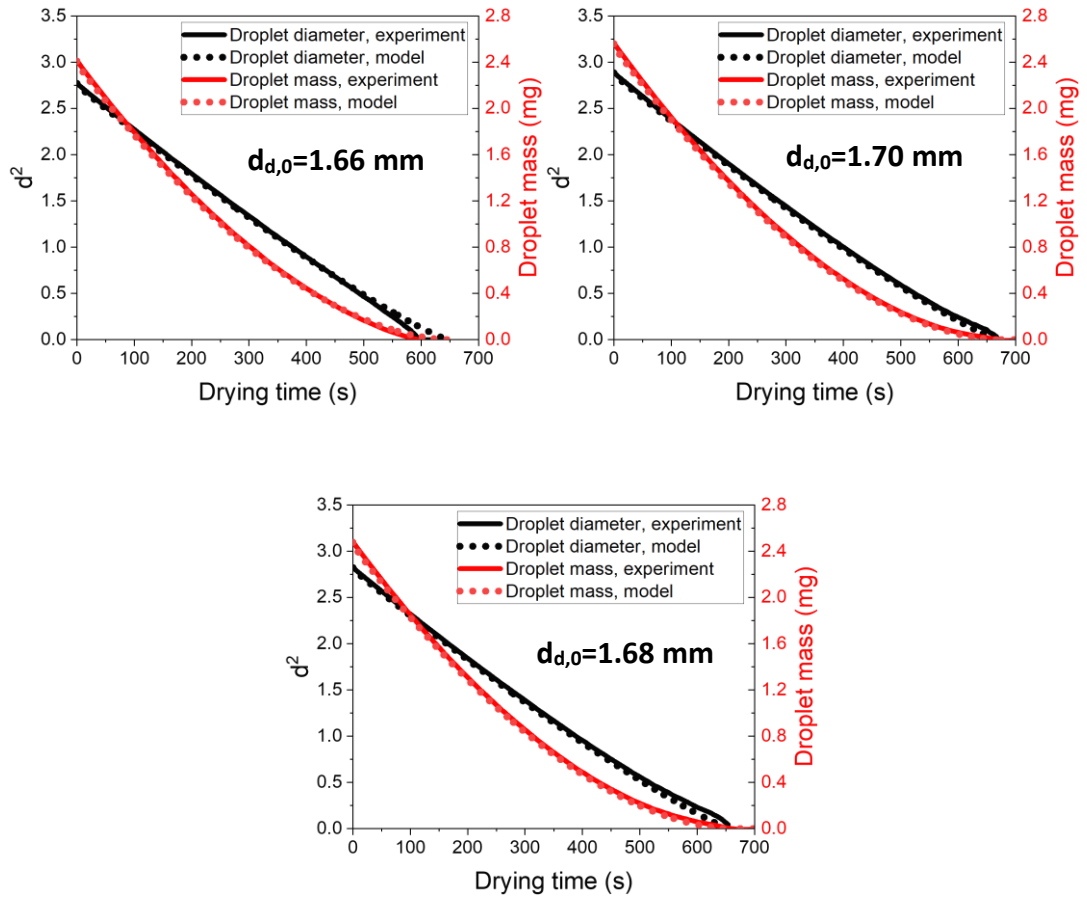
Figure B.7 Comparison of experimental drying runs of pure water vs Ranz-Marshall model

Appendix B.2 Validation at T_{air}=60 ˚C
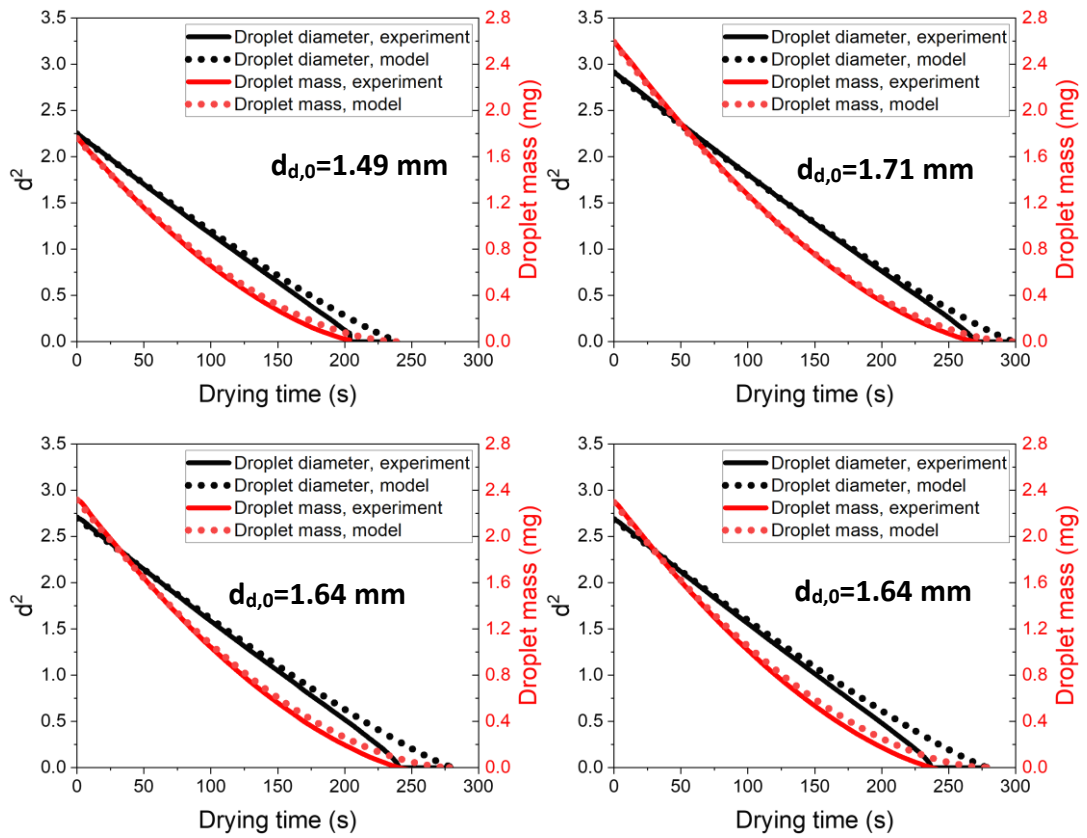
Figure B.8 Comparison of experimental drying runs of pure water vs Ranz-Marshall model at T_{air}=60 ˚C

Appendix B.3 Validation at T_{air}=100 ˚C
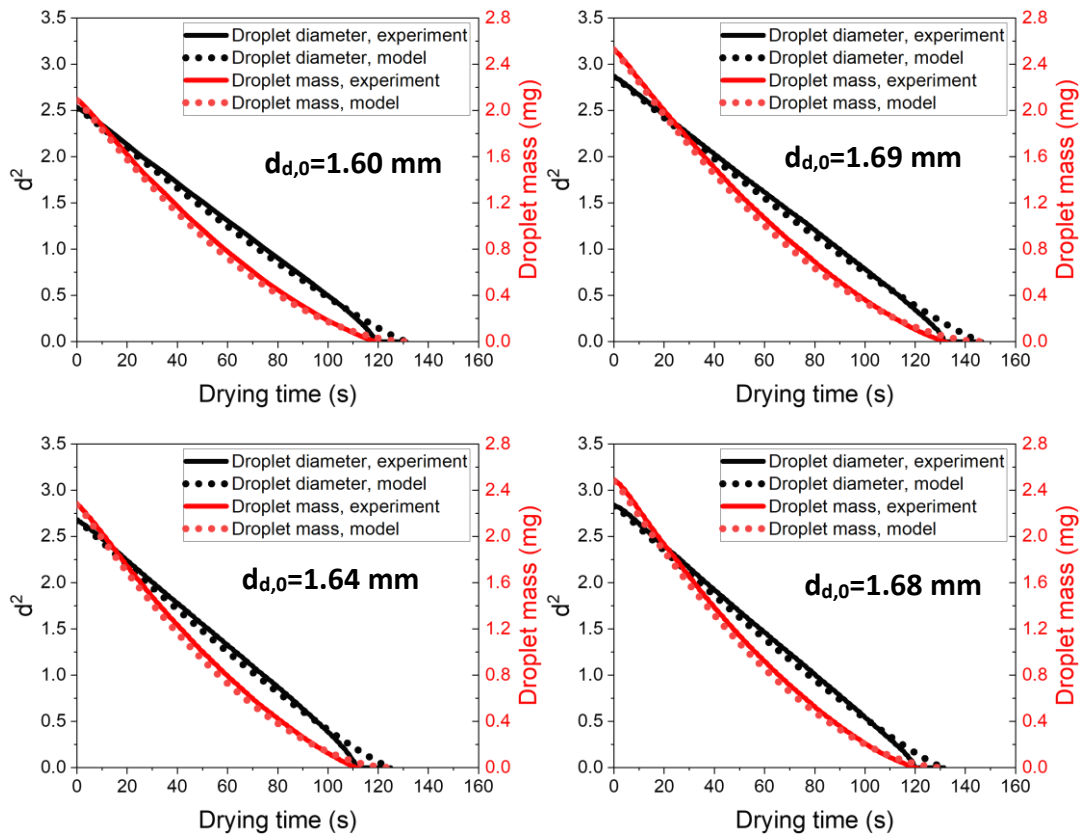
Figure B.9 Comparison of experimental drying runs of pure water vs Ranz-Marshall model at T_{air}=100 ˚C

Appendix B.4 Validation at T_{air} =160 ˚C
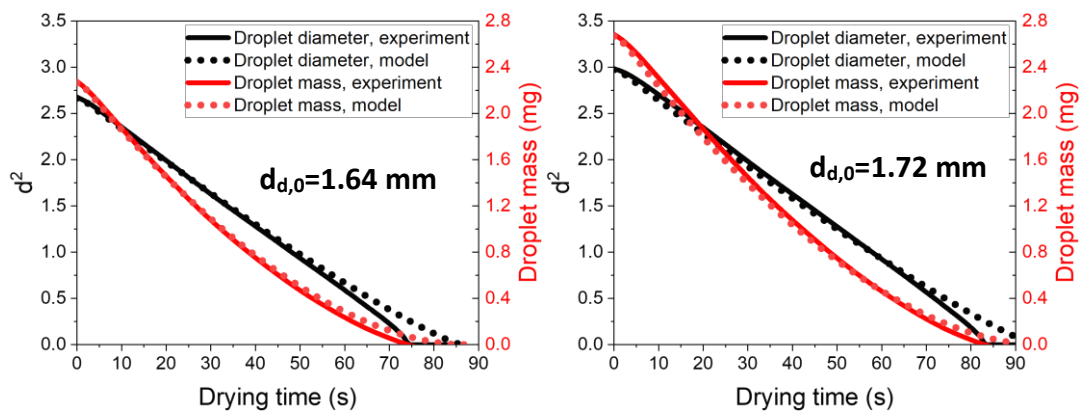
Figure B.10 Comparison of experimental drying runs of pure water vs Ranz-Marshall model at T_{air}=160 ˚C

Appendix B.5 Validation at T_{air} =180 ˚C
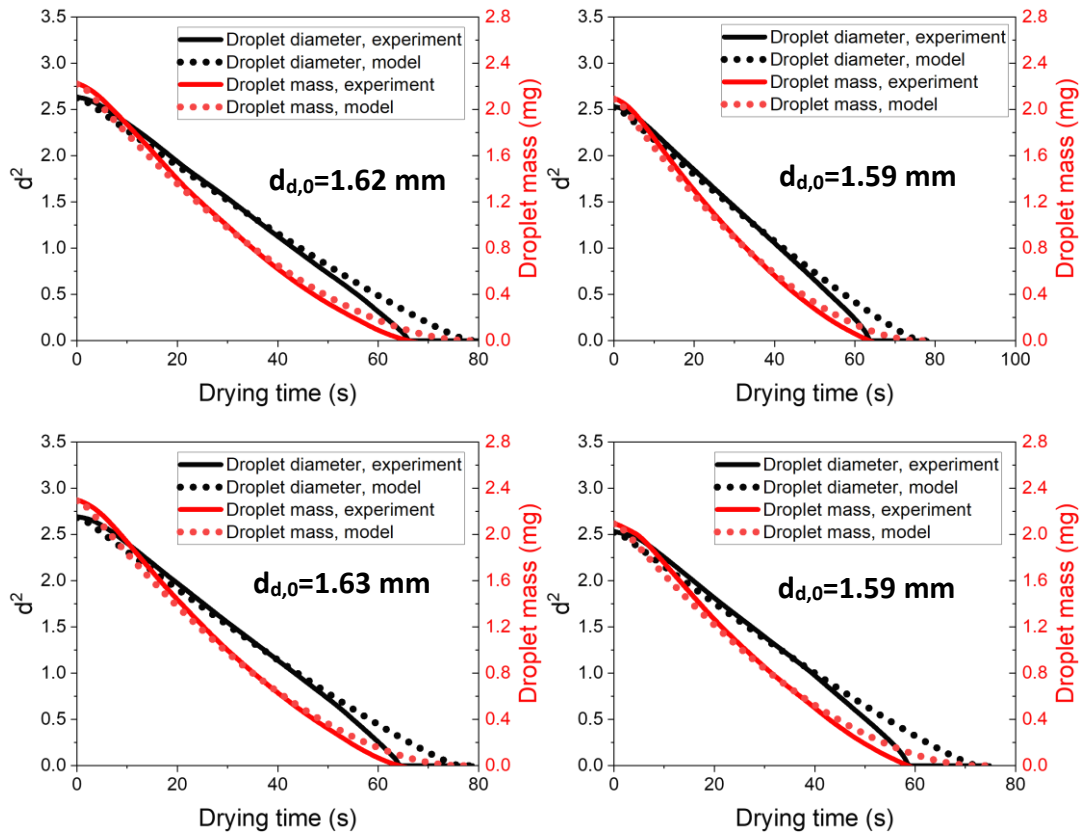
Figure B.11 Comparison of experimental drying runs of pure water vs Ranz-Marshall model at T_{air}=180 ˚C

Appendix C Sucrose diffusivity and rheology data

Table C.1 NMR Measurements of the Diffusion Coefficients (D) for sucrose in aqueous solutions (Ekdawi-Sever et al., 2003). Diffusion is reported as D×10^6 cm^2/s.

Sucrose Concentration (% w/w)	Temperature (˚C)		
	30	50	85
16	1.86	5.25	12.9
32	1.62	3.24	7.41
43	1.02	1.86	4.79
55	0.38	0.832	2.34
60	0.224	0.537	1.7
66	0.0933	0.269	1
68	0.049	0.182	0.776
72	0.0219	0.0851	0.49
74	0.0151	0.0589	0.355

Table C.2 Viscosities of sucrose solutions (Telis et al., 2007)

Concentration (% w/w)	10%	20%	30%	40%	50%	60%
Temperature (°C)		(mPa.s)				
0	1.98	3.8	6.3	14.77	40.44	206.08
5	1.76	3.15	5.12	11.53	30.19	148.76
10	1.61	2.68	4.58	9.88	27.02	114.37
15	1.41	2.26	3.77	7.47	19.02	74.98
20	1.26	1.96	3.21	6.2	15.04	56.76
25	1.13	1.7	2.65	5.17	11.49	43.88
35	0.89	1.35	2.07	3.8	8.69	26.67
40	0.82	1.2	1.79	2.25	6.35	21.32
45	0.74	1.06	1.51	2.84	5.04	17.2
50	0.66	0.98	1.36	2.52	4.78	14.07
55	0.57	0.89	1.2	2.22	3.56	11.72
60	0.52	0.81	1.06	1.98	2.98	9.88
65	0.45	0.74	0.92	1.77	2.42	8.35
70	0.42	0.69	0.85	1.62	2.34	7.2
80	0.32	0.59	0.68	1.33	1.52	5.43
85	0.28	0.55	0.59	1.22	1.31	4.75

The activity coefficient of water in sucrose solutions relationship was taken from (Hecht, 1999) and is based on measurements conducted by (Hirschmüller, 1953)

$$a_w = exp(3.63x_s^3 - 5.31x_s^2)$$ (8.1)

Appendix D Sodium silicate morphology time series
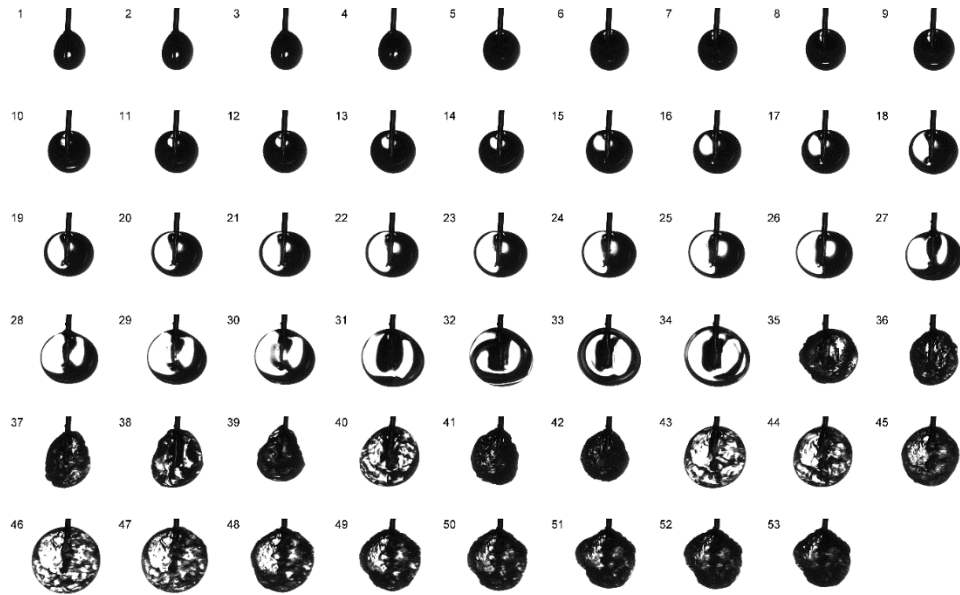
Figure D.12 Growing behaviour during boiling, drying of 17% w/w sodium silicate droplet at 180 ˚C
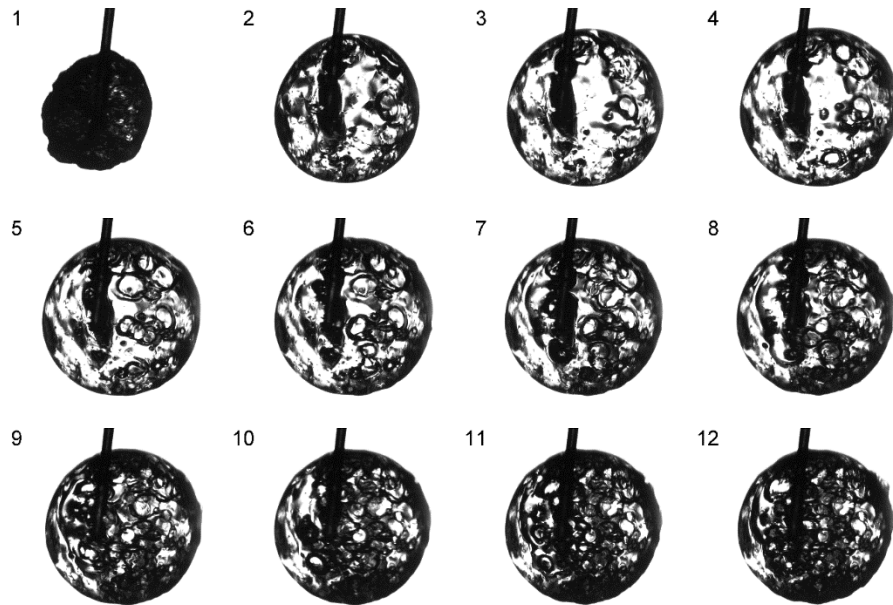
Figure D.13 Surface bubbling at the surface during an inflation cycle of 45% w/w silicate droplet at 180 ˚C

Appendix E Morphology time series

Table E.3: Morphology development of sucrose during single droplet drying with 15% initial solid concentration at v_{air}=0.57 m/s and different air temperatures

T_{air}=60°C										1.5 mm
t(s)	0	20	40	60	80	100	120	140	180	280
T_d(°C)	17	28	29	29	30	32	35	42	54	61

T_{air}=100°C										1.5 mm
t(s)	0	15	30	45	60	75	90	105	145	175
T_d(°C)	23	39	39	40	43	55	71	83	97	99

T_{air}=140°C										1.5 mm
t(s)	0	20	40	62	72	73	83	83	94	147
T_d(°C)	28	58	70	105	112	113	127	126	133	135
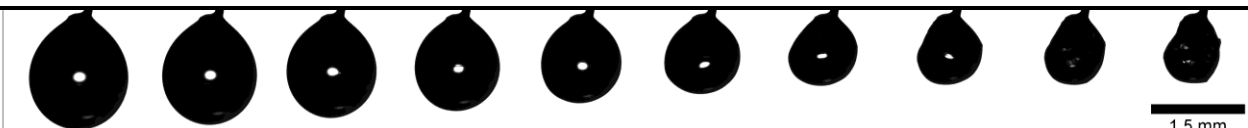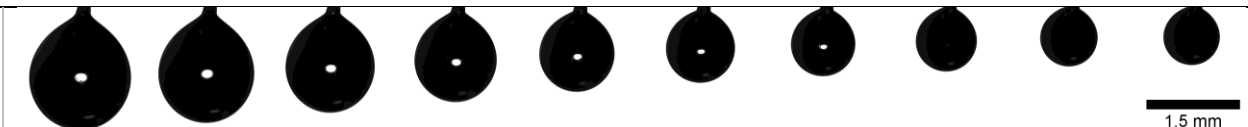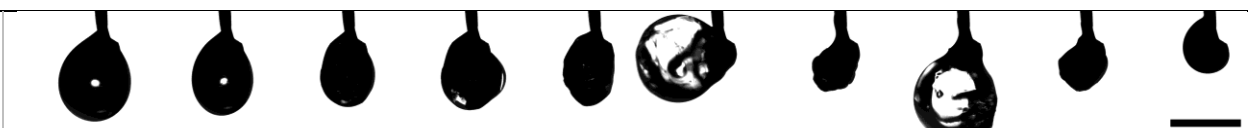
T_{air}=180°C										1.5 mm
t(s)	0	10	30	31	32	35	36	37	38	77
T_d(°C)	29	84	121	120	124	137	144	150	158	177

Table E.4 Morphology development during single droplet drying of sodium silicate with 17% initial solid concentration at v_{air}=0.57 m/s and different air temperatures.

T_{air}=60°C										
t(s)	0	20	40	60	80	100	120	140	180	280
T_d(°C)	18	29	31	35	38	43	47	50	54	58

T_{air}=100°C										
t(s)	0	15	30	45	60	75	90	105	145	175
T_d(°C)	22	42	47	53	62	70	77	83	93	96

T_{air}=140°C										
t(s)	0	20	60	89	89	104	107	118	123	138
T_d(°C)	27	64	104	113	113	128	128	132	132	134

T_{air}=180°C										
t(s)	0	20	40	59	59	63	64	69	75	145
T_d(°C)	25	79	111	126	127	132	134	153	163	167

Table E.5 Morphology development during single droplet drying of HPMC with 5% initial solid concentration at v_{air}=0.57 m/s and different air temperatures, the air is passing from right to left
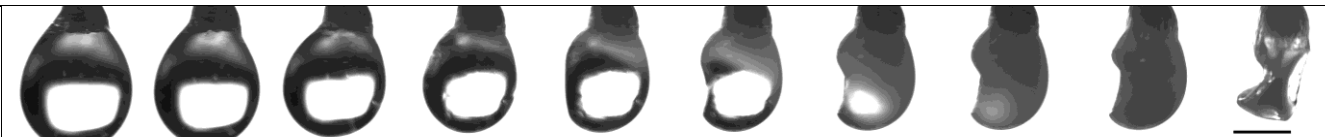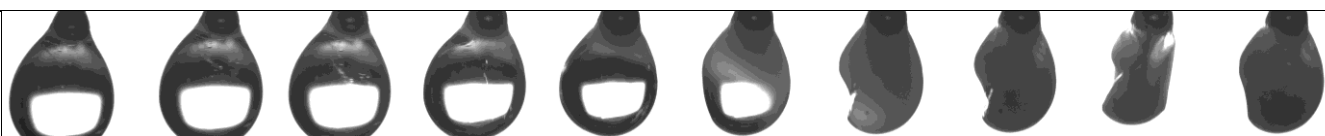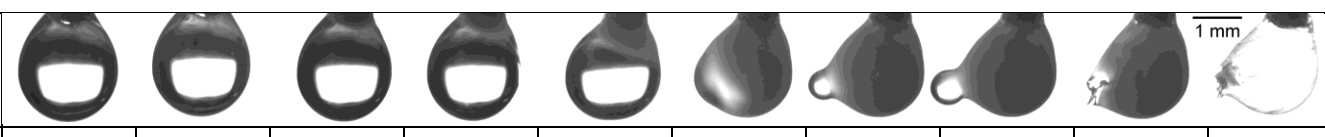
T_{air}=60°C										
t(s)	0	51	101	106	115	122	129	146	162	260
T_d(°C)	17	30	36	37	39	41	42	44	46	63

T_{air}=100°C										
t(s)	0	24	45	51	54	60	72	79	107	151
T_d(°C)	34	47	56	59	60	64	72	75	84	99

T_{air}=140°C										
t(s)	0	14	26	32	35	38	43	79	86	106
T_d(°C)	46	58	70	77	82	87	93	120	122	138

T_{air}=180°C										
t(s)	0	6	11	13	15	18	37	53	63	79
T_d(°C)	53	73	82	86	91	98	123	163	178	180

Table E.6 Morphology development during single droplet drying of HPMC with 15% initial solid concentration at v_{air}=0.57 m/s and different air temperatures,air is passing from right to left
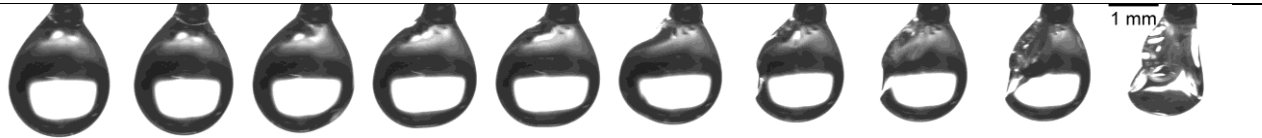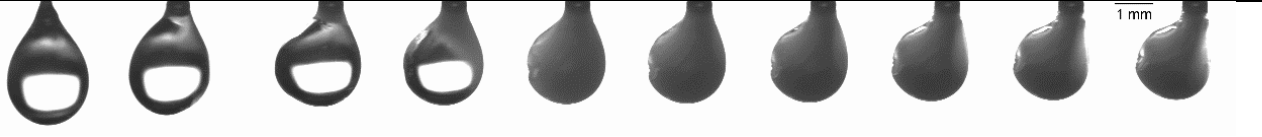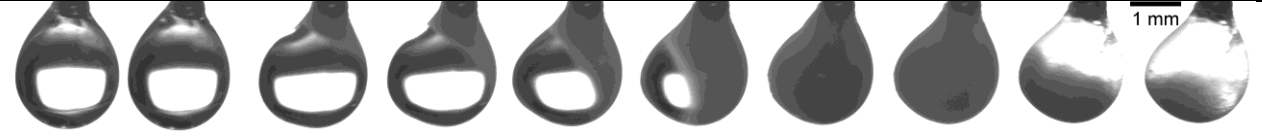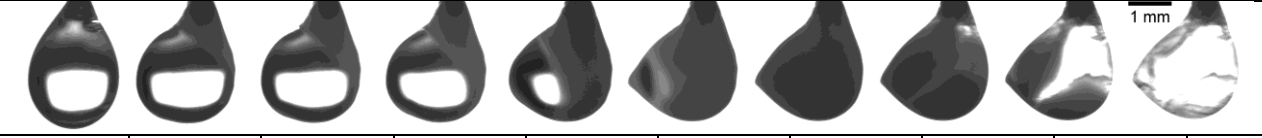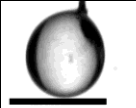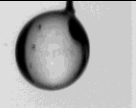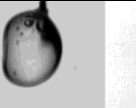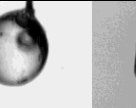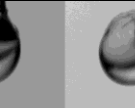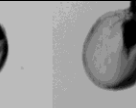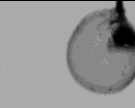
T_{air}=60 °C										
t(s)	0	31	49	59	67	78	89	106	132	214
T_d(°C)	17	34	38	41	42	44	45	47	48	57

T_{air}=100 °C										
t(s)	0	9	27	29	31	35	39	50	91	214
T_d(°C)	40	52	68	70	71	74	76	81	87	100

T_{air}=140 °C										
t(s)	0	10	11	13	15	17	19	78	103	119
T_d(°C)	26	69	72	77	82	86	93	127	137	138

T_{air}=180 °C										
t(s)	0	3	4	5	7	8	35	39	56	69
T_d(°C)	25	60	70	78	85	91	163	169	176	178

Table E.7: Morphology development of single droplets containing 5% w/w HPMC in a mixture of acetone and water with weight percentages of 70% w/w and 30% w/w respectively at v_{air}=0.57 m/s and different air temperatures.

T_{air}=60°C										
t(s)	0	11	29	34	39	50	58	67	81	129
T_d (°C)	5	26	35	37	39	42	44	45	48	61

T_{air}=100°C										
t(s)	0	4	10	14	19	26	33	36	42	54
T_d (°C)	35	48	59	63	69	75	84	85	87	105

T_{air}=140°C										
t(s)	0	7	13	20	23	30	35	42	47	54
T_d (°C)	9	46	62	71	75	71	89	122	135	136
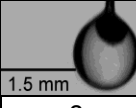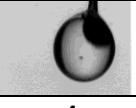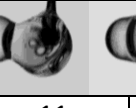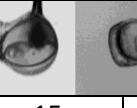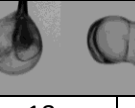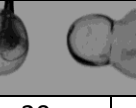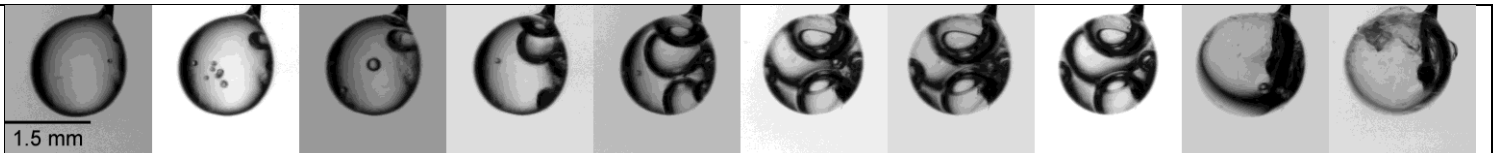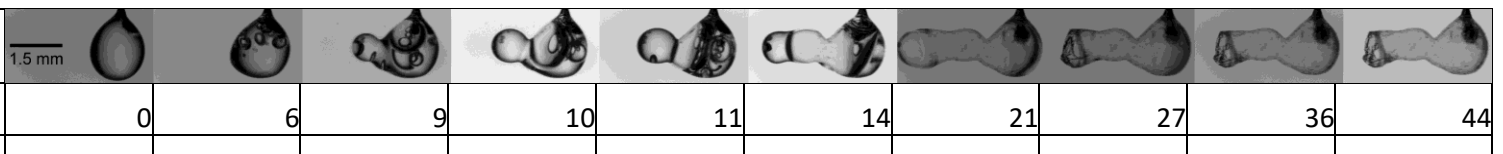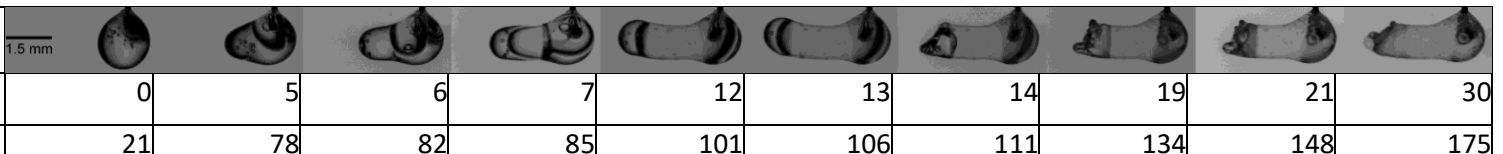
T_{air}=180°C										
t(s)	0	4	8	10	11	15	18	20	22	24
T_d (°C)	14	62	85	88	92	125	167	176	177	177

Table E.8: Morphology development of single droplets containing 15% w/w HPMC in a mixture of acetone and water with weight percentages of 70% w/w and 30% w/w respectively at v_{air}=0.57 m/s and different air temperatures.

T_{air}=60°C										
t(s)	0	4	8	12	15	22	32	47	65	122
T_d (°C)	16	32	39	42	44	46	49	51	54	60

T_{air}=100°C										
t (s)	0	7	13	16	22	30	37	42	51	68
T_d (°C)	17	57	64	66	69	72	73	75	76	102

T_{air}=140°C										
t(s)	0	6	9	10	11	14	21	27	36	44
T_d (°C)	21	71	74	75	77	79	98	112	137	138

T_{air}=180°C										
t(s)	0	5	6	7	12	13	14	19	21	30
T_d (°C)	21	78	82	85	101	106	111	134	148	175